THE EFFECTS OF ROTATION AND WALL COMPLIANCE ON HYDRODYNAMIC STABILITY

ALISON J. COOPER

B.Sc. (Hons)

A thesis submitted for the degree of Doctor of Philosophy

Department of Engineering

University of Warwick

Coventry CV4 7AL

January 1996

TO MY FAMILY

CONTENTS

LIST OF FIGURES

LIST OF TABLES

ACKNOWLEDGEMENTS

This thesis is dedicated to my Mum and Dad whose care and support has always been, and continues to be, of immense encouragement to me and is dearly appreciated.

I would like to thank my supervisor, Professor Peter W. Carpenter, for his guidance and to express my gratitude for his help over the last two years or so. I would also like to thank Dr. Tom J. Bridges who supervised my early work at the Mathematics Institute and Dr. Chris Davies for his helpful discussions.

Special thanks must also go to Matthew Keeling whose understanding and reassurance have been so important to me.

This degree programme was funded by the Engineering and Physical Sciences Research Council.

DECLARATION

I certify that this thesis is my own composition and that except where specific reference is made is an account of work undertaken by myself. No part of this thesis has been submitted for a degree at any other university.

Some of the work in Chapter 2 has been published in :
Bridges, T.J., and Cooper, A.J., (1995)
"Spanwise Modulation of Streamwise Rolls in Rotating Channel Flow", *Q. J. Mech. Appl. Math.*, **48**, pp. 257-284.

Parts of Chapter 6 appear in :
Cooper, A.J., and Carpenter, P.W., (1995)
"The Effects of Wall Compliance on Instability in Rotating Disc Flow", *AIAA 95-2257.*

SUMMARY

The effects of system rotation and passive wall compliance on hydrodynamic stability is investigated.

Rotating channel flow is studied where a Coriolis force instability mechanism produces streamwise rolls at modest Reynolds numbers and rotation rates. The linear stability of mean flow states consisting of a combination of plane Poiseuille and Couette flows is considered using spectral Chebyshev collocation with a staggered grid. A Newton algorithm is implemented in three-dimensional parameter space to calculate minimum points of the neutral surfaces. Weakly nonlinear behaviour of the rolls is studied using a Ginzburg-Landau formulation and accurate numerical values for the equation coefficients indicate supercritical instability.

Effects of external pressure gradient and three-dimensionality on boundary layer stability over compliant walls is examined. In these cases an inflexion point in the boundary layer profile promotes a powerful inviscid instability mechanism.

Two-dimensional profiles, including a Falkner-Skan representation, are considered in inviscid and viscous analyses with plate-spring and viscoelastic compliant wall models. Walls which are rendered stable with respect to hydroelastic instabilities are shown to reduce maximum spatial growth rates by up to 60%.

This work is extended to consider the three-dimensional boundary layer over a rotating disc where inviscid (Type 1) and viscous (Type 2) instabilities can coexist. A single layer viscoelastic wall model coupled to a sixth order system of fluid equations, which accounts for Coriolis and streamline curvature effects, is solved by a spectral Chebyshev tau technique. The Type 1 stationary instability is found to be significantly stabilised, whilst the effect on the Type 2 mode is complex but can be destabilising. For travelling-wave modes, across a band of positive frequencies, evidence of modal coalescence between the Type 1 and 2 instabilities leading to absolute instability is presented. This would constitute a major route to transition and appears to be caused by large values of viscous stress work at the wall/flow interface.

CHAPTER 1

INTRODUCTION.

1.1 General Overview.

The subject of hydrodynamic stability has remained a fundamental area of research in fluid mechanics since the pioneering work of Osborne Reynolds over a century ago. The tendency for laminar flows to become unstable leading to a turbulent state was first demonstrated by Reynolds' experiments in 1883 and this phenomenon continues to provide an important area of interest because of the implications of this in many real situations and engineering applications. As a whole the subject of hydrodynamic stability can cross over many scientific fields from engineering, meteorology and oceanography to more applied areas such as astrophysics and geophysics. Theoretical studies have always been hindered by the nonlinear nature of the governing stability equations and thus stability analyses have relied heavily on simplified problems and the use of linearised theory. The advancement of computing capabilities and the introduction of new mathematical techniques aimed at extracting some of the nonlinear characteristics now allows more complex stability problems to be analysed.

The way in which laminar flow becomes unstable and what determines when the transition process occurs are both dependent on flow configuration and external influences such as buoyancy effects brought about by fluids of variable density, magnetohydrodynamic forces, external pressure gradients and centrifugal and Coriolis effects brought about by system rotation. Laminar-turbulent transition is generally initiated by some change in the balance of forces within the flow system which acts to alter the flow structure. In boundary layer or plane channel flows, for example, instability first appears when travelling Tollmien-Schlichting (T-S) waves become amplified. When this occurs depends on certain parameters of the flow, characterised by the Reynolds number. For example, in the above two cases when the Reynolds number is raised above a critical value the driving pressure forces cease to be balanced by forces which are inertial and viscous in nature and amplification of disturbances in the flow are brought about. In general viscosity has a stabilising influence on a flow because of its ability to dissipate disturbance energy so only when viscosity is taken below some level will the equilibrium of forces be unbalanced.

In other flow configurations the forces required to maintain laminar flow are of a completely different origin and when laminar flow breaks down the instability observed takes on

a different form to that of the propagating T-S waves. The appearance of stationary roll cells is the result of the departure from the laminar state when a fluid layer between two plates is heated from below. In this case density divisions instigate the onset of the instability. These roll cells also develop in geophysical flows where body forces govern the transition process and of particular importance in the formation of these roll cells are body forces arising as a result of system rotation. An imbalance between centrifugal force on the fluid particles and the local pressure gradient is responsible for the centrifugal instability observed in cylindrical Couette flow. When the angular velocity of the inner cylinder exceeds some critical value so-called Taylor vortices are generated which occur periodically in the axial direction and in this case each close to form a toroidal shape. The vortex structure then undergoes a series of secondary-type instabilities as the rotation speed is increased leading ultimately to a turbulent state. This type of phenomenon is also apparent for flows in curved channels and over concave walls. Roll cells can also develop as a result of a Coriolis force mechanism acting on flow systems and is a route to transition in shear flows.

Negative pressure gradients have a destabilising influence because adverse pressure gradients generate points of inflexion in the associated velocity profiles which is a condition originally shown by Rayleigh (1880) to give rise to an inviscid instability mechanism. This in turn generally leads to powerful instabilities.

Areas of commercial interest as far as stabilising flows is concerned lie in reducing drag over surfaces. In essence if the flow can be stabilised by external factors, such that the result is the maintenance of laminar flow over a greater part of the surface, then the drag reductions on bodies moving in a fluid achieved by this could be exploited to gain greater speeds/fuel efficiency. This process is generally known as laminar flow control and various methods have been used in attempts to achieve this. For application in air suction techniques have been applied both in theory and practise with theoretical results indicating the potential for this method as a means of laminar flow control but problems in practise have limited full-scale implementation of such a method. More recently wall compliance or boundary flexibility has been shown to be effective in postponing the laminar-turbulent transition process in marine applications.

1.2 Motivation.

This study is divided into two clearly defined areas but both involve the effect of external influences on clearly defined problems in hydrodynamic stability. What motivates the cur-

rent work is then two-fold.

1.2.1 The Effects of Rotation on Plane Channel Flow.

In the first case the effect of rotation on a well-known flow configuration is assessed where the influence of rotation is studied through the action of Coriolis forces rather than centrifugal influences. The centrifugal instability mechanism has received a considerable amount of attention, for example in the classical Taylor-Couette concentric cylinder problem, and has lead to a substantial understanding of the transition process in geometries affected by this mechanism. However, the Coriolis force instability mechanism which generates the roll-cell form of primary instability has received comparatively less consideration. A particular example of the effects of Coriolis forces on shear flow is that of a flow in plane channel subject to rotation about some spanwise axis. Over the past twenty years or so this problem has begun to attract more interest both theoretically and experimentally.

The work of Benton (1956) on the rotation of pipe flow was perhaps the first to give evidence of longitudinal roll cells, but it was not until Halleen and Johnston (1967) and Hart (1972) that experiments were undertaken on the rotating channel. Hart had recognised that the majority of experiments concerning rotating fluids had, up to that date, tended to concentrate on cylindrical systems. As well as focusing only on the centrifugal instability mechanism these experiments were designed for operation under high rates of rotation. A feature of the Coriolis force instability, which occurs in rotating channel flow, is the onset of streamwise roll cells at much lower rotation rates and Reynolds numbers than other unstable flows. For example, T-S waves in a plane channel become amplified at a Reynolds number almost two orders of magnitude higher than that required for the onset of roll cells when the system is subjected to spanwise rotation. This indicates the comparative strength of the Coriolis force instability mechanism. Further experimental investigations have been carried out more recently by Alfredsson and Persson (1989) who provide results in part through the use of flow visualisations. New work by Marliani *et al.* (1994) has sought to consider the effects of moderate acceleration and deceleration on rotating channel flow.

Alongside the experimental investigations are a number of numerical studies and of importance are the direct numerical simulations of Speziale and Thangham (1983), Ng *et al.* (1990), Guo and Finlay (1991), Yang and Kim (1991) and Kristofferson and Andersson (1993). The majority of this work has concentrated on laminar flow but some consideration has been made on the effect of rotation on fully turbulent channel flow. Interest here,

however, is mainly on the laminar flow case but some turbulent flow results will be discussed.

The instabilities which arise when a plane channel is subjected to rotation about a spanwise axis differ in a number of ways to the same flow situation in the absence of rotation. Knowledge about the behaviour of these roll cells is of fundamental importance in leading to a greater understanding of the physics of transition in shear flows. A number of such flows can be established within the channel geometry, the most widely studied being that of plane Poiseuille which possesses the characteristic parabolic streamwise velocity profile. Attention here will focus on a wider family of basic profiles which interpolates between plane Poiseuille flow and plane Couette flow which is linearly stable in the absence of rotation. This problem is also amenable to investigation of the role of nonlinear stability of the flow where previously the Stuart-Landau expansion or weakly nonlinear theory has been used to consider the nature of the bifurcation to streamwise rolls with Finlay (1989), Ng *et al.* (1990) and Singer (1992) establishing supercritical bifurcation to rolls in rotating Poiseuille flow which effectively means the roll cells settle down to form a new laminar flow. A variation on this method will be made through the derivation of a Ginzburg-Landau equation. This was originally derived by Newell and Whitehead (1969) when considering the stability problem of Bénard convection but has not commonly been used in the present context. One advantage of using this sort of equation rather than the standard weakly nonlinear theory is that the stability of the rolls to spanwise modulation may be considered. This type of instability, known as Eckhaus instability, can become significant in problems with large aspect ratio.

Exploring the instability characteristics in this geometry would be of interest in application to devices involving rotating fluids. Examples often cited are flows in turbine blades, inside impellers of centrifugal pumps and certain geophysical flows.

1.2.2 The Effects of Wall Compliance on Boundary Layer Stability.

The second case of interest is that of controlling laminar-turbulent transition through the use of wall compliance in an area that has to date been left largely unexplored. This involves applying existing knowledge on the effects of wall compliance to instabilities which are inviscid in nature rather than the T-S instability where results are well documented.

It has now been well established, both theoretically and experimentally, that the use of wall compliance can lead to the substantial postponement of laminar-turbulent transition. The benefits of such a response are open to exploitation particularly in the area of marine

applications. The skin friction drag reducing capabilities of compliant walls suggests increased vessel speeds and greater energy efficiency could be possible. The maintenance of laminar flow over a body is also known to greatly reduce the degree of noise it produces which would give submerged bodies an increased transparency to detection. Compliant walls could therefore also be useful as an acoustic application.

The original work in this novel field of laminar flow control was undertaken by Kramer (1960) under the inspiration of the phenomenal swimming speeds attained by dolphins after Gray (1936), from a purely observational point of view, first brought this subject to the attention of the scientific community. Kramer investigated the structure of the dolphin skin and developed several prototype coatings designed to simulate the skin properties. Testing was performed by measuring the drag on solid bodies covered with coatings of different material specification. Significant reductions in drag were recorded and Kramer implied this was possible as a result of distributed damping. In other words, the inclusion of a highly viscous fluid within the wall was thought to damp out the fluid instabilities which initiate the transition process.

Early theoretical work to follow was that of Benjamin (1960,1963) and Landahl (1962). This research supported the case for achieving drag reduction through the use of compliant walls but at the same time indicated the possibility of additional wall-based modes of instability absent in the case of rigid boundaries. Contrary to Kramer's theory on the control mechanism the work of Benjamin showed that wall damping actually destabilised T-S waves. Damping in the original walls was probably successful in suppressing wall-based instabilities rather than reducing the growth rates of the flow-based instabilities as first suggested by Kramer. Despite its apparent success Kramer's work was thrown heavily into doubt on the grounds of subsequent experimental research where verification of results was sought but no corroborative evidence was ever achieved.

The last decade, however, has seen a revival in the interest of wall compliance as a means of controlling the transition process following the theoretical work of Carpenter and Garrad (1985, 1986). This was able to confirm the valid performance of walls based on Kramer's original construction. It was also demonstrated that these original prototypes were close to so called optimum walls where optimum performance of a compliant wall is achieved through a critical choice of wall parameters which brings about the delicate balance between reduction of flow based instability growth rates and the generation of wall based instabilities of the type identified by Benjamin and Landahl. A substantial body of work followed and notable theoretical contributions have been made by Carpenter and Morris (1990) who used a novel plate-spring construction to represent an anisotropic compliant wall theoretically, Sen and

Arora (1988) and Yeo (1988) who modelled wall compliance with multiple layers of viscoelastic material. A breakthrough in carefully controlled experiments was made by Gaster (1987) and Daniel *et al.* (1987) who assessed the effects of wall compliance on Tollmien-Schlichting (T-S) waves in flat plate boundary layers. Results confirmed that wall compliance could have a significant stabilising influence on the T-S waves thus effectively leading to a delay in the onset of transition. Comprehensive reviews of the work have been made by Riley *et al.* (1988), where the emphasis is on experimental work, Gad-el-Hak (1986) and Carpenter (1990). More recent work by Dixon *et al.* (1994), not included in the aforementioned publications, has conservatively indicated six fold increases in transitional Reynolds number using specifically optimised compliant walls.

Most of the preceding research has concentrated on the effects of wall compliance in relation to the two-dimensional flat plate boundary layer with zero external pressure gradient. In this case the boundary layer disturbances take the form of T-S waves which become destabilised by an essentially viscous mechanism. Wall compliance basically controls this type of instability by reducing the rate of production of disturbance kinetic energy by the Reynolds stress, by increasing the viscous dissipation and bringing in additional energy dissipation mechanisms. The effect of a compliant boundary therefore alters the ratio between energy production and dissipation allowing the growth of boundary layer disturbances to be suppressed.

In real aerospace and marine applications, however, boundary layers are usually three-dimensional and/or develop in a non-zero pressure gradient which is likely to be adverse over some part of the surface. The effects of external pressure gradient and three-dimensionality of the boundary layer on compliant wall performance has remained largely unexamined. If wall compliance is ever to be viable as a practical means of maintaining laminar flow then its performance under these conditions must be critically assessed.

The instabilities which arise in boundary layers under these alternative flow conditions are of a different nature to the T-S instability. Velocity profiles with points of inflexion can develop either because of the effects of an adverse pressure gradient or as a result of the three-dimensionality of the flow. The presence of an inflexion point in the two-dimensional velocity profile promotes the more powerful inviscid intability mechanism identified by Rayleigh (1880). A physical reasoning for the occurrence of this type of instability was presented by Lin (1945) who considered the vorticity field associated with the mean undisturbed flow and identified an instability mechanism qualitatively through momentum transfer arguments. The growth of disturbances by this mechanism persists to indefinitely high Reynolds num-

ber with amplification rates considerably higher than those of the T-S instability and the transition region is typically shortened in two-dimensional flows by the presence of an adverse pressure gradient. It therefore needs to be established whether passive wall compliance is capable of controlling disturbance growth to a sufficient extent when this inflexion point instability dominates.

Three-dimensional flows of research interest include boundary layers which develop over sweptback wings, rotating cones and rotating discs as well as those specific to other aerospace and marine applications. Fully three-dimensional boundary layers are susceptible to a form of instability known as crossflow instability which invariably dominates the breakdown of laminar flow. This form of instability is common only to three-dimensional boundary layers and is a route to transition in the leading edge region of swept wings. A characteristic feature associated with the crossflow phenomenon is the presence of a velocity component within the boundary layer which exhibits a point of inflexion which then promotes an instability mechanism dominated by inviscid effects somewhat analogous to the Rayleigh instability of two-dimensional flows.

Discovery of the crossflow instability is attributed to Gray (1952) who observed, whilst studying the flow over sweptback wings, uniformly spaced vortices stationary with respect to the wing body prior to the onset of transition. This structure was absent over unswept wings where the flow is two-dimensional. An independent study by Owen and Randall (1952) interpreted these observations as the now termed crossflow phenomenon.

The first major theoretical contribution to instability in three-dimensional boundary layers was presented in the now classical paper of Gregory, Stuart and Walker (1955) where Stuart established general equations for the stability of three-dimensional flows in terms of curvilinear coordinates before looking specifically at the case of the boundary layer over a rotating disc. Alongside this theory an experimental investigation was undertaken. In practice the disc is rotated at a constant rate about an axis passing through its centre and normal to its surface and as the disc spins the surrounding fluid moves axially towards the disc. Centrifugal acceleration then drives an outward radial flow component and the crossflow instability arises as a result of a point of inflexion in this component of the velocity profile. Through the use of china-clay flow visualisation techniques a stationary vortex structure similar to that observed over swept wings was demonstrated. In this geometry the crossflow instability manifests itself in the form of co-rotating spiral vortices which spiral out towards the edge of the disc at a constant angle. The flow visualisation study revealed two critical radii with the first occurring at the edge of the central laminar flow region where the spiral vortices first set in. Moving further outwards a second radius identifies the onset of the

transition process.

The rotating disc boundary layer has long been use as a model problem for studying three-dimensional boundary layers since it exhibits so many of the features commonly found in more complex three-dimensional cases. It is particularly amenable to theoretical studies in view of the exact similarity solution of von Kármán (1921) to the Navier-Stokes equations for the mean flow field. The boundary layer is also of constant thickness so no assumptions about boundary layer growth have to be made. Experimentally the problem provides a relatively convenient and compact form. The effects of wall compliance on instability in three-dimensional boundary layers can therefore be investigated by considering this simpler model problem. However, despite the apparent simplicity of the flow field the instabilities which arise for a rigid boundary are considerably complex and have received substantial attention in their own right. Before wall compliance is introduced the form of the instabilities in this problem need to be clearly established. This is accomplished in part by a review of work to date on this subject.

1.3 Outline of Contents.

Following this brief introduction to the contents of this study each major section will be preceded by a review of literature relevant to the particular problem in question.

Chapter 2 provides the background required for the rotating channel problem. Aspects of both linear and weakly nonlinear theories are considered in relation to the rotating channel stability problem for a number of different mean shear flows established within the channel. Neutral stability curves and Ginzburg-Landau coefficients are used to establish stability characteristics for the family of mean flow fields.

Chapter 3 introduces the terminology essential to the study of problems involving wall compliance. Classification of instabilities is discussed, as are the types of instability which can arise as a direct result of wall compliance. A two-dimensional boundary layer which develops in the presence of an adverse pressure gradient and how the stability characteristics of this type of flow are affected by a compliant boundary is then investigated through the use of a plate-spring wall model and inviscid analysis.

Chapter 4 extends the work of the preceding chapter through the inclusion of viscous effects into the stability analysis and the use of the more realistic viscoelastic wall model.

Chapter 5 describes the differences which arise in the stability analysis of a three-dimensional boundary layer and how standard techniques are adapted to accommodate the additional dimension. This is followed by a review of work concerning the stability of the boundary layer which develops over a rotating disc.

Chapter 6 contains work concerning the rotating disc/compliant boundary problem focusing on a single-layer viscoelastic wall model. This chapter divides into three main areas which involve the analysis of stationary disturbances, travelling disturbances and the generation of hydroelastic instabilities in this flow geometry.

Chapter 7 draws general conclusions from this study and suggests possible areas of interest for future work.

CHAPTER 2

STABILITY OF ROTATING CHANNEL FLOW.

2.1 Introduction.

The aim of this section of work is to study the primary instability of spanwise periodic streamwise roll cells which occurs when plane channel flow is subjected to some constant spanwise rotation and in addition to the often studied plane Poiseuille mean flow a number of other basic states are considered. A general basic state is thus defined through the use of an interpolation parameter to provide a continuous family of mean velocity profiles. Linear stability analysis is first employed in order to determine whether the qualitative effects of rotation on the system remain essentially the same for all the shear flows investigated or whether some different characteristics arise.

With the introduction of rotation the stability characteristics become dependent on two parameters, the Reynolds number and rotation number (or dimensionless rotation rate) which define a neutral surface or paraboloid rather than the usual two-dimensional parabolic neutral curve of the non-rotating case. A Newton algorithm is used to determine accurately numerical values for the minimum point of the corresponding neutral surfaces in the full three-dimensional parameter space. This improves upon existing results where calculations have been confined to a restricted parameter space at fixed rotation rates. Consideration of such a two-dimensional section of the neutral surface means the rotation rate must be carefully selected if the true global minimum value is to be located.

A weakly nonlinear analysis is then applied in order to study the spanwise modulation of the streamwise rolls leading to the derivation of a Ginzburg-Landau equation. The coefficients of this equation are determined numerically in order to establish whether the bifurcation to rolls is supercritical or subcritical for the whole family of states investigated. However it must be recognised that supercritical bifurcation does not satisfactorily establish that the roll cells are stable to spanwise modulations since in large aspect ratio systems, the possibility of an Eckhaus-type instability arises.

The remainder of this chapter is as follows. A review of theoretical and experimental work is given to provide some historical background to this hydrodynamic stability problem. A description of a linear stability analysis follows and is used to determine neutral curves

for a number of different rotation rates and for a number of basic flow fields. The eigenvalue problem which results from this analysis is solved numerically using a spectral collocation method with a staggered grid. Minimum critical points are determined numerically and used in the subsequent calculation of the Ginzburg-Landau coefficients of the modulation equation.

2.2 Review of Theoretical and Experimental Works.

A brief outline of the original and main contributors to work in this field was made in Chapter 1 but this is now expanded upon in more detail.

A good description of the Coriolis force instability mechanism appears in Alfredsson and Persson (1989) where it is stated that a direct result of channel rotation about some spanwise axis normal to the streamwise flow direction is a Coriolis acceleration, $\boldsymbol{\Omega}^* \wedge \boldsymbol{U}$, where $\boldsymbol{\Omega}^*$ is the rotation vector and $\boldsymbol{U}$ the basic flow vector. This would give rise to a force normal to the channel walls and acts towards the channel leading edge. For the case of a parabolic mean flow profile the largest force occurs at the centre of the channel causing the leading side of the channel to be destabilised and the trailing side stabilised. Two parameters are thus needed to characterise the flow, the Reynolds number, $R = U_o h/\nu$ and the rotation number, $\Omega = \Omega^* h/U_o$ (the inverse of the Rossby number, R_o) where U_o is the maximum velocity of the mean flow, h the channel half width and Ω^* the dimensional rotation rate. Definitions of these parameters vary in the published work but whenever comparisons are made appropriate scalings have been implemented.

Tritton and Davies (1985) also give a description of the instability mechanism in terms of a "displaced particle" argument.

The physical transition process in this problem follows a general pattern, first exposed through the dye-technique experiments of Hart (1972). The flow is seen to pass through several different regimes as the rotation rate is increased. For plane Poiseuille flow the basic flow is one-dimensional and parabolic and is the state that exists for zero rotation. With the introduction of weak rotation a secondary circulation occurs seen as a double vortex (or a vortex pair with a single vortex compressed at each end of the channel). Increasing the rotation rate then sees the formation of the longitudinal roll cells which constitute the primary instability. Further increases in the rate of rotation then tends to stabilise the flow and a Taylor-Proudman regime comes into existence with the disappearance of the roll cells.

Typical apparatus for experimental studies consists of a channel of sufficient length for

the flow to be fully developed within the interior of the channel, making end effects negligible. The channel is mounted on a rotating table and the flow is driven by generating a constant pressure gradient across a chimney at each end of the channel.

The different stages of transition show up well in the flow visualisation studies of Alfredsson and Persson (1989) who add further observations to those of Hart. These flow visualisations were made through the introduction of titanium-dioxide coated platelets into the fluid which when illuminated show stream surfaces. In particular the roll cells show up as alternating bright and dark bands when viewed in the rotating frame. Alfredsson and Persson describe a secondary instability in evidence at higher Reynolds numbers which is seen as a twisting of the roll cells and if rotation is increased further at this stage a wavy disturbance arises and moves in the upstream direction. Both twisting and waviness is seen to originate at the downstream end of the channel. This type of secondary instability has also been found numerically by Finlay (1990) where it is described as being similar to the twisting of Dean vortices which can arise in curved channel flows and the numerical simulations of Yang and Kim (1991) have also been able to reproduce the wavy vortices observed in experiments. Turbulence develops with a further increase in rotation although some embedded roll cells still appear to be in existence. Another observation made from these experimental investigations was the possible splitting of the flow visualisation streaks at some downstream location. At this stage, however, it was unclear as to whether this was a manifestation of the flow visualisation technique or whether actual splitting of the streaks (implying a splitting of roll cells) was occurring. It was not until the work of Guo and Finlay (1991) that some reasoning behind these observations was formed. The theories developed in this case were based on consideration of Eckhaus-type instabilities which become important in large aspect ratio experiments and will be discussed later.

As well as some of the original experimental work Hart (1972) also considered the rotating channel problem theoretically. Within this study it was shown that the stability problem is directly analogous to the instability of a fluid between two plates which are heated differentially and using this analogy a necessary condition for roll cell formation was formulated and defined as $\Omega U_y > \frac{1}{3}$, where U_y is the gradient of the mean flow velocity. (This condition states that the total vorticity must be negative and comes from the requirement of a negative thermal gradient in the analogous problem.) This was applied to rotating Couette flow and Poiseuille flow to predict dividing regions for stability and instability (based on rotation rate and ratio of rotation rate to critical Reynolds number).

The first major theoretical work can be attributed to Lezius and Johnston (1976) who exploited Hart's analogy further and calculated the first neutral stability curves for rotating plane Poiseuille flow. Instability was predicted for Couette flow in the rotation number

range $0 < \Omega < \frac{1}{3}$ with critical parameters $\beta_c = 1.55$ and $R_c = 20.65$ at $\Omega = 0.25$ where β is the spanwise wavenumber. These values were predicted from the critical Rayleigh number in the analogous problem and in analogy with the small gap rotating cylindrical problem was used to determine stability characteristics for rotating plane Poiseuille flow. Using the critical Taylor number in this case determined $R_c = 66.4$ at $\Omega = 0.1667$. Symmetry of the basic profile in this case results in instability in the rotation range $0 < \Omega < 1$ for rotation in either direction. The values of these critical parameters have been repeated in a number of subsequent numerical calculations. However, a criticism of these results is that they are not actually calculated in the full three-dimensional parameter space and it may be possible that truly global minimum critical values have not been identified.

Linear stability theory limits the analysis of this problem to determining critical values and local amplification rates or neutral curves and in order to study more fully the instability of the roll cells weakly nonlinear theories, secondary stability analyses and full numerical simulations have been conducted. Finlay (1989), Ng *et al.* (1990) and Singer (1992) apply the Stuart-Landau theory to rotating plane Poiseuille flow all determining supercritical bifurcation to streamwise roll cells.

The flow visualisation experiments of Alfredsson and Persson (1989) indicated high amplification rates such that the amplitude of the roll cells may grow large enough to become unstable to oblique disturbances. Ng *et al.* undertake a secondary stability analysis at the parameter values for which Alfredsson and Persson made these observations ($R = 382$, $\Omega = 0.028$, spanwise wavenumber $\beta = 3.0$) and their theory indicated two ranges of streamwise wavenumber over which secondary instability exists. Alfredsson and Persson proposed a theory for the occurrence of this secondary instability based on the assumption that it arises as a result of the development of a point of inflexion in the basic velocity profile. This was subsequently discounted, however, following the calculation of only stable eigenvalues for a purely streamwise disturbance on an inflexional basic flow and all disturbance components were found to be required for this secondary instability to occur.

Major numerical results are given by Speziale (1982), Speziale and Thangham (1983) and Finlay (1990). Speziale considers rotating ducts of rectangular cross-section or small aspect ratio channels where the aspect ratio is given by the ratio of channel width to channel height. More detailed results will follow but the main point to state here is that the secondary flow which arises prior to the primary instability is found to have a negligible effect on the basic centre line flow for ducts of aspect ratio > 7. This underlines what is assumed in the majority of the stability analyses of large aspect ratio rotating channel problems. Speziale and Thangham undertake a thorough numerical study revealing the full transition process through numerical simulations and provide the first numerical representation of the

stabilisation to the Taylor-Proudman regime. The full nonlinear time-dependent Navier-Stokes equations are solved by finite difference techniques with the inclusion of end effects making it a particularly good comparison with experimental situations. For a channel of aspect ratio 8 and in the parameter range $0 < R < 375$, $1.66 \times 10^{-5} < \Omega < 1$ the following results are typical. The secondary flow, originally seen in the experiments of Hart, forms as two single vortices, one compressed against each end of the channel wall, with a length scale of the same order as the channel width. The development of this double-vortex structure into fully streamwise roll cells with increasing rotation rate is then calculated. Through the simulations (using a time-marching scheme) this is seen as a stretching of the double-vortex structure which eventually leads to the formation of an even number of counter-rotating vortices where the actual number of vortex pairs is dependent on the aspect ratio of the system. Finally, moving to higher rotation rates the roll cell vortices break down and restabilise to a Taylor-Proudman regime seen as a double-vortex structure similar to the secondary flow phenomenon but stretching further into the interior of the channel.

As mentioned earlier the numerical simulations of Finlay (1990) revealed the wavy-type of secondary instability that has been observed experimentally. Three-dimensional spectral simulations using the time-dependent Navier-Stokes equations reveal two types of wavy vortex flows named WVF1 and WVF2 by Finlay. WVF2 was found to occur only at low rotation rates and to have much lower amplification rates than the WVF1 structure whereas the WVF1 was found to develop at all rotation rates considered and is most likely to be the experimentally observed structure owing to the higher growth rates associated with it.

The weakly nonlinear analyses leading to prediction of supercritical bifurcation to rolls (Finlay, 1989, Ng *et al.*, 1990, Singer, 1992) is not strictly sufficient for roll cell stability when considering large aspect ratio systems. The Eckhaus instability becomes important in such cases and has been shown to be present in Taylor-Couette systems (Dominguez-Lerma *et al.*, 1986). The Eckhaus instability arises from the consideration of roll cells subjected to two-dimensional spanwise perturbations. At the critical point, predicted from linear stability theory, the critical and only wavenumber for the roll cells is β_c. As R is increased above R_c a band of wavenumbers which will give stable roll cells is expected. The width of this band is determined by the Eckhaus instability boundary where the two-dimensional vortices with wavenumbers within this boundary are stable with respect to perturbations. The original criterion, put forward by Eckhaus (1965), for the stable wavenumber band of T-S waves is

$$\frac{\beta_c - \beta_-}{\sqrt{3}} < \beta - \beta_c < \frac{\beta_+ - \beta_c}{\sqrt{3}}$$

where β_+, β_- correspond to wavenumbers at the upper and lower neutral points respectively. This criterion is valid for R near the critical point and has been satisfied in Rayleigh-Bénard

and Taylor-Couette problems. Eckhaus stable bands of wavenumbers have been found in these cases and the latter shown to have an Eckhaus boundary which is open ended and of the same form as the primary instability neutral curve and lies within the linearly unstable region. Guo and Finlay (1991) have analysed the rotating/curved channel system and found the Eckhaus boundary in this case to be a small closed region tangential to the critical point of the primary instability neutral curve. Outside this boundary splitting or merging of vortex pairs is predicted to be possible which lends support to the experimental observations of Alfredsson and Persson (1989). Wavenumbers selected by the Eckhaus instability appear to determine which process occurs. For small wavenumbers it is predicted that two vortex pairs can be split by a new pair to form three pairs, or if the wavenumber is large two vortex pairs will merge. Selection of spanwise wavenumbers is made by the Eckhaus instability for moderate Reynolds numbers and wavenumbers least unstable to spanwise perturbations appear to correspond to those observed experimentally.

Of note in this problem is the finding that the Eckhaus criterion is violated even for R close to R_c in some cases. A possible reason for this put forward by Guo and Finlay focuses on the differences in the basic flow between plane Poiseuille flow and the Taylor-Couette problem where the Eckhaus criterion is satisfied. In the latter case the velocity in the streamwise direction takes its maximum value at the wall whereas the maximum occurs in the centre of the channel for plane Poiseuille flow. This theory can be followed up by considering a family of basic states for the rotating channel problem which interpolates between rotating plane Poiseuille flow and Couette flow. Varying the interpolation parameter is effectively equivalent to moving the point of maximum streamwise velocity from the channel centre to the wall.

Many of the features associated with rotating channel flow and in particular the appearance of roll cells above critical parameter values are similar to occurrences in curved channel flow. In this configuration so-called Dean vortices can arise as a result of a centrifugal instability mechanism. Matsson and Alfredsson (1990) consider the combined effects of rotation and curvature on channel flow and this study reveals that compared to when there is just channel curvature the introduction of rotation can stabilise the flow if the centrifugal and Coriolis effects are counteractive. A particularly strong secondary instability found in curved channel flow was found to be completely removed if rotation was introduced in the right sense.

In a recent experimental study by Marliani *et al.* (1994) criticism is made concerning the sole use of parallel-walled channels which allows simplification of theoretical studies through the use of the parallel-flow approximation but does not represent fully what occurs in real flow systems of interest. Non-parallel effects have received comparatively more attention

in boundary layer flows but not in flow configurations where body forces are influential. The aim in this work was to consider non-parallel effects in the rotating channel problem with one example of direct practical relevance to this being the consideration of the effects of changes in cross-section of cooling passages of turbine blades. The apparatus for this investigation consisted of the usual channel mounted on a rotating table where acceleration or deceleration of the flow was made possible through the inclusion of wedge shaped end plates with the wedge angle determining the degree of acceleration or deceleration in the system. Experiments were performed keeping the flow rate (or Reynolds number) constant and increasing the rate of rotation. Flow visualisations for a parallel channel showed the longitudinal vortices as streaks occupying the whole space of the channel whereas for both accelerated and decelerated flows the streaks only occupied parts of the channel implying the simultaneous presence of both the roll cell state and the one-dimensional state. For the case of decelerated flow longitudinal vortices were in evidence at the entrance to the channel and disappeared as progression was made downstream. The opposite was true for the accelerated flow where the streaks were more pronounced at the downstream end of the channel. These observations are probably due to the influence of the flow rate on the production of roll cells since flow rate is directly related to the Reynolds number and if the acceleration or deceleration of the flow is enough to take flow parameters above or below the critical values required for the onset of the roll cells then this would explain the different structures observed along the channel length.

The effect of rotation on fully turbulent flow has many implications in real systems such as oceanic and atmospheric flows as well as engineering applications where rotation is a significant factor. Early experimental work to investigate the effects of Coriolis force on fully developed turbulent flow was performed by Johnston *et al.* (1972). Throughout references to stablisation/destabilisation of turbulent flow should be viewed in a slightly different context to that associated with laminar flow and are interpreted as a reduction/increase in turbulence intensity.

One of the features revealed in the study by Johnston *et al.* was that small rotations lead to the mean turbulent velocity profile taking on an asymmetric shape as a direct result of the Coriolis force action. At high rotation rates local production of turbulence was found to be eliminated in the low pressure wall region and the formation of a laminar wall layer was observed. Conversely, the turbulent flow was augmented at the high pressure wall resulting in a destabilised region and at this channel side a Taylor-Görtler vortex type structure was observed embedded within the turbulent flow.

Lezius and Johnston (1976) considered the turbulent flow problem theoretically through

the use of a two-layer model. Integrated averages of eddy viscosity were used to represent turbulence stress levels and numerical results were able to predict the onset of the vortex instability above $\Omega \approx 0.00667$ for the Reynolds number range 4500-26250 and were in good agreement with experimentally determined conditions for this instability. More recently Kristofferson and Andersson (1993) have performed direct numerical simulations for fully developed turbulent channel flow, subjected to this spanwise rotation, using finite difference techniques to solve the governing equations. These calculations confirm earlier results and give some additional features. For weak rotations ($\Omega = 0.00333$) the turbulent flow structure was found to change only slightly but the first signs of the rotation influence were revealed as opposing effects at each channel side with these differences becoming more prominent as the rotation rate is increased. Turbulence levels become greater at the high pressure side and decrease in intensity at the opposite side verifying the observations of Lezius and Johnston. This then results in the asymmetric appearance of the mean velocity and Reynolds stress profiles. At a value of $\Omega = 0.1667$ the total elimination of turbulence intensity is predicted at the stabilised side of the channel. The streamwise Taylor-Görtler vortex state arising as a direct result of system rotation is simulated well in these calculations and it was demonstrated that these counter-rotating vortices tend to migrate towards the high pressure wall and increase in number as the rotation rate is increased.

The work described above indicates many of the interesting features brought about by the influence of Coriolis force on laminar and turbulent channel flow and it is shown that rotation affects both the local and global nature of the flow. The following sections present an extension of the flow problem to consider a wider range of laminar flow fields.

2.3 Channel Geometry and Governing Equations.

Consider a parallel-walled channel extending infinitely in the streamwise, x, and spanwise, z, directions with walls located at $y = \pm h$ which is subjected to rotation about the spanwise axis at a constant dimensional rotation rate, Ω^*. The geometry and coordinate system are shown in Figure 2.1.

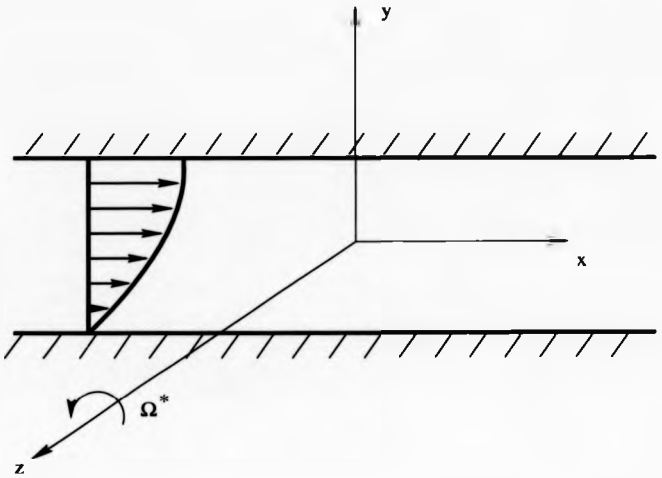

Figure 2.1: Geometry and coordinate system for rotating channel.

The motion of the fluid passing through the channel is governed by the Navier-Stokes equations together with the continuity equation which enforces the condition of fluid incompressibility. For clarity these equations are written in the rotating frame so that the velocity vector $\boldsymbol{u}^*$ and pressure p^* in that frame satisfy

$$\frac{\partial \boldsymbol{u}^*}{\partial t} + (\boldsymbol{u}^* \cdot \nabla)\boldsymbol{u}^* + 2\boldsymbol{\Omega}^* \wedge \boldsymbol{u}^* + \boldsymbol{\Omega}^* \wedge (\boldsymbol{\Omega}^* \wedge \boldsymbol{x}^*) = -\frac{1}{\rho}\nabla p^* + \nu \nabla^2 \boldsymbol{u}^* \qquad (2.1)$$

$$\nabla \cdot \boldsymbol{u}^* = 0 \qquad (2.2)$$

where $\boldsymbol{x}^*$ is the dimensional position vector and $\boldsymbol{\Omega}^* = [0, 0, \Omega^*]^T$. ρ is the fluid density and ν the kinematic viscosity.

The extra terms arising as a result of the rotation are a Coriolis acceleration, $\boldsymbol{\Omega} \wedge \boldsymbol{u}^*$, and a centripetal acceleration, $\boldsymbol{\Omega}^* \wedge (\boldsymbol{\Omega}^* \wedge \boldsymbol{x}^*)$. However, a modified pressure, p_m, can be defined which incorporates this centripetal term by using the following vector relation.

$$\boldsymbol{\Omega}^* \wedge (\boldsymbol{\Omega}^* \wedge \boldsymbol{x}^*) = -\nabla[\frac{1}{2}(\boldsymbol{\Omega}^* \wedge \boldsymbol{x}^*)^2]$$

The pressure can then be redefined as

$$p_m = p - \frac{1}{2}\rho(\boldsymbol{\Omega}^* \wedge \boldsymbol{x}^*)^2.$$

Henceforth the subscript on p_m will be dropped and any further expressions involving p will refer to the modified pressure. Using this expression and non-dimensionalising Eqs.(2.1) and (2.2) results in the following non-dimensional governing equations.

$$\frac{\partial \boldsymbol{u}}{\partial t} + (\boldsymbol{u} \cdot \nabla)\boldsymbol{u} + 2\boldsymbol{\Omega} \wedge \boldsymbol{u} + \nabla p - \frac{1}{R}\nabla^2 \boldsymbol{u} = 0 \tag{2.3}$$

$$\nabla \cdot \boldsymbol{u} = 0 \tag{2.4}$$

Velocities are scaled with respect to a fixed characteristic value, U_o, taken in this case to be the maximum value across the channel and lengths are non-dimensionalised by the channel half-width, h. This defines the two parameters which characterise the stability features for this problem, namely the Reynolds number

$$R = U_o h/\nu, \tag{2.5}$$

and the rotation number

$$\Omega = \Omega^* h/U_o. \tag{2.6}$$

For plane Poiseuille flow boundary conditions arise from the requirement of zero velocity at the walls. If $\boldsymbol{u} = [u, v, w]^T$ then

$$u = v = w = 0 \qquad \text{at} \qquad y = \pm 1. \tag{2.7}$$

The full nonlinear problem described by Eqs. (2.3), (2.4) and (2.7) has an exact solution which defines the mean state and is given by the following flow field.

$$u(x, y, z, t) = U(y) = 1 - y^2 \tag{2.8}$$

$$v(x, y, z, t) = 0 \tag{2.9}$$

$$w(x, y, z, t) = 0 \tag{2.10}$$

$$p(x, y, z, t) = P(x, y) = -\frac{2}{R}x - 2\Omega y + \frac{2}{3}\Omega y^3 + P_o \tag{2.11}$$

with P_o an arbitrary constant. The velocity field is unaffected by the system rotation, being identical to the non-rotating plane Poiseuille velocity field, but the pressure term contains additional elements dependent on the rotation rate. The whole flow field, however, reduces to the conventional plane Poiseuille flow field when $\Omega = 0$.

2.4 Linear Stability Analysis.

In order to establish some stability characteristics of the flow problem a space and time-dependent perturbation field, $\varepsilon[u', v', w', p']$, is imposed on the basic flow field where ε is an arbitrary constant introduced to represent small perturbations or infinitesimal disturbances.

$$u(x,y,z,t) = U(y) + \varepsilon u'(x,y,z,t) \tag{2.12}$$

$$v(x,y,z,t) = \varepsilon v'(x,y,z,t) \tag{2.13}$$

$$w(x,y,z,t) = \varepsilon w'(x,y,z,t) \tag{2.14}$$

$$p(x,y,z,t) = P(x,y) + \varepsilon p'(x,y,z,t) \tag{2.15}$$

The linear stability of the basic flow field is determined by substituting the above expressions into the governing equations and linearising with respect to the perturbation quantities about the basic state (i.e. terms of $O(\varepsilon^2)$ and smaller are neglected). This yields the following system of linear equations.

$$\frac{\partial u'}{\partial t} + U\frac{\partial u'}{\partial x} + U_y v' + \frac{\partial p'}{\partial x} - 2\Omega v' - \frac{1}{R}\nabla^2 u' = 0 \tag{2.16}$$

$$\frac{\partial v'}{\partial t} + U\frac{\partial v'}{\partial x} + \frac{\partial p'}{\partial y} + 2\Omega u' - \frac{1}{R}\nabla^2 v' = 0 \tag{2.17}$$

$$\frac{\partial w'}{\partial t} + U\frac{\partial w'}{\partial x} + \frac{\partial p'}{\partial z} - \frac{1}{R}\nabla^2 w' = 0 \tag{2.18}$$

$$\frac{\partial u'}{\partial x} + \frac{\partial v'}{\partial y} + \frac{\partial w'}{\partial z} = 0 \tag{2.19}$$

where $U_y \equiv \frac{dU}{dy}$,
with boundary conditions

$$u' = v' = w' = 0 \qquad \text{at} \qquad y = \pm 1. \tag{2.20}$$

These linearised equations are only valid for infinitesimal perturbations and results should be interpreted in accordance with this. Stability criteria determined using this method do not indicate stability of the basic flow with respect to finite disturbances for which the non-linear terms considered negligible here must be included.

The perturbation quantities can either be modelled as spatially or temporally developing disturbances. The spatial theory, first proposed by Gaster (1962), is the more physically realistic of the two in most cases when the instability is described as convective, but for neutrally stable disturbances the two forms are equivalent. Since the main purpose of this linear stability analysis is to determine neutral boundaries the perturbation field is assumed to be composed of an exponential time component, therefore developing temporally, with

amplitude functions dependent on the spatial variables such that

$$[u', v', w', p']^T = e^{\lambda t}[\tilde{u}(x, y, z), \tilde{v}(x, y, z), \tilde{w}(x, y, z), \tilde{p}(x, y, z)]^T + \text{c.c.} \tag{2.21}$$

where $\lambda = \lambda_r + i\lambda_i$ is complex valued with the real part of λ (or λ_r) giving the temporal growth rate.

Substitution of this form for the perturbation components into Eqs.(2.16)-(2.18) removes time derivatives to leave

$$\frac{1}{R}\nabla^2\tilde{u} - U\frac{\partial\tilde{u}}{\partial x} - \lambda\tilde{u} + (2\Omega - U_y)\tilde{v} - \frac{\partial\tilde{p}}{\partial x} = 0 \tag{2.22}$$

$$\frac{1}{R}\nabla^2\tilde{v} - U\frac{\partial\tilde{v}}{\partial x} - \lambda\tilde{v} - 2\Omega\tilde{u} - \frac{\partial\tilde{p}}{\partial y} = 0 \tag{2.23}$$

$$\frac{1}{R}\nabla^2\tilde{w} - U\frac{\partial\tilde{w}}{\partial x} - \lambda\tilde{w} - \frac{\partial\tilde{p}}{\partial z} = 0 \tag{2.24}$$

$$\frac{\partial\tilde{u}}{\partial x} + \frac{\partial\tilde{v}}{\partial y} + \frac{\partial\tilde{w}}{\partial z} = 0 \tag{2.25}$$

with

$$\tilde{u} = \tilde{v} = \tilde{w} = 0 \qquad \text{at} \qquad y = \pm 1. \tag{2.26}$$

For fixed values of Ω and R the basic flow is then deemed to be linearly unstable if the perturbations grow exponentially in time, i.e. $\lambda_r > 0$, and stable if $\lambda_r < 0$.

The system of stability equations can be rearranged into a matrix form to define an eigenvalue problem for λ as follows.

$$\boldsymbol{L}(\lambda; \Omega, R)\boldsymbol{V} = 0 \tag{2.27}$$

where $\boldsymbol{V} = [\tilde{u}, \tilde{v}, \tilde{w}, \tilde{p}]^T$. Therefore, for given values of Ω and R, non-trivial solutions are determined by requiring that $\det(\boldsymbol{L}) = 0$.

A number of numerical techniques can be employed to solve this type of eigenvalue problem and the particular method of spectral collocation is employed here. The following section introduces this numerical technique and moves on to describe its application with respect to this specific problem.

2.5 Numerical Method - Spectral Techniques.

Spectral methods are one means of determining numerical solutions to differential equations through discretisation. The foundations of this particular technique are based on the finite series expansion of the solution in terms of some orthogonal expansion functions. The type

of expansion functions used gives the main difference between spectral and finite-element methods. In the spectral formulation the functions are global whereas the subdivision of the computational domain involved in the finite-element technique means the functions used are local to each subdomain. Spectral techniques are inherently accurate and generally if the appropriate type of method is used to suit the problem they are computationally efficient methods of solution.

Within the overall framework of spectral techniques there are a number of different schemes, namely Galerkin, collocation and tau which differ in the way the problems are required to be satisfied. A requisite condition in all cases is that the residual, or difference in the differential equation given by the series solution and the actual solution, be minimised. The collocation technique which will be used here tends to be the simplest of the three methods to implement and describes the problem in terms of the discretised solution. The criterion for a satisfactory solution in this case is that the differential equation be satisfied exactly at a number of discrete points known as collocation points.

As well as the different types of method used to formulate the problem there are also a number of choices for the expansion functions used to construct the solution. The most commonly used are trigonometric, Chebyshev and Legendre polynomials chosen appropriate to the particular problem since optimum accuracy is dependent on the selected expansion functions. For example, in a problem which exhibits periodicity the Fourier series expansion would be the most suitable choice, but Chebyshev polynomials prove to be adaptable to a number of different problems and are much more versatile. In numerical studies of instability in plane Poiseuille flow Orszag (1971) has demonstrated that Chebyshev polynomials are better adapted than other orthogonal functions for hydrodynamic stability problems and also lead to more efficient calculations and storage than finite-element techniques. Orszag has also recommended the use of these polynomials because of the rapid decrease in truncation error as the number of polynomials used in the series expansion increases.

The following section describes spectral collocation method using Chebyshev polynomials as the expansion polynomials.

2.5.1 Chebyshev Collocation.

Chebyshev polynomials are defined on the interval [-1,1] by

$$T_n(x) = \cos n\theta \qquad \text{where} \qquad \theta = \cos^{-1}(x), \qquad n = 0, 1, 2, \ldots \tag{2.28}$$

The solution, $\psi(x)$, to a particular problem is written as a finite series expansion in terms

of these polynomials up to some value N.

$$\psi(x) = \sum_{n=0}^{N} a_n T_n(x) \tag{2.29}$$

In order to implement the collocation method distinct points, x_j, in the domain [-1,1] must be defined with the number of points required being equal to the order of the approximating polynomial expansion. The usual choice for the Chebyshev collocation technique are the Gauss-Lobatto points defined as follows.

$$x_j = \cos\frac{\pi j}{N} \qquad j = 0, \ldots, N \tag{2.30}$$

These are not evenly distributed across the interval but are more closely spaced at the interval ends and this concentration of points near the boundaries generally leads to more accurate results since in fluid problems this is the region where the most significant effects occur. As such this is also a more economical distribution since if the points were evenly spaced a greater number would be required to give sufficient resolution near the boundaries and the same degree of accuracy in the solution.

Once the collocation points have been defined the solution is evaluated at each of these locations.

$$\psi_j = \psi(x_j) = \sum_{n=0}^{N} a_n T_n(x_j) = \sum_{n=0}^{N} a_n \cos\frac{n\pi j}{N} \tag{2.31}$$

If two vectors $\boldsymbol{\Psi} = [\psi_0, \ldots, \psi_N]^T$ and $\boldsymbol{a} = [a_0, \ldots, a_N]^T$ are defined then a matrix equation can be constructed.

$$\boldsymbol{\Psi} = \boldsymbol{C}\boldsymbol{a} \qquad \text{where} \qquad C_{ij} = \cos\frac{\pi ij}{N} \qquad i, j = 0, \ldots, N \tag{2.32}$$

An inversion formula is employed in order to express the expansion coefficients a_k ($k = 0, \ldots, N$) as a series expansion in terms of the ψ_j. Given the expression in Eq.(2.31) and using the orthogonality relation

$$\sum_{k=0}^{N} \frac{1}{\bar{c}_k} \cos\frac{mk\pi}{N} \cos\frac{pk\pi}{N} = \begin{cases} N & \text{if} \quad m = p = 0, N \\ N/2 & \text{if} \quad m = p \neq 0, N \\ 0 & \text{if} \quad m \neq p \end{cases} \tag{2.33}$$

where

$$\bar{c}_k = \begin{cases} 2 & \text{if} \quad k = 0, N \\ 1 & \text{if} \quad 1 \leq k \leq N-1 \end{cases} \tag{2.34}$$

the expansion coefficients can be written

$$a_k = \frac{2}{N\bar{c}_k} \sum_{j=0}^{N} \frac{\psi_j}{\bar{c}_j} \cos\frac{\pi jk}{N} \qquad k = 0, \ldots, N \tag{2.35}$$

or

$$\boldsymbol{a} = \boldsymbol{P\Psi} \qquad \text{with} \qquad P_{ij} = \frac{2}{N\bar{c}_i\bar{c}_j}\cos\frac{\pi ij}{N}. \tag{2.36}$$

In order to apply the spectral technique the differential equation(s) under question must be evaluated and satisfied at the collocation points and the end result is a set of $N+1$ simultaneous equations in terms of the $N+1$ unknowns $\psi_0, \ldots, \psi_N$.

Expressions for the derivatives are obtained by using the properties of the Chebyshev polynomials (Fox and Parker, 1968). Given that

$$T_n(\cos\theta) = \cos(n\theta)$$

then differentiating with respect to θ gives

$$\frac{d}{d\theta}\left(T_n(\cos\theta)\right) = -T_n'(\cos\theta)\sin\theta = -n\sin n\theta$$

Hence

$$T_n'(\cos\theta) = \frac{n\sin n\theta}{\sin\theta} \tag{2.37}$$

where primes denote differentiation with respect to $x = \cos\theta$.
In order to evaluate the derivatives at the end points, $x = \pm 1$, l'Hôpital's rule must be applied to obtain

$$\begin{aligned} T_n'(+1) &= \left.\frac{n\sin n\theta}{\sin\theta}\right|_{\theta\to 0} = n^2, \\ T_n'(-1) &= \left.\frac{n\sin n\theta}{\sin\theta}\right|_{\theta\to \pi} = (-1)^{n+1}n^2. \end{aligned} \tag{2.38}$$

The derivative vector $\boldsymbol{\Psi}' = [\psi_0', \ldots, \psi_N']^T$ can then be written in terms of the expansion coefficients.

$$\boldsymbol{\Psi}' = \boldsymbol{Da} \qquad \text{where} \qquad D_{ij} = \begin{cases} k^2 & \text{if} \quad j = 0 \\ \frac{k\sin\pi jk/N}{\sin\pi j/N} & \text{if} \quad 1 \le j \le N-1 \\ (-1)^{k+1}k^2 & \text{if} \quad j = N \end{cases} \tag{2.39}$$

Using Eq.(2.36) allows the discretised derivatives to be written in terms of the solution vector.

$$\boldsymbol{\Psi}' = \boldsymbol{DP\Psi} = \boldsymbol{A\Psi} \tag{2.40}$$

where

$$A_{00} = -A_{NN} = \frac{2N^2+1}{6} \tag{2.41}$$

$$A_{jj} = \frac{-x_j}{2(1-x_j^2)} \quad \text{if} \quad j \neq 0, N \tag{2.42}$$

$$A_{jk} = \frac{\bar{c}_j(-1)^{j+k}}{\bar{c}_k(x_j - x_k)} \quad \text{if} \quad j \neq k. \tag{2.43}$$

Higher derivatives can also be expressed in terms of the solution vector where for example

$$\left.\frac{d^2\psi}{dx^2}\right|_{x_j} = \sum_{k=0}^{N} B_{jk}\psi_k \qquad j = 0, \ldots, N \qquad \text{with} \qquad B_{jk} = \sum_{m=0}^{N} A_{jm}A_{mk}.$$

2.6 Application of Spectral Collocation to Rotating Channel Problem.

For a fully nonlinear problem the flow field would be discretised by expanding each component of the solution in the form

$$\tilde{u}(x,y,z) = \sum_{m=0}^{N}\sum_{n=0}^{N} u_{mn}(y)e^{i(m\alpha x + n\beta z)}$$

where α and β are wavenumbers in the x and z directions respectively. However, periodicity is assumed in these directions such that

$$\tilde{u}(x + \frac{2\pi}{\alpha}, y, z) = \tilde{u}(x,y,z)$$

$$\tilde{u}(x,y,z + \frac{2\pi}{\beta}) = \tilde{u}(x,y,z)$$

The problem is also linear which means the terms decouple and a solution can be obtained by considering a single term of the form

$$\begin{bmatrix} \tilde{u}(x,y,z) \\ \tilde{v}(x,y,z) \\ \tilde{w}(x,y,z) \\ \tilde{p}(x,y,z) \end{bmatrix} = Re\left\{ \begin{bmatrix} \hat{u}(y) \\ \hat{v}(y) \\ \hat{w}(y) \\ \hat{p}(y) \end{bmatrix} e^{i(\alpha x + \beta z)} \right\}.$$

The result of this is to simplify the spectral analysis considerably since spectral discretisation is now only required in the y direction.

Recalling the set of Eqs.(2.22)-(2.26) then substitution of the above form reduces these to a set of ordinary differential equations and the matrix construction of the eigenvalue problem is then as follows.

$$\begin{bmatrix} \frac{1}{R}\Delta - i\alpha U - \lambda & 2\Omega - U_y & 0 & -i\alpha \\ -2\Omega & \frac{1}{R}\Delta - i\alpha U - \lambda & 0 & -\frac{d}{dy} \\ 0 & 0 & \frac{1}{R}\Delta - i\alpha U - \lambda & -i\beta \\ i\alpha & \frac{d}{dy} & i\beta & 0 \end{bmatrix} \begin{bmatrix} u \\ v \\ w \\ p \end{bmatrix} = \begin{bmatrix} 0 \\ 0 \\ 0 \\ 0 \end{bmatrix} \tag{2.44}$$

where $\Delta = d^2/dy^2 - (\alpha^2 + \beta^2)$,

with boundary conditions

$$u(\pm 1) = v(\pm 1) = w(\pm 1) = 0. \tag{2.45}$$

At this stage the set of equations is ready to be discretised, but using the standard Gauss-Lobatto set of grid points poses the problem of the appropriate boundary conditions to enforce concerning the pressure term. To overcome this, the staggered grid system used by Khorrami (1991) is implemented which places a secondary set of collocation points between the standard points. The terms u, v and w and the three momentum equations are then evaluated at the Gauss-Lobatto points

$$x_j = \cos\frac{\pi j}{N}, \qquad j = 0, \ldots, N$$

and the perturbation pressure and continuity equation are evaluated at the intermediate or half points, $x_{j+\frac{1}{2}}$, which exclude the two boundaries.

$$x_{j+\frac{1}{2}} = \cos\frac{(2j+1)\pi}{2N} \qquad j = 0, \ldots, N-1$$

This removes any ambiguity concerned with defining pressure boundary conditions.

Since the velocity and pressure terms cross-over into the continuity and momentum equations respectively some interpolation formulae are required to take values between the main and secondary grid points. For example matrices $\boldsymbol{M}, \boldsymbol{E}, \boldsymbol{M}^*$ and $\boldsymbol{A}^*$ can be defined such that

$$\bar{p}_j = \sum_{k=0}^{N-1} M_{jk}\bar{p}_{k+\frac{1}{2}}, \qquad \left.\frac{d\bar{p}}{dy}\right|_j = \sum_{k=0}^{N-1} E_{jk}\bar{p}_{k+\frac{1}{2}},$$

$$\bar{u}_{j+\frac{1}{2}} = \sum_{k=0}^{N} M^*_{jk}\bar{u}_k, \qquad \left.\frac{d\bar{u}}{dy}\right|_{j+\frac{1}{2}} = \sum_{k=0}^{N} A^*_{jk}\bar{u}_k.$$

Subscripts j and $j+\frac{1}{2}$ refer to evaluation at points x_j and $x_{j+\frac{1}{2}}$ respectively. Explicit entries for these matrices appear in the work of Khorrami.

The discretised momentum equations for $j = 1, \ldots, N-1$ are thus

$$\frac{1}{R}\sum_{k=0}^{N} B_{jk}\bar{u}_k - \left[\frac{\alpha^2+\beta^2}{R} + i\alpha U_j + \lambda\right]\bar{u}_j + [2\Omega - U_y(x_j)]\,\bar{v}_j - i\alpha\sum_{k=0}^{N-1} M_{jk}\bar{p}_{k+\frac{1}{2}} = 0 \quad (2.46)$$

$$\frac{1}{R}\sum_{k=0}^{N} B_{jk}\bar{v}_k - \left[\frac{\alpha^2+\beta^2}{R} + i\alpha U_j + \lambda\right]\bar{v}_j - 2\Omega\bar{u}_j - \sum_{k=0}^{N-1} E_{jk}\bar{p}_{k+\frac{1}{2}} = 0 \quad (2.47)$$

$$\frac{1}{R}\sum_{k=0}^{N} B_{jk}\bar{w}_k - \left[\frac{\alpha^2+\beta^2}{R} + i\alpha U_j + \lambda\right]\bar{w}_j - i\beta\sum_{k=0}^{N-1} M_{jk}\bar{p}_{k+\frac{1}{2}} = 0 \quad (2.48)$$

where U_j and $U_y(x_j)$ are the basic flow and its derivative with respect to y evaluated at the point x_j. The conditions for $j = 0, N$ arise from the boundary conditions in Eq.(2.45). Expressing the continuity equation at the half points completes the discretisation.

$$i\alpha\sum_{k=0}^{N} M^*_{jk}\bar{u}_k + \sum_{k=0}^{N} A^*_{jk}\bar{v}_k + i\beta\sum_{k=0}^{N} M^*_{jk}\bar{w}_k = 0, \qquad j = 0, \ldots, N-1 \quad (2.49)$$

By defining various block matrices the problem can be written more concisely as follows.

$$\begin{bmatrix} \boldsymbol{\Gamma} & \boldsymbol{D}_2 & 0 & -i\alpha\boldsymbol{M} \\ \boldsymbol{D}_1 & \boldsymbol{\Gamma} & 0 & -\boldsymbol{E} \\ 0 & 0 & \boldsymbol{\Gamma} & -i\beta\boldsymbol{M} \\ i\alpha\boldsymbol{M}^* & \boldsymbol{A}^* & i\beta\boldsymbol{M}^* & 0 \end{bmatrix} \begin{bmatrix} \bar{\boldsymbol{u}} \\ \bar{\boldsymbol{v}} \\ \bar{\boldsymbol{w}} \\ \bar{\boldsymbol{p}} \end{bmatrix} = \lambda \begin{bmatrix} \tilde{\boldsymbol{I}} & 0 & 0 & 0 \\ 0 & \tilde{\boldsymbol{I}} & 0 & 0 \\ 0 & 0 & \tilde{\boldsymbol{I}} & 0 \\ 0 & 0 & 0 & 0 \end{bmatrix} \begin{bmatrix} \bar{\boldsymbol{u}} \\ \bar{\boldsymbol{v}} \\ \bar{\boldsymbol{w}} \\ \bar{\boldsymbol{p}} \end{bmatrix} \quad (2.50)$$

where $\bar{\boldsymbol{u}} = [\bar{u}_0, \ldots, \bar{u}_N]^T$ and similarly for $\bar{\boldsymbol{v}}$ and $\bar{\boldsymbol{w}}$ whilst $\bar{\boldsymbol{p}} = [\bar{p}_0, \ldots, \bar{p}_{N-1}]^T$.

$\tilde{\boldsymbol{I}} \in \mathbb{R}^{(N+1)\times(N+1)}$ is an identity matrix but with the first and last rows set to zero in accordance with the boundary conditions.

$$\boldsymbol{D}_1 = -2\Omega\tilde{\boldsymbol{I}}, \qquad \boldsymbol{D}_2 = d_j\tilde{\boldsymbol{I}}_{jj} \qquad \text{with} \qquad d_j = 2\Omega - U_y(x_j) \qquad j = 0, \ldots, N$$

$\boldsymbol{\Gamma}$ is the matrix representing the operator $\frac{1}{R}\frac{d^2}{dy^2} - \left(\frac{\alpha^2+\beta^2}{R} + i\alpha U_j\right)$ such that

$$\begin{aligned} \Gamma_{00} &= 1, \quad \Gamma_{0k} = 0 \quad k = 1, \ldots, N-1 \\ \Gamma_{jk} &= \tfrac{1}{R}B_{jk} - \left(\tfrac{\alpha^2+\beta^2}{R} + i\alpha U_j\right)\delta_{jk} \quad j = 1, \ldots, N-1, \quad k = 0, \ldots, N \\ \Gamma_{Nk} &= 0, \quad \Gamma_{NN} = 1 \quad k = 0, \ldots, N-1. \end{aligned}$$

The remaining entries are constructed from the interpolation matrices with modification to $\boldsymbol{E}$ and $\boldsymbol{M}$ to accommodate the boundary conditions. The information given in the discretised form of Eq.(2.50) is now in the form of a generalised eigenvalue problem.

$$\boldsymbol{L}_o(\Omega, \alpha, \beta, R)\boldsymbol{\Psi} = \lambda\boldsymbol{K}\boldsymbol{\Psi} \qquad \text{where} \qquad \boldsymbol{\Psi} = [\bar{\boldsymbol{u}}, \bar{\boldsymbol{v}}, \bar{\boldsymbol{w}}, \bar{\boldsymbol{p}}]^T \in \mathbb{R}^{4N+3} \quad (2.51)$$

The linear dependence on λ means it is suitable for application of the QZ algorithm which calculates, if necessary, all the eigenvalues associated with the problem.

One advantage of the collocation method is that the problem is formulated in terms of the discretised solution vector rather than the expansion coefficients so that numerical solutions for the eigenvector at a given value of λ are solved for directly and can be obtained simultaneously with the eigenvalue itself.

2.7 Code Validation.

The case of non-rotating plane Poiseuille flow was used to validate the computational code as well as comparing previously documented results for the rotating channel flow case.

For $\Omega = 0$, $\beta = 0$ values given in Drazin and Reid (1981) are $\alpha = 1.02056$ at $R = 5772$ and $\lambda = 0.26943i$. Agreement to at least four significant figures was found using $N = 48$ collocation points, a value subsequently used in all the calculations. For plane Poiseuille flow under spanwise rotation good agreement was found when comparing results with the values of Alfredsson and Persson (1989). For example the minimum critical point at a rotation number of $\Omega = 1/6$ was found here to be at $R = 66.5$ and $\beta = 2.46$ compared to experimental values of $R \approx 67$ and $\beta \approx 2.5$.

2.8 Stability Results for Family of Velocity Profiles.

As discussed in the introduction plane Poiseuille flow is just one of a number of shear flows that can be established within the channel configuration. The basic parabolic profile can be extended to define a family of profiles through the introduction of an interpolation parameter, θ, such that the basic flow field, $[U, 0, 0, P]$, becomes a function of this interpolation parameter in addition to the streamwise and normal positions. Figure 2.2 shows the form of the velocity profiles for a number of values of θ given by the following analytical expressions.

$$U(y,\theta) = (1-\theta)(1-y^2) + \theta u_w y \qquad \text{with} \qquad \theta \in [0,1] \tag{2.52}$$

$$P(x,y,\theta) = -\frac{2}{R}(1-\theta)x - 2\Omega(1-\theta)y + \frac{2}{3}\Omega(1-\theta)y^3 - \theta u_w \Omega y^2 + P_o \tag{2.53}$$

A continuous set of profiles moving from plane Poiseuille flow ($\theta = 0$) to plane Couette flow ($\theta = 1$) is thus obtained with u_w a scaling factor or dimensionless wall velocity taken in this instance to be unity.

The purpose of the linear stability analysis is to determine neutral curves for a number of different rotation rates and values of θ and to calculate minimum critical parameters for these different flow configurations.

The choice of a value for the streamwise wavenumber, α, is somewhat arbitrary but results in Figure 2.3 indicate that $\alpha = 0$ gives the lowest critical Reynolds number as well as the lowest values of R for neutral stability across the whole β range. This suggests some form of Squire's theorem may be applicable and as a consequence all the subsequent calculations were obtained with $\alpha = 0$.

The effect of rotation on Poiseuille flow is shown by the neutral curves in Figures 2.4(a) and (b). The critical value of Ω for which the roll cells first appear is adjudged to lie in the vicinity of $\Omega = 1/6$ given that rotation rates both above and below this value result in increases in the critical Reynolds number. It is noted that even for very small rotations, for example $\Omega = 1/600$, the onset of the roll cell instability still occurs at a significantly lower Reynolds number than that required to amplify the T-S instability. This is indicative of the strength of effect of the Coriolis force instability mechanism and it appears unlikely that the two instabilities would ever coincide (or appear simultaneously) since extremely small rotation rates would be required in order to shift the critical Reynolds number up to the magnitude required for this to occur. The roll cell instability will likely dominate even at small rotation rates and the transition process associated with this instability should evolve well before T-S waves become unstable.

At a fixed rotation rate of $\Omega = 1/6$ neutral curves are shown in Figure 2.5 for a number of values of θ. From these results is can be ascertained that Couette flow is the most unstable at this rotation rate with a critical Reynolds number of $R_c = 21.9$. As θ is decreased from unity the critical values rise up to $R_c = 66.5$ for plane Poiseuille flow. The Coriolis force instability mechanism was described qualitatively in the introduction but is recalled here. The Coriolis acceleration induced by the action of rotation gives rise to a force in the opposite direction which is directed towards the leading side of the channel. This then becomes destabilised and the form of the basic velocity profile determines the distribution of the Coriolis force across the channel. For example, maximum force occurs at the channel centre for Poiseuille flow but for plane Couette flow the maximum occurs at the wall. This change in distribution would likely explain the more pronounced effect of rotation on the stability of the shear flows as θ changes.

A Newton algorithm is now implemented in order to determine accurate numerical values for these critical points in the full three-dimensional flow parameter space.

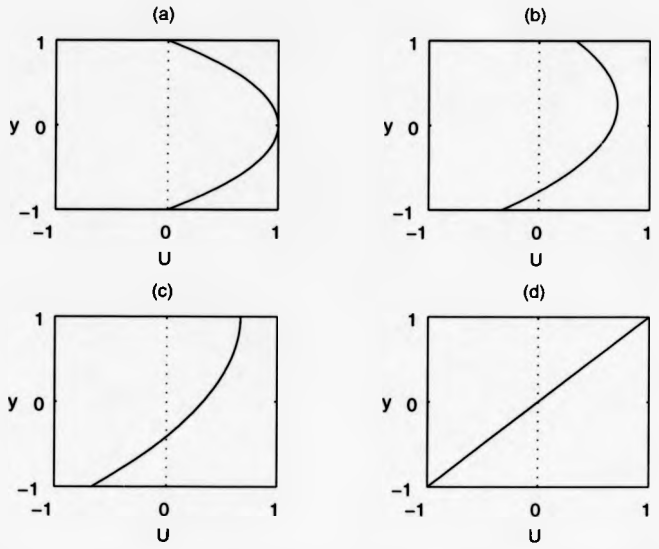

Figure 2.2: Variation of mean streamwise (U) velocity with channel height for plane channel flow. (a) $\theta = 0$, (b) $\theta = \frac{1}{3}$, (c) $\theta = \frac{2}{3}$, (d) $\theta = 1$.

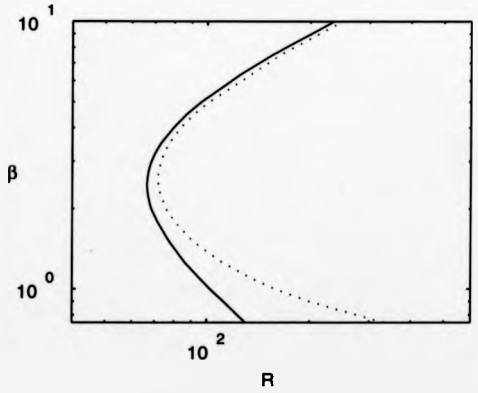

Figure 2.3: The effect of non-zero α on the neutral curve for $\theta = 0$, $\Omega = \frac{1}{6}$. $\alpha = 0.0$: —, $\alpha = 0.5$: $\cdots$.

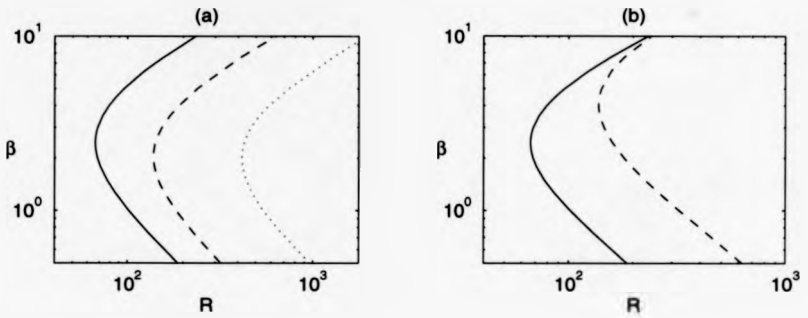

Figure 2.4: Neutral curves for plane Poiseuille flow at different rotation numbers. (a) $\Omega = \frac{1}{6}$: —, $\Omega = \frac{1}{60}$: - - , $\Omega = \frac{1}{600}$: ···, (b) $\Omega = \frac{1}{6}$: —, $\Omega = \frac{1}{2}$: - -.

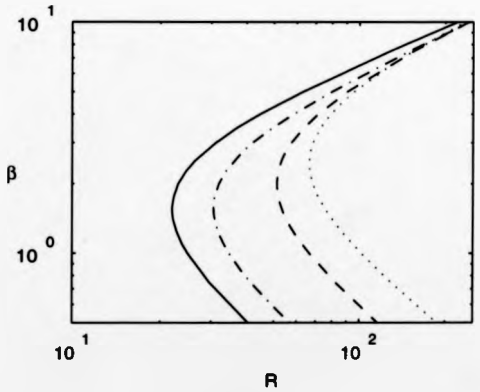

Figure 2.5: Neutral curves for a number of basic states at $\Omega = \frac{1}{6}$. $\theta = 0$: ···, $\theta = \frac{1}{3}$: - -, $\theta = \frac{2}{3}$: – · –, $\theta = 1$: —.

2.9 Algorithm to Determine Minimum Point of Neutral Surface.

Any point on the neutral surface has a zero eigenvalue by definition and thus satisfies the following conditions which are obtained by setting $\lambda = 0$ in Eq.(2.51).

$$\boldsymbol{L}_o\boldsymbol{\Psi} = 0 \qquad \text{and} \qquad \boldsymbol{L}_o^*\boldsymbol{\Psi}^* = 0 \tag{2.54}$$

$\boldsymbol{\Psi}$ and $\boldsymbol{\Psi}^*$ are the right and left eigenvectors of $\boldsymbol{L}_o$ respectively and $\boldsymbol{L}_o^*$ is the adjoint operator defined by the inner product relation for general vectors $\boldsymbol{W}$ and $\boldsymbol{\Phi}$.

$$< \boldsymbol{W}, \boldsymbol{L}_o\boldsymbol{\Phi} >=< \boldsymbol{L}_o^*\boldsymbol{W}, \boldsymbol{\Phi} > \tag{2.55}$$

In this case $\boldsymbol{L}_o^*$ is the complex conjugate adjoint of the matrix operator $\boldsymbol{L}_o$ appearing in Eq.(2.51). For the numerical calculations the discrete inner product is applied such that if $\boldsymbol{A}, \boldsymbol{B} \in \mathbb{R}^{4N+3}$ then this relation is defined as follows where an overbar denotes complex conjugation.

$$< \boldsymbol{A}, \boldsymbol{B} >= \sum_{i=0}^{4N+2} \overline{A}_i B_i \tag{2.56}$$

In order to determine conditions for the neutral point in (Ω, β, R) parameter space consider the following generalised eigenvalue problem. (Eq.(2.51).)

$$\boldsymbol{L}_o\boldsymbol{\Psi} = \lambda \boldsymbol{K}\boldsymbol{\Psi}. \tag{2.57}$$

If $\boldsymbol{L}_o = \boldsymbol{L}_o(R(\Omega))$ then differentiating Eq.(2.57) above with respect to Ω gives

$$\begin{aligned} \frac{\partial \boldsymbol{L}_o}{\partial R}\frac{\partial R}{\partial \Omega}\boldsymbol{\Psi} + \boldsymbol{L}_o\frac{\partial \boldsymbol{\Psi}}{\partial \Omega} &= \frac{\partial \lambda}{\partial \Omega}\boldsymbol{K}\boldsymbol{\Psi} + \lambda \boldsymbol{K}\frac{\partial \boldsymbol{\Psi}}{\partial \Omega} \\ \Rightarrow \quad \frac{\partial \boldsymbol{L}_o}{\partial R}\frac{\partial R}{\partial \Omega}\boldsymbol{\Psi} &= \frac{\partial \lambda}{\partial \Omega}\boldsymbol{K}\boldsymbol{\Psi}. \end{aligned} \tag{2.58}$$

Taking the inner product of Eq.(2.58) with the left eigenvector, $\boldsymbol{\Psi}^*$, leaves

$$\frac{\partial R}{\partial \Omega} < \boldsymbol{\Psi}^*, \boldsymbol{L}_R\boldsymbol{\Psi} >= \lambda_\Omega < \boldsymbol{\Psi}^*, \boldsymbol{K}\boldsymbol{\Psi} > \tag{2.59}$$

where subscripts on $\boldsymbol{L}$ and λ represent the partial derivatives of $\boldsymbol{L}_o$ and λ with respect to that particular variable.

If a neutral paraboloid of the form shown in Figure 2.6 is assumed then $\partial R/\partial \Omega = 0$ at the critical point. With $< \boldsymbol{\Psi}^*, \boldsymbol{K}\boldsymbol{\Psi} > \neq 0$ Eq.(2.59) implies that λ_Ω must be zero. Similarly by considering $\boldsymbol{L}_o = \boldsymbol{L}_o(\beta(\Omega))$ the condition $\lambda_\beta = 0$ is also obtained. Therefore at the critical point of the paraboloid the following three conditions must be satisfied

$$\lambda = \lambda_\Omega = \lambda_\beta = 0. \tag{2.60}$$

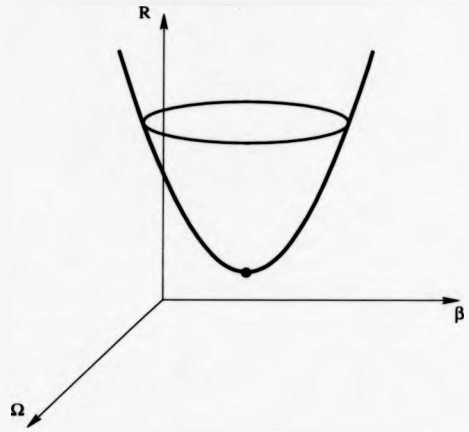

Figure 2.6: Neutral paraboloid in (Ω, β, R) parameter space.

The eigenvalue, λ, is now treated as a function of Ω, β and R and expanded in a Taylor series about the critical point (Ω_c, β_c, R_c). If λ° is the minimum value on the neutral surface then

$$\begin{aligned} \lambda &= \lambda^\circ + \lambda_\Omega(\Omega - \Omega_c) + \lambda_\beta(\beta - \beta_c) + \lambda_R(R - R_c) + \\ &\quad \frac{1}{2}\lambda_{\Omega\Omega}(\Omega - \Omega_c)^2 + \frac{1}{2}\lambda_{\beta\beta}(\beta - \beta_c)^2 + \lambda_{\Omega\beta}(\Omega - \Omega_c)(\beta - \beta_c) + \ldots \end{aligned} \tag{2.61}$$

Expressions for the first and second partial derivatives of λ are thus required in order to implement a form of Newton's method.

Consider the expression

$$\boldsymbol{L}\boldsymbol{F} = \lambda \boldsymbol{K}\boldsymbol{F} \tag{2.62}$$

where $\boldsymbol{F}$ is a general eigenvector of $\boldsymbol{L}$ and let X represent any one of the parameters, Ω, β or R. Differentiating Eq.(2.62) with respect to X gives

$$\boldsymbol{L}_X\boldsymbol{F} + \boldsymbol{L}\boldsymbol{F}_X = \lambda_X \boldsymbol{K}\boldsymbol{F} + \lambda \boldsymbol{K}\boldsymbol{F}_X. \tag{2.63}$$

Evaluation at the critical point, $\lambda = 0$, and taking the inner product with the left eigenvector, $\boldsymbol{F}^*$, returns an expression for λ_X.

$$\begin{aligned} \lambda_X < \boldsymbol{F}^*, \boldsymbol{K}\boldsymbol{F} > &= < \boldsymbol{F}^*, \boldsymbol{L}_X\boldsymbol{F} > + < \boldsymbol{F}^*, \boldsymbol{L}\boldsymbol{F}_X > \\ \text{but} \quad < \boldsymbol{F}^*, \boldsymbol{L}\boldsymbol{F}_X > &= < \boldsymbol{L}^*\boldsymbol{F}^*, \boldsymbol{F}_X > = 0 \qquad \text{by definition} \\ \Rightarrow \quad \lambda_X &= \frac{< \boldsymbol{F}^*, \boldsymbol{L}_X\boldsymbol{F} >}{< \boldsymbol{F}^*, \boldsymbol{K}\boldsymbol{F} >}. \end{aligned} \tag{2.64}$$

In order to evaluate the second derivatives Eq.(2.63) is differentiated with respect to some

variable Y say, which again represents any one of the three parameters involved.

$$\begin{aligned} \frac{\partial}{\partial Y}\{\boldsymbol{L}_X\boldsymbol{F} + \boldsymbol{L}\boldsymbol{F}_X &= \lambda_X \boldsymbol{K}\boldsymbol{F} + \lambda \boldsymbol{K}\boldsymbol{F}_X\} \\ \boldsymbol{L}_{XY}\boldsymbol{F} + \boldsymbol{L}_X\boldsymbol{F}_Y + \boldsymbol{L}_Y\boldsymbol{F}_X + \boldsymbol{L}\boldsymbol{F}_{XY} &= \lambda_{XY}\boldsymbol{K}\boldsymbol{F} + \lambda_X\boldsymbol{K}\boldsymbol{F}_Y + \\ & \quad \lambda_Y\boldsymbol{K}\boldsymbol{F}_X + \lambda\boldsymbol{K}\boldsymbol{F}_{XY} \end{aligned} \tag{2.65}$$

Evaluating at the critical point leaves

$$\boldsymbol{L}\boldsymbol{F}_{XY} = \lambda_{XY}\boldsymbol{K}\boldsymbol{F} + \lambda_X\boldsymbol{K}\boldsymbol{F}_Y + \lambda_Y\boldsymbol{K}\boldsymbol{F}_X - \boldsymbol{L}_{XY}\boldsymbol{F} - \boldsymbol{L}_X\boldsymbol{F}_Y - \boldsymbol{L}_Y\boldsymbol{F}_X \tag{2.66}$$

To obtain an expression for the second derivative, λ_{XY}, the following solvability condition is applied :

Solvability condition.

Suppose $\boldsymbol{F}^*$ is a solution of the adjoint problem $\boldsymbol{L}^*\boldsymbol{F}^* = 0$ then $\boldsymbol{L}\boldsymbol{G} = \boldsymbol{g}$ is solvable if and only if $< \boldsymbol{F}^*, \boldsymbol{g} >= 0$.

In order to prove this the inner product of $\boldsymbol{F}^*$ with $\boldsymbol{L}\boldsymbol{G} = \boldsymbol{g}$ is taken.

$$\begin{aligned} & < \boldsymbol{F}^*, \boldsymbol{L}\boldsymbol{G} > \;=\; < \boldsymbol{F}^*, \boldsymbol{g} > \\ \text{but} \quad & < \boldsymbol{F}^*, \boldsymbol{L}\boldsymbol{G} > \;=\; < \boldsymbol{L}^*\boldsymbol{F}^*, \boldsymbol{G} > \;=\; 0 \quad \text{since} \quad \boldsymbol{L}^*\boldsymbol{F}^* = 0 \\ \Rightarrow \quad & < \boldsymbol{F}^*, \boldsymbol{g} > \;=\; 0 \end{aligned} \tag{2.67}$$

Applying this solvability condition to the expression in Eq.(2.66) then gives the result

$$\begin{aligned} \lambda_{XY} < \boldsymbol{F}^*, \boldsymbol{K}\boldsymbol{F} > + \lambda_X < \boldsymbol{F}^*, \boldsymbol{K}\boldsymbol{F}_Y > + \lambda_Y < \boldsymbol{F}^*, \boldsymbol{K}\boldsymbol{F}_X > - \\ < \boldsymbol{F}^*, \boldsymbol{L}_{XY}\boldsymbol{F} > - < \boldsymbol{F}^*, \boldsymbol{L}_X\boldsymbol{F}_Y > - < \boldsymbol{F}^*, \boldsymbol{L}_Y\boldsymbol{F}_X >= 0 \end{aligned} \tag{2.68}$$

or

$$\begin{aligned} \lambda_{XY} = \{ < \boldsymbol{F}^*, \boldsymbol{L}_{XY}\boldsymbol{F} > + < \boldsymbol{F}^*, \boldsymbol{L}_X\boldsymbol{F}_Y > - \lambda_X < \boldsymbol{F}^*, \boldsymbol{K}\boldsymbol{F}_Y > - \\ \lambda_Y < \boldsymbol{F}^*, \boldsymbol{K}\boldsymbol{F}_X > \} / < \boldsymbol{F}^*, \boldsymbol{K}\boldsymbol{F} > . \end{aligned} \tag{2.69}$$

The only undetermined values are those of $\boldsymbol{F}_X$ (or $\boldsymbol{F}_Y$) which can be obtained from Eq.(2.63) where evaluation at the critical point leaves

$$\boldsymbol{L}_o\boldsymbol{F}_X = \lambda_X\boldsymbol{K}\boldsymbol{F} - \boldsymbol{L}_X\boldsymbol{F}. \tag{2.70}$$

Once λ_X has been calculated it would appear that this could be solved directly through the application of a standard numerical routine but problems arise since $\boldsymbol{L}_o$ is in fact singular

and $\boldsymbol{F_X}$ must be determined by solving an augmented problem. Eq.(2.70) is therefore enlarged as follows with the details of the method described in § 2.12.

$$\begin{bmatrix} \boldsymbol{L_o} & -\boldsymbol{KF} \\ \boldsymbol{F}^{*T} & 0 \end{bmatrix} \begin{bmatrix} \boldsymbol{F_X} \\ \lambda_X \end{bmatrix} = \begin{bmatrix} -\boldsymbol{L_X F} \\ 0 \end{bmatrix} \tag{2.71}$$

This now gives a non-singular problem from which $\boldsymbol{F_X}$ can be obtained using a standard linear system solver.

In order to apply Newton's method to this problem an initial estimate $(\Omega, \beta, R)_0$ is made for the critical point, (Ω_c, β_c, R_c). An improvement on this initial value is made by applying the following iterative formula.

$$\begin{bmatrix} \Omega \\ \beta \\ R \end{bmatrix}_{n+1} = \begin{bmatrix} \Omega \\ \beta \\ R \end{bmatrix}_n - \boldsymbol{J}_n{}^{-1} \begin{bmatrix} \lambda(\Omega, \beta, R)_n \\ \lambda_\beta(\Omega, \beta, R)_n \\ \lambda_\Omega(\Omega, \beta, R)_n \end{bmatrix} \qquad n = 0, 1, \ldots \tag{2.72}$$

where

$$\boldsymbol{J}_n = \begin{bmatrix} \lambda_\Omega & \lambda_\beta & \lambda_R \\ \lambda_{\beta\Omega} & \lambda_{\beta\beta} & \lambda_{\beta R} \\ \lambda_{\Omega\Omega} & \lambda_{\Omega\beta} & \lambda_{\Omega R} \end{bmatrix} \qquad \text{evaluated at} \quad (\Omega, \beta, R)_n \tag{2.73}$$

$\boldsymbol{J}_n$ is invertible in the neighbourhood of the critical point since $\lambda_R \neq 0$ and the subdeterminant formed from the second derivatives of λ with respect to Ω and β is also non-zero. The process in Eq.(2.72) is repeated iteratively until some convergence condition is satisfied and in this particular case a convergence tolerance of 10^{-8} was used.

Throughout the numerical calculations the value of λ° is retained to reduce errors in the subsequent calculations although it is assumed to be exactly zero in the analysis.

Numerical values obtained using the above method are shown in Table 2.1. These points correspond to the minima of the neutral paraboloids in (Ω, β, R) parameter space. Values for λ, $\partial\lambda/\partial\beta$ and $\partial\lambda/\partial\Omega$ are calculated to be 10^{-8} or less confirming that the minima have in fact been correctly located. Figures 2.7(a)-(d) show numerically calculated neutral contours for different values of θ indicating the structure of the neutral paraboloids.

The critical points are found to occur at different rotation rates with higher rotation speeds required to give the minimum as plane Couette flow is approached. The fact that all the states investigated have well defined minimum points suggests that the three-dimensional

neutral paraboloid surface in (Ω, β, R) parameter space exists for the whole family of profiles given by Eqs.(2.52) and (2.53). Existing results for plane Poiseuille flow are in fact very close to the global minimum point calculated here with $\Omega = 0.1667$, $\beta = 2.45$ and $R = 66.5$ often quoted as the critical parameters. The minimum critical values predicted for Couette flow agree well with those of Lezius and Johnston (1976) given in the review text.

θ	Ω_c	β_c	R_c
0	0.1683	2.4592	66.4476
$\frac{1}{3}$	0.1433	2.2460	51.2680
$\frac{2}{3}$	0.1718	1.5790	30.5300
1	0.2500	1.5582	20.6625

Table 2.1: Minimum neutral points.

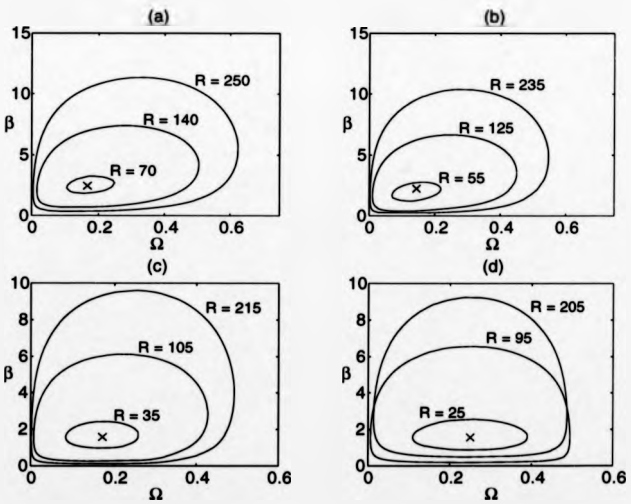

Figure 2.7: Numerically determined neutral contours in (Ω, β) parameter space. (a) : $\theta = 0$, (b) : $\theta = \frac{1}{3}$, (c) : $\theta = \frac{2}{3}$, (d) : $\theta = 1$. × marks the position of the critical point.

2.10 Weakly Nonlinear Theory.

The weakly nonlinear behaviour of the streamwise rolls in the neighbourhood of the critical point, (Ω_c, β_c, R_c), is studied assuming a channel of infinite spanwidth through the use of a Ginzburg-Landau (G-L) equation valid in the vicinity of this critical point and derived by means of a weakly nonlinear analysis. This covers some of the points neglected by linear theory which always returns amplified or damped solutions that are independent of the initial amplitude of the perturbation. The perturbations in linear theory are also assumed to either grow or decay indefinitely in space or time, depending on the form chosen, which does not occur physically in real flow problems when a flow becomes unstable. The coefficients of the resulting G-L equation will indicate whether the bifurcation to streamwise rolls is supercritical or subcritical which then gives information of importance in the transition process. In the case of supercritical bifurcation the flow is considered to be stable below the linearly predicted critical Reynolds number and above this value the flow solution becomes unstable but a new branch of stable periodic solutions is formed which eventually reaches a state of amplitude equilibrium and constitutes a new laminar flow. In the subcritical case, however, only an unstable solution is found above the linear critical value and unstable solutions can exist below that value in the region of linear stability if the initial perturbation amplitude is large enough. This type of instability is particularly dangerous since it is not revealed by linear theory and small perturbations on the laminar flow in this case can quickly lead to turbulent states.

Standard weakly nonlinear theory is generally based on the Landau equation.

$$\frac{\partial A}{\partial t} = a_1 A + a_2 |A|^2 A + O(|A|^4) \tag{2.74}$$

where A is the amplitude of the perturbation and a_2 is known as the Landau constant which determines the nonlinear behaviour of the system. Setting $a_2 = 0$ is equivalent to the linear case where an exponential solution of the form $A_o e^{a_1 t}$ is returned. If a_2 is real and negative then for the linearly unstable case ($a_1 > 0$) the perturbation will reach a finite-amplitude steady state satisfying $|A|^2 = -(a_1/a_2)$ which corresponds to supercritical instability. On the other hand, if a_2 is positive then amplification ($\frac{\partial A}{\partial t} > 0$) of linearly stable modes ($a_1 < 0$) is possible if the initial amplitude of the perturbation meets the requirement $|A|^2 > -(a_1/a_2)$ and this condition then corresponds to subcritical instability.

However, this form of weakly nonlinear analysis does not allow for any spatial or spanwise variation; but the G-L formulation of Newell and Whitehead (1969) accommodates this and can also be useful in considering sideband or Eckhaus instability. Similar deductions

about the nature of the instability can be made from the relative signs of the coefficients in the G-L equation and in this case accurate numerical values for the coefficients are obtained through extension of the spectral code used in the preceding linear analysis.

Supercritical bifurcation has been predicted for rotating Poiseuille flow but the nature of the bifurcation has not been established for other channel flows.

2.11 Derivation of the Ginzburg-Landau Equation.

The general form of the Ginzburg-Landau equation, originally given by Newell and Whitehead, with appropriate scalings is

$$\frac{\partial A}{\partial t} = b_1 \frac{\partial^2 A}{\partial z^2} + b_2 A - b_3 |A|^2 A. \tag{2.75}$$

A numerical version of this equation is obtained by considering the form of the roll cells. The streamwise roll cells, or primary instability in the channel, appear stationary in the rotating reference frame, arise periodically in the spanwise direction and are infinite in extent in the streamwise direction. The weakly nonlinear theory is thus based on the assumption of spanwise periodic solutions which are independent of streamwise distance, x, and time, t. With the (x,t) dependence removed from the original set of governing equations a new set is obtained for the bifurcating streamwise roll cells.

$$(U_y + \bar{u}_y)\bar{v} + \bar{w}\bar{u}_z - 2\Omega\bar{v} - \frac{1}{R}\nabla^2\bar{u} = 0 \tag{2.76}$$

$$\bar{v}_y\bar{v} + \bar{w}\bar{v}_z + 2\Omega\bar{u} + \bar{p}_y - \frac{1}{R}\nabla^2\bar{v} = 0 \tag{2.77}$$

$$\bar{w}_y\bar{v} + \bar{w}\bar{w}_z + \bar{p}_z - \frac{1}{R}\nabla^2\bar{w} = 0 \tag{2.78}$$

$$\bar{v}_y + \bar{w}_z = 0 \tag{2.79}$$

Suffices y and z denote differentiation with respect to these variables and $\bar{u}, \bar{v}, \bar{w}$ and $\bar{p}$ are now functions of y and z.

From the linear theory the problem is assumed to have a neutral surface with a minimum point located at (Ω_c, β_c, R_c) and bifurcating periodic solutions in the neighbourhood of this critical point are sought. The terms appearing in the governing equations are expressed as a power series in terms of some small parameter, ε, with expansion about the point (β_c, R_c) for a fixed value of Ω.

$$R = R_c + \varepsilon R_1 + \varepsilon^2 R_2 + O(\varepsilon^3) \tag{2.80}$$

$$\beta = \beta_c + \varepsilon\beta_1 + \varepsilon^2\beta_2 + O(\varepsilon^3) \tag{2.81}$$

$$\boldsymbol{\Phi} = \begin{bmatrix} \bar{u} \\ \bar{v} \\ \bar{w} \\ \bar{p} \end{bmatrix} = \varepsilon \begin{bmatrix} u_1 \\ v_1 \\ w_1 \\ p_1 \end{bmatrix} + \varepsilon^2 \begin{bmatrix} u_2 \\ v_2 \\ w_2 \\ p_2 \end{bmatrix} + O(\varepsilon^3) \tag{2.82}$$

Substitution into the governing equations and equating like powers of ε yields the following sequence of problems. The spanwise variable is scaled by β_c such that $z \mapsto \beta_c z$.

$$U_y v_j - 2\Omega v_j - \frac{1}{R_c}\left(\frac{\partial^2 u_j}{\partial y^2} + \beta_c^2 \frac{\partial^2 u_j}{\partial z^2}\right) = f_j^{(1)} \tag{2.83}$$

$$\frac{\partial p_j}{\partial y} + 2\Omega u_j - \frac{1}{R_c}\left(\frac{\partial^2 v_j}{\partial y^2} + \beta_c^2 \frac{\partial^2 v_j}{\partial z^2}\right) = f_j^{(2)} \tag{2.84}$$

$$\beta_c \frac{\partial p_j}{\partial z} - \frac{1}{R_c}\left(\frac{\partial^2 w_j}{\partial y^2} + \beta_c^2 \frac{\partial^2 w_j}{\partial z^2}\right) = f_j^{(3)} \tag{2.85}$$

$$-\frac{\partial v_j}{\partial y} - \beta_c \frac{\partial w_j}{\partial z} = f_j^{(4)} \tag{2.86}$$

where $j = 1, 2, \ldots$ denotes the order of the problem.

This system of equations can be written in the more concise form

$$\boldsymbol{L}_o \boldsymbol{\Phi}_j = \boldsymbol{f}_j \tag{2.87}$$

where

$$\boldsymbol{L}_o = \begin{bmatrix} -\frac{1}{R_c}\nabla_o^2 & U_y - 2\Omega & 0 & 0 \\ 2\Omega & -\frac{1}{R_c}\nabla_o^2 & 0 & \frac{\partial}{\partial y} \\ 0 & 0 & -\frac{1}{R_c}\nabla_o^2 & \beta_c \frac{\partial}{\partial z} \\ 0 & -\frac{\partial}{\partial y} & -\beta_c \frac{\partial}{\partial z} & 0 \end{bmatrix} \quad \text{with} \quad \nabla_o^2 = \frac{\partial^2}{\partial y^2} + \beta_c^2 \frac{\partial^2}{\partial z^2}$$

$$\boldsymbol{\Phi}_j = [u_j, v_j, w_j, p_j]^T \quad \text{and} \quad \boldsymbol{f}_j = [f_j^{(1)}, f_j^{(2)}, f_j^{(3)}, f_j^{(4)}]^T.$$

$\boldsymbol{L}_o$ is simply the linear operator of the preceding linear theory with the x dependence suppressed and evaluation of the operators at (β_c, R_c).

The first order problem is the linear case (since $\boldsymbol{f}_1 = 0$) and the form of the solutions is already established. $\boldsymbol{L}_o \boldsymbol{\Phi}_1 = 0$ has a general spanwise periodic solution of the form

$$\boldsymbol{\Phi}_1 = \begin{bmatrix} u_1 \\ v_1 \\ w_1 \\ p_1 \end{bmatrix} = \begin{bmatrix} \hat{u}_1(y) \\ \hat{v}_1(y) \\ i\hat{w}_1(y) \\ \hat{p}_1(y) \end{bmatrix} \begin{bmatrix} Ae^{iz} + \bar{A}e^{-iz} \\ Ae^{iz} + \bar{A}e^{-iz} \\ Ae^{iz} - \bar{A}e^{-iz} \\ Ae^{iz} + \bar{A}e^{-iz} \end{bmatrix}. \tag{2.88}$$

The functions $\hat{u}_1, \hat{v}_1, \hat{w}_1$ and $\hat{p}_1$ can be obtained numerically using the same Chebyshev

technique of the linear theory by solving $\hat{\boldsymbol{L}}(\beta_c)\hat{\hat{\boldsymbol{\Phi}}}_1 = 0$ where $\hat{\hat{\boldsymbol{\Phi}}}_1 = [\hat{u}_1, \hat{v}_1, i\hat{w}_1, \hat{p}_1]^T$ and

$$\hat{\boldsymbol{L}}(\beta_c) = \begin{bmatrix} \boldsymbol{\Gamma}_c & \boldsymbol{D}_2 & 0 & 0 \\ \boldsymbol{D}_1 & \boldsymbol{\Gamma}_c & 0 & -\boldsymbol{E} \\ 0 & 0 & \boldsymbol{\Gamma}_c & -i\beta_c\boldsymbol{M} \\ 0 & \boldsymbol{A}^* & i\beta_c\boldsymbol{M}^* & 0 \end{bmatrix}. \tag{2.89}$$

The submatrices of $\hat{\boldsymbol{L}}(\beta_c)$ are defined in § 2.6 and $\boldsymbol{\Gamma}_c = \boldsymbol{\Gamma}(\alpha = 0, \beta_c, R_c)$. It should be noted that with $\alpha = 0$, u, v and p are real and w is imaginary so that the system can be converted to purely real arithmetic for more efficient computation. The operator $\hat{\boldsymbol{L}}(\beta_c)$ is thus redefined as

$$\boldsymbol{L}(\beta_c) = \begin{bmatrix} \boldsymbol{\Gamma}_c & \boldsymbol{D}_2 & 0 & 0 \\ \boldsymbol{D}_1 & \boldsymbol{\Gamma}_c & 0 & -\boldsymbol{E} \\ 0 & 0 & \boldsymbol{\Gamma}_c & -\beta_c\boldsymbol{M} \\ 0 & \boldsymbol{A}^* & -\beta_c\boldsymbol{M}^* & 0 \end{bmatrix} \tag{2.90}$$

which operates on the new vector $\hat{\boldsymbol{\Phi}}_1 = [u_1, v_1, \hat{w}_1, \hat{p}_1]^T$. The first order problem $\boldsymbol{L}(\beta_c)\hat{\boldsymbol{\Phi}}_1 = 0$ and its adjoint $\boldsymbol{L}^*\hat{\boldsymbol{\Phi}}_1^* = 0$ are then solved to obtain right (the first order solution) and left eigenvectors. The first order solutions are shown in Figure 2.8 for the different mean flow fields where the effect of the change in mean flow is most apparent in the profiles for u. The point of maximum amplitude is shown to move towards the upper wall of the channel and u becomes positive for all positions within the channel for $\theta > \frac{2}{3}$.

In order to obtain higher order solutions the solvability condition of § 2.9 must be implemented.

Numerical solutions to the second order problem are required for use in the modulation equation to be defined below. Suppose $\boldsymbol{f}_2 = [f_2^{(1)}, f_2^{(2)}, f_2^{(3)}, f_2^{(4)}]^T$ then $\boldsymbol{f}_2$ takes the form

$$\boldsymbol{f}_2 = \boldsymbol{f}_{21}Ae^{iz} + \boldsymbol{f}_{22}A^2e^{2iz} + \text{c.c.} + \boldsymbol{f}_{23}|A|^2 \tag{2.91}$$

These terms must be considered since they contribute to the required periodic terms, e^{iz}, in problems of higher order. Expressions for $\boldsymbol{f}_{2j}, j = 1, 2, 3$ appear in Appendix A.

Assuming the form of $\boldsymbol{f}_2$ the second order solution $\boldsymbol{\Phi}_2$ is constructed in a similar manner.

$$\boldsymbol{\Phi}_2 = \beta_1\boldsymbol{\Phi}_{21}Ae^{iz} + \boldsymbol{\Phi}_{22}A^2e^{2iz} + \text{c.c.} + \boldsymbol{\Phi}_{23}|A|^2 \tag{2.92}$$

Substitution into $\boldsymbol{L}_o\boldsymbol{\Phi}_2 = \boldsymbol{f}_2$ yields the relation

$$\begin{aligned} & \boldsymbol{L}_o\{\beta_1\boldsymbol{\Phi}_{21}Ae^{iz} + \boldsymbol{\Phi}_{22}A^2e^{2iz} + \text{c.c.} + \boldsymbol{\Phi}_{23}|A|^2\} \\ = \; & \beta_1\boldsymbol{L}(\beta_c)\boldsymbol{\Phi}_{21}Ae^{iz} + \boldsymbol{L}(2\beta_c)\boldsymbol{\Phi}_{22}e^{2iz} + \text{c.c.} + \boldsymbol{L}(0)\boldsymbol{\Phi}_{23}|A|^2 \\ = \; & \boldsymbol{f}_{21}Ae^{iz} + \boldsymbol{f}_{22}A^2e^{2iz} + \text{c.c.} + \boldsymbol{f}_{23}|A|^2. \end{aligned} \tag{2.93}$$

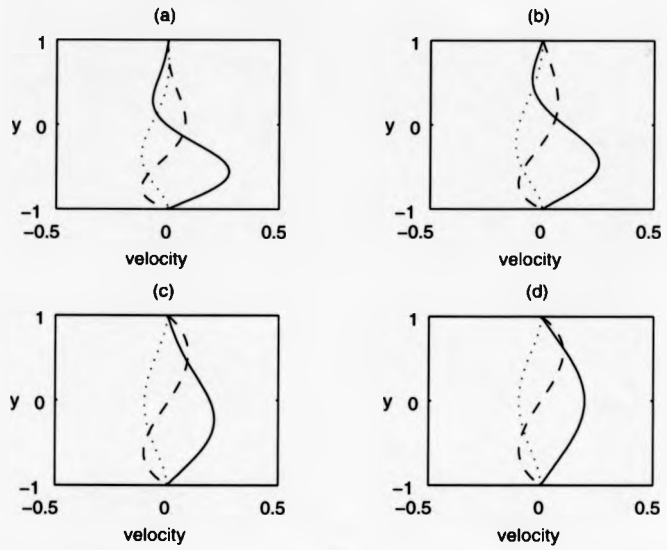

Figure 2.8: First order solutions (a) : $\theta = 0$, (b) : $\theta = \frac{1}{3}$, (c) : $\theta = \frac{2}{3}$, (d) : $\theta = 1$. $\hat{u}$: —, $\hat{v}$: $\cdots$, $\hat{w}$: - -.

Equating the coefficients of e^{iz}, e^{2iz} and $|A|^2$ results in three component problems.

$$\beta_1 \boldsymbol{L}(\beta_c)\boldsymbol{\Phi}_{21} = \boldsymbol{f}_{21} \tag{2.94}$$

$$\boldsymbol{L}(2\beta_c)\boldsymbol{\Phi}_{22} = \boldsymbol{f}_{22} \tag{2.95}$$

$$\boldsymbol{L}(0)\boldsymbol{\Phi}_{23} = \boldsymbol{f}_{23} \tag{2.96}$$

$\boldsymbol{L}(\beta_c)$ and $\boldsymbol{L}(0)$ are singular operator matrices and the associated problems must be solved by the method described in § 2.12. The first of these problems can also be simplified to $\boldsymbol{L}(\beta_c)\Phi_{21} = \boldsymbol{f}_{212}$ where $\boldsymbol{f}_{212}$ is a reduced version of $\boldsymbol{f}_{21}$. The analysis of this is given in § 2.13.

In the third order problem $\boldsymbol{f}_3$ takes the following form.

$$\boldsymbol{f}_3 = \beta_1^2 \boldsymbol{f}_{31} + R_2 \boldsymbol{f}_{32} + |A|^2 \boldsymbol{f}_{33} + \beta_2 \boldsymbol{f}_{34} \tag{2.97}$$

By a similar argument to the second order problem (§ 2.13) terms involving β_2 vanish in the solvability condition and therefore applying that condition leaves

$$\beta_1^2 < \boldsymbol{\Phi}^*, \boldsymbol{f}_{31} > + R_2 < \boldsymbol{\Phi}^*, \boldsymbol{f}_{32} > + |A|^2 < \boldsymbol{\Phi}^*, \boldsymbol{f}_{33} >= 0. \tag{2.98}$$

The inner products give real coefficients which can be determined numerically using the definition of the discrete inner product of Eq.(2.56). Renaming these coefficients a_1, a_2 and a_3 and multiplying through by ε^2 returns the modulation equation in its final form from which information about the nature of the bifurcation can be obtained.

$$a_1(\beta - \beta_c)^2 + a_2(R - R_c) + a_3|\bar{A}|^2 = 0 \tag{2.99}$$

This is analogous to the G-L formulation of Eq.(2.75) for stationary states. The rolls take the form $A = \mathcal{A}e^{i\varepsilon\beta_1 z}$ where β_1 is the change in the wavenumber in the weakly nonlinear analysis. If z is scaled by ε then Eq.(2.75) for stationary solutions becomes

$$-b_1\beta_1^2\mathcal{A} + \tilde{b}_2R_2\mathcal{A} - b_3|\mathcal{A}|^2\mathcal{A} = 0. \tag{2.100}$$

Multiplying throughout by $-\varepsilon^2/\mathcal{A}$ then gives

$$b_1(\beta - \beta_c)^2 - \tilde{b}_2(R - R_c) + b_3(\varepsilon\mathcal{A})^2 = 0 \tag{2.101}$$

which is equivalent to the form of Eq.(2.99).

It is the relative signs of the coefficients a_1, a_2 and a_3 which determines the possible solutions. Numerical results are given in Table 2.2 for $\theta = 0, \frac{1}{3}, \frac{2}{3}$ and 1. In all cases $a_1 > 0, a_2 < 0$ and $a_3 > 0$.

θ	Ω_c	β_c	R_c	a_1	a_2	a_3
0	0.1683	2.4592	66.4476	0.0330	-0.0043	0.5835
$\frac{1}{3}$	0.1433	2.2460	51.2680	0.0382	-0.0078	0.3469
$\frac{2}{3}$	0.1718	1.5790	30.5300	0.0673	-0.0077	0.1085
1	0.2500	1.5582	20.6625	0.1010	-0.0164	0.0687

Table 2.2: Coefficients of the modulation equation at the minimum critical point for a number of basic states.

With the coefficients holding these signs for the whole family of basic flow fields Eq.(2.99) can be used to determine the permissible solutions for the amplitude function $|\bar{A}|^2$.

- For $R < R_c$ no solutions can exist.

This infers that no spanwise periodic solutions of the kind considered in the analysis appear below the critical Reynolds number predicted using linear theory.

- At $R = R_c$ there exists one solution : $|\bar{A}|^2 = 0$ with $\beta = \beta_c$.
- For $R > R_c$ solutions satisfy the following equation.

$$|\bar{A}|^2 = c_1(\beta - \beta_c)^2 + c_2(R - R_c)$$

where $c_1 = -\frac{a_1}{a_3} < 0$ and $c_2 = -\frac{a_2}{a_3} > 0$.

This gives a band of spanwise wavenumbers between $\beta_\pm = \beta_c \pm \sqrt{\frac{c_2}{c_1}(R_c - R)}$, for which solutions of bounded amplitude exist. This corresponds to the formation of roll cells above $R = R_c$ in the linearly unstable region with maximum amplitude occurring at $\beta = \beta_c$ so that the most unstable mode of the linear theory is the important mode as far as nonlinear amplitude is concerned. This mode is therefore likely to exert the most influence on what occurs in the nonlinear region.

Figure 2.9 shows the amplitude $|\bar{A}|^2$ as a function of β for the different mean states investigated at Reynolds numbers approximately $R_c + 5$. Of significance is the increase in the magnitude of the amplitude as θ is increased. The absence of solutions below R_c and the finite amplitude solutions above R_c across a band of wavenumbers indicates supercritical bifurcation for all the states investigated.

Recall that $a_2 = < \boldsymbol{\Phi}^*, \boldsymbol{f}_{32} >$ with $\boldsymbol{f}_{32}$ as defined in Appendix A. However

$$\boldsymbol{f}_{32} = -\boldsymbol{L}_R\boldsymbol{\Phi} \qquad \Rightarrow \qquad a_2 = - < \boldsymbol{\Phi}^*, \boldsymbol{L}_R\boldsymbol{\Phi} >$$

and using Eq.(2.64)

$$a_2 = -\lambda_R < \boldsymbol{\Phi}^*, \boldsymbol{K}\boldsymbol{\Phi} > .$$

Similarly it can be shown that

$$a_1 = -\frac{1}{2}\lambda_{\beta\beta} < \boldsymbol{\Phi}^*, \boldsymbol{K}\boldsymbol{\Phi} > .$$

The Taylor expansion of the eigenvalue,λ, appearing in Eq(2.61) and the conditions $\lambda = \lambda_\Omega = \lambda_\beta = 0$ are used to obtain

$$\lambda = \lambda_R(R - R_c) + \frac{1}{2}\lambda_{\beta\beta}(\beta - \beta_c)^2.$$

For λ on the neutral surface λ_R must be positive and therefore from the above expression $\lambda_{\beta\beta} < 0$ which is consistent with the numerical results presented in Table 2.2. This then leaves a_3 as the critical coefficient in the modulation equation with $a_3 = 0$ representing the cross-over between supercritical and subcritical bifurcation. Negative values of a_3 would give rise to solutions for $R < R_c$ and if $R > R_c$ solutions with unbounded amplitude are predicted indicating subcritical instability.

From the results in Table 2.2 it can be seen that this critical coefficient decreases by an order of magnitude as θ moves from 0 to 1 but remains positive throughout. Thus no fundamental differences arise in the nature of the nonlinear solutions in the vicinity of the critical point. However, even though supercritical bifurcation is predicted for plane Couette flow the roll cells formed when the streamwise laminar flow becomes unstable will have significantly larger amplitudes than those associated with plane Poiseuille flow as indicated in Figure 2.9. This may be an important feature in a fully nonlinear analysis since it could be argued that this flow is only just within the confines of supercritical instability.

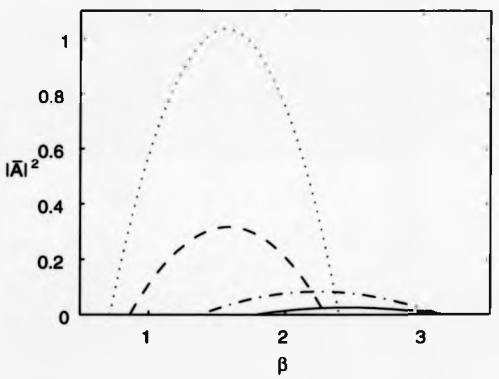

Figure 2.9: (a) : Roll cell amplitude as a function of spanwise wavenumber, β. $\theta = 0$, $R = 70$: —, $\theta = \frac{1}{3}$, $R = 55$: – · –, $\theta = \frac{2}{3}$, $R = 35$: - -, $\theta = 1$, $R = 25$: · · ·.

2.12 Numerical Solution to Singular Systems.

In § 2.9 the calculation of the minimum point of the neutral paraboloid gives rise to a singular system of equations which cannot be solved directly using the standard numerical techniques. This type of problem also occurs in § 2.10 when determining the second order solutions in the weakly nonlinear theory. The singular operators involved are $\boldsymbol{L}_o$ appearing in Eq.(2.70) or equivalently $\boldsymbol{L}(\beta_c)$ of Eq.(2.94) and $\boldsymbol{L}(0)$ of Eq.(2.96). In the first case the singular system is of the following form.

$$\boldsymbol{L}_o \boldsymbol{F}_X = \lambda_X \boldsymbol{K}\boldsymbol{F} - \boldsymbol{L}_X \boldsymbol{F} \tag{2.102}$$

The operator $\boldsymbol{L}_o$ has a single zero eigenvalue and the corresponding right and left eigenvectors are $\boldsymbol{F}$ and $\boldsymbol{F}^*$. If the normalisation condition, $< \boldsymbol{F}^*, \boldsymbol{F}_X >= 0$ is also imposed then following the techniques of Crouch and Herbert (1993) the singular system of Eq.(2.102) can be augmented and written as follows.

$$\begin{bmatrix} \boldsymbol{L}_o & -\boldsymbol{K}\boldsymbol{F} \\ \boldsymbol{F}^{*T} & 0 \end{bmatrix} \begin{bmatrix} \boldsymbol{F}_X \\ \lambda_X \end{bmatrix} = \begin{bmatrix} -\boldsymbol{L}_X \boldsymbol{F} \\ 0 \end{bmatrix} \tag{2.103}$$

The inclusion of the normalisation condition only increases the order of the discretised matrix problem by 1 where the unknown vector is now the original unknown, $\boldsymbol{F}_X$, with the addition of λ_X as the final entry. This augmented equation satisfies all the required conditions, but it must be verified that this extended system is nonsingular and that the solvability condition is also satisfied in this case.

Using matrix theory (Magnus and Neudecker, 1988) if vectors $\boldsymbol{\xi}$ and $\boldsymbol{\eta} \in \mathbb{R}^n$ and $\boldsymbol{B} \in \mathbb{R}^{n \times n}$ then

$$\begin{vmatrix} \boldsymbol{B} & \boldsymbol{\xi} \\ \boldsymbol{\eta}^T & 0 \end{vmatrix} = - < \boldsymbol{\eta}, \boldsymbol{B}^{\#} \boldsymbol{\xi} >$$

where $\boldsymbol{B}^{\#}$ is the transpose of the cofactor matrix of $\boldsymbol{B}$. If $\boldsymbol{B}$ has a simple zero eigenvalue with right and left eigenvectors $\boldsymbol{\Phi}$ and $\boldsymbol{\Phi}^*$ respectively then $\boldsymbol{B}^{\#}$ can be expressed as

$$\boldsymbol{B}^{\#} = \mu(\boldsymbol{B}) \frac{\boldsymbol{\Phi}\boldsymbol{\Phi}^{*T}}{< \boldsymbol{\Phi}^*, \boldsymbol{\Phi} >}$$

where $\mu(\boldsymbol{B})$ is the product of the remaining non-zero eigenvalues. If this is applied to the problem in Eq.(2.103) then

$$\begin{vmatrix} \boldsymbol{L}_o & -\boldsymbol{K}\boldsymbol{F} \\ \boldsymbol{F}^{*T} & 0 \end{vmatrix} =< \boldsymbol{F}^*, \boldsymbol{L}_o^{\#} \boldsymbol{K}\boldsymbol{F} >= \mu(\boldsymbol{L}_o) < \boldsymbol{F}^*, \boldsymbol{K}\boldsymbol{F} > .$$

In the case of a simple zero eigenvalue $< \boldsymbol{F}^*, \boldsymbol{F} >\neq 0$ and for the augmented matrix to be nonsingular the only other requirement is that $< \boldsymbol{F}^*, \boldsymbol{K}\boldsymbol{F} >\neq 0$.

The existence of the solvability condition within this extended problem can be demonstrated using Cramer's rule as performed by Crouch and Herbert where λ_X can be expressed as

$$\lambda_X = \frac{\begin{vmatrix} \boldsymbol{L}_o & -\boldsymbol{L}_X\boldsymbol{F} \\ \boldsymbol{F}^{*T} & 0 \end{vmatrix}}{\begin{vmatrix} \boldsymbol{L}_o & -\boldsymbol{K}\boldsymbol{F} \\ \boldsymbol{F}^{*T} & 0 \end{vmatrix}} = \frac{< \boldsymbol{F}^*, \boldsymbol{L}_o{}^{\#}\boldsymbol{L}_X\boldsymbol{F} >}{\mu(\boldsymbol{L}_o) < \boldsymbol{F}^*, \boldsymbol{K}\boldsymbol{F} >} = \frac{< \boldsymbol{F}^*, \boldsymbol{L}_X\boldsymbol{F} >}{< \boldsymbol{F}^*, \boldsymbol{K}\boldsymbol{F} >}.$$

The result using this method is exactly that required by the solvability condition, see Eq.(2.64) and thus the augmented formulation is consistent.

$\boldsymbol{L}(0)$ of Eq.(2.96) is singular with the non-trivial eigenvector $\boldsymbol{\psi}_p = [\boldsymbol{0}, \boldsymbol{0}, \boldsymbol{0}, \boldsymbol{\pi}]^T$ where $\boldsymbol{\pi} = [1, \ldots, 1]^T \in I\!R^N$. This corresponds to zero velocity and constant pressure and is also the left eigenvector of $\boldsymbol{L}(0)$. The singularity in this case is removed by solving

$$\begin{bmatrix} \boldsymbol{L}(0) & \boldsymbol{\psi}_p \\ \boldsymbol{\psi}_p^T & 0 \end{bmatrix} \begin{bmatrix} \boldsymbol{\Phi}_{23} \\ c \end{bmatrix} = \begin{bmatrix} \boldsymbol{f}_{23} \\ 0 \end{bmatrix}$$

where c is a dummy constant.

2.13 Terms Vanishing in the Solvability Condition.

The problem $\beta_1 \boldsymbol{L}(\beta_c)\boldsymbol{\Phi}_{21} = \boldsymbol{f}_{21}$ in Eq.(2.94) can be simplified by applying the solvability condition which also reveals that $R_1 = 0$ and can subsequently be neglected in any further analyses.

If $\boldsymbol{\Phi}^*$ is the adjoint eigenvector of $\boldsymbol{L}(\beta_c)$ then the solvability condition states that $< \boldsymbol{\Phi}^*, \boldsymbol{f}_{21} >= 0$ must be satisfied for the existence of a solution to the stated problem. The vector $\boldsymbol{f}_{21}$ can be divided into two components as follows.

$$\boldsymbol{f}_{21} = R_1 \boldsymbol{f}_{211} + \beta_1 \boldsymbol{f}_{212} \tag{2.104}$$

$$\text{with} \quad \boldsymbol{f}_{211} = -\frac{1}{R_c^2} \begin{bmatrix} \dot{\Delta}_c \hat{u}_1 \\ \dot{\Delta}_c \hat{v}_1 \\ \dot{\Delta}_c \hat{w}_1 \\ 0 \end{bmatrix} \quad \text{and} \quad \boldsymbol{f}_{212} = -\frac{2\beta_c}{R_c} \begin{bmatrix} \hat{u}_1 \\ \hat{v}_1 \\ \hat{w}_1 \\ 0 \end{bmatrix} - \begin{bmatrix} 0 \\ 0 \\ \hat{p}_1 \\ \hat{w}_1 \end{bmatrix}$$

and where $\dot{\Delta}_c = \frac{d^2}{dy^2} - \beta_c^2$.

It will be shown that at this order β_1 is arbitrary and $R_1 = 0$, i.e. $< \boldsymbol{\Phi}^*, \boldsymbol{f}_{212} >= 0$.

Consider the operator

$$\boldsymbol{K}(\beta, R) = \begin{bmatrix} -\frac{1}{R}\Delta_c & U_y - 2\Omega & 0 & 0 \\ 2\Omega & -\frac{1}{R}\Delta_c & 0 & \frac{d}{dy} \\ 0 & 0 & -\frac{1}{R}\Delta_c & \beta \\ 0 & -\frac{d}{dy} & \beta & 0 \end{bmatrix}.$$

Differentiating $\boldsymbol{K}(\beta, R)\boldsymbol{\Phi}$ with respect to β gives

$$\frac{\partial \boldsymbol{K}}{\partial \beta}\boldsymbol{\Phi} + \frac{\partial R}{\partial \beta}\frac{\partial \boldsymbol{K}}{\partial R}\boldsymbol{\Phi} + \boldsymbol{K}\frac{\partial \boldsymbol{\Phi}}{\partial \beta} = 0. \tag{2.105}$$

Evaluation at the critical point (β_c, R_c), and noting that $\boldsymbol{K}(\beta_c, R_c) = -\boldsymbol{L}(\beta_c)$ when discretised, gives the following expression.

$$\boldsymbol{L}(\beta_c)\frac{\partial \boldsymbol{\Phi}}{\partial \beta} = \left(\frac{\partial \boldsymbol{K}}{\partial \beta}\boldsymbol{\Phi} + \frac{\partial R}{\partial \beta}\frac{\partial \boldsymbol{K}}{\partial R}\boldsymbol{\Phi}\right) \tag{2.106}$$

but

$$\frac{\partial \boldsymbol{K}}{\partial \beta}\boldsymbol{\Phi} = -\boldsymbol{f}_{212} \quad \text{and} \quad \frac{\partial \boldsymbol{K}}{\partial R}\boldsymbol{\Phi} = -\boldsymbol{f}_{211}$$

$$\Rightarrow \quad \boldsymbol{L}(\beta_c)\frac{\partial \boldsymbol{\Phi}}{\partial \beta} = -\boldsymbol{f}_{212} - \frac{\partial R}{\partial \beta}\boldsymbol{f}_{211}. \tag{2.107}$$

Taking the inner product of Eq.(2.107) with $\boldsymbol{\Phi}^*$ and using the solvability condition again gives

$$< \boldsymbol{\Phi}^*, \boldsymbol{f}_{212} > + \frac{\partial R}{\partial \beta} < \boldsymbol{\Phi}^*, \boldsymbol{f}_{211} >= 0. \tag{2.108}$$

At the critical point

$$\frac{\partial R}{\partial \beta} = 0 \quad \Rightarrow \quad < \boldsymbol{\Phi}^*, \boldsymbol{f}_{212} >= 0.$$

This indicates that terms involving β_1 vanish exactly in the solvability condition. With this result the existence of a solution to the original problem is conditional on the following.

$$R_1 < \boldsymbol{\Phi}^*, \boldsymbol{f}_{211} > + \beta_1 < \boldsymbol{\Phi}^*, \boldsymbol{f}_{212} >= 0 \quad \Rightarrow \quad R_1 = 0 \text{ if } < \boldsymbol{\Phi}^*, \boldsymbol{f}_{211} > \neq 0$$

It can be established that $< \boldsymbol{\Phi}^*, \boldsymbol{f}_{211} > \neq 0$ and therefore R_1 must be exactly zero.
Thus

$$\beta_1 \boldsymbol{L}(\beta_c)\boldsymbol{\Phi}_{21} = \boldsymbol{f}_{21} \quad \text{is equivalent to} \quad \boldsymbol{L}(\beta_c)\boldsymbol{\Phi}_{21} = \boldsymbol{f}_{212}.$$

2.14 Summary.

Linear stability analysis for rotating channel flow reveals the critical Reynolds number for the onset of roll cell instability ($R_c = 66.5$) almost two orders of magnitude lower than that for the onset of unstable Tollmien-Schlichting (T-S) waves ($R_c = 5772$) in the absence of rotation for plane Poiseuille flow. This would imply that even for very small system rotations the appearance of this form of instability and the subsequent breakdown of the flow to a turbulent state would occur well before the appearance of any T-S waves.

Changing the mean flow field through the use of an interpolation parameter generates a family of shear flows moving from plane Poiseuille flow to Couette flow. In making this change the critical Reynolds number is found to systematically decrease with that for Couette flow being $R_c = 20.66$. This is thought to arise as a result of the alteration in the distribution of Coriolis force within the channel.

The effect of rotation on neutral curves for plane Poiseuille flow indicates the existence of a critical rotation number where rotations both above and below this value increase the value of R_c. A Newton algorithm is thus applied in order to determine the critical parameter values in the full three-dimensional parameter space. The results obtained are consistent with the existence of a neutral paraboloid surface for all members of the family of mean flow profiles.

A Ginzburg-Landau equation for the streamwise rolls is derived through a weakly nonlinear analysis and the coefficients in the equation reveal that supercritical instability to rolls occurs for all the flows investigated. However, significantly larger roll cell amplitudes are predicted for Couette flow in comparison with plane Poiseuille flow suggesting Couette flow in a rotating channel to be only just in the region of supercritical instability. This may have consequences if the fully nonlinear problem were considered.

CHAPTER 3

THE EFFECT OF WALL COMPLIANCE ON THE RAYLEIGH INSTABILITY.

Part 1 : Inviscid Analysis.

3.1 Introduction.

This chapter begins with a brief description of the classification schemes for instabilities in the coupled compliant wall/fluid boundary layer problem which are often used as a means of identifying modes of instability. Also presented are basic definitions of flow-based (or hydroelastic) instabilities which can arise as a direct result of the presence of a compliant boundary.

The main body of the chapter then considers the stability of a two-dimensional boundary layer which develops in the presence of an adverse pressure gradient and gives rise to the powerful inviscid instability mechanism described in the introductory chapter. It has yet to be established whether wall compliance has any beneficial effect on this so-called Rayleigh instability and initial investigations consider a polynomial approximation to the boundary layer profile and introduce wall compliance through a plate-spring model. Emphasis in this section of work is placed on bringing about significant reductions in growth rates of this instability without inducing any hydroelastic instabilities. The plate-spring model allows optimal wall properties, which give marginal stability with respect to these wall-based instabilities, to be determined and is thus useful in gauging what potential exists for the use of wall compliance as a means of controlling this type of instability.

Although the use of optimal parameters is the main focus of attention the occurrence of hydroelastic instability for this flow configuration is also demonstrated within the analysis through the use of a global eigenvalue search procedure.

Following the account of the instability classification schemes there is a description of the boundary layer representation used for the inviscid analysis and the derivation of the relevant governing stability equations. A global Chebyshev-tau eigenvalue search scheme is then outlined which permits the inclusion of a compliant boundary for the plate-spring theoretical model. Results are obtained using the optimal wall parameters and compared to the corresponding rigid wall values. The final sections consider hydroelastic instability and

the effect of wall damping on instabilities in the system.

3.2 Classification of Instabilities.

The presence of a compliant wall in fluid boundary layer problems generates the possibility of numerous modes of instability and with this comes a need for a clear classification scheme for instabilities. The features of instability associated with each classification category often provide a means of identification of unstable modes in this type of flow system and there are essentially three main ways of categorising instabilities which arise in the coupled fluid boundary layer/compliant wall flow problem.

3.2.1 Convective and Absolute Instability.

Perhaps the simplest form of classification is the idea of convective and absolute instability which is applicable to any flow problem since the definitions are exclusive of any reference to wall compliance.

An instability is defined as being *convective* if amplification of a disturbance occurs as it moves downstream from its point of initiation so that the growth of an unstable mode arises with propagation distance as opposed to growth in time at a fixed spatial location which is the classic temporal view of unstable disturbances.

Absolute instabilities, however, are more akin to this temporal description and are usually associated with disturbances which have zero group velocity which results in disturbance kinetic energy not being convected away from its point of origin and disturbances of this type grow indefinitely at a given location. Absolute instabilities therefore tend to dominate other modes of instability and significantly affect the process of transition.

3.2.2 Wall-based and Flow-based Instability.

Compliant wall are themselves wave-bearing media and above some threshold level of wall compliance become susceptible to so-called wall-based instabilities. This type of instability occurs in the wall itself as a result of the action of the surrounding fluid on the flexible boundary and has no rigid wall counterpart. This is in contrast to flow-based instabilities which are essentially modified flow instabilities which would also arise in the presence of a rigid boundary. The characteristics of the rigid wall instability are largely unaffected by wall compliance. Examples of flow-based modes are the Tollmien-Schlichting instability, the Rayleigh instability in two-dimensional boundary layers and the crossflow instability common to three-dimensional boundary layers.

There are two main types of wall-based (or hydroelastic) instability, namely travelling wave flutter (TWF) and divergence.

Divergence is basically induced by an imbalance between the wall's structural forces and the conservative hydrodynamic pressure forces generated by fluid disturbances on the surface. It has also been identified as an absolute instability and as such its presence is particularly damaging to the prospects of using wall compliance as an effective means of transition delay.

TWF is a convective instability brought about by an essentially inviscid mechanism. It is characterised by high phase speeds close to the freestream value and grows by the irreversible transfer of energy from the flow to the wall as a result of work done by the fluctuating pressure.

Both divergence and TWF have their origins in the free wave modes of the compliant wall and the presence of wall-based instabilities introduces the possibility of coalescence with other modes to generate powerful new modes of instability.

3.2.3 Energy Classification.

The classification of Benjamin (1960, 1963) and Landahl (1962) is based on the effect of energy exchange between the wall and fluid and the response to damping in the wall. There are three types of instability within this classification scheme.

Class A : Irreversible energy transfer to/from the compliant wall has a stabilising/destabilising effect on the instability and damping tends to destabilise this mode of instability.

Class B : Stabilised by wall damping and the effect of irreversible energy transfer in the wall/flow system is opposite to that of the Class A instability.

Class C : This category is associated with instabilities which are unaffected both by energy exchanges and wall damping.

The T-S instability is an example of a Class A instability and TWF belongs to Class B. Divergence has been shown to belong to Class C.

The terms *negative energy* and *positive energy waves* are now commonly used for Class A and Class B instabilities in other applications.

3.3 Boundary Layer in an Adverse Pressure Gradient.

Consider a two-dimensional boundary layer which develops in the presence of an adverse pressure gradient. Exact solutions to the boundary layer equations do not exist for flow configurations of this kind and it is necessary to use some alternative method of obtaining the velocity profile. The governing equations can be solved numerically but for the preliminary investigations the approximate method of von Kármán and Pohlhausen (1921) is used. This provides a solution where the boundary layer equations are satisfied on average and is in a convenient form for use in many numerical calculations.

The velocity along the boundary of the potential flow for this problem is assumed to be of the form

$$U_e(x) = Ax^m \tag{3.1}$$

where x is the streamwise distance, A is some arbitrary constant and in the presence of an adverse/favourable pressure gradient m is a negative/positive constant.

In order to obtain the associated velocity profile the approximate method assumes a fourth order polynomial description for the velocity across the boundary layer.

$$\frac{u}{U_e} = a\bar{y} + b\bar{y}^2 + c\bar{y}^3 + d\bar{y}^4 \qquad \text{where} \qquad \bar{y} = \frac{y}{\delta(x)} \tag{3.2}$$

The local boundary layer thickness $\delta(x)$ is used to non-dimensionalise lengths with y the dimensional distance from the wall in the direction normal to the flow and a - d are constant coefficients.

This approximation to the boundary layer profile must conform to a number of physical conditions. The requirement of zero velocity at the wall is automatically satisfied from the form given in Eq.(3.2). The other necessary conditions are that the solution be continuous and join the potential flow smoothly at the edge of the boundary layer. In the presence of a pressure gradient the solution must also be able to distinguish between regions of adverse and favourable pressure gradients and generate a point of inflexion in the former case. These conditions can be expressed as follows.

$$y = 0 \quad : \quad u = 0, \quad \nu\frac{\partial^2 u}{\partial y^2} = \frac{1}{\rho}\frac{dp}{dx} = -U_e\frac{dU_e}{dx} \tag{3.3}$$

$$y = \delta \quad : \quad u = U_e, \quad \frac{\partial u}{\partial y} = 0, \quad \frac{\partial^2 u}{\partial y^2} = 0 \tag{3.4}$$

where ν is the kinematic viscosity.

The second condition in Eq.(3.3) relates the curvature of the profile to the presence of a pressure gradient and is responsible for generating points of inflexion in regions of increasing pressure.

If a dimensionless quantity or shape factor, Γ, related to the pressure gradient is introduced such that

$$\Gamma = \frac{\delta^2}{\nu}\frac{dU_e}{dx} = -\frac{\delta^2}{\nu}\frac{1}{\rho U_e}\frac{dp}{dx}, \tag{3.5}$$

then four simultaneous equations in terms of a - d are obtained.

$$a + 2b + 3c + 4d = 0 \tag{3.6}$$

$$b + 3c + 6d = 0 \tag{3.7}$$

$$a + b + c + d = 1 \tag{3.8}$$

$$2b = -\Gamma. \tag{3.9}$$

Solving these equations in terms of Γ gives the following expression for the non-dimensional velocity profile.

$$\bar{U}(\bar{y}) = (2\bar{y} - 2\bar{y}^3 + \bar{y}^4) + \frac{\Gamma}{6}(\bar{y} - 3\bar{y}^2 + 3\bar{y}^3 - \bar{y}^4) \tag{3.10}$$

For $\bar{y} \geq 1$ it is assumed that $\bar{U}(\bar{y}) \equiv 1$ and that the boundary layer joins the potential flow at the finite distance $y = \delta(x)$ from the wall.

Physically Γ represents a measure of the ratio of pressure forces to viscous forces and it also provides a relationship between the boundary layer thickness, δ, and the displacement thickness, δ^*.

$$\frac{\delta^*}{\delta} = \frac{3}{10} - \frac{\Gamma}{120} \tag{3.11}$$

Separation occurs when $\frac{\partial u}{\partial y}(0) = 0$ which corresponds to $a = 0$ and in turn implies that $\Gamma = -12$. For $\Gamma > 12$, $\bar{U}(\bar{y}) > 1$ for some $\bar{y} < 1$. Therefore, for steady flow the value of Γ is restricted to the range $-12 \leq \Gamma \leq 12$. In the present calculations a value of $\Gamma = -7$ is chosen to represent a moderately adverse pressure gradient so that the boundary layer profile can be expressed as

$$\bar{U}(\bar{y}) = \frac{13}{6}\bar{y}^4 - \frac{11}{2}\bar{y}^3 + \frac{7}{2}\bar{y}^2 + \frac{5}{6}\bar{y} \qquad \text{for} \qquad 0 \leq \bar{y} \leq 1. \tag{3.12}$$

This exhibits a point of inflexion, where $\bar{U}''(\bar{y}_s) = 0$, at $\bar{y}_s = \frac{7}{26} = 0.2692$.

3.4 Instability of Two-dimensional Parallel Flows at Infinite Reynolds Number.

The Rayleigh equation is a linearised disturbance equation governing the stability of parallel flows at infinite Reynolds number where the parallel flow approximation assumes boundary layer growth in the streamwise direction to be negligible. In the derivation of

the Rayleigh equation disturbance velocities $u'(x,y,t), v'(x,y,t)$ and pressure $p'(x,y,t)$ are superimposed on the mean flow field and are taken to be of the following travelling wave form.

$$[\boldsymbol{u}', p']^T = [u', v', p']^T = [U_e\,\bar{u}(\bar{y}), U_e\,\bar{v}(\bar{y}), \rho U_e^2\,\bar{p}(\bar{y})]^T e^{i\alpha(x-ct)} + \text{c.c.} \tag{3.13}$$

where α is the streamwise wavenumber and c the corresponding phase speed. The disturbances are assumed to be infinitesimal and the fluid incompressible. The perturbed flow field is then

$$[\boldsymbol{u}, p]^T = [\boldsymbol{U}, P]^T + \varepsilon[\boldsymbol{u}', p']^T \tag{3.14}$$

where $\boldsymbol{U}$ and P denote the mean velocity and pressure and ε is an arbitrarily small parameter. Viscous effects are necessarily included for the formation of the mean flow field. This form is substituted into the following governing momentum and continuity equations where the effects of viscosity have been neglected.

$$\frac{\partial \boldsymbol{u}}{\partial t} + (\boldsymbol{u}\cdot\nabla\boldsymbol{u}) + \frac{1}{\rho}\nabla p = 0 \tag{3.15}$$

$$\nabla\cdot\boldsymbol{u} = 0 \tag{3.16}$$

Subsequent linearisation with respect to the disturbance quantities, where terms of $O(\varepsilon^2)$ and higher are neglected, and elimination of the pressure term, $\bar{p}$, yields the Rayleigh equation, a second order ordinary differential equation in terms of the normal perturbation velocity.

$$(\bar{U}-\bar{c})(\bar{v}''-\bar{\alpha}^2\bar{v}) - \bar{U}''\bar{v} = 0 \tag{3.17}$$

Overbars are used throughout to denote non-dimensionalised quantities. Velocities are made dimensionless using the local free stream velocity, U_e, and lengths are scaled by the local boundary layer thickness, δ.

With the effects of viscosity being neglected the two boundary conditions for this second order problem are simply

$$\bar{v}(0) = 0 \tag{3.18}$$

$$\bar{v} \to 0 \quad \text{as} \quad \bar{y} \to \infty. \tag{3.19}$$

This enforces the no penetration condition at the wall and the requirement that disturbances should decay exponentially beyond the edge of the boundary layer.

The physical situation being considered is the onset of an adverse pressure gradient at some streamwise location, L, before which the freestream velocity takes a constant value U_∞. The local dimensional freestream velocity can therefore be expressed as

$$U_e = U_\infty, \quad x < L \qquad \text{and} \qquad U_e = U_\infty\left(\frac{x}{L}\right)^m, \quad x \geq L. \tag{3.20}$$

The coordinate system used throughout this chapter and the variation of freestream velocity with distance along the boundary is shown in Figure 3.1.

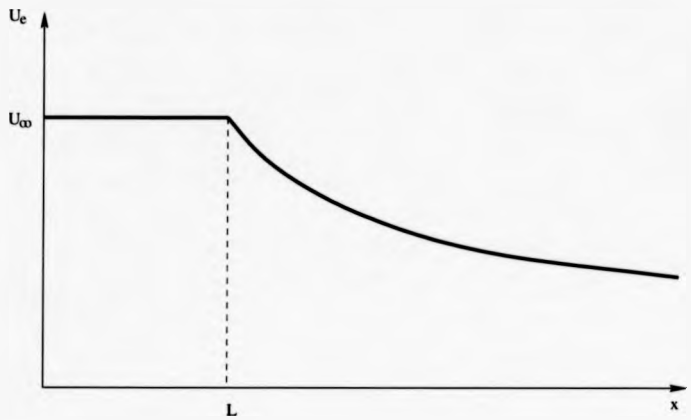

Figure 3.1: Coordinate system and flow configuration.

If the disturbances are taken to be temporally growing then $\bar{\alpha}$ is a real quantity and the phase velocity is complex such that $\bar{c} = \bar{c}_r + i\bar{c}_i$. The temporal growth rate is then $\bar{\alpha}\bar{c}_i$ where positive values of this quantity will indicate the growth of disturbances in time. For spatially developing disturbances $\bar{\alpha} = \bar{\alpha}_r + i\bar{\alpha}_i$ is complex with $\bar{\alpha}_r$ denoting the wavenumber and $-\bar{\alpha}_i$ the spatial growth rate and $\bar{c}$ can be replaced by $\bar{\omega}/\bar{\alpha}$ where $\bar{\omega}$ is the non-dimensional real disturbance frequency. For neutral disturbances, when the growth rate is zero, the two cases are equivalent.

Assuming the polynomial approximation for $\bar{U}(\bar{y})$ in Eq.(3.12) then $\bar{U}''(\bar{y}) = 0$ for $\bar{y} \geq 1$ in which case the Rayleigh equation becomes

$$(\bar{U} - \bar{c})(\hat{v}'' - \bar{\alpha}^2\hat{v}) = 0 \quad \text{for} \quad \bar{y} \geq 1. \tag{3.21}$$

This can be solved to give a solution of the form

$$\hat{v}(\bar{y}) = De^{-\bar{\alpha}\bar{y}} \quad \text{for} \quad \bar{y} \geq 1, \tag{3.22}$$

where D is some arbitrary complex constant chosen depending on any normalisation condition imposed.

The outer boundary condition for this problem given in Eq.(3.19) can then be replaced by

$$\hat{v}'(1) + \bar{\alpha}\hat{v}(1) = 0. \tag{3.23}$$

The Rayleigh equation together with the boundary conditions in Eqs.(3.18) and (3.23) constitute an eigenvalue problem of the form

$$\mathcal{F}(\bar{\alpha}, \bar{c})\hat{v} = 0 \tag{3.24}$$

from which stability features of the flow can be determined.

In order to study the stability characteristics of the inflexional velocity profile the above eigenvalue problem must be solved numerically. There are number of methods available for the numerical integration of differential equations including spectral, finite-difference and shooting methods. The latter tends to be more efficient and easier to implement but with the means of constructing a global search scheme the Chebyshev-tau spectral method was employed. The following section outlines the techniques behind this particular technique and describes the formulation of the global search procedure.

3.5 Formulation of Global Eigenvalue Scheme.

Chebyshev polynomials are defined on the interval [-1,1] by

$$T_n(x) = \cos n\theta \qquad \text{where} \qquad \theta = \cos^{-1}(x), \qquad n = 0, 1, 2, \ldots \tag{3.25}$$

With Chebyshev polynomials as the expansion or basis functions the problem is transformed from $0 \leq \bar{y} \leq 1$ to $-1 \leq z \leq 1$ using the transformation

$$z = 2\bar{y} - 1 \tag{3.26}$$

The Rayleigh equation in terms of the new variable, z, then becomes

$$(\bar{U} - \bar{c})(4\hat{v}'' - \bar{\alpha}^2) - 4\bar{U}''\hat{v} = 0 \tag{3.27}$$

with boundary conditions

$$2\hat{v}'(1) + \bar{\alpha}\hat{v}(1) = 0 \tag{3.28}$$

$$\hat{v}(-1) = 0. \tag{3.29}$$

where primes now indicate differentiation with respect to z.
The solution is written as a finite Chebyshev series of polynomials up to order N.

$$\hat{v}(z) = \sum_{n=0}^{N} a_n T_n(z) \tag{3.30}$$

It is generally easier to work with integrals of Chebyshev polynomials than derivatives and so the Rayleigh equation is integrated indefinitely twice with respect to z.

$$4\bar{U}\hat{v} - 8\int \bar{U}'\hat{v}dz - \bar{\alpha}^2 \iint \bar{U}\hat{v}dz + \bar{c}\left\{\bar{\alpha}^2 \iint \hat{v}dz - 4\hat{v}\right\} - b_0 z - b_1 = 0 \qquad (3.31)$$

with b_0 and b_1 constants of integration. Eq.(3.31) is then discretised through substitution of the series expansion in Eq.(3.30). A set of discretised equations is thus obtained by equating the coefficients of T_n using the following relations.

$$\int T_n(z)dz = \begin{cases} \frac{T_{n+1}(z)}{2(n+1)} - \frac{T_{n-1}(z)}{2(n-1)} & n \geq 2 \\ \frac{1}{4}\{T_o(z) + T_2(z)\} & n = 1 \\ T_1(z) & n = 0 \end{cases} \qquad (3.32)$$

Implementation of the tau method requires a term of the form

$$\tau_1 T_{N+1}(z) + \tau_2 T_{N+2}(z) \qquad (3.33)$$

to be placed on the right hand side of Eq(3.31). The tau terms can be determined by equating coefficients of $T_{N+1}(z)$ and $T_{N+2}(z)$ and give an indication of the error in the solution but are not specifically required in order to solve the eigenvalue problem whilst the two equations obtained for $n = 0, 1$ only serve to determine the constants of integration, b_0 and b_1, and are not directly related to the eigenvalue problem. The discretised form of Eq.(3.31) for $n = 2, \ldots, N$ is

$$4d_n + \frac{4}{n}\{e_{n+1} - e_{n+1}\} - \bar{\alpha}^2\left\{\frac{d_{n-2}}{4n(n-1)} - \frac{d_n}{2(n+1)(n-1)} + \frac{d_{n+2}}{4n(n+1)}\right\} +$$

$$\bar{c}\left\{\bar{\alpha}^2\left[\frac{a_{n-2}}{4n(n-1)} - \frac{a_n}{2(n+1)(n-1)} + \frac{a_{n+2}}{4n(n+1)}\right] - 4a_n\right\} = 0 \qquad (3.34)$$

where

$$\bar{U}(z)\hat{v}(z) = \sum_{n=0}^{N} d_n T_n(z) \quad \text{and} \quad \bar{U}'(z)\hat{v}(z) = \sum_{n=0}^{N} e_n T_n(z).$$

The problem is then fully specified by the inclusion of the two boundary conditions which replace the equations for $n = 0, 1$.

$$2\sum_{n=0}^{N} a_n n^2 + \bar{\alpha}\sum_{n=1}^{N} a_n = 0 \qquad (3.35)$$

$$\sum_{n=1}^{N} (-1)^n a_n = 0 \qquad (3.36)$$

This then leaves a system of $N + 1$ simultaneous equations in terms of the $N + 1$ unknowns $a_o, \ldots, a_N$ which can be written in matrix form.

$$\boldsymbol{S}(\bar{\alpha}, \bar{c})\boldsymbol{a} = 0 \qquad (3.37)$$

where $\boldsymbol{a} = [a_o, \ldots, a_N]^T$ and $\boldsymbol{S}$ is a complex square matrix of order $N+1$.

If the temporal formulation is used then the eigenvalue $\bar{c}$ appears linearly

$$\boldsymbol{S}(\bar{\alpha}, \bar{c}) = \bar{c}\boldsymbol{C}_1(\bar{\alpha}) + \boldsymbol{C}_o(\bar{\alpha}) \tag{3.38}$$

and Eq.(3.37) is already in the form of a generalised eigenvalue problem.

$$-\boldsymbol{C}_o\boldsymbol{a} = \bar{c}\boldsymbol{C}_1\boldsymbol{a} \tag{3.39}$$

The QZ algorithm available in a number of numerical schemes can be applied to problems of this form and the NAG library routine F02GJF was used to determine the eigenvalue spectrum in this case.

For the spatial formulation the eigenvalue $\bar{\alpha}$ appears nonlinearly and a corresponding generalised eigenvalue problem is generated by forming a linear companion matrix using the method of Bridges and Morris (1984). The relation

$$\boldsymbol{S}(\bar{\alpha}, \bar{c})\boldsymbol{a} = \{\bar{\alpha}^2\boldsymbol{C}_2(\bar{c}) + \boldsymbol{C}_0(\bar{c})\}\boldsymbol{a} \tag{3.40}$$

can be augmented to give

$$\begin{bmatrix} 0 & -\boldsymbol{C}_0 \\ \boldsymbol{I} & 0 \end{bmatrix} \begin{bmatrix} \bar{\alpha}\boldsymbol{a} \\ \boldsymbol{a} \end{bmatrix} = \bar{\alpha} \begin{bmatrix} \boldsymbol{C}_2 & 0 \\ 0 & \boldsymbol{I} \end{bmatrix} \begin{bmatrix} \bar{\alpha}\boldsymbol{a} \\ \boldsymbol{a} \end{bmatrix} \tag{3.41}$$

where $\boldsymbol{I}$ is the identity matrix of order $N+1$ and the problem can then be solved in the same way as that of Eq.(3.39).

The corresponding eigenfunctions can be obtained from the eigenvector of expansion coefficients, $a_o, \ldots, a_N$, which are returned automatically through the use of the numerical routine. The solution $\hat{v}$ can then be evaluated at the points

$$z_j = \cos\frac{\pi j}{N} \qquad j = 0, \ldots, N$$

such that

$$\hat{v}(z_j) = \sum_{n=1}^{N} a_n T_n(z_j) = \sum_{n=1}^{N} a_n \cos\frac{n\pi j}{N}. \tag{3.42}$$

This is then transformed back to the original variable, y, using the relation in Eq.(3.26) and the eigenfunctions are normalised to unity at the edge of the boundary layer. This normalisation condition was implemented to enable correspondence with the forthcoming compliant wall case. Any normalisation conditions imposed at the boundary of the compliant wall are not as appropriate for direct comparison with the rigid wall case because of the zero velocity constraint imposed there.

3.6 Results for Rigid Wall.

Calculations were performed using a value of $N = 40$ in the spectral scheme throughout for the rigid wall problem which was sufficient to give well converged solutions.

Figure 3.2 shows the temporal and spatial growth rates for the polynomial form of the inflexional boundary layer profile obtained using this method. It is shown that the temporal approach produces lower growth rates than the spatial theory with the maximum value being 0.047286 in the former case compared to 0.11045 assuming spatially growing disturbances but in order for the temporal theory to correspond to the physical case a group velocity transformation must be imposed. The frequency ranges do, however, compare directly with the unstable range extending to a frequency of 0.556.

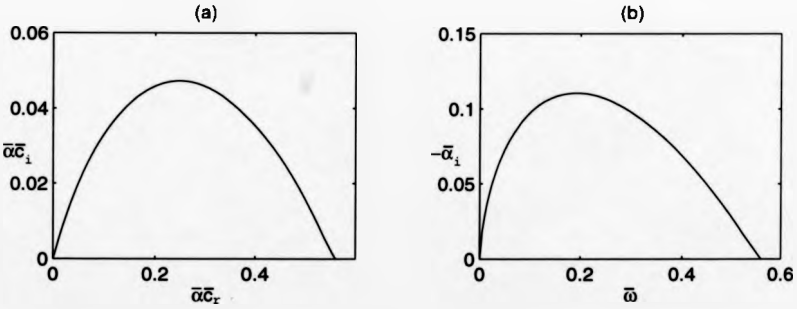

Figure 3.2: Growth rates for rigid wall boundary. (a) : Temporal growth rate against $\bar{\alpha}\bar{c}_r$, (b) : Spatial growth rate against frequency.

From the theory of Tollmien (1935) a neutrally stable solution exists which must satisfy the following criterion.

$$\bar{c}_r = \bar{U}(\bar{y}_s)$$

where $\bar{y}_s$ denotes the point of inflexion and c_r is the phase speed of the neutral disturbance. This implies that the critical layer, defined as the region where $\bar{U} = \bar{c}$, coincides with the point of inflexion of the velocity profile. In both the temporal and spatial analyses this is verified with the following numerical results where $\bar{U}(\bar{y}_s) = 0.3821$.

Temporal : $\bar{c}_i = 0, \quad \bar{c}_r = 0.3821 \quad \text{at} \quad \bar{\alpha} = 1.457.$

Spatial : $\bar{\alpha}_i = 0 \quad \text{at} \quad \bar{\omega} = 0.5556, \quad \bar{\alpha}_r = 1.454 \quad \Rightarrow \quad \bar{c}_r = 0.3821.$

Figure 3.3 shows wavenumber, $\bar{\alpha}_r$, plotted against frequency, $\bar{\omega}$ and from inspection there are no obvious maxima or minima in evidence which would suggest that the group velocity, $\bar{c}_g = \frac{d\bar{\omega}}{d\bar{\alpha}}$, is everywhere non-zero and consequently the Rayleigh instability could be interpreted as being a convective instability. The spatial formulation of the problem would therefore be the most appropriate.

Eigenfunctions for a number of frequencies are shown in Figure 3.4 and indicate that the maximum amplitude occurs some way into the boundary layer and identifies the flow-based nature of the instability.

Having established the inviscid instability characteristics of this flow the effect of wall compliance on the growth rates of the Rayleigh instability are now investigated.

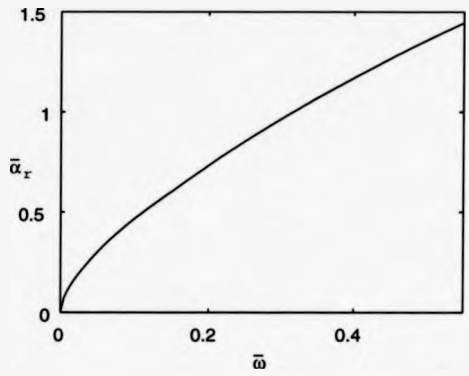

Figure 3.3: Variation of wavenumber, $\bar{\alpha}_r$, with frequency, $\bar{\omega}$, for the rigid wall.

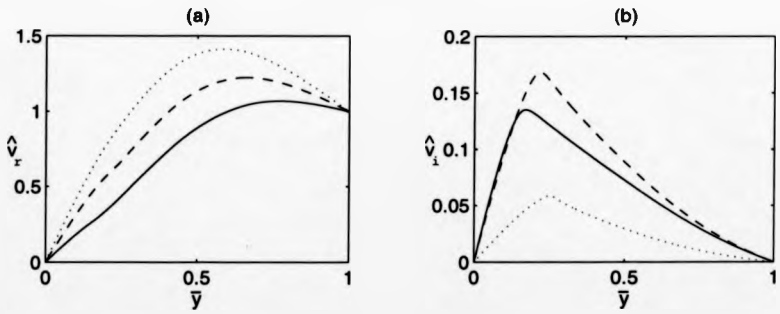

Figure 3.4: Rigid wall eigenfunctions corresponding to positions of maximum growth rate at a number of frequencies. (a) $\hat{v}_r$, (b) $\hat{v}_i$. $\bar{\omega} = 0.1$: —, $\bar{\omega} = 0.3$: - -, $\bar{\omega} = 0.5$: $\cdots$.

3.7 Theoretical Model for Compliant Wall.

Two types of compliant wall model have generally been used in previous theoretical work and can be described as either surface-based or volume-based depending on the basic construction.

Surface-based models are simpler to implement with equations for the wall motion used directly as replacements for the rigid wall boundary conditions. This ensures that the physical requirements of continuity of velocity and stress across the wall/flow interface are automatically satisfied. In the volume-based model framework these continuity conditions have to be imposed explicitly.

For preliminary investigations a simple plate-spring surface-based model of the type shown in Figure 3.5 and described in Carpenter and Gajjar (1990) was used. This is a somewhat idealistic model and does not accurately represent the type of wall used in experimental studies. It is, however, sufficient to gauge what effect wall compliance might have on the inviscid Rayleigh instability and has the advantage of presenting a problem which is computationally efficient to solve.

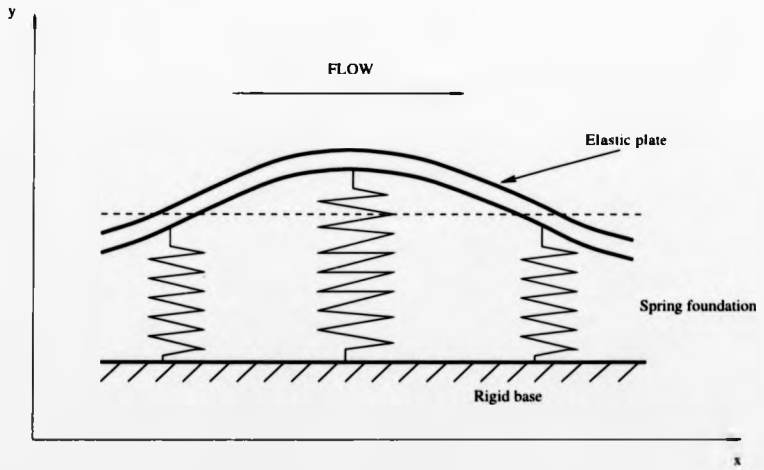

Figure 3.5: Plate-spring model for compliant wall.

The plate-spring compliant wall model is formulated assuming the wall to be constructed with a series of vertically aligned springs attached to a rigid base and supporting above a

thin elastic plate. The presence of a viscous fluid substrate beneath the upper plate can also be incorporated. This isotropic wall is free to move under the influence of the fluid flow and becomes displaced by the fluid motion. For a travelling-wave disturbance the wall displacement vector, $\boldsymbol{\eta}$, takes the form

$$\boldsymbol{\eta}(x,y,t) = [\xi(x,y,t), \eta(x,y,t)]^T = \delta[\hat{\xi}(y), \hat{\eta}(y)]^T e^{i(\alpha x - \omega t)} + \text{c.c.} \tag{3.43}$$

For an isotropic wall of this type the displacement is restricted to motion in the normal direction only such that $\hat{\xi}(y) = 0$.

Boundary conditions for any flow problem involving a compliant boundary require continuity of normal velocity across the wall/flow interface. If ε is taken to be a small quantity then this can be expressed as

$$\varepsilon\dot{\boldsymbol{\eta}}(x,0) = \{\boldsymbol{U} + \varepsilon\boldsymbol{u}'\}(x, \varepsilon\eta) \tag{3.44}$$

for any time t. The above expression is expanded in a Taylor series about the mean undisturbed wall position $(x, 0)$ to yield

$$\varepsilon\dot{\boldsymbol{\eta}}(x,0) = \boldsymbol{U}(x,0) + \varepsilon\boldsymbol{u}'(x,0) + \varepsilon\eta\frac{\partial \boldsymbol{U}}{\partial y}(x,0) + O(\varepsilon^2). \tag{3.45}$$

Substituting in the assumed travelling wave forms the two components of this Taylor expansion give linearised conditions for the continuity of velocity across the wall/flow interface.

$$-i\bar{\omega}\hat{\xi}(0) = \hat{u}(0) + \hat{\eta}(0)\bar{U}'_w \tag{3.46}$$

$$-i\bar{\omega}\hat{\eta}(0) = \hat{v}(0) \tag{3.47}$$

where $\bar{U}'_w$ is the non-dimensional undisturbed velocity gradient at the wall. Suffix w on all subsequent terms will indicate evaluation at the mean undisturbed wall position, $y = 0$. In the inviscid case only the second velocity condition is required.

An equation of motion for the wall can be derived in terms of the normal wall displacement by considering the different forces per unit plate area acting on the wall.

$$b\rho_m\frac{\partial^2\eta}{\partial t^2} + B\frac{\partial^4\eta}{\partial x^4} + K_E\eta = -p'_w \tag{3.48}$$

b and ρ_m are plate thickness and density respectively. K_E denotes the equivalent spring stiffness, B the flexural rigidity of the plate and p'_w the fluctuating pressure acting on the plate.

The first term in the equation represents the plate mass per unit area multiplied by acceleration and represents the driving forces due to the boundary layer disturbances. The remaining terms represent the restorative structural forces due to the compliant wall.

The flexural rigidity of the plate is related to the elastic modulus, E, in the following way.

$$B = \frac{Eb^3}{12(1-\nu_p^2)} \tag{3.49}$$

where ν_p is the Poisson ratio.

Equivalent spring stiffness can be defined in terms of the actual spring stiffness K.

$$K_E = K - g(\rho_f - \rho_s) \tag{3.50}$$

where g is the acceleration due to gravity, ρ_s the substrate material density and ρ_f the density of the mainstream fluid.

Eq.(3.48) is derived using classical thin-plate theory so its validity assumes disturbance wavelengths are much greater than the plate thickness.

The equation of motion can be used as the lower boundary condition in the eigenvalue problem formed from the Rayleigh equation where fluid and wall motions are coupled by the substitution of the velocity condition in Eq.(3.47) into Eq.(3.48) to give

$$(-\omega^2 b\rho_m + B\alpha^4 + K_E)v_w\delta = i\bar{\omega}\hat{p}_w\rho U_e^2. \tag{3.51}$$

The fluid perturbation pressure at the wall, $\hat{p}_w$, can be obtained from the linearised x-momentum equation.

$$i\bar{\alpha}\hat{p}_w = (\bar{U}_w - \frac{\bar{\omega}}{\bar{\alpha}})\frac{d\hat{v}_w}{d\bar{y}} - \bar{U}'_w\hat{v}_w = -\frac{\bar{\omega}}{\bar{\alpha}}\frac{d\hat{v}_w}{d\bar{y}} - \bar{U}'_w\hat{v}_w \tag{3.52}$$

Hence the lower boundary condition becomes

$$(-\omega^2 b\rho_m + \alpha^4 B + K_E)\hat{v}_w\delta = -\frac{\bar{\omega}}{\bar{\alpha}}\rho_f U_e^2\left(\frac{\bar{\omega}}{\bar{\alpha}}\frac{d\hat{v}_w}{d\bar{y}} + \bar{U}'_w\hat{v}_w\right). \tag{3.53}$$

The equation can be written in totally non-dimensional form by introducing the following dimensionless wall parameters.

$$C_M = \frac{b\rho_m}{\rho_f\delta}, \qquad C_B = \frac{B}{\rho_f U_e^2\delta^3}, \qquad C_{KE} = \frac{K_E\delta}{\rho_f U_e^2} \tag{3.54}$$

Substitution of these wall parameters into Eq.(3.53) gives the governing equation for the compliant wall motion in terms of the normal perturbation velocity, $\hat{v}$.

$$(-\bar{\omega}^2 C_M + \bar{\alpha}^4 C_B + C_{KE} + \frac{\bar{\omega}}{\bar{\alpha}}\bar{U}'_w)\hat{v}_w + \left(\frac{\bar{\omega}}{\bar{\alpha}}\right)^2\frac{d\hat{v}_w}{d\bar{y}} = 0 \tag{3.55}$$

For implementation into the spectral code described in the preceding section the transformed boundary equation is

$$\left\{\bar{\alpha}^2\bar{c}^2 C_M + \bar{\alpha}^4 C_B + C_{KE} + 2\bar{c}\bar{U}'_w\right\}\hat{v}(-1) + 2\bar{c}^2\hat{v}'(-1) = 0. \tag{3.56}$$

This generates a quadratic polynomial for the temporal eigenvalue, $\bar{c}$.

$$\boldsymbol{S}(\bar{\alpha},\bar{c}) = \bar{c}^2\boldsymbol{C}_2(\bar{\alpha}) + \bar{c}\boldsymbol{C}_1(\bar{\alpha}) + \boldsymbol{C}_o(\bar{\alpha}) \tag{3.57}$$

and the corresponding linear companion matrix is

$$\begin{bmatrix} -\boldsymbol{C}_1 & -\boldsymbol{C}_o \\ \boldsymbol{I} & 0 \end{bmatrix} \begin{bmatrix} \bar{\alpha}\boldsymbol{a} \\ \boldsymbol{a} \end{bmatrix} = \bar{c} \begin{bmatrix} \boldsymbol{C}_2 & 0 \\ 0 & \boldsymbol{I} \end{bmatrix} \begin{bmatrix} \bar{\alpha}\boldsymbol{a} \\ \boldsymbol{a} \end{bmatrix}. \tag{3.58}$$

For the case of spatially growing disturbances the eigenvalue $\bar{\alpha}$ appears to the power of 5 which would increase the order of the linear companion matrix considerably. Since the calculating time for the QZ algorithm is of the order $4m^3$, where m is the order of the matrices involved, this global matrix method is less computationally efficient within the spatial formulation of the problem and therefore, for lengthy investigations a less costly local iterative method would perhaps be more appropriate.

The compliant wall in general supports free waves which are the origins of hydroelastic instabilities which may develop under certain conditions with the inclusion of the flow. Free wave solutions are determined by satisfying zero stress conditions at the wall interface. Thus returning to Eq.(3.53) and setting the right hand side to zero gives

$$-\omega^2 b\rho_m + \alpha^4 B + K_E = 0 \tag{3.59}$$

which when non-dimensionalised returns an expression for the dimensionless free wave speed, $\bar{c}_o$.

$$\bar{c}_o^2 = \frac{\bar{\alpha}^4 C_B + C_{KE}}{\bar{\alpha}^2 C_M} \tag{3.60}$$

Free waves are shown in Figure 3.6 for a given set of wall parameters and a clearly defined minimum free wave speed is indicated at $\bar{\alpha} \approx 0.75$. The occurrence of a minimum free wave speed is a characteristic of plate-spring constructions and any wall surmounted by a thin plate.

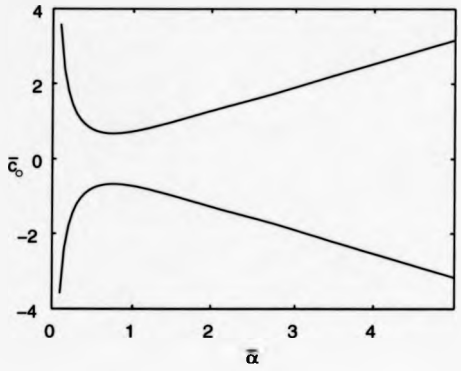

Figure 3.6: Free wave speeds as a function of wavenumber for a plate-spring compliant wall.

3.8 Optimal Wall Properties.

The main emphasis of this work is placed on determining whether a significant reduction in growth of the Rayleigh instability can be achieved through the use of wall compliance and to achieve the best possible results any hydroelastic or wall-based instabilities need to be avoided. Following Carpenter and Morris (1990) optimal wall properties can be determined which make the wall marginally stable with respect to both travelling-wave flutter and divergence at infinite Reynolds number and this is accomplished by matching the critical onset speeds for divergence and TWF with the freestream speed. This then determines the greatest effective degree of wall compliance but one which lies below the threshold of the hydroelastic instabilities.

From Carpenter and Morris (1990) the critical speeds and associated wavenumbers are

$$U_d = c_o \left(\frac{b\rho_m \alpha_d}{\rho_f} \right)^{\frac{1}{2}}, \qquad \alpha_d = \left(\frac{(12BK_E)^{\frac{1}{2}}}{6B} \right)^{\frac{1}{2}} \tag{3.61}$$

for divergence, where c_o is the dimensional free wave speed and for TWF the corresponding expressions are

$$U_c = \left(\frac{2(BK_E)^{\frac{1}{2}}}{b\rho_m} \right)^{\frac{1}{2}}, \qquad \alpha_c = \left(\frac{K_E}{B} \right)^{\frac{1}{4}}. \tag{3.62}$$

In this particular problem the presence of an adverse pressure gradient results in the external freestream speed decreasing with distance along the boundary. By requiring the freestream speed to equal the critical onset speeds for the hydroelastic instabilities at the start of the

pressure gradient it is ensured that these flow-induced surface instabilities will not arise at any subsequent point along the wall. The effective wall compliance will decrease with the reduction in velocity external to the boundary layer and the effect of the adverse pressure gradient will be to take the freestream speed below the critical values required for the onset of the hydroelastic instabilities. Matching of the velocities at the onset of the pressure gradient may therefore be over constrained and it is conceivably possible that the wall could be made more flexible as progression is made downstream from the initial point through systematic matching of the freestream and critical velocity values. It should therefore be stressed that the wall properties determined here are not optimal in the same sense as for zero pressure gradient flow and the results should be interpreted in accordance with this. The most effective results will coincide with the position at the onset of the adverse pressure gradient.

A condition for marginal stability requires $U_\infty = U_d$ from which the following expressions are obtained.

$$B = \frac{\rho_f U_\infty^2}{4\alpha_d^3}, \qquad K_E = \frac{3}{4}\rho_f U_\infty^2 \alpha_d \tag{3.63}$$

Requiring $U_\infty = U_c$ provides a restriction on the plate thickness, b such that

$$b = \frac{\sqrt{3}}{2\alpha_d} \tag{3.64}$$

The advantage of using this scheme lies in the fact that the three wall parameters C_M, C_B and C_{KE} can now be expressed in terms of a single parameter. The subsequent variation of this parameter generates a family of compliant walls each of which render the wall/flow system marginally stable to wall-based modes at the onset of the pressure gradient and the single parameter characterising this family of walls is the non-dimensional critical divergence wavenumber, $\bar{\alpha}_d$. Non-dimensionalisation of parameters in this case involves the length scale ν/U_∞ which is invariant with x and in turn gives non-dimensional wall parameters which remain fixed with streamwise distance. The non-dimensional wall parameters expressed in this way are then as follows.

$$\bar{\alpha}_d = \frac{\alpha_d \nu}{U_\infty}, \qquad C_M = \frac{\sqrt{3}}{2\bar{\alpha}_d}, \qquad C_B = \frac{1}{4\bar{\alpha}_d^3}, \qquad C_{KE} = \frac{3}{4}\bar{\alpha}_d \tag{3.65}$$

The use of the new reference length introduces an effective Reynolds number, $R = U_\infty \delta/\nu$, into the wall boundary equation.

The lower boundary condition for the Rayleigh problem written in terms of the optimisation parameter, $\bar{\alpha}_d$, becomes

$$\left(-\frac{\bar{\omega}^2\sqrt{3}}{2\bar{\alpha}_d R} + \frac{\bar{\alpha}^4}{4\bar{\alpha}_d^3 R^3}\left(\frac{L}{x}\right)^2 + \frac{3}{4}\bar{\alpha}_d R\left(\frac{L}{x}\right)^2 + \frac{\bar{\omega}}{\bar{\alpha}}\bar{U}_w'\right)\hat{v}_w + \left(\frac{\bar{\omega}}{\bar{\alpha}}\right)^2 \frac{d\hat{v}_w}{d\bar{y}} = 0. \tag{3.66}$$

The terms $(L/x)^2$ arise as a result of initially using U_e to non-dimensionalise velocities.

Growth rate curves were calculated for a number of $\bar{\alpha}_d$ values and Figure 3.7 indicates the shape of these curves for three different values of $\bar{\alpha}_d$ together with the rigid wall curve as a reference. By increasing the value of $\bar{\alpha}_d$ the critical onset speeds for divergence and TWF are lowered which effectively increases the wall compliance. The curves presented in Figure 3.7 indicate some characteristic features. For values of $\bar{\alpha}_d$ up to about 90×10^{-6} results show a significant reduction in growth rates at the lower frequency range. A double peak in the growth rate curve is in evidence with the global maximum amplification rate reduced in value but shifted to higher frequencies compared to that of the rigid wall. The two maxima level out to give an optimum value for $\bar{\alpha}_d$ at which the greatest reduction in maximum amplification rate is achieved. This is indicated in Figure 3.7 for $\bar{\alpha}_d = 95.3 \times 10^{-6}$. For $\bar{\alpha}_d$ above this optimum value the higher frequency disturbances continue to respond to increases in compliance shown by the persistence in growth rate reduction. For frequencies at the lower end of the unstable range, however, increased values of $\bar{\alpha}_d$ now result in increased growth rates although still below those of the rigid boundary. This would infer that the wall starts to appear stiffer to disturbances of these frequencies as the value of the characterising parameter increases. These lower frequency disturbances typically have lower phase speeds and longer wavelengths as $\bar{\alpha}_d$ is increased and the results suggest that the wall is no longer able to accommodate these longer wavelength waves and thus the effectiveness of the compliance is lost. Similar trends were found to occur in a corresponding temporal analysis.

The optimum value of $\bar{\alpha}_d$ can be demonstrated by plotting the maximum amplification rate against $\bar{\alpha}_d$ as in Figure 3.8. This shows a clearly defined minimum value corresponding to $\bar{\alpha}_d = 95.3 \times 10^{-6}$ for the spatial analysis.

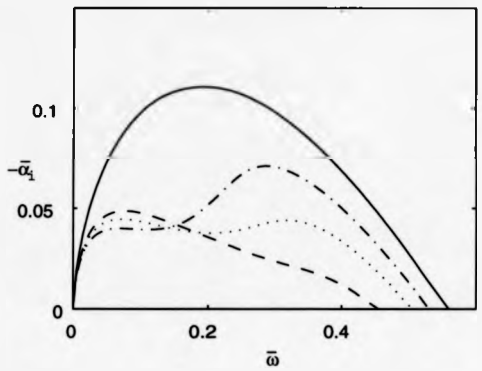

Figure 3.7: Reductions in spatial growth rate using optimum wall parameters. Rigid wall : —, $\bar{\alpha}_d = 80 \times 10^{-6}$: — · —, $\bar{\alpha}_d = 95.3 \times 10^{-6}$: · · ·, $\bar{\alpha}_d = 110 \times 10^{-6}$: - -.

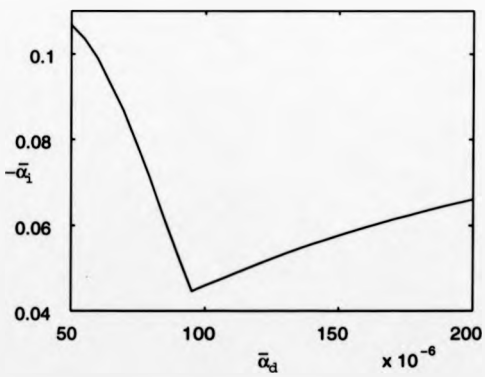

Figure 3.8: Variation of maximum spatial growth rate with $\bar{\alpha}_d$.

Wall parameters corresponding to different values of $\bar{\alpha}_d$ are given in Table 3.1. This verifies that effective values of $\bar{\alpha}_d$ for this flow problem, and the optimum value in particular, translate back into material properties that are physically realistic.

$\bar{\alpha}_d \times 10^6$	b (mm)	K_E (GNm^{-3})	E (MNm^{-2})
60.0	0.722	0.360	1.386
70.0	0.619	0.420	1.386
80.0	0.541	0.480	1.386
90.0	0.481	0.540	1.386
95.3	0.454	0.572	1.386
100.0	0.433	0.600	1.386
120.0	0.361	0.720	1.386
140.0	0.309	0.840	1.386
160.0	0.271	0.960	1.386
180.0	0.241	1.080	1.386
200.0	0.217	1.200	1.386

Table 3.1: Optimal wall properties defined by the wall parameter $\bar{\alpha}_d$. ($U_\infty = 20ms^{-1}$, $\nu = 10^{-6}m^2s^{-1}$)

The reduction in the $\bar{\omega}$-range of instability as wall compliance increases now means that the theory of a neutral mode occurring only at the point of inflexion no longer holds. A modified theorem as given in Yeo and Dowling (1987) is however valid. This states that critical points of neutral modes cannot be points of inflexion, except for the static case of $\bar{\omega} = 0$ and is demonstrated by considering the Reynolds stress for a neutral mode. The violation of the rigid wall theorem can be verified by calculating the phase velocity at the outer neutral point. Results demonstrating the change in phase speed of the upper neutral point with $\bar{\alpha}_d$ are given in Table 3.2.

Conclusions to draw at this stage are that through the use of physically realistic optimal wall parameters the reduction in maximum growth rate of the inviscid Rayleigh instability which can be brought about through the use of wall compliance is significant. With a value of $\bar{\alpha}_d = 95.3 \times 10^{-6}$ used to characterise the wall parameters reductions of up to 60% of the rigid wall maximum are shown to be achievable. This completes the preliminary in-

Wall type	Phase speed at upper neutral point
Rigid wall	0.3821
$\bar{\alpha}_d = 80 \times 10^{-6}$	0.3822
$\bar{\alpha}_d = 95.3 \times 10^{-6}$	0.3823
$\bar{\alpha}_d = 110 \times 10^{-6}$	0.3823

Table 3.2: Variation of phase speed at upper neutral point with wall type.

vestigation into whether there exists potential for the use of wall compliance as a means of controlling this type of instability.

The following section considers the effect of taking the degree of wall compliance above that set by the requirement of marginal stability and calculations demonstrate the onset of the travelling wave flutter instability and characteristic features associated with this flow problem.

3.9 Hydroelastic Instabilities.

The occurrence of hydroelastic instabilities restricts the degree of wall compliance that can be considered for any flow configuration and the effectiveness of wall flexibility becomes impaired in the presence of such wall-based instabilities.

In this section non-optimised wall parameters are used and show the presence of the travelling-wave flutter type of instability and also included in this analysis is the effect of wall damping. In previous investigations wall damping has been shown to destabilise the T-S instability but have a stabilising effect on TWF and this differing effect is due to the different mechanisms of the two instabilities. It is expected therefore that wall damping in this problem will still act to stabilise the TWF but its effect on the Rayleigh instability remains to be determined.

The global eigenvalue scheme used in the preceding sections serves to locate all unstable modes and was particularly useful here in locating the eigenvalues associated with TWF.

Wall parameters were initially fixed at the level set by the optimisation process of the preceding section. The parameter C_{KE} was then decreased in stages to represent increases in the flexibility of the spring foundation while the remaining parameters were kept fixed.

3.9.1 Results.

The results to follow were calculated using the values $C_M = 1.5143$ and $C_B = 1.3370$ with C_{KE} taking values between 0.4289 (optimal $\equiv \bar{\alpha}_d = 95.3 \times 10^{-6}$) and 0.15.

Figure 3.9 shows the amplification rates calculated for the various cases and indicates the variation of the Rayleigh instability growth rate with C_{KE}. Alongside this an additional mode of instability is apparent which becomes unstable above some level of wall compliance. As the compliance increases the Rayleigh instability undergoes continual stabilisation; the characteristic double maxima profile becomes more pronounced and complete stabilisation occurs across a finite central frequency band. Coinciding with this central band of frequencies is the appearance of the additional mode of instability whose growth is promoted by increased wall compliance indicating the possible hydroelastic nature of the mode. For walls defined by C_{KE} between 0.3 and 0.2 the growth of this second mode with C_{KE} is relatively uniform but decreasing to $C_{KE} = 0.15$ brings about a rapid acceleration in the growth rate, as demonstrated in Figure 3.9(b), taking the maximum value close to that of the rigid boundary. Wall compliance in this case has therefore gone beyond a level at which it is beneficial to any boundary layer stabilisation. The corresponding phase speeds are shown in Figure 3.10. The new mode of instability is shown to set in when its phase speed falls below unity and increasing the level of compliance decreases its minimum phase speed.

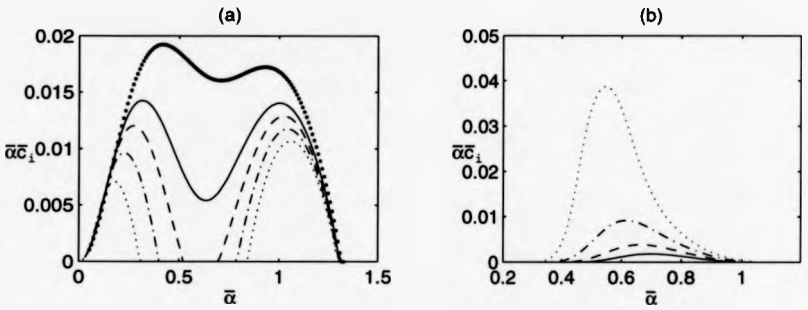

Figure 3.9: Onset of TWF with variation in C_{KE}. (a) Amplification rates for the Rayleigh instability, (b) Amplification rates for the TWF mode. $C_M = 1.5143$, $C_B = 1.3370$. $C_{KE} = 0.4289$: • (optimal), $C_{KE} = 0.3$: —, $C_{KE} = 0.25$: - -, $C_{KE} = 0.2$: – · –, $C_{KE} = 0.15$: · · ·.

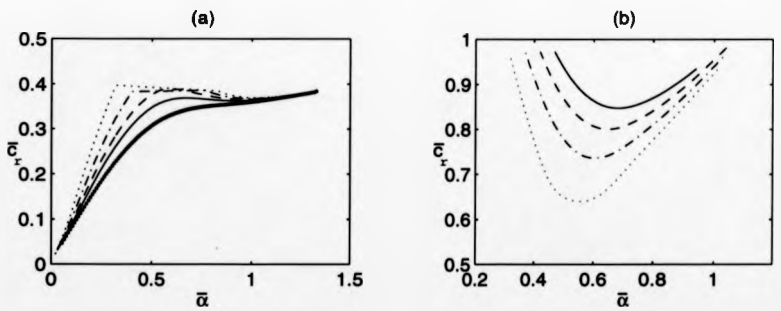

Figure 3.10: Variation of phase speeds with C_{KE}. (a) Rayleigh instability, (b) TWF instability. $C_M = 1.5143$, $C_B = 1.3370$. $C_{KE} = 0.4289$: • (optimal), $C_{KE} = 0.3$: —, $C_{KE} = 0.25$: - -, $C_{KE} = 0.2$: – · –, $C_{KE} = 0.15$: · · ·.

In order to verify that these eigenvalues correspond to an actual instability and are not some spurious numerical mode the complete eigenvalue spectrum was plotted in the form $(\bar{c}_r, \bar{c}_i)$. Here N is the highest order of Chebyshev polynomial used for the solution expansion and the two values of N = 48 and 54 were used. This process distinguishes between eigenvalues which approximate the continuous spectrum and any discrete eigenvalues which indicate an unstable mode. The discrete eigenvalues tend to remain fixed as N increases whereas eigenvalues associated with the continuous spectrum move position.

A position where the two instabilities in Figure 3.9 appear to coincide was selected and the corresponding spectra are shown in Figure 3.11. It should be noted that the numerical solution of the Rayleigh equation gives rise to eigenvalues of the form $\bar{c}_r \pm i\bar{c}_i$ but only the solutions with $\bar{c}_i > 0$ are taken to have any physical meaning. Two neutrally stable points which remain fixed under changes in N are evident in Figure 3.11 and the eigenvalue with positive phase speed, $\bar{c}_r$, is that corresponding to the stabilised Rayleigh mode. The second neutrally stable point occurs with a negative value of $\bar{c}_r$ and could possibly represent a neutral divergence mode which is characterised by upstream travelling waves. However, no actual unstable modes of this kind were located throughout the computations. The third fixed point with large value of $\bar{c}_i$ indicates the presence of an additional mode of instability.

Eigenfunctions for the Rayleigh instability and this second instability are shown in Figures 3.12(a) and (b) respectively where the two modes can easily be distinguished as flow- and wall-based instabilities. The eigenfunction associated with the Rayleigh instability has maximum amplitude near the edge of the boundary layer and is similar in form to the rigid profiles of Figure 3.4 but with some modification at the wall whereas the eigenfunction associated with the new mode reaches maximum amplitude directly at the wall. This additional mode possesses features in common with the travelling wave flutter instability and is identified as such.

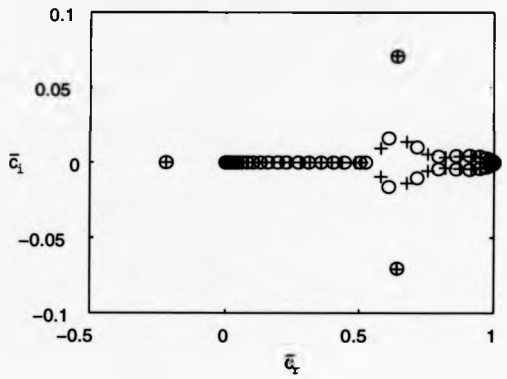

Figure 3.11: Complete eigenvalue spectrum for N = 48 (o) and 54 (+). $\bar{\alpha} = 0.55$, $C_{KE} = 0.15$, $C_M = 1.5143$, $C_B = 1.3370$.

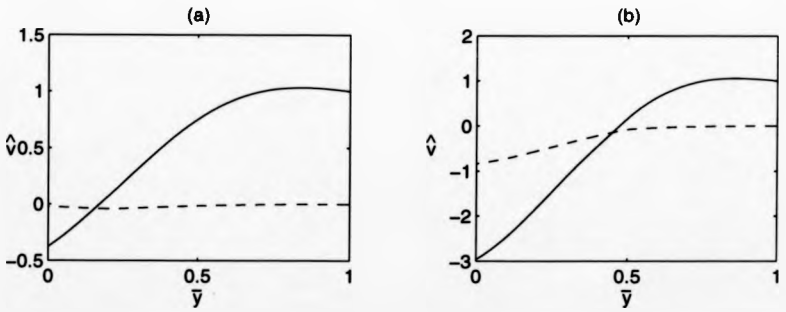

Figure 3.12: Eigenfunctions for flow-based and wall-based instabilities. $C_{KE} = 0.2$, $C_M = 1.5143$, $C_B = 1.3370$. $\hat{v}_r$: —, $\hat{v}_i$: - -. (a) Rayleigh instability : $\bar{\alpha} = 0.3$, $\bar{c} = 0.30962 + 0.02526i$. (b) TWF instability : $\bar{\alpha} = 0.6$, $\bar{c} = 0.7363 + 0.01514i$.

One further set of calculations is undertaken within this section in order to study the effects of wall damping. In order to incorporate damping the lower boundary condition is slightly modified to include the term $d\frac{\partial \eta}{\partial t}$, where d is a damping coefficient. This expression when non-dimensionalised defines the wall parameter C_D and the expression for the lower boundary condition can be written

$$(-\bar{\alpha}^2\bar{c}^2C_M + \bar{\alpha}^4C_B + C_{KE} - i\bar{\alpha}\bar{c}C_D + \bar{c}\bar{U}'_w)\hat{v}_w + \bar{c}^2\frac{d\hat{v}_w}{d\bar{y}} = 0. \tag{3.67}$$

The inclusion of wall damping provides a possible means of improved compliant wall performance by influencing the high growth rates of the TWF instability which occur as the wall is made softer. Results shown in Figure 3.13 for $C_{KE} = 0.2$, $C_M = 1.5143$ and $C_B = 1.3370$ indicate that the complete suppression of the TWF mode is possible for small levels of wall damping. The effect on the Rayleigh instability was negligible such that a far improved wall performance occurred through the inclusion of damping.

Moving on to the wall which gave the most unstable TWF values for the undamped case higher levels of damping were required to bring about significant reductions in the maximum growth rate. At $C_D = 0.025$ the Rayleigh eigenvalues remained largely similar in value to the undamped results but this value of C_D was enough to reduce the maximum growth rate of the TWF instability from a value of 0.038 to 0.03. Subsequent increases in the parameter C_D up to 0.0625 resulted in further stabilisation of the TWF mode. At this degree of wall damping the Rayleigh mode at the upper wavenumber range was still largely unaffected but at the lower wavenumber range there is some evidence of possible modal coalescence. The two distinct modes of instability in the wavenumber range 0.2 - 0.4, as shown in Figure 3.9(a) and (b), for the undamped case begin to merge into a single branch and this apparent coalescence becomes more accentuated as C_D is increased above the value of 0.0625. Figure 3.14 shows the results for $C_D = 0.0625$, 0.075 and 0.1 and compares them to the corresponding undamped values. As well as the pronounced merging of the two modes increasing the value of C_D promotes the growth of the instability across the wavenumber range associated with the TWF mode. Thus there appears to be some optimum level of wall damping ($C_D \approx 0.0625$) at which the TWF mode is suppressed to the greatest extent after which a further increase in wall damping then has an opposing or detrimental effect.

Coalescence of modes in the presence of wall damping has been observed by Carpenter and Garrad (1986), Yeo (1988) and Gyorgyfalvy (1967) with Carpenter and Garrad highlighting the dangers of this type of coalescence and showing that this behaviour leads to very powerful instabilities. The type of behaviour observed here is similar to that of Gyorgyfalvy for a spring backed membrane where increases in compliance were introduced through softer

spring foundations. In this case and that of Yeo coalescence occurred when the wave speed of the wall mode and the hydrodynamic instability (T-S instability in both these cases) coincided. In the present investigation introducing sufficiently high levels of wall damping was enough to reduce the TWF phase speeds close to those of the Rayleigh instability thereby providing a possible means for coalescence. For the wall defined by $C_{KE} = 0.2$, where no evidence of this behaviour was found the minimum phase speed of the TWF mode remained a significant degree higher than the maximum phase speed of the Rayleigh mode. Coalescence within this wall/flow configuration therefore appears to be confined to the softer walls whose properties do not make wall damping a viable means of suppressing the TWF instability.

3.10 Summary.

It has been shown that wall compliance can have a significant effect on the inviscid Rayleigh instability which occurs in two-dimensional boundary layers possessing a point of inflexion. Optimal wall properties have been found which can give reductions in maximum growth rate of up to 60 % of the corresponding rigid wall value. Taking wall parameters beyond the constraints set by the marginal stability criterion sees the onset of the travelling wave flutter instability with growth rates rising to values of the order of the rigid wall maximum as wall compliance is increased through softer spring foundations. Small levels of wall damping were found to suppress the TWF mode for a moderately soft wall with insignificant effects on the Rayleigh instability growth rates. For the softest wall investigated higher levels of wall damping were required to give any substantial effect on the TWF instability but above some critical level of damping, however, evidence of possible modal coalescence is presented.

Although the Rayleigh instability mechanism is essentially inviscid, viscous effects should be considered if growth rates are to be represented realistically. The following chapter therefore moves on to incorporate these effects into the stability analysis.

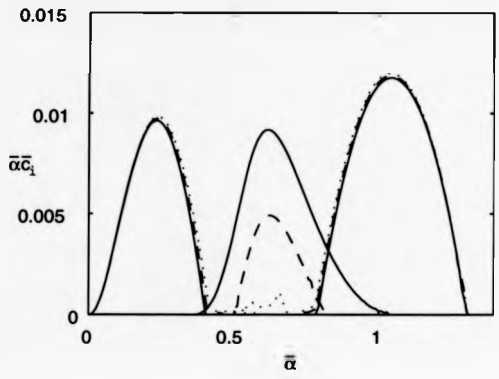

Figure 3.13: Effect of wall damping at $C_{KE} = 0.2$. Undamped : —, $C_D = 0.01$: – –, $C_D = 0.02$: · · ·.

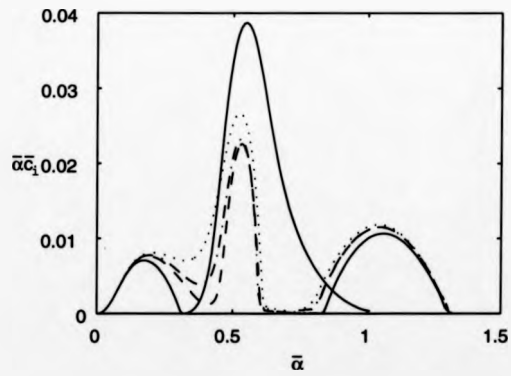

Figure 3.14: Effect of wall damping at $C_{KE} = 0.15$. Undamped : —, $C_D = 0.0625$: – –, $C_D = 0.075$: – · –, $C_D = 0.1$: · · ·.

CHAPTER 4.

THE EFFECT OF WALL COMPLIANCE ON THE RAYLEIGH INSTABILITY.

Part 2 : Viscous Analysis.

4.1 Introduction.

Having obtained preliminary results using inviscid theory viscous terms are now incorporated into the problem and the approximate boundary layer profile replaced by one of the Falkner-Skan velocity profiles. These are a family of profiles which represent two-dimensional laminar boundary layer flows in the presence of a streamwise pressure gradient. Along with this more exact representation of the flow the volume-based viscoelastic compliant wall model is introduced which resembles more closely the type of walls used in experimental investigations.

The first section to follow introduces the Falkner-Skan equation from which the boundary layer profile is obtained. Governing equations for the flow are then given which are used to define the flow stability equation or the well-known Orr-Sommerfeld equation. The associated eigenvalue problem is solved numerically using a Runge-Kutta integration scheme along with Gram-Schmidt orthonormalisation which is required in order to overcome certain numerical difficulties associated with the Orr-Sommerfeld equation.

Upon introducing the more realistic viscoelastic compliant wall model, governing equations are given which describe the wall motion. The coupling of the wall and flow equations which follows leads to the definition of appropriate wall boundary conditions and the formation of an eigenvalue relation. The effect of a compliant boundary is considered with the use of previously determined optimal wall parameters. The final section applies an energy balance equation to the flow problem which leads in some way to a reasonable understanding of the physical processes which occur when a compliant wall replaces the rigid boundary and how this consequently affects the Rayleigh instability.

4.2 Falkner-Skan Velocity Profiles.

The Falkner-Skan boundary layer profiles are a family of similar solutions to Prandtl's boundary layer equations.

$$u\frac{\partial u}{\partial x} + v\frac{\partial u}{\partial y} = U_e\frac{dU_e}{dx} + \nu\frac{\partial^2 u}{\partial y^2} \tag{4.1}$$

$$\frac{\partial u}{\partial x} + \frac{\partial v}{\partial y} = 0 \tag{4.2}$$

$$y = 0 \quad : \quad u = 0, \quad v = 0$$

$$y = \infty \quad : \quad u = U_e(x)$$

where U_e is the potential flow and takes the same form as in Chapter 3.

$$U_e(x) = U_\infty \left(\frac{x}{L}\right)^m \tag{4.3}$$

where L is some fixed length in the streamwise direction. (See Figure 3.1, p. 55.)

Solutions to these boundary layer equations are described as similar if two velocity profiles $u(x, y)$ at different streamwise positions differ only by scale factors in u and y. Therefore by making the coordinates dimensionless, velocity profiles at different values of x in terms of these scaled variables will appear identical. Velocities can be made dimensionless with respect to the local potential velocity $U_e(x)$ and lengths non-dimensional with respect to some factor of the local boundary layer thickness.

A scaled dimensional y coordinate, η, is introduced where

$$\eta = \left(\frac{m+1}{2}\right)^{\frac{1}{2}} \frac{y}{x}\left(\frac{U_e x}{\nu}\right)^{\frac{1}{2}}. \tag{4.4}$$

The velocity component u can be written in terms of some function f of η, such that $u = U_e f'(\eta)$, in which case the non-dimensional mean flow velocity can be written in the following way.

$$\bar{U}(\eta) = f'(\eta) \tag{4.5}$$

Substitution of this form for u into the boundary layer equations yields the following ordinary differential equation for f first derived by Falkner and Skan (1930).

$$f''' + ff'' + \beta(1 - f'^2) = 0 \tag{4.6}$$

$$\text{with} \qquad f(0) = f'(0) = 0 \quad \text{and} \quad f' \to 1 \quad \text{as} \quad \eta \to \infty \tag{4.7}$$

β is a constant whose sign indicates whether the flow is accelerated ($\beta > 0$) or whether an adverse pressure gradient exists ($\beta < 0$) and is related to the constant m.

$$\beta = \frac{2m}{m+1} \tag{4.8}$$

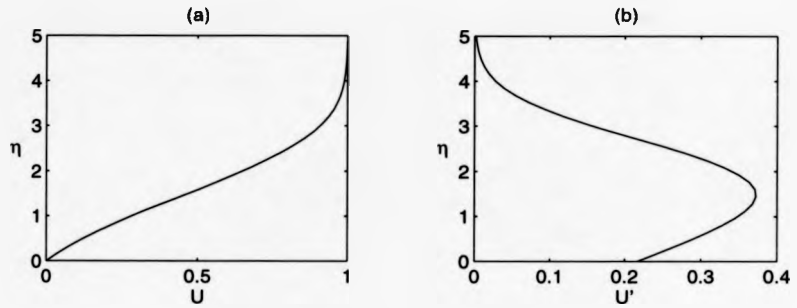

Figure 4.1: Falkner-Skan profile for $\beta = -0.15$.

$\beta = 0$ indicates the absence of any pressure gradient and gives the equation for the well-studied Blasius solution used to represent the boundary layer profile above a flat plate.

A value of $\beta = -0.15$ was chosen here as the profile to study (with a corresponding value of $m = -0.0698$) thereby giving a profile with a point of inflexion at $\eta \approx 1.4$. Figure 4.1(a) and (b) show the boundary layer profile and its derivative respectively as a function of η.

Eq.(4.6) is solved numerically as a two-point boundary value problem to obtain accurate values for f and its derivatives.

The Falkner-Skan equation and Orr-Sommerfeld equation which will follow are written in terms of different variables (η and $\bar{y}$ respectively) and one of these equations must therefore use some transformation of coordinates. A scaling factor between the physical variable, $\bar{y}$, and the Falkner-Skan variable, η, is required and the whole flow problem is subsequently formulated in terms of η. The local dimensional (denoted subscript d) displacement thickness δ_d^* is given by

$$\delta_d^* = \left(\frac{2}{m+1}\right)^{\frac{1}{2}} \left(\frac{\nu x}{U_e}\right)^{\frac{1}{2}} \int_0^\infty (1 - f')d\eta. \tag{4.9}$$

$\mathcal{D}$ is introduced as the required scaling parameter such that

$$\mathcal{D} = \int_0^\infty (1 - f')d\eta = \delta_d^* \left(\frac{m+1}{2}\right)^{\frac{1}{2}} \left(\frac{U_e}{\nu x}\right)^{\frac{1}{2}} = \delta_d^* \frac{\eta}{\bar{y}}. \tag{4.10}$$

If lengths are non-dimensionalised with respect to local displacement thickness then the relation between η and $\bar{y}$ is

$$\eta = \mathcal{D}\bar{y}. \tag{4.11}$$

For the eigenvalue problems which follow all values involving non-dimensional lengths, such as the wavenumber, are scaled by $\mathcal{D}$ before any numerical calculations are made and rescaled upon exit from these to obtain the correctly proportioned eigenvalues. For the Blasius profile $\mathcal{D} = 1.72079$ and for $\beta = -0.15$ the corresponding value is 1.64698.

4.3 Flow Disturbance Equations.

The fluid is taken to be incompressible with the motion of the fluid governed by the Navier-Stokes equations and the Falkner-Skan profile is used to describe the mean flow.

Small perturbations are assumed on this mean flow and with subsequent linearisation of the momentum and continuity equations the disturbance equations for the perturbation quantities are formed. This follows the method of the previous section except that viscous terms are now retained. Perturbation velocity components and pressure are expressed in the usual way.

$$[u'(x,y,t), v'(x,y,t), p'(x,y,t)]^T = [U_e\,\bar{u}(y), U_e\,\bar{v}(y), \rho U_e^2\,\bar{p}(y)]^T e^{i(\alpha x - \omega t)} + \text{c.c.} \qquad (4.12)$$

For this analysis disturbances are assumed to grow spatially such that ω is a real frequency and α a complex wavenumber.

The equations for $\bar{u}$, $\bar{v}$ and $\bar{p}$ are then

$$-i(\bar{\omega} - \bar{\alpha}\bar{U})\bar{u} + D\bar{U}\bar{v} + i\bar{\alpha}\bar{p} - \frac{1}{R_{\delta^*}}(D^2 - \bar{\alpha}^2)\bar{u} = 0 \qquad (4.13)$$

$$-i(\bar{\omega} - \bar{\alpha}\bar{U})\bar{v} + D\bar{p} - \frac{1}{R_{\delta^*}}(D^2 - \bar{\alpha}^2)\bar{v} = 0 \qquad (4.14)$$

$$i\bar{\alpha}\bar{u} + D\bar{v} = 0. \qquad (4.15)$$

where $D \equiv \frac{d}{dy}$. Lengths have been non-dimensionalised using local boundary layer displacement thickness, δ^*, and velocities with respect to the local free-stream velocity U_e. This is the same equation for the disturbances as for the inviscid theory except that terms of order $1/R_{\delta^*}$ are retained where R_{δ^*} is the Reynolds number based on local displacement thickness:

$$R_{\delta^*} = U_e\delta^*/\nu. \qquad (4.16)$$

It is assumed throughout that the perturbation amplitudes are sufficiently small for linear theory to hold and that the flow is locally parallel. With these assumptions $\bar{u}$ and $\bar{p}$ can be eliminated from Eqs.(4.13)-(4.15) to obtain the well-known fourth-order Orr-Sommerfeld equation.

$$(\bar{U} - \frac{\bar{\omega}}{\bar{\alpha}})(\bar{v}'' - \bar{\alpha}^2\bar{v}) - \bar{U}''\bar{v} + \frac{i}{\bar{\alpha}R_{\delta^*}}(\bar{v}^{iv} - 2\bar{\alpha}^2\bar{v}'' + \bar{\alpha}^4\bar{v}) = 0 \qquad (4.17)$$

This fourth-order equation now requires two boundary conditions in addition to those of the inviscid problem. For the rigid wall the no-slip condition must now be enforced and for any type of boundary the remaining condition is that the derivative of the normal perturbation velocity should decay beyond the edge of the boundary layer. Thus the four boundary conditions for the rigid wall viscous problem are

$$v(0) = v'(0) = 0 \tag{4.18}$$

$$v(\bar{y}), \quad v'(\bar{y}) \to 0 \quad \text{as} \quad \bar{y} \to \infty. \tag{4.19}$$

Eqs.(4.17)-(4.19) then constitute an eigenvalue relation.

4.4 Formulation of the Rigid Wall Eigenvalue Problem

4.4.1 Integration of the Orr-Sommerfeld Equation.

Determining a numerical solution to the Orr-Sommerfeld equation for the rigid wall is by no means a trivial problem and less straightforward than that posed by the Rayleigh equation. The semi-infinite fluid domain brought about by the use of the Falkner-Skan profile results in the need for a more complex transformation to the Chebyshev spectral domain than in the inviscid problem and the form of the compliant wall boundary conditions in the viscoelastic model also means a global eigenvalue scheme is no longer possible. With these observations and for efficiency in formulation and computation a shooting method was chosen as the numerical integration technique for this problem. The shooting method basically consists of integration of the Orr-Sommerfeld equation using initial values which satisfy the boundary conditions at one end of the physical domain and subsequent matching of the integrated solution to the second set of boundary conditions. This integration procedure can be carried out in either direction (i.e. direction of increasing or decreasing $\bar{y}$) but it was considered most appropriate in this case to start the integration process at the wall and move out to the edge of the boundary layer. This allows simultaneous integration of the Falkner-Skan equation which behaves well to integration outwards from the wall and then allows ready access to the required mean flow values.

The Orr-Sommerfeld equation is rewritten as four first order differential equations and the wall boundary or initial conditions can be written in the form

$$\boldsymbol{AV} = 0 \tag{4.20}$$

where $\boldsymbol{A}$ is a 2×4 matrix and $\boldsymbol{V}$ is the vector formed from $\hat{v}$ and its first three derivatives.

$$\boldsymbol{V} = [\hat{v}, D\hat{v}, D^2\hat{v}, D^3\hat{v}]^T \tag{4.21}$$

In the case of the rigid wall all entries in $\boldsymbol{A}$ are zero except for A_{11} and A_{22} which take the value of unity in accordance with the conditions in Eq.(4.18).

The Orr-Sommerfeld equation is a fourth-order differential equation so there exists four fundamental solutions $\boldsymbol{V}_i$ $(i = 1, \ldots, 4)$ where at the wall $\boldsymbol{V}_1 = [1, 0, 0, 0]^T$, $\boldsymbol{V}_2 = [0, 1, 0, 0]^T$, etc. and a general solution can be written as a linear combination of these solutions.

$$\boldsymbol{V} = \sum_{i=1}^{4} D_i \boldsymbol{V}_i. \tag{4.22}$$

D_i are constants of integration but two of these can be eliminated by implementing the wall boundary conditions. It is easy to deduce that for the rigid wall $D_1 = D_2 = 0$ and hence two linearly independent starting solutions, $\tilde{\boldsymbol{V}}_1$ and $\tilde{\boldsymbol{V}}_2$, are obtained.

$$\tilde{\boldsymbol{V}}_1 = [0, 0, 1, 0]^T \tag{4.23}$$

$$\tilde{\boldsymbol{V}}_2 = [0, 0, 0, 1]^T \tag{4.24}$$

The remaining integration constants are determined by any normalisation condition which is imposed. These two starting solutions are then used in a fixed step size fourth-order Runge-Kutta integration scheme which integrates both solutions simultaneously. Having taken into account any numerical problems which arise from this, which will be covered in the following section, these two fundamental solutions when integrated must match those at the edge of the boundary layer.

Beyond the edge of the boundary layer $(\bar{y} \geq \bar{y}_e)$, $\bar{U}(\bar{y}) = 1$ and $\bar{U}''(\bar{y}) = 0$ and so the Orr-Sommerfeld equation reduces to

$$(1 - \frac{\bar{\omega}}{\bar{\alpha}})(\bar{v}'' - \bar{\alpha}^2 \bar{v}) + \frac{i}{\bar{\alpha} R_{\delta^*}}(\bar{v}^{iv} - 2\bar{\alpha}^2 \bar{v}'' + \bar{\alpha}^4 \bar{v}) = 0. \tag{4.25}$$

Two exponentially decaying solutions are obtained from Eq.(4.25)

$$\exp(-\bar{\alpha}\bar{y}) \quad \text{and} \quad \exp(-\bar{\beta}\bar{y}) \quad \text{where} \quad \bar{\beta} = \sqrt{\bar{\alpha}^2 + iR_{\delta^*}(\bar{\alpha} - \bar{\omega})} \tag{4.26}$$

and these can be used to form two orthonormal fundamental solutions, $\tilde{\boldsymbol{V}}_3$ and $\tilde{\boldsymbol{V}}_4$, at the edge of the boundary layer. In order to determine the eigenvalues the integrated solutions should then correlate with these fundamental solutions at $\bar{y}_e$ such that

$$B_1 \tilde{\boldsymbol{V}}_1(\bar{y}_e) + B_2 \tilde{\boldsymbol{V}}_2(\bar{y}_e) = B_3 \tilde{\boldsymbol{V}}_3(\bar{y}_e) + B_4 \tilde{\boldsymbol{V}}_4(\bar{y}_e) \tag{4.27}$$

where B_i are constants.

This constraint can be written in matrix form.

$$\begin{bmatrix} -\tilde{V}_1 & -\tilde{V}_2 & 1 & 1 \\ -D\tilde{V}_1 & -D\tilde{V}_2 & -\bar{\alpha} & -\bar{\beta} \\ -D^2\tilde{V}_1 & -D^2\tilde{V}_2 & \bar{\alpha}^2 & \bar{\beta}^2 \\ -D^3\tilde{V}_1 & -D^3\tilde{V}_2 & \bar{\alpha}^3 & -\bar{\beta}^3 \end{bmatrix} \begin{bmatrix} B_1 \\ B_2 \\ B_3 \\ B_4 \end{bmatrix} = \begin{bmatrix} 0 \\ 0 \\ 0 \\ 0 \end{bmatrix} \tag{4.28}$$

or

$$\boldsymbol{M}\boldsymbol{B} = 0. \tag{4.29}$$

The conditions for solving the eigenvalue relation arise from the need to have non-trivial solutions for $\boldsymbol{B} = [B_1, \ldots, B_4]^T$ which is satisfied if $\det(\boldsymbol{M}) = 0$.

For given values of R_{δ^*} and $\bar{\omega}$ this eigenvalue problem is solved using the method of false position to determine the complex value of $\bar{\alpha}$. This local iterative method to determine eigenvalues requires two initial estimates and if $F(\bar{\alpha}_i) = \det(\boldsymbol{M}(\bar{\alpha}_i))$, then an improvement on the initial guesses is made using the following algorithm.

$$\bar{\alpha}_{i+2} = \frac{\bar{\alpha}_{i+1}F(\bar{\alpha}_i) - \bar{\alpha}_i F(\bar{\alpha}_{i+1})}{F(\bar{\alpha}_i) - F(\bar{\alpha}_{i+1})}$$

This process is repeated, with successive updating of the values, until $|F(\bar{\alpha}_i)| <$ some specified tolerance.

4.4.2 Numerical Method - Gram-Schmidt Orthonormalisation.

Numerical integration of the Orr-Sommerfeld equation is not a straightforward process owing to the so-called stiff nature of the equation. Stiffness occurs when there are two or more very different scales governing the solutions. The two solutions $\tilde{\boldsymbol{V}}_1$ and $\tilde{\boldsymbol{V}}_2$ are initially linearly independent but this independence is lost as the integration proceeds but this is, however, a purely numerical problem due in part to computer roundoff/truncation error. In this case $\tilde{\boldsymbol{V}}_1$ and $\tilde{\boldsymbol{V}}_2$ contain parts of the rapidly varying viscous solutions which tend to dominate the slower varying components and become increasingly more dominant as the integration proceeds. If this loss of independence is not checked the result is a rapid accumulation in the numerical values of the solutions and this parasitic growth then renders the results meaningless and even if the exact initial conditions were known this numerical difficulty would still occur.

A number of methods have been formulated to deal with this problem and the use of Gram-Schmidt orthonormalisation to maintain numerical independence allows the basic framework of the shooting method of integration to be retained. This method was originally introduced by Godunov (1961) and subsequent details appear in Scott and Watts (1977). The basic theory behind the method will be outlined below.

One way of ensuring numerical independence of the solutions over the whole integration range is to keep the vectors mutually orthogonal as necessary. This means that each time the vectors start to lose their independence some form of normalisation process must take place. A key question therefore is what constitutes a loss of numerical independence and how often should this reorthonormalisation take place.

One simple rule which is effective when used in conjunction with fixed step integrators is to perform reorthonormalisation each time the magnitude of one of the vectors exceeds some specified value. This criterion proves easy to incorporate and efficient to compute. A suitable value for this tolerance on the magnitude has to be found for each particular problem and once this value, M, has been chosen then the orthonormalisation process is as follows.

Suppose the two vectors are $\boldsymbol{w}_1$ and $\boldsymbol{w}_2$.
If $||\boldsymbol{w}_1|| > M$ then $\boldsymbol{w}_1$ is normalised to give a new vector $\boldsymbol{v}_1$.

$$\boldsymbol{w}_1 \rightarrow \frac{\boldsymbol{w}_1}{||\boldsymbol{w}_1||} = \boldsymbol{v}_1$$

The second vector is then made orthogonal to this new first vector using the Gram-Schmidt transformation.

$$\boldsymbol{w}_2 \rightarrow \boldsymbol{w}_2 + < \boldsymbol{w}_2, \boldsymbol{v}_1 > \boldsymbol{v}_1 = \boldsymbol{v}_2$$

where $< \boldsymbol{a}, \boldsymbol{b} >= a_i^* b_i$. (Repeated suffices imply summation from $i = 1$ to 4 and a^* denotes the complex conjugate of a.) The second vector can also be normalised but this is not essential.

It is desirable for efficiency of computation to have the minimum number of reorthonormalisations whilst maintaining the required degree of accuracy in the eigenvalues. For a given number of integration steps a value of $M = 1000$ was found to be sufficient and typically this results in about 10 reorthonormalisations in the integration process for the rigid wall problem. As a particularly stringent test on this value of M results were compared to eigenvalues obtained with reorthonormalisation performed at every integration step which guarantees numerical independence in the integrated solutions. No change in the eigenvalues was observed indicating the suitability of the chosen value of M.

This orthonormalisation method thus results in a set of K orthonormalisation points $\bar{y}_1 < \bar{y}_2 < \cdots < \bar{y}_K = \bar{y}_e$ and intermediate solutions $\boldsymbol{v}_m$ on the interval $[\bar{y}_m, \bar{y}_{m+1}]$.

$$\boldsymbol{v}_m(\bar{y}) = a_m \boldsymbol{v}_m^{(1)}(\bar{y}) + \boldsymbol{v}_m^{(2)}(\bar{y}) \tag{4.30}$$

where $\boldsymbol{v}_m^{(1)}$ and $\boldsymbol{v}_m^{(2)}$ are the two independent integrated solutions. For calculation of the eigenvalues alone there is no further need for these solutions but if eigenfunctions are required then the intermediate solutions must be matched at the orthonormalisation points by determining the constants a_m. This matter is discussed in § 4.13.

4.5 Comparison With Existing Results for the Rigid Wall.

Since the stability characteristics of the Blasius boundary layer flow over a rigid wall have been well-studied the accuracy of the integration scheme described above was tested for Blasius flow against existing results.

Using 200 equal integration steps out to a value of 8.0 (Blasius coordinate) at the edge of the boundary layer good agreement with the neutral points of Jordinson (1970) was achieved. Eigenvalues and spatial amplification data calculated for non-dimensional frequencies $F = 32 \times 10^{-6}$ and $F = 28.5 \times 10^{-6}$, where $F = \bar{w}/R_{\delta^*}$, were found to be in agreement to at least four significant figures with the results of Carpenter (1994).

A further test was required on the accuracy of the Falkner-Skan solution. Using the same integration parameters as above eigenvalues for a number of different Reynolds numbers were compared with the comprehensive results presented in Arnal (1986) and agreement to within three or four significant figures was generally found. No mention is made in this report of the method of integration or parameters used in determining the Falkner-Skan solution but nevertheless the comparisons were satisfactory enough, together with the calculated results for Blasius flow, to give confidence in the accuracy of both the integration routine and the boundary layer profile being used.

Growth rate values obtained for the Falkner-Skan profile were found to be almost an order of magnitude greater than the corresponding values for the Blasius profile indicating the much more powerful instability mechanism of the Rayleigh mode compared to that of the Tollmien-Schlichting instability.

4.6 Volume-based Compliant Wall.

The theoretical viscoelastic compliant wall provides a more realistic framework in which to study the effects of wall compliance on flow instability and possesses features that are desirable in a wall design for practical use. These walls are of the type that have been used in previous experimental investigations (Daniel *et al.*, 1987) and will be used in ongoing experimental work.

The theoretical calculations for this type of wall are more complex than for the spring backed plate model where the effects of wall compliance can be incorporated into a single equation. The same integration routine as for the rigid wall can be used, however, once the appropriate (wall) boundary conditions have been determined. These are formed from the coupling of wall and fluid motion which provides the main body of additional calculation.

Viscoelastic walls of the type shown in Figure 4.2 can be constructed using a number of

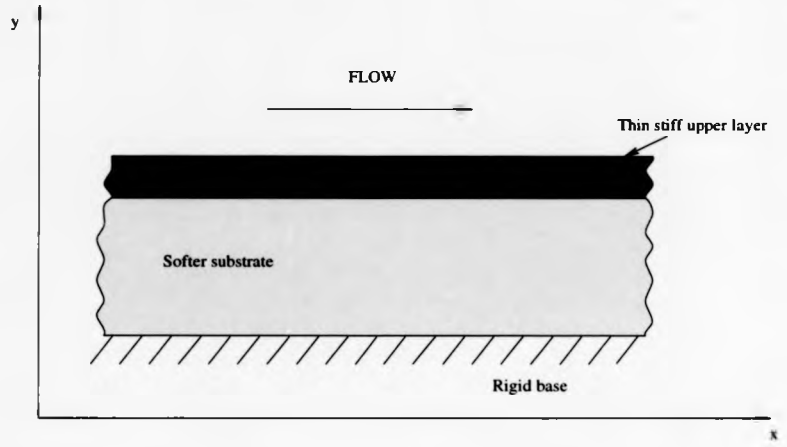

Figure 4.2: Double layer viscoelastic compliant wall construction.

different substrate layers but attention here concentrates on the double-layer wall construction as in Dixon *et al.* (1994).

The wall model basically comprises a soft viscoelastic substrate above which is attached a much stiffer, thin outer layer with the lower part of the substrate firmly attached to a rigid base. It is quite possible to omit the upper layer and study just the effects of a single layer construction which was one of the walls investigated by Yeo (1988). The original principle behind attaching this upper layer was one of guarding against damage to the soft substrate but this has in fact been found to lead to an improvement in the growth rate reduction properties of the wall for the instability due to disturbances in a flat plate boundary layer. Duncan (1988) concluded that the presence of a stiff upper layer delayed the onset of this instability to higher flow speeds in comparison with a single layer wall.

The theory set out below is required in order to determine the initial values for the two fundamental solutions used in the integration process and to solve for the eigenvalues. The governing equations for the wall motion are first introduced and are derived from theories concerning the propagation of waves in a viscoelastic material. These are then coupled to the corresponding flow equations in order to satisfy the physical requirements of velocity and stress continuity across the wall/flow interface which then enables the appropriate wall boundary conditions/initial integration values to be determined.

4.7 Governing Equations for the Wall Motion.

Unlike the isotropic plate-spring model used in the preceding section the volume-based model allows both vertical and horizontal displacement of the wall to take place in response to the action of the fluid. The wall is assumed to be constructed from an homogeneous isotropic material which extends infinitely in the streamwise direction and is of a finite thickness in the direction normal to the flow. The dynamics of the soft substrate layer are described by the Navier equations and concern the propagation of waves in a viscoelastic material, whilst the thin stiffer outer layer is assumed to be governed by classic thin plate theory. If ξ is the wall displacement in the x-direction (parallel to the flow) and η the wall displacement normal to the flow, then for an isotropic viscoelastic solid the wall motion is described by the following equations.

$$\rho_s \frac{\partial^2 \xi}{\partial t^2} = G_s \left(\frac{\partial^2 \xi}{\partial x^2} + \frac{\partial^2 \xi}{\partial y^2} \right) + \left(K_s + \frac{1}{3} G_s \right) \frac{\partial}{\partial x} \left(\frac{\partial \xi}{\partial x} + \frac{\partial \eta}{\partial y} \right) \tag{4.31}$$

$$\rho_s \frac{\partial^2 \eta}{\partial t^2} = G_s \left(\frac{\partial^2 \eta}{\partial x^2} + \frac{\partial^2 \eta}{\partial y^2} \right) + \left(K_s + \frac{1}{3} G_s \right) \frac{\partial}{\partial y} \left(\frac{\partial \xi}{\partial x} + \frac{\partial \eta}{\partial y} \right) \tag{4.32}$$

Here G_s and K_s are the dimensional shear and bulk moduli respectively which are related to the elastic modulus of the material, E_s, and the Poisson ratio, ν_s, as follows.

$$G_s = \frac{E_s}{2(1+\nu_s)}, \qquad K_s = \frac{E_s}{3(1-2\nu_s)}$$

where ρ_s is the density of the wall body.

Viscoelastic damping can be modelled using a complex shear modulus.

$$G_s = G_s^R (1 - i\gamma_s) \tag{4.33}$$

where γ_s is a dimensionless, real damping coefficient (or loss tangent) which can also be modified to incorporate Voigt damping, where γ_s becomes dependent on frequency.

Expressions for both normal and tangential stresses in the wall are required and for the substrate these are, respectively

$$\sigma_s = 2G_s \frac{\partial \eta}{\partial y} + \left(K_s + \frac{1}{3} G_s \right) \left(\frac{\partial \xi}{\partial x} + \frac{\partial \eta}{\partial y} \right) \tag{4.34}$$

$$\tau_s = G_s \left(\frac{\partial \xi}{\partial y} + \frac{\partial \eta}{\partial x} \right). \tag{4.35}$$

With the thin, stiff upper layer being modelled using classical thin plate theory, rather than as another viscoelastic layer as in the formulation of Yeo (1988), the corresponding plate

stress terms are

$$\sigma_p = \rho_p b \frac{\partial^2 \eta}{\partial t^2} + B_p \frac{\partial^4 \eta}{\partial x^4} \tag{4.36}$$

$$\tau_p = \rho_p b \frac{\partial^2 \xi}{\partial t^2} - E_p b \frac{\partial^2 \xi}{\partial x^2} \tag{4.37}$$

where E_p and b are the modulus of elasticity of the plate and the plate thickness and B_p is the flexural rigidity of the plate.

$$B_p = \frac{E_p b^3}{12(1-\nu_p^2)}$$

This approximation introduces a stress discontinuity at the interface of the layers, but as long as the upper plate thickness is small compared to the disturbance wavelength, the thin plate approximation is appropriate. This was validated to some extent in Dixon *et al.* (1994) where a comparison of free waves is made between a double layer compliant wall with the thin plate approximation and that with the upper layer modelled as another viscoelastic material and revealed little significant difference between the two cases under the small wavenumber constraint.

For purposes of non-dimensionalisation the wall parameters are scaled with respect to fixed quantities; that is, unlike the local displacement thickness, δ^*, which is dependent on streamwise location. This ensures that for a given set of non-dimensional values the actual wall parameters remain constant at any point in the streamwise direction. In order to achieve this a fixed reference Reynolds number R_L is introduced:

$$R_L = \frac{U_\infty L}{\nu}. \tag{4.38}$$

This provides suitable values of velocity, U_∞, and a length scale, L, which are then used in the non-dimensionalisation process. U_∞ is taken to be the value of the freestream velocity at the onset point of the pressure gradient (see Figure 3.1). Then, for example, dimensionless wall parameters are written

$$\bar{G}_s = \frac{G_s}{\rho_f U_\infty^2}, \qquad \bar{B}_p = \frac{B_p}{\rho_f U_\infty^2 L^3}, \qquad \bar{b} = \frac{b}{L} \tag{4.39}$$

where an overbar denotes the non-dimensional value.

On the other hand quantities associated with the flow, such as the flow eigenvalues, are made dimensionless in the usual way via a conventional Reynolds number based on boundary layer displacement thickness.

$$R_{\delta^*} = \frac{U_e \delta^*}{\nu}, \qquad \bar{\alpha} = \alpha \delta^*, \qquad \bar{\omega} = \frac{\omega \delta^*}{U_e} \tag{4.40}$$

where U_e is the local freestream velocity in the region where the pressure gradient acts.

Disturbances are assumed to be of the travelling-wave form so that the displacement vector can be expressed in a similar manner.

$$\boldsymbol{\eta} = [\xi(x,y,t), \eta(x,y,t)]^T = \delta^*[\hat{\xi}(y), \hat{\eta}(y)]^T e^{i(\alpha x - \omega t)} + \text{c.c.} \tag{4.41}$$

The displacement vector field can be written as a sum of rotational and irrotational terms.

$$\boldsymbol{\eta} = \nabla\phi + \nabla \wedge \boldsymbol{\psi} \tag{4.42}$$

and the Navier equations then reduce to two wave equations for ϕ and $\boldsymbol{\psi}$.

$$\frac{\partial^2 \phi}{\partial t^2} = c_L^2 \nabla^2 \phi \tag{4.43}$$

$$\frac{\partial^2 \boldsymbol{\psi}}{\partial t^2} = c_T^2 \nabla^2 \boldsymbol{\psi} \tag{4.44}$$

where

$$c_L^2 = \frac{1}{\rho_s}\left(K_s + \frac{4G_s}{3}\right), \qquad c_T^2 = \frac{G_s}{\rho_s}. \tag{4.45}$$

c_L and c_T are respectively the dilational and transverse wave speeds in the material and using the representations

$$\phi(x,y,t) = \hat{\phi}(y)e^{i(\alpha x - \omega t)} + \text{c.c.} \qquad \boldsymbol{\psi}(x,y,t) = [0, \hat{\psi}(y), 0]^T e^{i(\alpha x - \omega t)} + \text{c.c.} \tag{4.46}$$

the wave equations reduce further to two ordinary differential equations. The vector form of $\boldsymbol{\psi}$ is taken to ensure a two-dimensional displacement field consistent with two-dimensional disturbance propagation.

$$\hat{\phi}'' = \alpha^2 K_L^2 \hat{\phi} \quad \text{with} \quad K_L^2 = 1 - \frac{\bar{c}^2}{\bar{c}_L^2} \tag{4.47}$$

$$\hat{\psi}'' = \alpha^2 K_T^2 \hat{\psi} \quad \text{with} \quad K_T^2 = 1 - \frac{\bar{c}^2}{\bar{c}_T^2} \tag{4.48}$$

where primes denote differentiation with respect to y.

The solutions to each of these equations are a sum of exponential terms and the non-dimensional amplitudes can then be expressed as follows.

$$\begin{aligned}\bar{\xi} = {} & i\bar{\alpha}\sinh(\bar{\alpha}K_L l\bar{y})C_1 + i\bar{\alpha}\cosh(\bar{\alpha}K_L l\bar{y})C_2 + \\ & \bar{\alpha}K_T \cosh(\bar{\alpha}K_T l\bar{y})C_3 + \bar{\alpha}K_T \sinh(\bar{\alpha}K_T l\bar{y})C_4\end{aligned} \tag{4.49}$$

$$\begin{aligned}\bar{\eta} = {} & \bar{\alpha}K_L \cosh(\bar{\alpha}K_L l\bar{y})C_1 + \bar{\alpha}K_L \cosh(\bar{\alpha}K_L l\bar{y})C_2 - \\ & i\bar{\alpha}\sinh(\bar{\alpha}K_T l\bar{y})C_3 - i\bar{\alpha}\cosh(\bar{\alpha}K_T l\bar{y})C_4\end{aligned} \tag{4.50}$$

where $C_1, \ldots, C_4$ are constants of integration.

The parameter l is the ratio of the two reference length scales involved in the non-dimensionalisation process which for flow over a flat plate is simply $l = L/\delta^* = R_L/R_{\delta^*}$ but in this case, owing to the streamwise variation in the freestream velocity, its form is not so simple. In the presence of a pressure gradient

$$l = \frac{L}{\delta^*} = \frac{R_L}{R_{\delta^*}} \frac{U_e}{U_\infty} = \frac{R_L}{R_{\delta^*}} \left(\frac{x}{L}\right)^m \tag{4.51}$$

where m is the power appearing in the expression for the potential flow. x can be eliminated from Eq.(4.51) using the expression for δ^* in Eq.(4.9) to leave

$$l = \frac{L}{\delta^*} = \left[\frac{R_L}{R_{\delta^*}^{1-m}} \left(\frac{m+1}{2}\right)^m\right]^{\frac{1}{1+m}}. \tag{4.52}$$

In the absence of any pressure gradient $m = 0$ and this reduces to R_L/R_{δ^*} as required.

The equations describing the motion of the wall must now be coupled to the equations for the flow in order to determine the correct boundary conditions.

4.8 Coupling of Wall and Flow Equations.

For two-dimensional travelling wave disturbances the normal, σ, and shear, τ, stresses due to the perturbation are written

$$[\sigma, \tau] = \rho U_e^2 [\bar{\sigma}, \bar{\tau}] e^{i(\alpha x - \omega t)} + \text{c.c.} \tag{4.53}$$

Fluid stresses will be denoted by subscript f. The wall stresses are divided into two components, the contribution from the substrate layer (subscript s) and that from the upper plate (subscript p).

Wall and flow equations are then coupled through the requirement of continuity of velocity and stress across the wall/flow boundary. Using the appropriate linearised velocity boundary conditions defined in § 3.7 the velocity constraint is

$$\hat{u}_w = -i\bar{\omega}\hat{\xi}_w - \bar{U}'_w \hat{\eta}_w \tag{4.54}$$

$$\hat{v}_w = -i\bar{\omega}\hat{\eta}_w \tag{4.55}$$

where subscript w denotes evaluation at the mean undisturbed position of the wall ($\bar{y} = 0$).

The fluid stresses at the interface are obtained by using Newton's law of viscosity.

$$\sigma_{jk} = -p\delta_{jk} + \frac{1}{R_{\delta^*}} \left(\frac{\partial u_j}{\partial x_k} + \frac{\partial u_k}{\partial x_j}\right) \qquad j = 1, 2 \tag{4.56}$$

($\sigma_{12} = \sigma_{21} \equiv \tau$ and $\sigma_{22} \equiv \sigma$).

In order to obtain the conditions for continuity of stress across the wall/flow interface the following relation must be satisfied.

$$[\sigma, \tau]_w(x, 0) = [\sigma_f, \tau_f](x, \varepsilon\eta) \tag{4.57}$$

By splitting the stress terms into mean and perturbation contributions this condition becomes

$$\left\{[\sigma, \tau]^M + \varepsilon[\sigma, \tau]\right\}_w (x, 0) = \left\{[\sigma_f, \tau_f]^M + \varepsilon[\sigma_f, \tau_f]\right\} (x, \varepsilon\eta) \tag{4.58}$$

where M indicates the mean stress contribution.

Neglecting any variation in mean stress with streamwise location (consistent with the parallel flow approximation) the Taylor expansion about the mean undisturbed wall position, $(x, 0)$, results in

$$[\sigma, \tau]_w(x, 0) = [\sigma_f, \tau_f] + \eta \frac{\partial}{\partial y}[\sigma_f, \tau_f]^M \tag{4.59}$$

Therefore at the interface and using the continuity equation to eliminate terms in $\hat{u}$ the continuity of stress condition requires

$$\bar{\sigma}_s + \bar{\sigma}_p = \bar{\sigma}_f = -\frac{1}{\bar{\alpha}^2 R_{\delta^*}} \hat{v}''' + (3 - i\bar{\omega})\, \hat{v}' + \frac{i\bar{U}}{\bar{\alpha}} \hat{v}' - \frac{i\bar{U}'}{\bar{\alpha}} \hat{v} \tag{4.60}$$

$$\bar{\tau}_s + \bar{\tau}_p = \bar{\tau}_f = \frac{1}{R_{\delta^*}} \left(i\hat{v}'' + \left[i\bar{\alpha} + \frac{i\bar{U}''}{\bar{\omega}} \right] \hat{v} \right). \tag{4.61}$$

4.9 Boundary Conditions for the Orr-Sommerfeld Equation.

Four boundary conditions are required to describe fully the eigenvalue problem posed by the Orr-Sommerfeld equation. Here the method used is similar to the one introduced by Yeo (1988). The outer boundary equations for the flow remain the same as in the rigid wall case and the two remaining boundary conditions come from the requirement that the substrate be firmly bonded to the rigid base. For a wall of depth d this condition can be written

$$\hat{\xi}(-\bar{d}) = 0, \tag{4.62}$$

$$\hat{\eta}(-\bar{d}) = 0. \tag{4.63}$$

By using the coupled wall/flow equations outlined in the previous section these boundary conditions can be determined explicitly. In order to formulate the problem the above conditions can be written in matrix form and subsequent manipulation of the matrix equations then allows various transformations to be made in order to find the conditions required to satisfy Eqs.(4.62) and (4.63).

The zero displacement condition at the base of the wall can be written in terms of the vector obtained from the four integration constants C_i $(i = 1, \ldots, 4)$ which appear in Eqs.(4.49) and (4.50) for the wall displacement amplitudes.

$$[\hat{\xi}(-\bar{d}), \hat{\eta}(-\bar{d})]^T = \boldsymbol{Q}\boldsymbol{C} = 0 \tag{4.64}$$

where $\boldsymbol{Q}$ is a 2 × 4 complex matrix and $\boldsymbol{C} = [C_1, \ldots, C_4]^T$.

A displacement-stress vector of values at the mean undisturbed wall position can also be written in terms of the vector $\boldsymbol{C}$, with pre-multiplication by a complex 4 × 4 matrix $\boldsymbol{P}$.

$$[\hat{\xi}(0), \hat{\eta}(0), \hat{\sigma}(0), \hat{\tau}(0)]^T = \boldsymbol{P}\boldsymbol{C} \tag{4.65}$$

The unknown vector $\boldsymbol{C}$ can now be eliminated to give an expression for the wall displacements at the base of the layer in terms of the displacement-stress vector at the wall/flow interface.

$$[\hat{\xi}(-\bar{d}), \hat{\eta}(-\bar{d})]^T = \boldsymbol{Q}\boldsymbol{P}^{-1}[\hat{\xi}(0), \eta(0), \hat{\sigma}(0), \hat{\tau}(0)]^T = 0 \tag{4.66}$$

Application of the coupling conditions in Eqs.(4.54) - (4.55) allows a further transformation to be made.

$$[\hat{\xi}(0), \hat{\eta}(0), \hat{\sigma}(0), \hat{\tau}(0)]^T = \boldsymbol{D}[\hat{v}_w, \hat{v}'_w, \hat{v}''_w, \hat{v}'''_w]^T \tag{4.67}$$

This then gives the boundary conditions in the same form as that presented for the rigid wall (Eq. 4.20).

$$[\hat{\xi}(-\bar{d}), \hat{\eta}(-\bar{d})]^T = \boldsymbol{Q}\boldsymbol{P}^{-1}\boldsymbol{D}[\hat{v}_w, \hat{v}'_w, \hat{v}''_w, \hat{v}'''_w]^T = \boldsymbol{A}\boldsymbol{V} = 0 \tag{4.68}$$

Specific entries for the matrices $\boldsymbol{Q}, \boldsymbol{P}$ and $\boldsymbol{D}$ appear in Appendix B.

Again assuming a general solution in terms of the four fundamental solutions such that $\boldsymbol{V} = D_i\boldsymbol{V}_i$ then two constants of integration are eliminated to yield the following starting solutions.

$$\hat{\boldsymbol{V}}_1 = \left[\frac{A_{13}A_{22} - A_{12}A_{13}}{A_{21}A_{12} - A_{11}A_{22}}, \quad \frac{A_{11}A_{21} - A_{21}A_{13}}{A_{21}A_{12} - A_{11}A_{22}}, \quad 1, \quad 0\right]^T \tag{4.69}$$

$$\hat{\boldsymbol{V}}_2 = \left[\frac{A_{14}A_{22} - A_{12}A_{24}}{A_{21}A_{12} - A_{11}A_{22}}, \quad \frac{A_{11}A_{24} - A_{21}A_{14}}{A_{21}A_{12} - A_{11}A_{22}}, \quad 0, \quad 1\right]^T \tag{4.70}$$

Integration to determine the eigenvalues can now proceed as for the rigid wall boundary. However, an increase in the number of integration steps to 500 was required in order to determine the compliant wall eigenfunctions to the same degree of accuracy as for the rigid wall boundary.

4.10 Wall Parameters.

Attention again focuses on the effect of wall compliance on the rigid wall instability rather than on any hydroelastic instabilities which may occur. A significant reduction in maximum local amplification rate of the Rayleigh instability is being sought and for this to occur wall properties are ideally required to be marginally stable with respect to both travelling-wave flutter and divergence.

A global eigenvalue search cannot be employed in this problem as a means of checking on the various instability modes since the lower boundary conditions generate transcendental equations in the eigenvalue, $\bar{\alpha}$, rather than the more straightforward polynomial equation obtained with the plate-spring model. This, together with the large number of wall parameters involved with the viscoelastic compliant wall makes the process of finding optimal wall properties much more complex. As a consequence it would be a very time-consuming task to embark on a full optimisation process for this particular problem. At this stage therefore some existing values of the wall parameters which have been calculated to be marginally stable with respect to the hydroelastic instabilities have been taken from the results of Dixon *et al.* (1994). Although these were calculated for an investigation into transition delay over a flat plate boundary layer the property of marginal stability at the onset of the pressure gradient and stability with respect to the hydroelastic modes thereafter will hold for this flow configuration if the level of wall compliance remains fixed. In this sense the wall properties are not optimised for this particular flow configuration, following the same lines as the inviscid analysis; but, importantly, the absence of hydroelastic modes can be established.

A range of wall parameters are available and results presented are used to gauge the effects of the various wall properties on this type of flow. Wall parameters in general tend to be tailored to a particular Reynolds number at which the maximum reduction in growth rate can be achieved and these parameter values vary strongly with streamwise distance. It is determined to a certain extent which Reynolds number is the optimum value for the available set of parameters used for the flow under consideration.

4.11 Code Validation.

Before any results are presented for the inflexional velocity profile a preliminary check on the code is performed using the Blasius profile and comparisons made with some results published in Yeo (1988).

A robust check on the predictions of spatial amplification rate is made using one of Yeo's single layer walls. Modification is made to accommodate the frequency dependent

wall damping model for the viscoelastic properties used by Yeo and results are shown in Figure 4.3.

A double-layer wall was also considered and neutral points determined for the TWF instability mode. For this wall model results were also available from a calculation using the same thin plate approximation for the upper layer as described above but using a Chebyshev spectral solver for the eigenvalue problem. There was some discrepancy between the results of Yeo and those obtained here but more satisfactory agreement was obtained with the results from the Chebyshev spectral method. The results of the single layer wall together with the three cases for the TWF neutral curves were sufficient to give confidence in the accuracy of the results which follow.

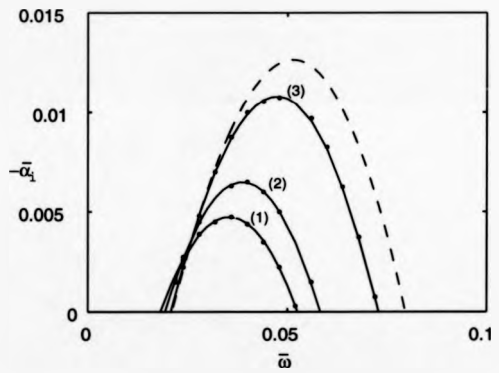

Figure 4.3: Comparison with results of Yeo (1988). Spatial amplification rates at $R_{\delta^*} = 4000$ for a single layer wall with $\bar{G}_s = 0.49(1 - i\bar{\omega}(0.05))$, $\bar{K}_s = 1020.4\bar{G}_s$. Points are values taken from the results of Yeo. (1) : $\bar{d} = 5.0$, (2) : $\bar{d} = 3.0$, (3) : $\bar{d} = 1.0$. Reference rigid wall values : - - -.

4.12 Growth Rates Obtained Using Optimal Wall Properties.

Figure 4.4 shows the spatial growth rates for a given set of wall parameters at a number of different Reynolds numbers. This gives some indication as to the Reynolds number range over which these wall parameters are most effective in terms of maximum growth rate reduction. An increase in R_δ^* from 3000 to 5000 results in both a reduction in growth rate and the unstable frequency range. Further increases in R_δ^* bring about additional reductions in the unstable range but at the expense of higher growth rates at lower frequencies. This figure is somewhat analogous to that of Figure 3.7 in Chapter 3. Higher values of R_δ^* arise as a result of greater freestream speeds if the streamwise position remains unchanged and increases in Reynolds number can therefore be interpreted as increases in wall compliance if the non-dimensional wall parameters are fixed. Increasing wall compliance, as in the inviscid case, is seen to be effective up to some optimum value of R_δ^*, after which further increases see the production of higher growth rates at lower frequencies. Reasons for this follow similar arguments to the inviscid case where the wall behaves differently according to the disturbance wavelengths. Subsequent calculations using the remaining sets of wall parameters are thus performed at $R_{\delta^*} = 5000$ where appropriate. For Figures 4.5 to 4.7 all parameters are calculated to be marginally stable at the onset of the pressure gradient with respect to divergence and stable with respect to travelling-wave flutter up to a value of $R_{\delta^*} = 5700$. Parameters giving the results in Figure 4.8 are stable with respect to travelling-wave flutter up to $R_{\delta^*} = 3600$.

The effect of upper layer stiffness is shown in Figure 4.5 where the parameter $\bar{E}_p$ characterises the plate stiffness. The other parameters do not remain fixed but alter only in order to maintain the marginal stability requirements. In this sense the upper layer stiffness is not the only varying factor but the variation in the other parameters is dependent on the value of $\bar{E}_p$. Reducing the upper plate stiffness sees a flattening of the growth rate curve together with a significant reduction in maximum growth rate for the plate stiffness given by $\bar{E}_p = 55.6$. Of all the parameter sets available that denoted by (1) in Figure 4.5 had the most significant effect on maximum growth rate with a reduction in excess of 50% of the rigid wall maximum. This occurred for parameters not specifically tailored to this flow configuration and suggests the greater potential that exists for the use of wall compliance with this type of instability.

Plate damping is found to have little effect on the calculated growth rates as shown in Figure 4.6.

The results for different substrate thicknesses are shown in Figure 4.7. These indicate that there appears to be some optimal depth of substrate at which compliance is most

effective. Again the characteristic feature of increases in growth rates at the lower frequency range can be seen as the wall depth becomes greater. Results suggest the optimal depth to be in the region of $\bar{d} = 1.5$. Of note also is the lack of variance in the results for substrate depths of $\bar{d} = 3.6$ and 5.4 indicating that if the wall is made sufficiently deep then it will appear infinitely deep to disturbances in the boundary layer and thus the effectiveness of increased depth at any frequency will cease beyond a certain value.

The effect of changing the substrate shear modulus on the local growth rates is given in Figure 4.8. In this case $R_\delta^* = 3000$ and the remaining wall parameters are fixed. Some reduction in spatial amplification rates is observed for all the walls tested with greater reductions achieved as $\bar{G}_s$ is decreased. The frequency range over which the disturbances experience positive growth is little different from the rigid wall case. This might suggest that the upper plate is the major contributor to reductions in the unstable frequency range which is observed in the previous figures.

It should be noted that at $R_\delta^* = 5000$ the reduced growth rates are still comparatively high compared even to the rigid wall growth rates of the T-S instability. However, it is known from the work of Carpenter (1993) and Carpenter and Morris (1990) that precise optimal wall parameters are highly Reynolds number dependent and so similar results to those presented here could theoretically be obtained for different combinations of wall parameters at lower values of R_δ^*.

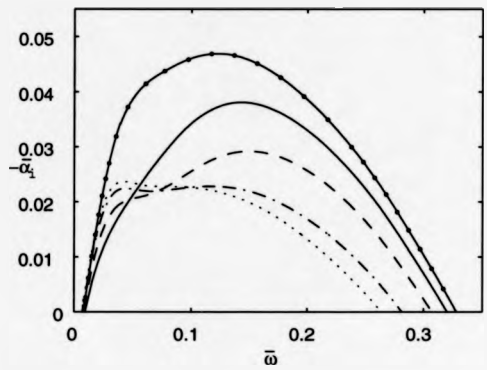

Figure 4.4: Spatial growth rates at a number of R_{δ^*} for a double layer viscoelastic wall with wall properties : $\bar{B}_p = 0.01067$, $\gamma_p = 0.0$, $\bar{b} = 1.2$, $\bar{E}_p = 55.6$, $\bar{G}_s = 0.435$, $\gamma_s = 0.0375$, $\bar{d} = 1.8$. $R_{\delta^*} = 3000$: —, $R_{\delta^*} = 4000$: - -, $R_{\delta^*} = 5000$: – · –, $R_{\delta^*} = 5500$: · · ·. Rigid wall at $R_{\delta^*} = 5000$: —●—.

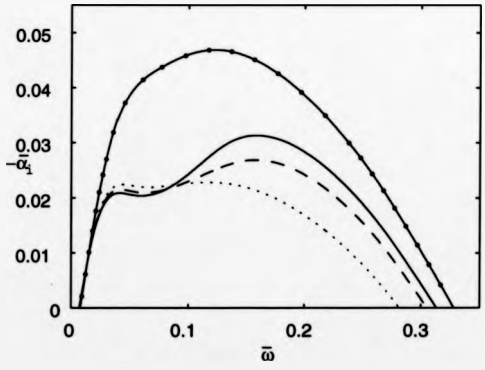

Figure 4.5: Effect of upper layer stiffness at $R_{\delta^*} = 5000$. Rigid wall : —●—. Compliant wall properties are $\bar{d} = 1.8$ and $\gamma_p = 0.0$ in all cases. (1) · · · : $\bar{B}_p = 0.01067$, $\bar{G}_s = 0.435$, $\gamma_s = 0.0375$, $\bar{b} = 0.12$, $\bar{E}_p = 55.6$, (2) - - : $\bar{B}_p = 0.02131$, $\bar{G}_s = 0.403$, $\gamma_s = 0.0296$, $\bar{b} = 0.12$, $\bar{E}_p = 111.0$, (3) — : $\bar{B}_p = 0.03200$, $\bar{G}_s = 0.380$, $\gamma_s = 0.0254$, $\bar{b} = 0.0101$, $\bar{E}_p = 166.7$.

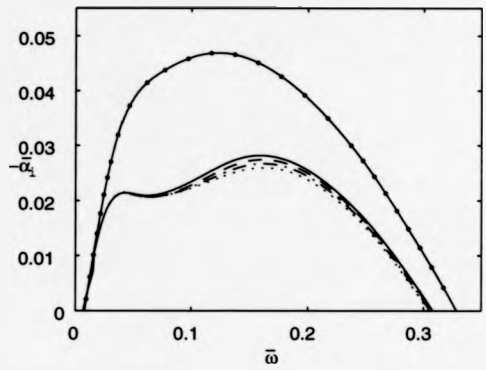

Figure 4.6: Effect of upper plate damping at $R_{\delta^*} = 5000$. Rigid wall : —●—. Wall properties are $\bar{b} = 0.12$ and $\bar{d} = 1.8$ in all cases. (1) — : $\gamma_p = 0.0$, $\bar{B}_p = 0.0239$, $\bar{G}_s = 0.400$, $\gamma_s = 0.028$, (2) - - : $\gamma_p = 0.025$, $\bar{B}_p = 0.0220$,$\bar{G}_s = 0.400$, $\gamma_s = 0.023$, (3) — · — : $\gamma_p = 0.050$, $\bar{B}_p = 0.0200$, $\bar{G}_s = 0.405$, $\gamma_s = 0.019$, (4) · · · : $\gamma_p = 0.0754$, $\bar{B}_p = 0.0181$, $\bar{G}_s = 0.412$, $\gamma_s = 0.015$.

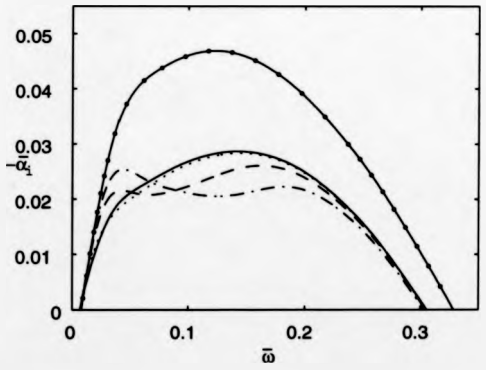

Figure 4.7: Effect of substrate thickness on spatial growth rates at $R_{\delta^*} = 5000$. Rigid wall : —●—. Wall properties are $\bar{b} = 0.12$ and $\gamma_p = 0.075$ in all cases. (1) — : $\bar{d} = 1.2$, $\bar{G}_s = 0.329$, $\gamma_s = 0.0061$, $\bar{B}_p = 0.01900$, (2) - - : $\bar{d} = 1.8$, $\bar{G}_s = 0.412$, $\gamma_s = 0.0152$, $\bar{B}_p = 0.01824$, (3) — · — : $\bar{d} = 3.6$, $\bar{G}_s = 0.477$, $\gamma_s = 0.0153$, $\bar{B}_p = 0.01732$, (4) · · · : $\bar{d} = 5.4$, $\bar{G}_s = 0.491$, $\gamma_s = 0.0125$, $\bar{B}_p = 0.01728$.

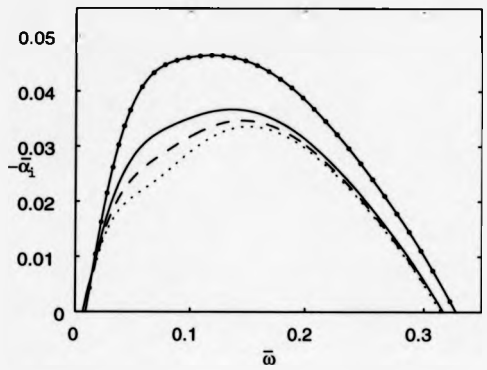

Figure 4.8: Spatial growth rates resulting from different substrate shear moduli at $R_{\delta^*} = 3500$. Rigid wall : —●—. Fixed wall properties are $\bar{d} = 1.8$, $\bar{B}_p = 0.01067$, $\bar{b} = 0.1910$, $\gamma_p = 0.0$. (1) — : $\bar{G}_s = 0.787$,$\gamma_s = 0.002$, (2) - - : $\bar{G}_s = 0.574$, $\gamma_s = 0.011$, (3) $\cdots$: $\bar{G}_s = 0.463$, $\gamma_s = 0.023$.

As stated previously the wall properties were taken from an investigation into the effect of wall compliance on boundary layer stability over a flat plate. It was found in this study that best results were achieved in the Reynolds number range $R_{\delta^*} = 2000$-3000 but in this case, as indicated in Figure 4.4, the corresponding optimum Reynolds number occurs at the higher value of $R_{\delta^*} \approx 5000$. With these observations in mind a simple study of optimal wall parameters was undertaken for the two boundary layer profiles under consideration. In order to accomplish this the plate-spring model and optimisation scheme described in § 3.8 was implemented.

In general it was found that as the Reynolds number was increased the value of the free parameter, $\bar{\alpha}_d$, which determines the optimal wall parameters, decreased in value. A comparison of $\bar{\alpha}_d$ values which gave the maximum reduction in local spatial growth rate at $R_{\delta^*} = 2240$ was then made for the Blasius and Falkner-Skan profiles and this revealed a value of $\bar{\alpha}_d \approx 70 \times 10^{-6}$ for the Blasius case compared to a value in the region of 130×10^{-6} for the Falkner-Skan profile. A possible conclusion to draw from this would be that the use of wall parameters optimised for the flat plate boundary layer, at a given Reynolds number, would tend to be tailored to higher Reynolds numbers for this inflexional velocity profile and would explain the high Reynolds number required to achieve significant growth rate reductions with the wall parameters optimised for the Blasius boundary layer.

In terms of actual material properties the results reveal that for the same Reynolds

number softer substrates and thinner, stiffer upper layers are more likely to be suitable for the stabilisation of the Rayleigh instability in comparison with the properties required for the T-S instability.

4.13 Determining the Eigenfunctions.

The response of the wall to the boundary layer disturbances and the effect of the compliant wall on the disturbance amplitudes can be determined to some degree by considering the wall and flow eigenfunctions. The flow eigenfunctions and corresponding energy distributions which can be obtained from them are invaluable in providing some understanding of the physical processes which occur when instability arises and how they change when wall compliance is introduced. The following subsections describe how the eigenfunctions are calculated for this problem and observations are then discussed.

4.13.1 Flow Eigenfunctions.

As stated previously a consequence of the Gram-Schmidt process required to numerically integrate the Orr-Sommerfeld equation is that the eigenfunctions cannot be obtained as a direct result of the eigenvalue calculation. However, there does exist a set of intermediate solutions which are valid between the orthonormalisation points $\bar{y}_1 < \bar{y}_2 < \cdots < \bar{y}_K = \bar{y}_e$ and these are required to match at each of the orthonormalisation points in order to generate the eigenfunctions subject to some normalisation condition.

The intermediate solutions take the form

$$v_m(\bar{y}) = a_m v_m^{(1)}(\bar{y}) + v_m^{(2)}(\bar{y}) \qquad \text{for} \quad \bar{y} \in [\bar{y}_m, \bar{y}_{m+1}] \tag{4.71}$$

where $v_m^{(i)}$, $i = 1, 2$, are the two fundamental solutions and a_m, for $m = 1, \ldots, K$, are the constants to be determined.

From the requirement of continuity across an orthonormalisation point the solutions must satisfy

$$v_{m-1}(\bar{y}_m) = v_m(\bar{y}_m) \tag{4.72}$$

$$\text{or} \qquad a_{m-1} v_{m-1}^{(1)}(\bar{y}_m) + v_{m-1}^{(2)}(\bar{y}_m) = a_m v_m^{(1)}(\bar{y}_m) + v_m^{(2)}(\bar{y}_m). \tag{4.73}$$

However, from the Gram-Schmidt orthonormalisation process itself

$$v_m^{(1)}(\bar{y}_m) = \frac{v_{m-1}^{(1)}(\bar{y}_m)}{||v_{m-1}^{(1)}(\bar{y}_m)||} \tag{4.74}$$

and

$$v_m^{(2)}(\bar{y}_m) = v_{m-1}^{(2)}(\bar{y}_m) - < v_{m-1}^{(2)}, v_m^{(1)} > v_m^{(1)}(\bar{y}_m). \tag{4.75}$$

Substitution of the expression in Eq.(4.75) into Eq.(4.73) gives

$$a_{m-1}\boldsymbol{v}_{m-1}^{(1)}(\bar{y}_m) + \boldsymbol{v}_{m-1}^{(2)}(\bar{y}_m) = a_m\boldsymbol{v}_m^{(1)}(\bar{y}_m) + \boldsymbol{v}_{m-1}^{(2)}(\bar{y}_m) - < \boldsymbol{v}_{m-1}^{(2)}, \boldsymbol{v}_m^{(1)} > \boldsymbol{v}_{m-1}^{(1)}.$$

Using the form in Eq.(4.74) then determines an iterative formula for the constants, a_m.

$$a_{m-1}\boldsymbol{v}_{m-1}^{(1)}(\bar{y}_m) = \frac{a_m\boldsymbol{v}_{m-1}^{(1)}(\bar{y}_m)}{||\boldsymbol{v}_{m-1}^{(1)}(\bar{y}_m)||} - \frac{< \boldsymbol{v}_{m-1}^{(2)}, \boldsymbol{v}_m^{(1)} > \boldsymbol{v}_{m-1}^{(1)}(\bar{y}_m)}{||\boldsymbol{v}_{m-1}^{(1)}(\bar{y}_m)||}$$

$$\Rightarrow \qquad a_{m-1} = \frac{a_m - < \boldsymbol{v}_{m-1}^{(2)}, \boldsymbol{v}_m^{(1)} >}{||\boldsymbol{v}_{m-1}^{(1)}(\bar{y}_m)||} \tag{4.76}$$

At the edge of the boundary layer, $\bar{y}_K$, a suitable value for a_K is chosen and in this case the initial value is determined by normalising the eigenfunctions to unity at the edge of the boundary layer. Eigenfunctions obtained for the Blasius profile were found to be in good agreement with those published in Yeo (1988).

A comparison of the eigenfunctions for the Falkner-Skan profile at $R_\delta^* = 5000$ for the rigid wall and the compliant wall which gave the maximum reduction in growth rate is made in Figures 4.9 and 4.10. These show similar characteristics to those which have been observed for Blasius flow in that wall compliance brings about a reduction in amplitude of the normal perturbation velocity and generates non-zero values at the wall in accordance with the changes in wall boundary conditions. The point of maximum amplitude is still found to occur some way into the boundary layer region near $\eta = 2$. The rigid wall eigenfunction for the streamwise component of the perturbation velocity shows a double peak in the real part near the wall which becomes smoothed out when the compliant wall is introduced.

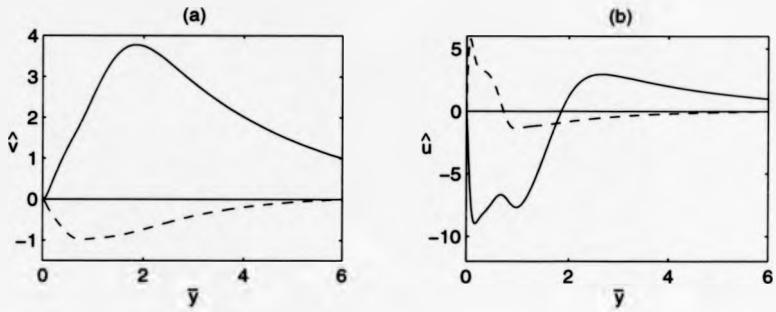

Figure 4.9: Eigenfunctions for rigid wall at $\bar{\omega} = 0.125$ and $R_{\delta^*} = 5000$ corresponding to position of maximum growth rate. $\bar{\alpha} = 0.3528 - 0.04689i$. (a) $\hat{v}$, (b) $\hat{u}$. Real part : —, Imaginary part : - -.

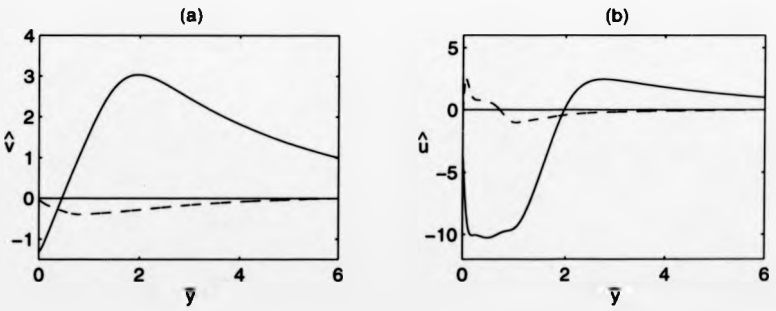

Figure 4.10: Eigenfunctions for compliant wall (1) of Figure 4.5 at $\bar{\omega} = 0.125$ and $R_{\delta^*} = 5000$ corresponding to position of maximum growth rate. $\bar{\alpha} = 0.2992 - 0.02209i$. (a) $\hat{v}$, (b) $\hat{u}$. Real part : —, Imaginary part : - -.

4.13.2 Wall Eigenfunctions.

Wall eigenfunctions give some insight into the response of the compliant wall to the disturbances within the boundary layer and indicate the effect within the wall itself.

Once the eigenvalues have been calculated the wall eigenfunctions can be easily determined. The constants of integration C_i can be calculated from the zero dispacement condition at the base of the wall along with the continuity of velocity condition at the wall/flow interface. Given

$$[\bar{\xi}(-\bar{d}), \bar{\eta}(-\bar{d}), \bar{\xi}(0), \bar{\eta}(0)]^T = \boldsymbol{RC} = [0, 0, \frac{\bar{U}'_w}{\bar{\omega}^2}\hat{v}_w - \frac{1}{\bar{\alpha}\bar{\omega}}\hat{v}'_w, \frac{i}{\bar{\omega}}\hat{v}_w]^T \tag{4.77}$$

then

$$\boldsymbol{C} = \boldsymbol{R}^{-1}[0, 0, \frac{\bar{U}'_w}{\bar{\omega}^2}\hat{v}_w - \frac{1}{\bar{\alpha}\bar{\omega}}\hat{v}'_w, \frac{i}{\bar{\omega}}\hat{v}_w]^T. \tag{4.78}$$

The wall response for a given set of wall parameters is shown in Figures 4.11 and 4.12 for two different Reynolds numbers, $R_{\delta^*} = 3000$ and 5000, where the greatest growth rate reduction is achieved at $R_{\delta^*} = 5000$. The results explain in part the differences observed in the calculated growth rates for the two cases since at $R^*_\delta = 5000$ both horizontal and vertical wall displacement occurs throughout the whole depth of the layer but at $R_{\delta^*} = 3000$ the disturbance effects do not penetrate right down to the base. Overall, the displacements are greater in magnitude at $R^*_\delta = 5000$ with in both cases the main horizontal motion being confined to the upper third of the wall and the maximum vertical displacement amplitude occurring at the surface.

A comparison of wall eigenfunctions for different depths is given in Figure 4.13 at a Reynolds number of 5000. Of particular note here is the remarkable similarity in form of the displacements for the two walls with $\bar{d} = 3.6$ and $\bar{d} = 5.4$. Both vertical and horizontal displacements are almost identical in feature and the corresponding growth rate results for these two cases were also very similar. This provides evidence for the conclusion that disturbances are only able to penetrate to a certain depth and beyond this any increases in wall thickness serve no beneficial purpose. Walls of smaller depth are seen to be affected fully by the boundary layer disturbances with the result of horizontal and vertical displacements throughout the complete wall layer.

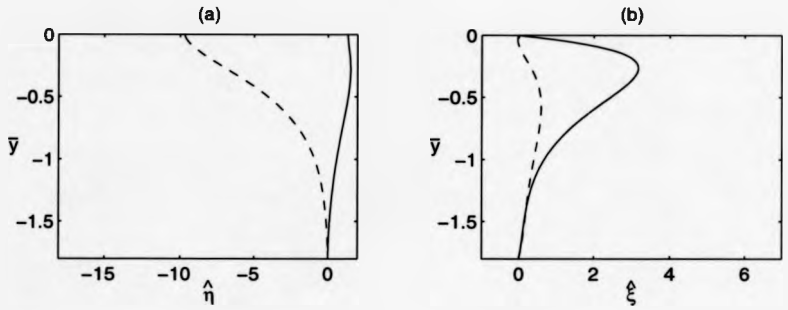

Figure 4.11: Wall eigenfunctions for compliant wall (1) of Figure 4.5 at position of maximum growth rate and $R_{\delta^*} = 3000$. (a) Vertical displacement $\hat{\eta}$, (b) Horizontal displacement $\hat{\xi}$. Real part : —, Imaginary part : - -.

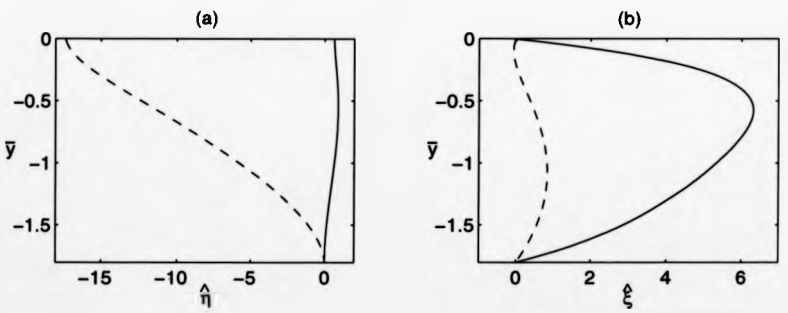

Figure 4.12: Wall eigenfunctions for compliant wall (1) of Figure 4.5 at position of maximum growth rate and $R_{\delta^*} = 5000$. (a) Vertical displacement $\hat{\eta}$, (b) Horizontal displacement $\hat{\xi}$. Real part : —, Imaginary part : - -.

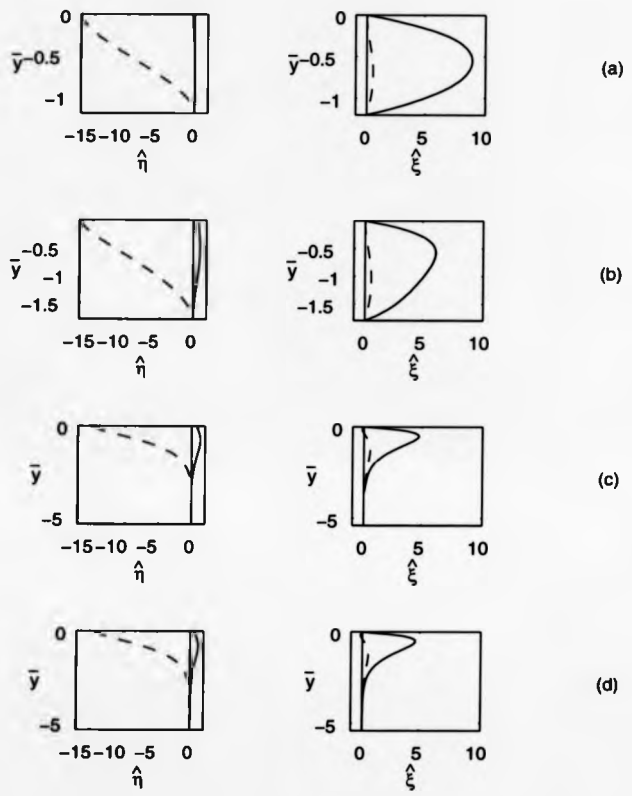

Figure 4.13: Wall displacements for walls of different depths. Vertical displacement $\bar{\eta}$, horizontal displacement $\bar{\xi}$. (a) : $\bar{d} = 1.2$, (b) : $\bar{d} = 1.8$, (c) $\bar{d} = 3.6$, (d) $\bar{d} = 5.$. For other wall parameters refer to caption of Figure 4.7. Real part : —, Imaginary part : - -.

4.14 Energy Balance Equation.

A consideration of the various energy distributions associated with the spatial growth or decay of disturbances now follows along with an energy balance equation for two-dimensional disturbances. This sort of energy balance not only indicates the relative influences of the various energy transfer mechanisms affecting the destabilisation of fluid disturbances within the boundary layer but also serves as another method of checking the accuracy of the calculation through the numerical values obtained.

The energy balance equation is obtained by firstly taking the u-momentum equation and multiplying by the perturbation velocity, u. The result is then added to the product of velocity component v and the v-momentum equation. Assuming the fluid incompressibility condition, $\nabla \cdot \boldsymbol{u} = 0$, the following equation is obtained.

$$\left(\frac{\partial}{\partial t} + U\frac{\partial}{\partial x}\right)\left(\frac{1}{2}\rho(u^2+v^2)\right) + \rho uvU' + \frac{\partial(up)}{\partial x} + \frac{\partial(vp)}{\partial y} = \frac{\partial}{\partial x_i}(u_j\sigma_{ij}) - \sigma_{ij}\frac{\partial u_j}{\partial x_i} \quad (4.79)$$

where σ_{ij}, $i,j = 1,2$ are the viscous stress terms. (The usual convention is applicable here where repeated indices indicate summation.)

For time periodic disturbances the time derivative can be removed by averaging over one time period and if in addition integration is performed across the boundary layer then the following equation is obtained where overbars indicate a time-averaged quantity.

$$\frac{d}{dx}\left[\rho\int_0^\infty U(\overline{u^2}+\overline{v^2})\,dy + \int_0^\infty \overline{up}\,dy - \int_0^\infty (\overline{u\sigma_{11}} + \overline{v\sigma_{12}})\,dy\right] =$$
$$\rho\int_0^\infty (-\overline{uv})U'\,dy - \int_0^\infty \overline{\sigma_{ij}\frac{\partial u_j}{\partial x_i}}\,dy + \overline{v_w p_w} - \overline{u_w(\sigma_{21})_w} - \overline{v_w(\sigma_{22})_w} \quad (4.80)$$

In the time-average procedure $\overline{uv} = u^*v + uv^*$, where superscript $*$ indicates the complex conjugate.

The first term on the left hand side of Eq.(4.80) represents the average disturbance energy convected by the mean flow past a specified point, whilst the second term is a measure of the work done by the disturbances against the perturbation pressure across some arbitrary boundary in the fluid at a given location. Similarly the final two terms represent the work done by the disturbances against the viscous stresses generated with respect to the same internal boundary. In a similar study of energy contributions, but associated with the spatial instability of jets, Morris (1976) neglects the last two terms, assuming that their

contribution is negligible, and describes the left hand side as the streamwise derivative of the integrated mechanical energy flux.

Terms on the right hand side of the equation are identified using descriptions more appropriate to the temporal formulation but still retain meaning within the spatial context. The first integral is the Reynolds stress production term but with temporal averaging of the terms involved. This is a measure of the energy transfer to the disturbances from the mean flow and is the principal mechanism responsible for the growth of the Tollmien-Schlichting instability. The second integral is identified as the viscous dissipation or energy removal mechanism. The remaining, non-integral terms, are zero for rigid wall boundaries owing to the wall velocity constraints and thus the two right hand side integrals give the relative energy production and removal contributions. Destabilisation occurs when there is sufficient energy production by positive Reynolds stress to outweigh the viscous dissipation. The remaining terms are generally non-zero for a compliant wall when boundary conditions no longer require zero velocity at the wall.

The term $\overline{v_w p_w}$ is a measure of the work done by the perturbation pressure on the boundary. A negative value represents a transfer of energy from the fluid to the wall and has a stabilising influence on the flow in this case. The remaining terms indicate work done by fluctuations in viscous shear and normal stresses on the boundary.

Returning to the energy balance equation integrals are normalised by the so-called integrated mechanical energy flux so that Eq.(4.80) becomes

$$-2\alpha_i = \rho \int_0^\infty (-\overline{uv})U'\,dy - \int_0^\infty \overline{\sigma_{ij}\frac{\partial u_j}{\partial x_i}}\,dy + \overline{v_w p_w} - \overline{u_w(\sigma_{21})_w} - \overline{v_w(\sigma_{22})_w}. \qquad (4.81)$$

Before evaluation of the components numerically attention is brought to the distributions of the constituent terms across the boundary layer. Figure 4.14(a) compares the Reynolds stress distributions for a rigid wall and the optimum compliant wall at frequencies which give maximum spatial growth rate in both cases. Observations indicate that there is in fact a positive increase in Reynolds stress value in the neighbourhood of the wall when the compliant boundary is introduced which arises as a result of the modification to the wall boundary conditions. It is often thought that the stabilising effect of wall compliance occurs through reductions in the Reynolds stress production term but observations in the wall region would appear to go against this. The Reynolds stress term is, however, reduced across the main body of the boundary layer which suggests that the influence of wall compliance goes far beyond simple modification at the wall.

An additional peak in the Reynolds stress distribution is also seen for the compliant

wall. The main peak in the Reynolds stress distribution occurs as a result of the jump in Reynolds stress in the neighbourhood of the critical layer (Yeo, 1988) but this secondary peak near the wall is more likely to be an artifact of the wall/flow interaction.

The viscous dissipation (or energy removal mechanism which occurs in the rigid wall problem) is seen to decrease when wall compliance is introduced and when other energy transfer mechanisms/energy removal processes become possible as shown in Figure 4.14(b).

If P is defined such that

$$\int_0^\infty P d\bar{y} = \overline{v_w p_w}$$

then the distribution of P across the boundary layer shown in Figure 4.15 indicates a significant lowering in value in the wall region and a general reduction in magnitude across the boundary layer. When integration over the boundary layer is performed a non-zero value for $\overline{v_w p_w}$ is obtained unlike in the rigid wall case. This indicates that positive work is done on the wall with removal of energy from the flow.

Figure 4.16(a) compares the numerical values for the integrated terms appearing in the energy balance equation. Both sides of the energy equation were found to agree numerically to at least three significant figures further validating the accuracy of the computational code. As can be seen there is a net reduction in the Reynolds stress production term and also in the energy removal due to the conventional viscous dissipation for the compliant wall boundary configuration. This reduction in viscous dissipation is compensated for by further energy removal terms present for the compliant wall case. Contributions due to $\overline{v_w(\sigma_{22})_w}$ were found to be negligible owing to the small value of the viscous stress term, $(\sigma_{22})_w$.

A similar study for the Blasius profile at the same Reynolds number and for conditions which also give maximum growth rate was carried out in order to verify whether wall compliance had the same overall effect on the energy transfer mechanisms for the different type of rigid wall instability which occurs for the two different boundary layer profiles. Figure 4.16(b) shows the relevant energy terms and overall the trends are similar for the Blasius case. The only exception is a proportionately lower value for the pressure work term in the Blasius case which would indicate that less transfer of energy from the flow to the wall occurs due to work done by the perturbation pressure. For the Falkner-Skan profile this pressure work term actually exceeds the energy removal due to conventional viscous dissipation for the rigid wall whereas for the Blasius profile the corresponding term is just a fraction of the viscous dissipation contribution and this remains the major mechanism for energy removal. The energy scales for the two boundary layer profiles in Figures 4.16(a) and (b) are indicative of the relative strengths of the two instability mechanisms.

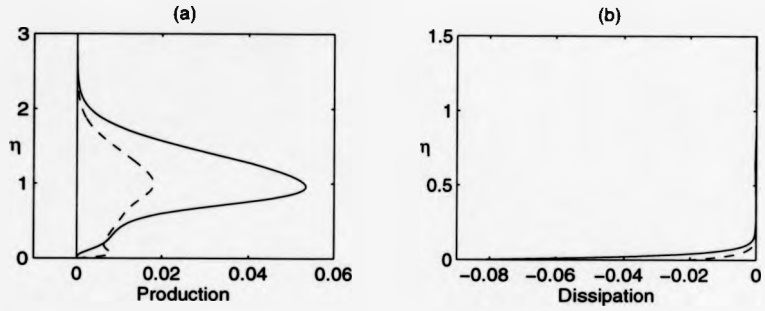

Figure 4.14: Reynolds stress (a) and viscous dissipation (b) distributions for rigid wall :— and compliant wall (1) : - - of Figure 4.5. η is the scaled $\bar{y}$ coordinate. $R_{\delta^*} = 5000$ in each case and eigenvalues correspond to positions of maximum growth rate.

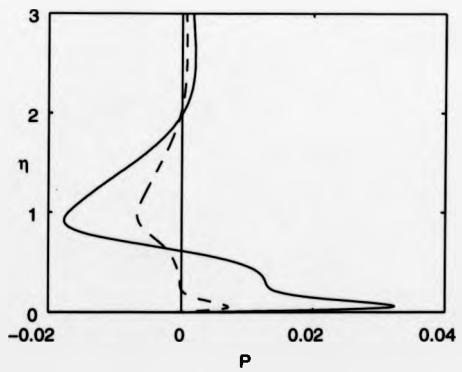

Figure 4.15: Pressure work distribution where $\int_0^\infty P d\bar{y} = \overline{v_w p_w}$. Rigid wall : —, compliant wall : - -. Wall conditions are as in Figure 4.14.

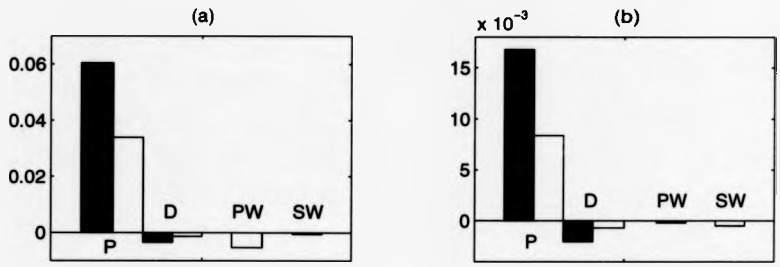

Figure 4.16: Comparison of numerical values between rigid and compliant wall contributions to terms in the energy balance equation for (a) Falkner-Skan profile and (b) Blasius profile at $R_{\delta^*} = 5000$. Shaded regions represent the rigid wall contributions. P : Reynolds stress production term, D : viscous dissipation, PW : work done by perturbation pressure on the wall, SW : work done by viscous stresses on the wall. Eigenvalues corresponding to positions of maximum growth rate are (a) $\bar{\omega} = 0.125$. Rigid wall: $\bar{\alpha} = 0.3528 - 0.04689i$. Compliant wall : $\bar{\alpha} = 0.2992 - 0.02209i$, (b) Rigid wall : $\bar{\omega} = 0.046, \bar{\alpha} = 0.1771 - 0.012698i$. Compliant wall : $\bar{\omega} = 0.034, \bar{\alpha} = 0.1186 - 0.006485i$.

The results showing the effect of wall compliance on the constituent terms of the energy balance equation suggest that wall compliance has the same physical influence on the energy mechanisms for the inviscid, inflexion point instability as it does on the T-S instability.

4.15 Summary.

A more realistic wall model has been used in conjunction with the introduction of viscous effects into the stability analysis of the inviscid Rayleigh instability.

Wall parameters for a series of double-layer viscoelastic walls previously tailored to give optimum performance for zero pressure gradient flow were used in this adverse pressure gradient flow where the optimum level of wall compliance was assumed at the onset of the pressure gradient. A series of changes to the wall parameters indicated that upper layer stiffness and substrate depth had significant effects on growth rate reduction and a substantial stabilisation was found in particular cases. Wall eigenfunctions show that the greatest reductions in amplification rate were achieved when the boundary layer disturbance effect was felt throughout the full depth of the layer.

An energy balance analysis shows the drop in growth rate is brought about by a reduction in energy production by the Reynolds stress and increased energy dissipation through work done by the fluctuating pressure on the wall.

All the numerical calculations were carried out at $R_\delta^* = 5000$ which was the Reynolds number at which these walls gave best performance. It could be argued that the reduced growth rates are still higher than the rigid wall Tollmien-Schlichting instability and therefore using wall compliance as a possible means of transition delay where this inviscid instability dominates appears pessimistic. This work is, however, not intended to suggest that these particular walls could be used to obtain substantial transition delay but the results do indicate the potential for doing so. It has been demonstrated how optimal parameters vary for zero and adverse pressure gradient flows and a more rigorous investigation into wall structure and specific tailoring of wall parameters would surely reveal that transition delay due to the suppression of the inviscid instability is possible through the use of wall compliance.

CHAPTER 5

INSTABILITIES IN THE ROTATING DISC BOUNDARY LAYER.

5.1 Three-dimensional Instability.

Some subtle differences arise in the linear stability analysis of three-dimensional disturbances in comparison with the two-dimensional case. The general form of the three-dimensional disturbance in cartesian coordinates can be written

$$\boldsymbol{F}(x,y,z,t) = \tilde{\boldsymbol{F}}(z)\exp\{i(\alpha x + \beta y - \omega t)\} + \text{c.c.}$$

where α and β are wavenumbers in the x and y directions respectively and ω is the disturbance frequency.

For a temporal approach to the problem both α and β are taken to be real and the frequency becomes the complex eigenvalue, $\omega_r + i\omega_i$, to be determined and in general the eigenvalue problem takes the form

$$\mathcal{F}(\omega,\alpha,\beta) = 0$$

where $\mathcal{F}$ is a complex relation. Two equations can thus be obtained (from the real and imaginary parts of $\mathcal{F}$) which are solved in order to obtain ω_r and ω_i.

The spatial approach to stability problems is, however, often the most appropriate physical interpretation and in this case the frequency is specified and real. The wavenumbers, α and β, are then the complex unknowns but the eigenvalue relation still only provides two equations. Two more conditions are therefore required in order to establish the values of the four unknowns $\alpha_r, \alpha_i, \beta_r$ and β_i; but there is a certain degree of ambiguity as to how to specify the problem fully and assumptions are generally made about the value of β. There are two options to consider for the direction of disturbance growth which put constraints on the value of β_i as outlined by Mack (1985). One choice is to take the direction of growth to be the same as the direction of the group velocity and the second, more favoured, alternative is to examine an axisymmetric distribution for the normal modes so that $\beta_i = 0$. If considering a single normal mode disturbances thus grow in the streamwise direction. Physically,

however, the superposition of such a spectrum of normal modes can produce an effective non-zero imaginary part for β.

The calculation of temporal eigenvalues would appear to be the simplest approach to the problem, and free from any assumptions on the form of the normal modes, but in order to interpret the results in a physical sense some form of group velocity transformation is required. This then poses the question of what is the most proper three-dimensional analogue to the two-dimensional Gaster (1962) transformation. In the subsequent review of previous work on instability in the rotating disc boundary layer the majority of work considers spatially developing disturbances with $\beta_i = 0$.

A number of vector quantities arise in this type of three-dimensional stability problem and are outlined below.

$$\text{Magnitude of wavenumber vector} : \lambda = \sqrt{\alpha_r^2 + \beta_r^2}$$
$$\text{Propagation direction of disturbances} : \varepsilon = \tan^{-1}\left(\frac{\beta_r}{\alpha_r}\right)$$

$$\text{Magnitude of growth rate} : \sigma = \sqrt{\alpha_i^2 + \beta_i^2}$$
$$\text{Growth rate direction} : \varepsilon_\sigma = \tan^{-1}\left(\frac{\beta_i}{\alpha_i}\right)$$

$$\text{Magnitude of group velocity vector} : c_g = \sqrt{\left(\frac{\partial\omega}{\partial\alpha}\right)_r^2 + \left(\frac{\partial\omega}{\partial\beta}\right)_r^2}$$
$$\text{Group velocity angle} : \varepsilon_{cg} = \tan^{-1}\left(\left(\frac{\partial\beta}{\partial\alpha}\right)_r\right)$$

All directions in the case of the rotating disc are taken to be relative to the radial direction and ordinarily $\varepsilon, \varepsilon_\sigma$ and ε_{cg} are distinct from each other.

5.2 Review of Work on the Rotating Disc.

The earliest experimental studies concerning transition on the rotating disc were undertaken by Smith (1946) who found sinusoidal disturbances and measured approximately 32 oscillations per disc revolution and these were found to propagate at angles near to 14° to the radial direction. The flow visualisation study of Gregory *et al.* (1956) discussed previously revealed stationary vortices numbering 28 to 32 with the spiral angle varying between 11° and 14°. These were found to occur from a Reynolds number, R, of 430 up to a transitional radius defined by $R = 530$, where the Reynolds number is expressed in terms of local dimensional radius, rotation speed of the disc and the kinematic viscosity of the fluid. This definition is largely consistent throughout the literature. The theoretical results of Stuart presented simultaneously in this paper (Gregory *et al.*, 1956) are based on a transformation which allows the three-dimensional problem to be reduced to a two-dimensional one. Stuart worked with a local cartesian coordinate system obtained from resolving the two coordinates in the plane of the disc through an angle ε and two-dimensional mean flow profiles were thus formed from a combination of radial and tangential velocity components. This provided a continuous set of profiles with each constituent member corresponding to a different direction; $\varepsilon = 0$ giving the purely radial profile and $\varepsilon = \pi/2$ the purely azimuthal profile. As ε increases the point of inflexion of the combined profile moves to smaller values of the distance normal to the disc surface passing through zero at $\varepsilon \approx 13°$ and Stuart, using a purely inviscid analysis, proposed the existence of this particular critical profile which would produce a disturbance with zero phase velocity and used this as an explanation for the presence of the stationary vortices. This was a direct application of the theorem of Tollmien (1935) concerning the generation of neutral disturbances with phase velocities equal to the value of the mean flow at a point of inflexion. Stuart had success with this inviscid theory in predicting the wave angle to be 13.3° in good agreement with the stationary vortex spiral angles observed experimentally but calculation of the corresponding wavenumber using this inviscid theory gave the number of vortices to be between 113 and 140. This was about three times the number in the experiment and demonstrated the influence of viscosity on the disturbance wavenumber. The streamline pattern associated with the disturbances was also obtained using the inviscid calculation and indicated a "cat's eye" type of structure comprising two rows of co-rotating vortices; a type of vortex structure thought to be typical of all three-dimensional crossflow instabilities. Streaks in flow visualisations were found to occur underneath the wall vortices in this case and the interpretation was that each streak corresponds to one disturbance wavelength. This is in contrast to the single layer of counter rotating Görtler vortices associated with flows over concave walls where flow visualisation

streaks occur between vortex pairs.

Yamashita and Takematsu (1974) argued that although Stuart's prediction of the wave angle was in the region of that observed experimentally the stationary vortex pattern was more likely to arise from the presence of a dominant non-propagating mode with large amplitude rather than a neutral mode. This study extended the work of Stuart and considered a number of profiles in directions near to the experimentally observed propagation angles in both inviscid and viscous calculations. The eigenvalue problems were solved numerically to obtain complex phase speeds as a function of the disturbance wavenumber and it was found that each profile was able to generate two modes of disturbance with zero phase velocity and that those with the lower wavenumber were associated with high growth rates. In solving the Orr-Sommerfeld equation, with ε slightly less than Stuart's critical value, it was shown that there exists a wavenumber close to the experimental value which generates disturbances of zero phase speed and maximum growth rate. It was surmised that this profile is more likely to be ultimately responsible for the formation of the stationary vortices.

Many experimental investigations set out to establish critical and transitional Reynolds numbers, denoted R_c and R_T. Kobayashi *et al.* (1980) and Malik *et al.* (1981) both used hot wire techniques to establish values for R_c at 297 and 294 respectively for stationary vortices oriented at 14°. This is in contrast to the early predictions using flow visualisation where the stationary vortex pattern was first observed at values in the vicinity of $R = 400$. In fact, values as far apart as 280 and 530 at this angle have been reported. The discrepancies are generally put down to the varying accuracy in the different detection techniques and physical differencies in the disc itself such as the quality of the disc surface. The experimental results of Fedorov *et al.* (1976) revealed evidence of stationary vortices spiraling at an angle of 20° in addition to the generally accepted stationary vortices at 14°. Naphthalene sublimation and acoustic techniques were used to observe 14-16 vortices propagating at the larger angle and these were found to occur at the lower Reynolds number range of 182-242. No previous evidence of such vortices had been found and no explanation for their occurrence was made.

As far as transition prediction is concerned values in the range 500-560 have been determined. In the experiments of Wilkinson and Malik (1983, 1985) disturbances were excited by the use of a single roughness element on the disc surface. Ensemble averages of hot wire measured fluctuations in the radial component of velocity were normalised and the resulting phase plot suggested that steady wave patterns emanate from point sources on the surface. These wave patterns were shown to spread out circumferentially from the source and merge to generate the structures seen in flow visualisations. The measurements were compared

to those for a clean disc and the patterns which formed were found to be accentuated by the artificial roughness element. The subsequent theoretical work of Mack (1985) verified that normal modes of zero frequency across the whole azimuthal wavenumber spectrum combine to form the wave patterns. Mack assumed uniform initial disturbance amplitude and phase and obtained the resulting azimuthal distribution at a number of radii. These distributions were obtained from the integration of contributions to the complex amplitude over all azimuthal wavenumbers. The constant phase lines mapped out on the disc were shown to generate the same form of spiral wave pattern as that obtained from the experimental measurements of Wilkinson and Malik. Close agreement with other experimental results was also obtained. Mack concluded that the streaks in flow visualisations represent constant phase lines of several merged wave packets generated by an arbitrary number of small roughness elements on the disc surface. Amplification rates measured by Wilkinson and Malik indicated a value of $N = 9$ at breakdown to turbulence. Transitional Reynolds numbers of 521-530 were documented for the disc with the roughness element and 543-556 for a clean disc. No growth of vortices was observed below $R = 300$.

Early theoretical predictions of the critical Reynolds number for stationary disturbances failed to agree with existing experimental values. Brown (1959, 1961) and Cebeci and Stewartson (1980) both used linear stability theory and solved the Orr-Sommerfeld equation to obtain values of $R_c = 178, 176$ using temporal and spatial stability formulations respectively. Justification of the use of linear stability analyses for this flow configuration was made by appealing to the experimental results of Kitamura (1973) where circumferential velocity fluctuations were measured using hot wire techniques and a linear region of experimental growth was found for $R = 430$-490. The low values for R_c calculated theoretically were thus adjudged not to be largely due to the misuse of any linear stability analysis. Cebeci and Stewartson also performed e^N calculations and found the N-factor at transition, using a transitional Reynolds number of 510, to be approximately 20, a value far higher than that found experimentally so it was clear that the Orr-Sommerfeld equation did not account for all the factors influencing the stability characteristics of this problem.

Malik *et al.* (1981) were able subsequently to account for the large discrepancies between experimental and theoretical predictions for the onset of stationary vortices. Earlier work on the stability of the Ekman boundary layer by Lilley (1966) had indicated that the inclusion of Coriolis effects had a strongly stabilising influence. Malik *et al.* incorporated streamline curvature effects as well as Coriolis acceleration terms in the stability analysis to obtain a sixth order system of governing equations. This system is composed of two coupled equations in terms of the normal perturbation velocity and a variable proportional to the

normal component of perturbation vorticity. Neglecting the additional effects decouples the equations and the stability problem then reduces to that given by the Orr-Sommerfeld equation. In solving the relevant eigenvalue problems both of the additional terms were found to have a stabilising effect in terms of the Reynolds number at which the instability was found to first set in. Temporal eigenvalues from the resulting eigenvalue problem were obtained using a global Chebyshev spectral scheme and then converted to spatial eigenvalues using the group velocity transformation of Gaster (1962). This predicted a value of $R_c = 287$ in excellent agreement with experimental values. In an independent study Kobayashi *et al.* (1980) included streamline curvature terms only and using temporal analysis found R_c to be 261. Malik *et al.* also conducted N-factor calculations to obtain a value of $N = 10.7$, based on a transitional Reynolds number of 513, which correlates more reasonably with N-factors at transition for two-dimensional flows. If Coriolis and streamline curvature effects were neglected the envelope method predicted a value of N$\approx$20 which gave conclusive support for the need to include Coriolis effects and to account for streamline curvature in the theoretical analysis. At the end of this study a brief mention was made of the occurrence of a non-stationary unstable mode at $R = 50$ but this observation was not enlarged upon further.

Theoretical studies after Malik *et al.* (1981) invariably use the sixth order system of equations which have been solved by a number of different numerical procedures. Mack (1985) used a fixed step-size, fourth-order, Runge-Kutta integration scheme and a Newton-Raphson local search technique to solve these equations. Temporal and spatial calculations for zero frequency normal modes revealed in both cases two families of eigensolutions at $R = 400$ where in each formulation the second family was found to be completely stable. In the temporal case family 1 was subdivided into two branches, the first of which contained both amplified and damped modes, whereas the second sub-branch was formed only from stable modes. In a rare mention of group velocity Mack found the group velocity vector to be oriented at angles of 10-15° to the azimuthal direction. Despite the large discrepancies in numerical value for the critical Reynolds number Cebeci and Stewartson also found group velocities to be aligned close to the azimuthal direction. In the spatial calculation a previously unfound third branch of solutions with apparently large growth rates was reported on by Mack. The associated group velocity vectors for these modes were, however, directed inwards and since the group velocity is associated with the propagation of disturbance kinetic energy they were adjudged to be strongly stable. No temporal counterparts to these waves were found to exist.

Malik (1986a) computes the neutral curve for stationary disturbances up to $R = 10^7$ using a compact fourth-order finite difference scheme with local iteration. A minimum critical Reynolds number of $R_c = 285.36$ was calculated with the other critical parameters

being $\alpha_c = 0.38482$, $\beta_c = 0.07759$, $\varepsilon_c = 11.4°$, where α and β are radial and azimuthal wavenumbers respectively. Upper branch values were found to asymptote towards Stuart's inviscid solution. This study also revealed a second minima in the neutral curve occurring at values of $R = 440.88$, $\alpha = 0.13228$, $\beta = 0.04672$ and $\varepsilon = 19.45°$. It was noted at the time that this wavenumber and angle seemed to correspond in some way to the anomalous results of Fedorov *et al.* but the Reynolds number was at variance. Solutions associated with this second minimum also matched in type the second family of eigensolutions identified by Mack. This second family of solutions was, however, found only to occur when the effects of Coriolis acceleration and streamline curvature were included and Malik found these lower branch solutions followed the direction of zero mean wall shear stress. In this paper velocity-vector plots were presented indicating the stationary vortex structures which were formed from the combination of relevant mean flow profiles and eigensolutions. Two cases were considered, the first being the upper branch neutral solution at $R = 285.36$ and the second a lower branch mode at the higher Reynolds number of $R = 15000$. In both cases only one set of vortices was formed from the calculations contrary to the earlier prediction of Stuart. Bearing in mind Stuart's inviscid calculation it was suggested that the inclusion of viscosity could be masking the second, near wall, row of vortices. The structure of the vortex pattern on each branch differed in a number of ways. For the upper branch the vortex centres were located at approximately 36% of the way into the boundary layer whereas in the lower branch case the wavelength of the disturbance was much longer and the centres of the vortices were located much nearer the wall at approximately 14% of the boundary layer thickness. It was noted that as R increased along the lower branch these centres migrated towards the wall but along the upper branch the opposite was true.

Some insight into the nature of this second branch of unstable modes can possibly be gained from preceding research on the Ekman layer. A similar second family of eigensolutions was found by Lilley (1966) when investigating the influence of Coriolis acceleration on the theoretical stability characteristics of the Ekman boundary layer. Lilley compared neutral curves obtained from solution of the Orr-Sommerfeld equation with those from an extended set of equations which included Coriolis effects. Changes in the shape of these curves suggested the presence of a separate instability mechanism dependent on Coriolis effects and viscosity. This hypothesis was verified to some extent by a simplified analytical approach to the problem where using various assumptions Lilley demonstrated that energy could be extracted from the mean flow component parallel to the disturbance bands. Disturbance growth from this energy was found to be reliant on the Coriolis terms which are of comparable magnitude to the viscous terms. As a result of this finding Lilley termed this

new instability *parallel instability* and also suggested it was essentially a viscous instability since it was found to vanish at large Reynolds number. Characteristic features associated with this mode were higher phase speeds and orientation at negative angles. Interestingly it was shown that for such negative angles the point of inflexion in the mean flow profile corresponding to this direction was less prominent and so it would be expected that the parallel instability might dominate the inviscid instability in this region.

Earlier experiments by Faller (1963) and Faller and Kaylor (1966) had already detected two separate unstable modes in the Ekman layer using dye flow visualisation. Faller termed disturbances analogous to those of Gregory *et al.* for the rotating disc Type 1 and a more rapidly moving disturbance which was reported to arise more sporadically and had wavelengths two to three times that of the Type 1 was referred to as Type 2. Techniques which favoured the detection of stationary disturbances had been able to establish a critical Reynolds number of $R_c = 130$ for the Type 1 disturbance. Later Tatro and Mollö-Christensen (1967) using the hot wire anemometry technique, with a relatively fast response and greater sensitivity than flow visualisation techniques, were able to detect the more rapidly travelling, small wavenumber disturbances. Wave traces from the hot wire measurements showed a relatively uniform periodic signal at $R = 126$ but as the Reynolds number increased to $R = 130$ the character of the signal was shown to change where modulation of the waveform gave evidence for the existence of two modes of instability at this Reynolds number. Within this study the Type 2 mode was always detected before any Type 1 mode. Unlike the Type 1 disturbance which remained within the boundary layer this Type 2 instability was found to persist beyond the boundary layer edge at higher Reynolds numbers.

The observation of Type 2 vortices with non-zero phase speeds in the Ekman and rotating disc boundary layers (Faller 1963, Fedorov *et al.* 1976) leads to speculation on the role of travelling disturbances and the Type 2 mode in the transition process.

The early theoretical calculations by Cebeci and Stewartson (1980), although subsequently shown not to be accurate in numerical value, did indicate that waves with negative phase speeds were the most amplified. Malik *et al.* (1981) also found this to be true for the full system of governing stability equations. These disturbances were for a long time rejected as playing a part in the natural transition process since they were considered to be effectively upstream propagating waves and unlikely to affect transition at higher Reynolds numbers or at radii downstream of their origin. Mack (1985), however, computed the maximum amplification rate as a function of frequency at $R = 400$ with negative frequencies taken to represent disturbances with inwardly directed phase speeds and positive frequen-

cies for those directed outwards. Maximum amplification rate was found to occur at a non-dimensional frequency of -8, where the frequency was referenced to the disc rotation speed, with the unstable frequency range extending from -25 to 20. It is notable that the corresponding group velocity vectors were found to be directed outwards in all cases indicating the outward transference of disturbance energy whatever the direction of the phase speed. With this evidence it would be unwise to totally discount the effect of these non-stationary disturbances on the breakdown of laminar flow. Mack reiterated the point that the theoretical wave pattern calculation described earlier demonstrates that the steady spiral patterns observed experimentally are directly related to stationary modes but these are most certainly not the most amplified disturbances to occur in the rotating disc boundary layer.

The first experimental evidence of travelling waves with higher amplification rates than the stationary case appears to have been demonstrated by Jarre *et al.* (1991). In this experimental investigation the disc was enclosed in a circular container of water designed to maintain the axisymmetry of the system. Fluctuations in the azimuthal velocity component were obtained using a single constant-temperature hot-film anemometer. Measurements were obtained at twenty different radial positions in the Reynolds number range $245 < R < 550$ and for each value of R Fourier power spectra were calculated from digitised data. Analysing the development of the averaged spectra with Reynolds number gave some evidence for the presence of a travelling disturbance.

Theoretically, Balakumar and Malik (1990) extended the previous work of Malik (1986a) to consider travelling disturbances. The same two-point, fourth-order compact scheme was used as in the previous paper to obtain numerical solutions to the eigenvalue problem. This more recent study leaves the governing equations in terms of primitive variables allowing direct calculation of the perturbation pressure and velocity components. This leads to slightly different, but not significant, changes in the values of the critical parameters. (R_c = 286.1, α_c = 0.38643, β_c = 0.07781, ε_c = 11.38° for the Type 1 mode and R = 451.4, α = 0.13109, β = 0.04641, ε = 19.5° for the Type 2 stationary mode.) The variance in results with previous calculations was put down to the different formulation of the problem. Neutral curves for a series of non-dimensional frequencies were presented with the definition of disturbance frequency redefined by scaling with respect to the Reynolds number such that $\omega = \bar{\omega}R$ where $\bar{\omega}$ is the frequency used formerly. Values of ω = -5.0, 0.0, 4.0, 7.9 and 10.0 were used and the characteristic shape of the neutral curve is shown to change markedly with frequency. For the negative frequency only one minimum is in evidence whereas increasing the frequency in the positive direction sees the second minimum become more pronounced and there evolves a clear demarcation between the two modes. Critical

values for the inviscid, Type 1 mode were established at $R = 283.6, \omega = -2.9, \alpha = 0.36661, \beta = 0.09379$ and $\varepsilon = 14.35°$; whilst the Type 2 disturbance was found to become unstable at the much lower Reynolds number of $R = 64.46$ at a frequency of $\omega = 7.9$ with $\alpha = 0.28027, \beta = -0.10594$ and $\varepsilon = -20.7°$. At all frequencies the upper branch wave angles tended to overlap and converge to the stationary value as the Reynolds number increased ($\varepsilon \approx 8°$). The lower branch neutral solutions, however, covered a wide range of angles. At the extremes the zero frequency waves tended to $\varepsilon = 25.86°$ whilst for $\omega = 7.9$ the corresponding angle was $-35.34°$. Increasing the frequency above $\omega = 7.9$ increased the value of this angle and it was inferred that there actually exists a minimum wave angle below which disturbances of all frequencies are stable. Some correlation between this minimum angle ($-35.34°$) and the angle of maximum mean wall shear ($-50.4°$) is made for the orientation of high frequency waves. The behaviour of the neutral curve wavenumber with increasing Reynolds number is also assessed. It is found that for frequencies up to $\omega = 4.0$ α behaves like $R^{-\frac{1}{2}}$ as is the case for stationary modes but for higher frequencies α first follows a path of R^{-1} and then begins to asymptote along the same line as the zero frequency disturbances. The point at which the behaviour changes moves to larger values of R with increasing frequency. Balakumar and Malik then speculate as to whether non-parallel effects would be of increased significance in the regions where α follows R^{-1} when both α and the mean flow vary on the same scale and variations in the mean flow may be important. Eigenfunctions calculated as part of this investigation are shown for stationary and $\omega = 7.9$ disturbances at $R = 4000$ along the lower branch. The structure of the two solutions indicates that the high frequency disturbance extends throughout the whole of the boundary layer whereas that associated with the stationary mode is restricted to the near wall region. Of particular significance is the difference in the value of the perturbation pressure. In both cases the pressure is approximately constant throughout the boundary layer but that for the stationary mode is near fifty times that for the travelling mode (where the stationary case corresponds to a Type 1 mode and the travelling case a Type 2 mode). In this respect the perturbation pressure is barely a significant feature for this Type 2 travelling disturbance. Values at lower Reynolds numbers or for different frequencies are not presented so whether this is a general result for the Type 2 mode remains to be established. Analysis of the relative growth rates of the two modes reveals a more rapid growth associated with the inviscid Type 1 mode which would suggest that even though it is the viscous Type 2 mode which first becomes unstable the growth of the inviscid mode would be sufficiently greater than the former to dominate at higher Reynolds numbers. This provides some explanation for the difficulty in detecting the Type 2 mode at higher Reynolds numbers in experiments. Numerical results are also presented for a third branch of eigensolutions for zero frequency modes of the same

kind mentioned by Mack (1985). It is shown that all have very large negative values of α_i and no neutral points but again for the most part the orientation of the group velocity indicates a transference of energy in the inward direction.

Recently Lingwood (1995) has demonstrated theoretically that this third family of eigensolutions is able to coalesce with the Type 1 modes to produce an absolute instability and suggests that this may give rise to the onset of transition. The existence of this absolute instability has been confirmed by the numerical simulations of Davies and Carpenter (1995).

Some asymptotic studies of this flow problem have been made including the triple deck asymptotic methods used by Hall (1986) to study the inviscid type, stationary disturbances. Within this analysis non-parallel effects were included and Hall was able to find close agreement with the numerical results of Malik (1986a) at high Reynolds numbers. A second stationary structure was also found and referred to at the time as arising as a result of a balance between viscous and Coriolis forces, presumably a reference to the now termed Type 2 mode. Bassom and Gajjar (1988) analysed the nonstationary crossflow instability and established a finite wave angle range of $10.8 - 39.6°$ for the existence of neutral modes. At each end of this range of angles the solutions were found to develop different characteristics. At the higher angle, which corresponds to the angle of zero mean wall shear, the solutions resembled those of the viscous type found by Hall and were approximately stationary with respect to the disc. As the angle of $10.8°$ was approached the solutions were found to travel faster and take on the characteristics of the inviscid type of solution. In investigating the influence of nonlinearity the wave angle range could be extended from the lower limit, dependent on the wave amplitude, but the upper limit remained fixed. The Type 2 viscous mode was studied by MacKerrell (1987) using a weakly nonlinear asymptotic method which showed that subcritical instability can arise for the case of such stationary disturbances and hence early transition could be possible via this route. This lends some support to the previously unexplained experimental findings of Fedorov *et al.* (1976).

Faller (1991) has gone on to use existing knowledge about the Type 2 mode in a paper addressing its possible role in the transition process over the rotating disc. An energy analysis is presented and four different transition mechanisms proposed each of which depends on the initial amplitude of disturbances.

Faller and Kaylor (1966) during an experimental investigation found that the Type 2 mode was easily excited by external disturbances. The Type 1 instability was found to be the dominant mode in carefully controlled environments but the strength of the Type 2 mode increased with increased disturbance levels. In this recent numerical study Faller

(1991) uses a rather convoluted modification to Stuart's local coordinate system to obtain numerical stability results. The starting point for the formulation is the conversion of the problem posed in polar coordinates to a local rectangular system. In this process some terms arising as a result of the polar coordinate system are dropped; in particular the additional $(1/r)$ entry in the continuity equation. Once the system is rectangularised it is rotated about the vertical axis so that the new x-axis lies at an angle ε to the azimuthal direction. The stability problem is then formulated in terms of the x-components of perturbation velocity and vorticity, using a Poisson equation to relate the vorticity to a streamfunction in the $y - z$ plane. Faller assumed two-dimensional disturbances and used the temporal stability formulation of the problem. Eigenvalues were obtained by integrating the governing equations with respect to time until constant values of phase speed and growth rate of perturbation kinetic energy were obtained. It should be noted that a reference time of Ω^{-1} was used in this study, where Ω is the angular rotation speed of the disc, as opposed to the conventional use of $(\delta^*/U_{\text{ref}})$, with δ^* the local boundary layer displacement thickness and any comparison of growth rate values must take this into account. As in previous studies the linear growth of the Type 1 disturbance is found to be much more rapid than the more parabolic type of growth associated with the Type 2 mode. Enforcing other previous findings group velocity directions are calculated to lie in the range 6.4-8.5° with actual numerical values for the group speed averaging 0.5 for the inviscid type mode. The corresponding values for the Type 2 mode were typically higher than for the Type 1 instability. In the first documentation of energy budgets two kinetic energy equations are derived expressing the rate of change of kinetic energy with time. These energy equations are expressed in terms of the x-component of the kinetic energy (UK) and the so-called kinetic energy of the overturning cells (CK) where the sum of UK and CK gives the total kinetic energy. In general UK was found to be significantly higher than CK with the ratio of UK to CK of the order of 20. The energy equations themselves each contain an energy production term representing the removal of energy from the mean flow by the Reynolds stresses. Transfer of energy between UK and CK is shown to be possible through the Coriolis effects and the conventional energy removal mechanism by viscous dissipation is also present. In addition there are several terms included which Faller calls Rossby number terms and were related to the 'geometrical effects' arising from the change in Reynolds number with radius. Energy flow diagrams typical of the Type 1 and 2 instability are presented. In the case of Type 1 results indicate that the growth of this mode occurs through the Reynolds stress production mechanism which is numerically by far the most dominant term in the energy equation and that the Coriolis energy transfer is from CK to UK. Characteristic features for the Type 2 instability are the transference of Coriolis energy from UK to CK, opposite to that of the

Type 1, where the cells (CK) are now fed more via this route than by the relevant Reynolds stress production term.

Faller, based on the results of the linear growth rates, goes on to speculate on possible transition mechanisms but recognised that linear results alone are not sufficient to infer categorically any transition mechanisms, a situation where nonlinear effects are important. They can, however, indicate to some extent the relative importance of each mode in the process. Four different mechanisms (A-D) are thus proposed each depending on the relative initial amplitudes of the disturbances in the system.

Mechanism A corresponds to the presence of disturbances with strong initial amplitude ($A_o > 0.0051$) where several Type 2 modes grow and reach finite amplitude simultaneously. A spectrum of low-level turbulence is produced through the interaction of these modes which develops as the Reynolds number is increased further. When the disturbance amplitudes are moderately high ($0.0027 < A_o < 0.0051$) Mechanism B is thought to operate where the growth of a single, dominant, Type 2 mode is enough to suppress all other modes and a nonlinear interaction takes place with the mean flow. If the initial disturbance level lies at the lower end of this range then the mechanism can be modified by the production of a small-scale secondary instability which interacts rapidly with the Type 2 vortices producing turbulence. Faller suggests that if the initial disturbance level is low then the transition process will almost certainly involve the Type 1 mode rather than solely Type 2. For $0.001 < A_o < 0.0027$ Mechanism C is proposed and involves the interaction of the two primary modes which are expected to reach finite amplitude in the same Reynolds number range. Nonlinear interaction would then produce a full spectrum of turbulence. For very low disturbance levels ($0.00055 < A_o < 0.0001$) the growth of the Type 1 mode is likely to suppress the Type 2 mode and transition occurs through the interaction of the Type 1 mode and the mean flow. It is also suggested that the details of this route may involve secondary instabilities of the Type 1 mode. Mechanisms A-D correspond to transition at different Reynolds numbers with only the latter in the vicinity of the generally considered transitional Reynolds number of $R = 520$. Mechanism A, for example, is thought to operate at Reynolds numbers as low as $R = 300$. Faller concludes that early transition would be probable through excitation of the Type 2 mode if the flow was subject to random, high level, fluctuations and the actual physical mechanism would then be dependent on the relative level of excitation of this mode. As far as corroborating these proposed mechanisms is concerned Faller has undertaken an experiment where photographic/dye evidence indicates the appearance of a secondary instability, or 'ribs', occurring at Reynolds numbers of $R = 356$, 385 and 390 leading to a turbulent state at $R = 402$. The orientation of these ribs is found to vary between being almost normal to the Type 2 bands through to angles

close to those associated with the Type 1 instability and Faller uses this as a demonstration for the B route to transition. No documentary evidence for Mechanism C was available at the time of publication but cine film evidence is cited as being sufficient to indicate the reality of this transition route. Wilkinson and Malik (1985) found the presence of stationary, secondary instabilities, showing up in experimental measurements as high wavenumber fluctuations near the onset of transition, of the type proposed for Mechanism D. In order to elucidate further on this issue more detailed experiments and computational analysis aimed specifically at these conjectures would ideally be required.

Secondary stability analyses can provide a step towards filling in some of the details. As early as Clarkson *et al.* (1980) observations of secondary vortex phenomena had been observed experimentally using dye techniques in water prior to the breakdown of laminar flow. The experiments of Kobayashi *et al.* (1980) and Kohama (1984, 1987) in air also discovered some secondary vortex structures which appeared as ring-like co-rotating vortices on the surface of the primary stationary crossflow vortices. However, these were purely observational results and no theoretical work came forward until that of Balachandar *et al.* (1992). This was aimed at studying the secondary instability phenomenon numerically and used a Floquet type analysis to develop an eigenvalue problem which was solved using the Chebyshev collocation method. Attention concentrated on the secondary instabilities of the stationary primary crossflow vortices and increases in Reynolds number and primary amplitude were found to increase both the secondary growth rate and unstable wavenumber range. An approximately constant phase speed for this type of instability was also calculated. These secondary instabilities were found to have higher growth rates than those of the associated primary instability. Perhaps the most significant results from this study come from the verification of a description by Kohama (1984, 1987) of the physical form of this secondary structure. The fundamental structure was found to consist of a pair of long counter-rotating vortices which form over the saddle points of the primary vortices with the axes of the secondary type lying at about 44° to the primary crossflow vortices with the tendency to tilt up towards the edge of the boundary layer. Some unexplained or unusual behaviour found to occur was that primary disturbances with shorter wavelengths appear to be more susceptible to this secondary instability but from linear theory these are not the most unstable primary modes. Balachandar *et al.* conclude that if disturbance energy is concentrated in a small range of wavenumbers then it is anticipated that this form of secondary instability will play a significant role in the transition process.

Linear theory is sufficient in bringing out the dominant features of the stability problem

but more detailed aspects require the use of different techniques such as direct numerical simulations where within this approach nonlinear effects can be accommodated. Malik (1986b) performs a Navier-Stokes simulation using a Fourier-Chebyshev spectral technique to study the nonlinear effects in this boundary layer stability problem. Computational results show traces indicating secondary instability and give similar forms to the experimental hot-wire traces of Wilkinson and Malik (1985). Direct numerical simulations of the parallel or Type 2 instability in the Ekman layer have been undertaken by Marlatt and Biringen (1995). Fourth order finite differences are used to spatially discretise the domain in the y-direction, Chebyshev spectral discretisation is used in the z-direction and Fourier expansions applied in the x-direction. These computations were aimed at validating some phenomena observed in the experiments of Faller for the Ekman layer. A very rapidly growing secondary instability of the Type 2 primary mode at oblique angles was demonstrated giving partial support for this as a route to transition. However, only two cases were considered corresponding to the least stable Type 2 eigenvalues at $R = 150$ and 350 and generalising from these limited results must be made with caution. However, if these results were fully verified through more comprehensive studies then a similar phenomenon could be demonstrated in the case of the rotating disc.

A limited amount of work has been done experimentally on the rotating disc with a compliant coating (Hansen and Hunston 1974, 1983, Chung and Merrill 1984 and Chung, 1985) with the aim of achieving drag reduction. Hansen and Hunston (1974) first considered this problem but investigated the effects of a compliant boundary on an already turbulent boundary layer. Using PVC plastisols for the coatings qualitative results were obtained through photographic evidence and torque measurements were used to gauge the effect on skin friction drag. Above a critical level of compliance ridges, or undulations, were found to develop and viewed from above these appeared as narrow, light bands stationary with respect to the disc surface and aligned normal to the local freestream direction against darker background bands. These wavecrests were confirmed as a hydrodynamic effect as opposed to any centrifugal mechanism by testing in air at all rotation speeds and were thus identified as the divergence instability. The number of crests were found to increase with the speed of disc rotation and the effect of the divergence ridges was to act similar to roughness elements on the surface and hence their presence brought about increases in drag compared to the non-compliant boundary results. Below the critical level for the onset of this instability no significant reductions in drag were noted. Hansen and Hunston (1983) went on to extend this work to consider the fluid-property effects on this type of instability. The effect of fluids of different viscosity and viscoelasticity on the divergence ridges

was assessed. Increasing the fluid viscosity was found to increase the critical onset speed and flow-generated waves were detected in the laminar flow region when the viscosity was sufficiently high. Viscoelastic fluids were formed using dilute solutions of high molecular weight polymers and were found to give rise to a more regular wave pattern but had little influence on the onset values. Interestingly drag was increased less by viscoelastic fluids than viscous fluids with the same viscosity. It should be noted that the disc geometry was chosen in these two studies for experimental ease rather than to specifically study the effects of wall compliance on three-dimensional boundary layers. This work does, however, provide some insight into the behaviour of the divergence instability within this flow configuration. Chung and Merrill (1984) used a double-layer wall construction of varying specification in an attempt to demonstrate drag reduction over the disc again using torque measurements. The experimental coatings used were of a complex construction and consisted of a layer of silicone gel impregnated with vertical fibres on a velvet base and in most cases covered by an upper layer film of either natural rubber or teflon which was then adhered to the rigid disc surface. A drag reduction ratio was calculated as a function of Reynolds number for a wide range of wall properties with teflon coated walls found to give the best results with slight reductions in drag . For walls coated in the natural rubber film or in the absence of any upper layer significant increases in drag were measured. In terms of substrate properties best results were achieved with coatings of low storage modulus and high damping at a rotation speed of about 80 rad/s (corresponding to a linear tip speed of 9.3m/s). This gave about a 20% reduction over the rigid wall value with reductions scattered around the 10% mark at higher Reynolds numbers. At higher rotation rates the beneficial effects of compliance were curtailed owing to the possible presence of the divergence instability. From these studies it is clear that drag reduction is possible through the use of wall compliance from which it could conservatively be inferred that some degree of transition delay would be possible but the consideration of only torque measurements means no underlying physical mechanisms can be investigated. The appearance of the divergence instability has been shown to severely limit the performance of wall compliance in this geometry although the wall properties used were by no means optimised to give best results. Theoretical work on this problem would therefore be invaluable in extracting information to assist in future experimental studies regarding the best choice of wall properties and possible mechanisms responsible for any drag reduction.

The only theoretical work to date in this area of any relevance is the brief communication of Denier and Hall (1991) on the effects of wall compliance on the Görtler vortex instability which indicated that wall compliance could only have a slight, insignificant effect on the

maximum growth rate of this type of instability. Although these vortices arise through an essentially inviscid mechanism, as is the case for the crossflow vortices, some fundamental differences between the form of the two types of vortices have already been outlined. Extending these unpromising results to cover all forms of instability brought about by inviscid mechanisms cannot be made unequivocally. Indeed this behaviour, or lack of response to wall compliance, may be a feature common to the Görtler instability rather than due to inviscid instability mechanisms in general.

CHAPTER 6

THE EFFECTS OF WALL COMPLIANCE ON INSTABILITY IN ROTATING DISC FLOW.

6.1 Introduction.

The work reviewed in the previous chapter indicates that the eigenvalue spectrum for the rotating disc stability problem is of considerable complexity with up to three families of eigensolutions present for the case of a rigid disc. The introduction of a compliant boundary greatly adds to this with a profusion of possible eigenmodes. As well as the modified versions of the rigid wall instabilities there is the possibility of the onset of TWF and divergence and then modal interactions between any of these eigensolutions. It would be an enormous task to investigate all of these forms of instability and a decision has to be made on which areas to focus attention.

With the results from Chapters 3 and 4 concerning an inviscid instability mechanism in operation in a boundary layer it is expected that wall compliance should have some effect on the crossflow instability in this three-dimensional boundary layer. It is also well known that in order for wall compliance to be most effective wall parameters should ideally be selected to give marginal stability with respect to wall-based instabilities. This offers one possible route for investigation; that is to consider the type of wall construction and wall parameters which give the best performance. The question then is: what constitutes an optimal wall, since the three-dimensional geometry introduces additional variants such as the disturbance propagation direction to an already complex problem ? This would also not necessarily give the most valuable information at this stage where the fundamental effects of wall compliance on instability in this three-dimensional boundary layer are unknown. An alternative route of investigation would therefore be to consider one simple wall type and examine its effects on the boundary layer instabilities but even restricting investigation to one wall type the question of what form of instability and parameter range to focus on still has to be answered. The stationary Type 1 mode has always been favoured for study in experimental investigations owing to its relative ease of excitation and detection and this form of disturbance is generally considered to give rise to the most common route to

transition. An initial investigation into the effects of wall compliance on these stationary modes is therefore judged to be the most appropriate. The role of travelling disturbances in natural transition however remains an unanswered question. Existing results for the rigid disc indicating some amplification rates higher than those of the stationary disturbances are enough to warrant research along these lines for the compliant boundary problem. This subject then provides the second main section of work within this chapter.

Compliant wall dynamics can be represented theoretically by using the plate-spring model of Carpenter and Garrad (1985) (Chapter 3) where the model is relatively simple to implement computationally, but in order to relate to ongoing experimental investigations the more realistic volume-based compliant wall model of Dixon *et al.* (1994) (Chapter 4) will be considered. The simplest form of this type of wall model is that of a single layer of viscoelastic material, but despite the apparent simplicity of this type of wall it has been observed for the two-dimensional Blasius boundary layer profile that the eigenvalue spectrum for the coupled wall/flow problem can be quite intricate. Yeo (1988) established numerically the existence of at least four unstable eigenmodes for zero pressure gradient flow over a single-layer viscoelastic wall. The instabilities which develop in this wall/flow configuration are also investigated by Fraser and Carpenter (1985) with the observation that in the absence of any flow there exists an infinite number of free wave modes and that at least the first three of these may develop into instabilities with the inclusion of some mean flow. In the three-dimensional geometry it is as yet unclear as to how these same free wave modes may develop as hydroelastic instabilities and this provides another area for consideration. The prediction of the onset and orientation of any such instability would be of use in subsequent experimental studies.

This chapter initially introduces the rotating disc boundary layer and mean flow field. The rigid wall and coupled compliant wall/flow eigenvalue problems are then described followed by the numerical method of solution. Results are then presented in three main sections; the response of stationary disturbances to the compliant wall, the effect of wall compliance on travelling disturbances and finally features of hydroelastic instability modes found to occur in this geometry.

6.2 Mean Flow Field.

For theoretical purposes the disc is considered to be infinite in diameter and rotating about an axis, z^*, perpendicular to its surface at a constant angular velocity Ω. The coordinate system, fixed relative to the disc, is cylindrical with radius r^*, azimuthal angle θ and normal direction z^* with the fluid assumed to occupy the region $z^* > 0$. The mean flow field is obtained from von Kármán's exact solution to the Navier-Stokes equations and the mean velocity components and pressure are written

$$\begin{aligned} \bar{u} &= r^*\Omega F(z), \quad \bar{v} = r^*\Omega G(z) \\ \bar{w} &= (\nu\Omega)^{\frac{1}{2}} H(z), \quad \bar{p} = \rho\nu\Omega P(z) \end{aligned}$$

where z is the non-dimensional length scaled by the constant boundary layer displacement thickness $\delta^* = (\nu/\Omega)^{\frac{1}{2}}$, with ν the kinematic viscosity and ρ the fluid density.

Using these expressions in the Navier-Stokes equations gives the following governing equations for the mean flow field where primes denote differentiation with respect to z.

$$F^2 - (G+1)^2 + F'H - F'' = 0 \tag{6.1}$$

$$2F(G+1) + G'H - G'' = 0 \tag{6.2}$$

$$P' + HH' - H'' = 0 \tag{6.3}$$

$$2F + H' = 0 \tag{6.4}$$

and with boundary conditions

$$F(0) = G(0) = H(0) = 0$$

$$F = 0, \qquad G = -1 \qquad \text{as} \qquad z \to \infty.$$

This system of equations is solved using a two-point boundary value problem solver which implements a finite difference scheme and Newton iteration (NAG routine D02RAF). Key values of $F'(0) = 0.51023$, $G'(0) = -0.61592$ and $H(\infty) = -0.8845$ agree well with documented results (Benton, 1966, Malik, 1986a and Balakumar and Malik, 1990).

The non-dimensional mean velocity components, F, G and H are shown in Figure 6.1 and this demonstrates the point of inflexion in the radial component of the velocity field which gives rise to the mechanism for crossflow instability. Within this three-dimensional field there exists an infinite family of two-dimensional profiles given by $F\cos\varepsilon + G\sin\varepsilon$ each corresponding to a propagation direction, ε, where the point of inflexion moves with the value of ε.

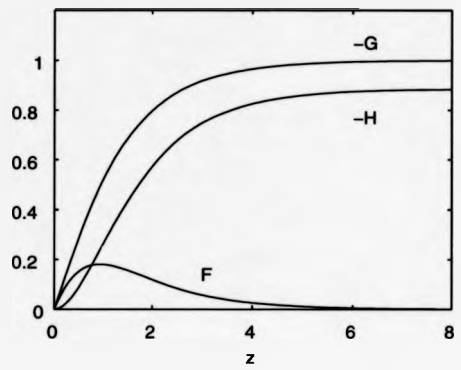

Figure 6.1: Radial (F), azimuthal (G) and axial (H) velocity components for boundary layer flow over a rotating disc.

6.3 Governing Stability Equations.

The linear stability analysis, following Malik *et al.* (1981), is formulated first for the rigid wall problem whilst the adaptation of this to incorporate a compliant boundary will be treated in a subsequent section.

A space-time dependent perturbation field of infinitesimal disturbances, $[\tilde{u}, \tilde{p}]$, is imposed on the mean flow field and throughout δ^*, $r_e^*\Omega$ and $\rho r_e^{*2}\Omega^2$ are used to non-dimensionalise length, velocity and pressure respectively with r_e^* taken to be the radial position for the stability analysis. This gives the following dimensionless form for the perturbed flow field.

$$u(r,\theta,z,t) = \frac{r}{R}F(z) + \tilde{u}(r,\theta,z,t) \tag{6.5}$$

$$v(r,\theta,z,t) = \frac{r}{R}G(z) + \tilde{v}(r,\theta,z,t) \tag{6.6}$$

$$w(r,\theta,z,t) = \frac{1}{R}H(z) + \tilde{w}(r,\theta,z,t) \tag{6.7}$$

$$p(r,\theta,z,t) = \frac{1}{R^2}P(z) + \tilde{p}(r,\theta,z,t) \tag{6.8}$$

$r = r^*(\Omega/\nu)^{\frac{1}{2}}$ is a general non-dimensional radius and the Reynolds number

$$R = r_e^*(\Omega/\nu)^{\frac{1}{2}}$$

is the non-dimensional value of the radial location at which the stability analysis is applied.

The non-dimensional form of the Navier-Stokes equations for this flow problem take the same form as that for the rotating channel of Chapter 2.

$$\frac{\partial \boldsymbol{u}}{\partial t} + (\boldsymbol{u} \cdot \nabla)\boldsymbol{u} + 2\boldsymbol{\Omega} \wedge \boldsymbol{u} + \nabla p - \frac{1}{R}\nabla^2 \boldsymbol{u} = 0 \tag{6.9}$$

$$\nabla \cdot \boldsymbol{u} = 0 \tag{6.10}$$

where $\boldsymbol{u} = [u, v, w]^T$ and again the centrifugal terms have been incorporated within a modified pressure term, p.

The perturbed flow field is substituted into the Navier-Stokes equations and linearisation about the mean flow field with respect to the perturbations is performed to yield the following set of linear equations.

$$\begin{aligned} \frac{\partial \tilde{u}}{\partial t} &+ \frac{r}{R}F\frac{\partial \tilde{u}}{\partial r} + \frac{G}{R}\frac{\partial \tilde{u}}{\partial \theta} + \frac{H}{R}\frac{\partial \tilde{u}}{\partial z} + \frac{F}{R}\tilde{u} - \frac{2}{R}(G+1)\tilde{v} + \frac{r}{R}F'\tilde{w} \\ &= -\frac{\partial \tilde{p}}{\partial r} + \frac{1}{R}\left[\frac{\partial^2 \tilde{u}}{\partial r^2} + \frac{1}{r^2}\frac{\partial^2 \tilde{u}}{\partial \theta^2} + \frac{\partial^2 \tilde{u}}{\partial z^2} + \frac{1}{r}\frac{\partial \tilde{u}}{\partial r} - \frac{2}{r^2}\frac{\partial \tilde{v}}{\partial \theta} - \frac{\tilde{u}}{r^2}\right] \end{aligned} \tag{6.11}$$

$$\begin{aligned} \frac{\partial \tilde{v}}{\partial t} &+ \frac{r}{R}F\frac{\partial \tilde{v}}{\partial r} + \frac{G}{R}\frac{\partial \tilde{v}}{\partial \theta} + \frac{H}{R}\frac{\partial \tilde{v}}{\partial z} + \frac{F}{R}\tilde{v} + \frac{2}{R}(G+1)\tilde{u} + \frac{r}{R}G'\tilde{w} \\ &= -\frac{1}{r}\frac{\partial \tilde{p}}{\partial \theta} + \frac{1}{R}\left[\frac{\partial^2 \tilde{v}}{\partial r^2} + \frac{1}{r^2}\frac{\partial^2 \tilde{v}}{\partial \theta^2} + \frac{\partial^2 \tilde{v}}{\partial z^2} + \frac{1}{r}\frac{\partial \tilde{v}}{\partial r} + \frac{2}{r^2}\frac{\partial \tilde{u}}{\partial \theta} - \frac{\tilde{v}}{r^2}\right] \end{aligned} \tag{6.12}$$

$$\begin{aligned} \frac{\partial \tilde{w}}{\partial t} &+ \frac{r}{R}F\frac{\partial \tilde{w}}{\partial r} + \frac{G}{R}\frac{\partial \tilde{w}}{\partial \theta} + \frac{H}{R}\frac{\partial \tilde{w}}{\partial z} + \frac{H'}{R}\tilde{w} \\ &= -\frac{\partial \tilde{p}}{\partial z} + \frac{1}{R}\left[\frac{\partial^2 \tilde{w}}{\partial r^2} + \frac{1}{r^2}\frac{\partial^2 \tilde{w}}{\partial \theta^2} + \frac{\partial^2 \tilde{w}}{\partial z^2} + \frac{1}{r}\frac{\partial \tilde{w}}{\partial r}\right] \end{aligned} \tag{6.13}$$

$$\frac{\partial \tilde{u}}{\partial r} + \frac{1}{r}\frac{\partial \tilde{v}}{\partial \theta} + \frac{\partial \tilde{w}}{\partial z} + \frac{\tilde{u}}{r} = 0 \tag{6.14}$$

Additional terms (compared to the channel problem) arise from the form of the vector operators in the cylindrical coordinate system, from the three-dimensional mean flow field and from the variation of this flow field with r. Boundary conditions appropriate to the rigid wall problem are that the perturbation velocities vanish at the wall ($z = 0$) and at $z = \infty$.

Following this several approximations must be made which allow the equations to become separable in r, θ and t. Firstly the quantity r is replaced by R which is generally accepted

as neglecting some 'non-parallel flow' effects. Terms of order R^{-2} and higher order terms are then assumed to be negligible. Having obtained a set of equations which is separable in r, θ and t the perturbation quantities can be expressed in the form of normal modes so that

$$[\tilde{u}, \tilde{v}, \tilde{w}, \tilde{p}]^T = [f(z), g(z), h(z), \pi(z)]^T E + \text{c.c.} \tag{6.15}$$

where $E = \exp\{i(\alpha r + \beta R\theta - \omega t)\}$.

Substitution of this disturbance form into Eqs.(6.11)-(6.14) gives the following non-dimensional governing stability equations.

$$i(\alpha F + \beta G - \omega)f + F'h + i\alpha\pi = \frac{1}{R}\left[f'' - \lambda^2 f - Ff + 2(G+1)g - Hf'\right] \tag{6.16}$$

$$i(\alpha F + \beta G - \omega)g + G'h + i\beta\pi = \frac{1}{R}\left[g'' - \lambda^2 g - Fg - 2(G+1)f - Hg'\right] \tag{6.17}$$

$$i(\alpha F + \beta G - \omega)h + \pi' = \frac{1}{R}\left[h'' - \lambda^2 h - Hh' - H'h\right] \tag{6.18}$$

$$\left[i\alpha + \frac{1}{R}\right] f + i\beta g + h' = 0 \tag{6.19}$$

with $\lambda^2 = \alpha^2 + \beta^2$.

Through the introduction of a new variable, $\gamma = \alpha g - \beta f$, related to the z-component of perturbation vorticity, the pressure term π can be eliminated to give two coupled equations in terms of h and γ.

$$(1/R)[i(D^2 - \lambda^2)(D^2 - \bar{\lambda}^2) + R(\alpha F + \beta G - \omega)(D^2 - \bar{\lambda}^2) - R(\bar{\alpha}F'' + \beta G'')$$
$$- iHD(D^2 - \bar{\lambda}^2) - iH'(D^2 - \bar{\lambda}^2) - iFD^2]h + (1/R)[2(G+1)D + 2G']\gamma = 0 \tag{6.20}$$

$$(1/R)[2(G+1)D - iR(\alpha G' - \beta F')]h + (1/R)[i(D^2 - \lambda^2)$$
$$+ R(\alpha F + \beta G - \omega) - iHD - iF]\gamma = 0 \tag{6.21}$$

where $D \equiv \frac{d}{dz}$, $\bar{\alpha} = \alpha - \frac{i}{R}$, $\bar{\lambda}^2 = \alpha\bar{\alpha} + \beta^2$.

The boundary conditions corresponding to this coupled system are

$$h(0) = h'(0) = \gamma(0) = 0,$$

$$h(\infty) = h'(\infty) = \gamma(\infty) = 0.$$

This sixth order system of equations as derived by Malik *et al.* (1981) retains the effects of Coriolis acceleration and streamline curvature and defines an eigenvalue problem of the form

$$\mathcal{F}(\alpha, \beta, \omega, R) = 0.$$

If these effects are subsequently neglected then Eqs.(6.20) and (6.21) decouple and the stability problem is reduced to that described by the Orr-Sommerfeld equation for the two-dimensional mean flow profile $\alpha F + \beta G$ and flow parameters ω, R and λ.

The most appropriate physical interpretation for this eigenvalue problem is to consider spatial modes where the frequency, ω, is real and following Mack (1985) it is assumed that the growth is in the radial direction only so that the amplitude distribution is axisymmetric with $\beta_i = 0$.

6.4 Numerical Solution of the Stability Equations.

The sixth order system of equations defined in the previous section is solved numerically using a Chebyshev-tau spectral method. Malik *et al.* (1981) used a similar spectral scheme but solved for the temporal case which reduces the size of the computational problem, but involves the use of a group velocity transformation to obtain spatial eigenvalues, whereas here the spatial eigenvalues are solved for directly. The spectral method was chosen over the shooting method used in the two-dimensional adverse pressure gradient problem of Chapter 4 because it allows a global scheme to be implemented for the rigid wall boundary problem. Group velocities can also be calculated at relatively little extra cost which give essential information regarding stability in this type of geometry. For example negative values of $-\alpha_i$ do not indicate a physically unstable mode if the group velocity vector is directed inwards since the associated disturbance kinetic energy is then decreasing in the outward direction. Knowledge about group velocities will be helpful, in particular, in identifying possible hydroelastic instabilities.

The numerical scheme begins by transforming the physical space to a suitable computational domain. Therefore the semi-infinite fluid domain $z \in [0, \infty)$ is mapped algebraically to the finite spectral interval $y \in [-1, 1]$ using the transformation

$$y = \frac{z - L}{z + L} \tag{6.22}$$

with $L = 2$.

Derivatives with respect to the physical variable, z, can then be expressed in terms of the transformed variable, y, in the following way.

$$\frac{d}{dz} = m(y)\frac{d}{dy} \quad \text{where} \quad m(y) = \frac{(1-y)^2}{2L}$$

The system of equations, Eqs.(6.20) and (6.21), written in terms of the computational

variable can be expressed in the form

$$\tilde{A}h + \tilde{B}h' + \tilde{C}h'' + \tilde{D}h''' + \tilde{E}h^{iv} + \tilde{F}\gamma + \tilde{G}\gamma' = 0 \tag{6.23}$$

$$\tilde{V}h + \tilde{W}h' + \tilde{X}\gamma + \tilde{Y}\gamma' + \tilde{Z}\gamma'' = 0 \tag{6.24}$$

where primes now denote derivatives with respect to y and $\tilde{A}$-$\tilde{G}$ and $\tilde{V}$-$\tilde{Z}$ are coefficients involving the flow parameters, the mean flow field and the function m. For example

$$\begin{aligned}\tilde{A} = i\lambda^2\bar{\lambda}^2 - \bar{\lambda}^2 R(\alpha F + \beta G - \omega) \quad &- \quad R(\bar{\alpha}[mm'F' + m^2F''] \\ &+ \quad \beta[mm'G' + m^2G''\,]) + iH'\bar{\lambda}^2 m.\end{aligned}$$

Full expressions for all of these coefficients are given in Appendix C.

Eq.(6.23) is now integrated indefinitely four times and Eq.(6.24) twice to give

$$\iiiint(\tilde{A} - \tilde{B}' + \tilde{C}'' - \tilde{D}''' + \tilde{E}^{iv})h\,dy + \iiint(\tilde{B} - 2\tilde{C}' + 3\tilde{D}'' - 4\tilde{E}''')h\,dy +$$

$$\iint(\tilde{C} - 3\tilde{D}' + 6\tilde{E}'')h\,dy + \int(\tilde{D} - 4\tilde{E}')h\,dy + \tilde{E}h + \iiiint(\tilde{F} - \tilde{G}')\gamma\,dy + \iiint \tilde{G}\gamma\,dy$$

$$= d_0 + d_1 y + d_2 y^2 + d_3 y^3 \tag{6.25}$$

$$\iint(\tilde{V} - \tilde{W}')h\,dy + \int \tilde{W}h\,dy + \int(\tilde{Y} - 2\tilde{Z}')\gamma\,dy + \iint(\tilde{X} - \tilde{Y}' + \tilde{Z}'')\gamma\,dy + \tilde{Z}\gamma$$

$$= e_0 + e_1 y \tag{6.26}$$

where the d_i and e_i are constants of integration.

The working variables h and γ in terms of the transformed coordinate are now written as two finite Chebyshev series expansions.

$$h = \sum_{n=0}^{N} a_n T_n(y) \tag{6.27}$$

$$\gamma = \sum_{n=0}^{N} b_n T_n(y) \tag{6.28}$$

The expansions in Eqs.(6.27) and (6.28) are then substituted into the above equations and equating coefficients of T_n for $n = 4, \ldots, N$ in Eq.(6.25) and $n = 2, \ldots, N$ in Eq.(6.26) returns $2N - 4$ discretised equations in terms of the unknowns $a_0, \ldots, a_N, b_0, \ldots, b_N$.

Each component integral term can then be separated into powers of the eigenvalue α and the eigenvalue problem can then be written in the following matrix form.

$$(\alpha^4 \boldsymbol{C}_4 + \alpha^3 \boldsymbol{C}_3 + \alpha^2 \boldsymbol{C}_2 + \alpha \boldsymbol{C}_1 + \boldsymbol{C}_0)\boldsymbol{a} + \boldsymbol{D}_0 \boldsymbol{b} = 0 \tag{6.29}$$

$$(\alpha^2 \boldsymbol{E}_2 + \alpha \boldsymbol{E}_1 + \boldsymbol{E}_0)\boldsymbol{b} + (\alpha \boldsymbol{F}_1 + \boldsymbol{F}_0)\boldsymbol{a} = 0 \tag{6.30}$$

The $\boldsymbol{C}_i$, $\boldsymbol{D}_i$, $\boldsymbol{E}_i$, $\boldsymbol{F}_i$ are all complex matrices of order $N+1$ and $\boldsymbol{a} = [a_0, \ldots, a_N]^T$, $\boldsymbol{b} = [b_0, \ldots, \boldsymbol{b}_N]^T$.

The problem is fully specified by the inclusion of six boundary conditions which replace the equations for $n = 0, \ldots, 3$ and $n = 0, 1$ in the respective discretised equations. The justification for this comes from the fact that these equations serve only to identify the integration constants d_i and e_i. Rigid wall boundary conditions for h then occupy the first four rows in the first equation and those for γ are placed in the first two rows of the second equation. The three outer boundary conditions in terms of the transformed coordinate common to both rigid and compliant problems are

$$h(1) = \sum_{n=0}^{N} a_n = 0 \tag{6.31}$$

$$h'(1) = \sum_{n=0}^{N} n^2 a_n = 0 \tag{6.32}$$

$$\gamma(1) = \sum_{n=0}^{N} b_n = 0 \tag{6.33}$$

and for the rigid wall the lower boundary conditions are expressed in a similar form but with evaluation at $y = -1$.

$$h(-1) = \sum_{n=0}^{N} (-1)^n a_n = 0 \tag{6.34}$$

$$h'(-1) = \sum_{n=0}^{N} (-1)^{n-1} n^2 a_n = 0 \tag{6.35}$$

$$\gamma(-1) = \sum_{n=0}^{N} (-1)^n b_n = 0 \tag{6.36}$$

This formulation of the eigenvalue problem thus allows a global eigenvalue search scheme to be implemented where the advantage of such a scheme in this particular case is in identifying the separate families of eigensolutions known to exist for the rotating disc. As in Chapter 3, where a similar global scheme was used, companion matrices $\boldsymbol{A}$ and $\boldsymbol{B}$ are constructed to define a generalised eigenvalue problem of the form $\boldsymbol{AV} = \alpha \boldsymbol{BV}$. The order of

the matrices is 6N+6 and $\boldsymbol{A}$ and $\boldsymbol{B}$ are defined as follows.

$$\boldsymbol{A} = \begin{bmatrix} -\boldsymbol{C}_3 & -\boldsymbol{C}_2 & -\boldsymbol{C}_1 & -\boldsymbol{C}_0 & 0 & -\boldsymbol{D}_0 \\ 0 & 0 & -\boldsymbol{F}_1 & -\boldsymbol{F}_0 & -\boldsymbol{E}_1 & -\boldsymbol{E}_0 \\ \boldsymbol{I} & 0 & 0 & 0 & 0 & 0 \\ 0 & \boldsymbol{I} & 0 & 0 & 0 & 0 \\ 0 & 0 & \boldsymbol{I} & 0 & 0 & 0 \\ 0 & 0 & 0 & 0 & \boldsymbol{I} & 0 \end{bmatrix}$$

$$\boldsymbol{B} = \begin{bmatrix} \boldsymbol{C}_4 & 0 & 0 & 0 & 0 & 0 \\ 0 & 0 & 0 & 0 & \boldsymbol{E}_2 & 0 \\ 0 & \boldsymbol{I} & 0 & 0 & 0 & 0 \\ 0 & 0 & \boldsymbol{I} & 0 & 0 & 0 \\ 0 & 0 & 0 & \boldsymbol{I} & 0 & 0 \\ 0 & 0 & 0 & 0 & 0 & \boldsymbol{I} \end{bmatrix}$$

where $\boldsymbol{I}$ is an identity matrix of order N+1.

The associated eigenvector, $\boldsymbol{V}$, is constructed in terms of the expansion coefficients for h and γ.

$$\boldsymbol{V} = [\alpha^3\boldsymbol{a}, \alpha^2\boldsymbol{a}, \alpha\boldsymbol{a}, \boldsymbol{a}, \alpha\boldsymbol{b}, \boldsymbol{b}]^T$$

Having set up a global formulation it is accepted that a local search procedure is more computationally efficient and once the desired branch of solutions is identified most numerical solutions were established using a local iterative scheme. In order to implement such a scheme the equations of the generalised eigenvalue problem are recast in the alternative form

$$\boldsymbol{D}(\alpha)\begin{bmatrix} \boldsymbol{a} \\ \boldsymbol{b} \end{bmatrix} = 0 \tag{6.37}$$

where $\boldsymbol{D}$ is a square matrix of order $2N + 2$ with the following construction.

$$\boldsymbol{D} = \alpha^4\begin{bmatrix} \boldsymbol{C}_4 & 0 \\ 0 & 0 \end{bmatrix} + \alpha^3\begin{bmatrix} \boldsymbol{C}_3 & 0 \\ 0 & 0 \end{bmatrix} + \alpha^2\begin{bmatrix} \boldsymbol{C}_2 & 0 \\ 0 & \boldsymbol{E}_2 \end{bmatrix} + \alpha\begin{bmatrix} \boldsymbol{C}_1 & 0 \\ \boldsymbol{F}_1 & \boldsymbol{E}_1 \end{bmatrix} + \begin{bmatrix} \boldsymbol{C}_0 & \boldsymbol{D}_0 \\ \boldsymbol{F}_0 & \boldsymbol{E}_0 \end{bmatrix}$$

Using the technique of Bridges and Morris (1984) eigenvalues, α, can be obtained iteratively from an initial estimate using the formula

$$\alpha_{k+1} = \alpha_k - \frac{1}{f(\alpha_k)} \qquad k = 0, 1, \ldots \tag{6.38}$$

where $f(\alpha_k) = Tr\{\boldsymbol{D}^{-1}(\alpha_k)\boldsymbol{D}^{(1)}(\alpha_k)\}$ and $Tr\{\boldsymbol{A}\}$ denotes the trace of matrix $\boldsymbol{A}$. $\boldsymbol{D}^{-1}(\alpha_k)$ is the inverse of $\boldsymbol{D}(\alpha_k)$ and $\boldsymbol{D}^{(1)}(\alpha_k)$ the first derivative of $\boldsymbol{D}(\alpha_k)$ with respect to α.

Figure 6.2 shows the neutral curve for stationary disturbances ($\omega = 0$) obtained using this method with a value of $N = 40$ for the Chebyshev expansions and this shows excellent agreement with Figure 1 of Malik (1986a). Shown clearly in this figure are two minimum neutral points at $R = 285$ and $R = 440$ established respectively as the critical Reynolds numbers for the Type 1 and Type 2 stationary modes of instability. Wavenumbers and wave angles also agree well in numerical value with those published by Malik.

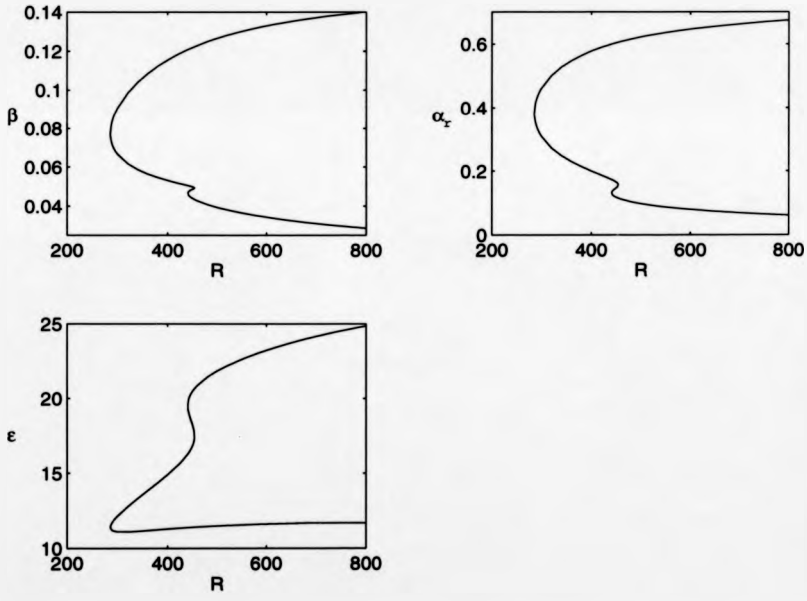

Figure 6.2: Neutral curve for stationary disturbances showing variation of R with (a) β, (b) α_r and (c) ε.

6.5 Wall Equations.

The single layer compliant wall chosen for this investigation is assumed for theoretical purposes to be of infinite depth which is probably a valid assumption in practice since if walls in reality are given sufficient depth they then appear infinitely deep to boundary layer disturbances. This approximation also serves to remove another wall parameter from the system so that the only parameter controlling the physical level of wall compliance is the shear modulus of the wall material.

It is necessary to solve for the wall motion and fluid motion separately for this compliant wall problem and then couple the two governing sets of equations through the appropriate dynamic and kinematic conditions at the wall/flow interface. The wall dynamics are again described by the Navier equations as for Chapter 4 but the displacement vector field is now a three-dimensional one. The non-dimensional displacement field, $\boldsymbol{\eta} = [\xi, \eta, \zeta]^T$, is thus governed by the following vector equation.

$$\ddot{\boldsymbol{\eta}} = \frac{\rho}{\rho_s} \left(G_s \nabla^2 \boldsymbol{\eta} + Y_s \nabla \nabla \cdot \boldsymbol{\eta} \right) \tag{6.39}$$

where $Y_s = K_s + G_s/3$. G_s and K_s are respectively the dimensionless shear and bulk moduli of the substrate material and ρ_s is the density of the substrate. Throughout a Poisson ratio of 0.49 is used, so that the material is almost incompressible, which generates the relation $K_s = 149 G_s/3$.

There is no clearly defined manner in which to express non-dimensional shear and bulk moduli which are invariant across the disc since the obvious reference velocity of $r_s^* \Omega$ means the effective freestream speed changes with radial location. The theoretical problem is therefore considered from a practical viewpoint where a layer of fixed material property is used and changes in wall compliance are assessed by varying the rotational speed of the disc. All calculations use a dimensional value of $G_s = 1000 \mathrm{N/m^2}$ (so that the effective non-dimensional value decreases with increased Reynolds number). Changes in the degree of wall compliance could equally be considered by fixing the rotation speed and changing the value of G_s. Since the rotating disc boundary layer is of constant thickness lengths in the wall equations can be non-dimensionalised with respect to the boundary layer displacement thickness unlike the walls of Chapter 4 where a reference Reynolds number was needed to provide a fixed scaling length for the wall equations.

The vector operators in the Navier equations are expressed in terms of cylindrical coordinate differential operators which affect the solution procedure. In the two-dimensional

cartesian problem it was possible to extract exact analytical solutions to these equations by separating the vector into rotational and irrotational components but introducing the third dimension and using the cylindrical coordinate system means such a method of solution is no longer possible. The equations governing the wall motion are thus obtained semi-analytically and solved for numerically in the computational problem.

The standard travelling-wave form is assumed for the non-dimensional displacements.

$$\boldsymbol{\eta} = [\hat{\xi}, \hat{\eta}, \hat{\zeta}]^T \exp\{i(\alpha r + \beta R\theta - \omega t)\} + \text{c.c.} \tag{6.40}$$

Substitution into the Navier equations then gives

$$\hat{\xi}'' = -\frac{1}{G_s}[G_s F_s + i\alpha Y_s \tilde{\alpha}]\hat{\xi} - \frac{i\alpha Y_s}{G_s}\hat{\zeta}' + \frac{1}{G_s}[\alpha\beta Y_s - 2\beta^2 G_s]\hat{\eta} \tag{6.41}$$

$$\hat{\eta}'' = -\frac{1}{G_s}[G_s F_s - \beta^2 Y_s]\hat{\eta} - \frac{i\beta Y_s}{G_s}\hat{\zeta}' - \frac{1}{G_s}[\frac{2i\beta G_s}{R} + i\beta Y_s \tilde{\alpha}]\hat{\xi} \tag{6.42}$$

$$\hat{\zeta}'' = -\frac{1}{(G_s + Y_s)}[G_s F_s \hat{\zeta} + Y_s \tilde{\alpha}\hat{\xi}' + i\beta Y_s \hat{\eta}'] \tag{6.43}$$

with $F_s = \frac{i\alpha}{R} - \alpha^2 - \beta^2 + \frac{\rho_s \omega^2}{\rho G_s}$ and $\tilde{\alpha} = \frac{1}{R} + i\alpha$.

Eqs.(6.41)-(6.43) can be written as

$$\tilde{\boldsymbol{\eta}}' = \boldsymbol{K}\tilde{\boldsymbol{\eta}} \tag{6.44}$$

where $\tilde{\boldsymbol{\eta}} = [\hat{\xi}', \hat{\eta}', \hat{\zeta}', \hat{\xi}, \hat{\eta}, \hat{\zeta}]^T$ and $\boldsymbol{K}$ takes the following form.

$$\boldsymbol{K} = \begin{bmatrix} 0 & 0 & k_{13} & k_{14} & k_{15} & 0 \\ 0 & 0 & k_{23} & k_{24} & k_{25} & 0 \\ k_{31} & k_{32} & 0 & 0 & 0 & k_{36} \\ 1 & 0 & 0 & 0 & 0 & 0 \\ 0 & 1 & 0 & 0 & 0 & 0 \\ 0 & 0 & 1 & 0 & 0 & 0 \end{bmatrix}$$

By solving $\det(\boldsymbol{K} - \mu\boldsymbol{I}) = 0$ six eigenvalues $\pm\mu_i$, $i = 1, 2, 3$, are returned from which the following general solution can be constructed.

$$\begin{bmatrix} \hat{\xi}(z) \\ \hat{\eta}(z) \\ \hat{\zeta}(z) \end{bmatrix} = \sum_{i=1}^{3} \begin{bmatrix} A_i \\ B_i \\ C_i \end{bmatrix} e^{\mu_i z} + \sum_{i=1}^{3} \begin{bmatrix} \bar{A}_i \\ \bar{B}_i \\ \bar{C}_i \end{bmatrix} e^{-\mu_i z} \tag{6.45}$$

For an infinitely deep layer the constants $\bar{A}_i, \bar{B}_i, \bar{C}_i$ must be zero in order to satisfy the requirement of zero displacement at infinite depth and the remaining constants are then related through Eqs.(6.41) -(6.43). Substitution of the solutions into Eq.(6.41) and some rearrangement gives

$$B_i = \frac{(\mu_i^2 - k_{14})A_i - k_{13}\mu_i C_i}{k_{15}}. \tag{6.46}$$

Eq.(6.42) can then be used to eliminate the B_i.

$$\begin{aligned} \mu_i^2 B_i &= k_{24}A_i + k_{25}B_i + k_{23}\mu_i C_i \\ \Rightarrow \quad A_i &= \frac{[k_{23}k_{15}\mu_i + k_{13}\mu_i(\mu_i^2 - k_{25})]C_i}{[\mu_i^4 - \mu_i^2(k_{14}+k_{25}) + k_{25}k_{14} - k_{24}k_{15}]} \\ \Rightarrow \quad A_i &= \Phi(\mu_i)C_i. \end{aligned} \tag{6.47}$$

Thus

$$\begin{aligned} B_i &= \frac{(\mu_i^2 - k_{14})\Phi(\mu_i)C_i - k_{13}\mu_i C_i}{k_{15}} \\ \Rightarrow \quad B_i &= \Psi(\mu_i)C_i. \end{aligned} \tag{6.48}$$

This then gives a solution for the displacement vector field in terms of three unknown constants of integration, C_i.

$$\begin{bmatrix} \bar{\xi}(z) \\ \bar{\eta}(z) \\ \bar{\zeta}(z) \end{bmatrix} = \sum_{i=1}^{3} \begin{bmatrix} \Phi(\mu_i) \\ \Psi(\mu_i) \\ 1 \end{bmatrix} C_i e^{\mu_i z} \tag{6.49}$$

Free wave solutions for the single-layer wall can be determined by satisfying a stress-free boundary (i.e. no flow solution) where the radial and azimuthal non-dimensional shear stresses in the wall, $\bar{\tau}_{zr}$ and $\bar{\tau}_{z\theta}$, and the normal wall stress, $\bar{\tau}_{zz}$. are expressed as follows.

$$\bar{\tau}_{zr} = G_s\left[i\alpha\bar{\zeta} + \bar{\xi}'\right] \tag{6.50}$$

$$\bar{\tau}_{z\theta} = G_s\left[i\beta\bar{\zeta} + \bar{\eta}'\right] \tag{6.51}$$

$$\bar{\tau}_{zz} = Y_s\left[i\alpha\bar{\xi} + \frac{\bar{\xi}}{R} + i\beta\bar{\eta} + \bar{\zeta}'\right] + 2G_s\bar{\zeta}' \tag{6.52}$$

With the wall solutions given by Eq.(6.49) free wave solutions are obtained directly by

solving

$$\boldsymbol{MC} = 0$$

where

$$\begin{aligned} M_{1j} &= G_s[i\alpha + \mu_j \Phi(\mu_j)] \\ M_{2j} &= G_s[i\beta + \mu_j \Psi(\mu_j)] \\ M_{3j} &= Y_s \left[\left(i\alpha + \frac{1}{R} \right) \Phi(\mu_j) + i\beta \Psi(\mu_j) + \mu_j \right] + 2G_s \mu_j \end{aligned}$$

and $\boldsymbol{C} = [C_1, C_2, C_3]^T$. For non-trivial solutions to this problem it is required that det($\boldsymbol{M}$) = 0 must be satisfied.

Inclusion of $1/R$ terms in the wall equations gives rise to non-zero imaginary parts for the free wave eigenvalues compared to zero values in any corresponding two-dimensional case. These free wave modes neither decay nor grow if considered in terms of energy transfer and the appearance of positive values for α_i is merely a consequence of the three-dimensional geometry. The apparent decay of these modes can be attributed to the pulse of energy which excites them spreading out radially. (It can be shown from considerations of energy flux that for a purely radial wave $\alpha_i = 1/2R$ which is indeed verified in the numerical results.) In order to correlate with the fluid stability problem, where $\alpha_i = 0$ denotes the boundary between stability and instability, terms of order R^{-1} and smaller are neglected in the wall formulation. This can be thought of as being analogous to ignoring 'non-parallel' effects in the flow.

Typical free wave solutions are given in Figure 6.3 which shows that there exists an infinite number of modes with phase speeds directed both inwards and outwards; the first three of which are shown in the figure. A feature of the single-layer wall is the occurrence of minimum free wave speed at an infinite wavenumber which has significance for the onset of hydroelastic instabilities and will be discussed in more detail in a subsequent section.

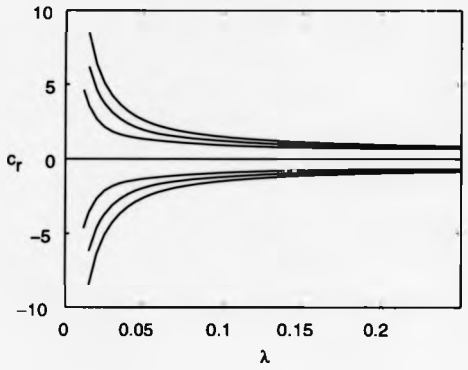

Figure 6.3: Typical free waves for an infinitely deep single-layer viscoelastic wall. c_r : dimensional phase speed, λ : dimensional wavenumber.

6.6 Coupling Fluid and Wall Equations.

For the full fluid/compliant wall problem boundary conditions are derived by satisfying the usual velocity and stress conditions at the interface.

Linearised boundary conditions for the three-dimensional velocity profile at the interface are

$$-i\omega\hat{\xi} = f + F'(0)\hat{\zeta} \tag{6.53}$$

$$-i\omega\hat{\eta} = g + G'(0)\hat{\zeta} \tag{6.54}$$

$$-i\omega\hat{\zeta} = h + H'(0)\hat{\zeta} \tag{6.55}$$

but from Eq.(6.4) $H'(0) = -2F(0) = 0$.

Fluid stresses at the wall expressed in terms of the physical variable, z, are defined below and these must be equated to the corresponding wall stresses given in Eqs.(6.50)-(6.52). Expressions are derived using the formula given in Chapter 4 where

$$\bar{\tau}_{wall}(r,\theta,0) = \bar{\tau}_{fluid}(r,\theta,0) + \hat{\zeta}\frac{\partial}{\partial z}[\bar{\tau}^M](r,\theta,0)$$

where M denotes the mean stress contribution. Therefore

$$\begin{aligned}\bar{\tau}_{zr} &= \frac{1}{R}[i\alpha h + f'] + \frac{\hat{\zeta}}{R}\frac{\partial}{\partial z}\left[\frac{1}{R}\frac{\partial H}{\partial r}(0) + F'(0)\right] \\ &= \frac{1}{R}[F''(0)\hat{\zeta} + i\alpha h + f'],\end{aligned} \tag{6.56}$$

$$\bar{\tau}_{z\theta} = \frac{1}{R}[i\beta h + g'] + \frac{\zeta}{R}\frac{\partial}{\partial z}\left[\frac{1}{R^2}\frac{\partial H}{\partial \theta}(0) + G'(0)\right]$$
$$= \frac{1}{R}[G''(0)\zeta + i\beta h + g'], \tag{6.57}$$
$$\bar{\tau}_{zz} = -\pi + \frac{2h'}{R} + \zeta\frac{\partial}{\partial z}\left[-\frac{P(0)}{R^2} + \frac{2H'(0)}{R^2}\right]$$
$$= -\pi + \frac{2h'}{R} + O\left(\frac{1}{R^2}\right). \tag{6.58}$$

It should be noted that in the case of the Blasius boundary layer the second derivative of the mean flow vanishes at the wall. In this case $G''(0) = 0$ but an additional term arises in the coupling conditions since $F''(0) \neq 0$.

An expression for the pressure term π at the mean undisturbed wall position is obtained from the radial momentum equation (Eq.(6.16)) such that

$$\pi(0) = \frac{1}{R}\left[f'' - \lambda^2 f + 2g\right] + i\omega f - F'(0)h. \tag{6.59}$$

The formulation of the fluid eigenvalue problem is made using the variables h and γ, but the above coupling conditions are expressed in terms of the three perturbation velocity components f, g and h. In order to adapt most efficiently the rigid wall computational code f and g are expressed in terms of h and γ using the continuity equation, Eq.(6.19), to give

$$f = \frac{\beta R}{(i\alpha - R\lambda^2)}\gamma - \frac{i\alpha R}{(i\alpha - R\lambda^2)}h' \tag{6.60}$$
$$g = \frac{i - \alpha R}{(i\alpha - R\lambda^2)}\gamma + \frac{i}{\beta}\left[1 - \frac{\alpha(i - \alpha R)}{(i\alpha - R\lambda^2)}\right]h'. \tag{6.61}$$

The coupling conditions described above involving the fluid perturbations are subsequently transformed to the computational variable y. Continuity of velocity across the wall/flow interface can then be written as a matrix equation involving $\boldsymbol{C} = [C_1, C_2, C_3]^T$, the vector of unknown Navier integration constants, and $\boldsymbol{H} = [h''', h'', h', h, \gamma'', \gamma', \gamma]^T$ evaluated at the wall/flow interface with primes denoting differentiation with respect to y.

$$[\xi, \dot{\eta}, \zeta]_w^T = [\boldsymbol{R}]\boldsymbol{C} = [\boldsymbol{S}]\boldsymbol{H} \tag{6.62}$$

The stress conditions at the wall can be expressed in a similar manner:

$$[\bar{\tau}_{zr}, \bar{\tau}_{z\theta}, \bar{\tau}_{zz}]_w^T = [\boldsymbol{X}]\boldsymbol{C} = [\boldsymbol{Y}]\boldsymbol{H}. \tag{6.63}$$

Elimination of the unknowns C_1, C_2, C_3 then gives rise to three wall conditions which replace the three rigid wall boundary conditions and are given by the following set of equations.

$$[\boldsymbol{R}^{-1}\boldsymbol{S} - \boldsymbol{X}^{-1}\boldsymbol{Y}]\boldsymbol{H} = [0,0,0]^T \tag{6.64}$$

In this three-dimensional boundary layer there exists a mean flow pressure gradient acting in the axial direction normal to the disc surface unlike any of the two-dimensional boundary layers considered previously. In the case of the Falkner-Skan profile, although an adverse pressure gradient exists in the streamwise direction, the pressure across the boundary layer at any given streamwise location is constant. The presence of the pressure gradient in the rotating disc boundary layer is likely to have some influence in experimental investigations where the disc is finite in diameter. It is expected that the pressure force exerted on the compliant material will cause a degree of displacement of the material layer, even in the absence of any boundary layer disturbances, and give rise to some form of 'bulging' at the edges. In the present theoretical calculations where the disc is assumed to be infinite in extent edge effects are not included in the problem formulation and the influence of this mean flow pressure gradient is neglected. It cannot in fact be incorporated into such a linear stability calculation, but would be a factor in direct numerical simulations where the finiteness of the disc is taken into consideration.

6.6.1 Numerical Aspects of the Coupled Problem.

Boundary conditions in Eq.(6.64) are formulated in terms of the expansion coefficients a_i and b_i to generate an eigenvalue problem analogous to the rigid wall problem.

$$\boldsymbol{D}(\alpha)\begin{bmatrix} \boldsymbol{a} \\ \boldsymbol{b} \end{bmatrix} = 0$$

Owing to the form of $\boldsymbol{H}$ this requires expressions for the first three derivatives of the Chebyshev expansions evaluated at $y = -1$. The second and third derivatives at this point are defined as follows.

$$h''(-1) = \sum_{n=0}^{N}(-1)^n\left[\frac{n^4 - n^2}{3}\right]a_n \tag{6.65}$$

$$h'''(-1) = \sum_{n=0}^{N}(-1)^{n-1}\left[\frac{8n^6 - 40n^4 + 32n^2}{120}\right]a_n \tag{6.66}$$

The form of the compliant wall boundary conditions destroys the polynomial form of the stability equations and removes the possibility of any global eigenvalue search procedure.

All eigenvalues for the compliant wall problem are thus obtained using the local iterative method where the derivative of $\boldsymbol{D}(\alpha_k)$ with respect to α is determined analytically for the main body of equations and numerically for the boundary terms.

6.6.2 Calculation of Eigenfunctions.

Flow eigenfunctions can be obtained directly from the eigenvalue calculations since once a particular eigenvalue is known the corresponding eigenvector, $[\boldsymbol{a}, \boldsymbol{b}]^T$, from the local itercation scheme can be determined. The vectors $\boldsymbol{a}$ and $\boldsymbol{b}$ contain the Chebyshev coefficients for h and γ respectively from which values at selected points in the spectral domain are calculated. These are then transformed back into physical space and the components f and g subsequently calculated from the formulae involving h and γ.

In order to determine the associated wall displacements numerical values for the constants, C_i, which appear in Eq.(6.49) must be established. This is done by using the following condition which expresses the stress conditions at the interface.

$$\begin{aligned} [\boldsymbol{X}]\boldsymbol{C} &= [\boldsymbol{Y}]\boldsymbol{H} \\ \Rightarrow \quad \boldsymbol{C} &= [\boldsymbol{X}^{-1}\boldsymbol{Y}]\boldsymbol{H} \end{aligned}$$

This is then used in the expression for the wall displacements.

$$\begin{bmatrix} \xi(z) \\ \eta(z) \\ \zeta(z) \end{bmatrix} = \sum_{i=1}^{3} \begin{bmatrix} \Phi(\mu_i) \\ \Psi(\mu_i) \\ 1 \end{bmatrix} C_i e^{\mu_i z}$$

with entries in $\boldsymbol{X}$ and $\boldsymbol{Y}$, the value of $\boldsymbol{H}$, the μ_i, $\Phi(\mu_i)$ and $\Psi(\mu_i)$ all evaluated at the chosen eigenvalue.

6.7 Validation of Rotating Disc/Compliant Wall Code.

Since there are no existing results on this stability problem with which values obtained here could be compared, a number of tests have been carried out in order to establish a correctly working code.

The first case is to take the limiting value of wall parameter which makes the boundary equivalent to a rigid wall (which is in effect to consider the limit $G_s \rightarrow \infty$). This gave satisfactory results and agreement with a wide range of rigid wall eigenvalues for $G_s/\rho \approx 20$.

The second check was to confirm, by increasing the value of N, that the code converged sufficiently well. Convergence on eigenvalues was achieved to an acceptable degree of tolerance for $N = 56$ compared to a value of $N = 40$ for the rigid wall code. This is generally the

case for compliant wall problems where greater variation occurs near the wall region and so increased resolution is required to give the same degree of accuracy.

A final test was to extract the Orr-Sommerfeld equation from the formulation and change the mean flow profile to that of the Falkner-Skan profile used in Chapter 4. Some slight manipulation of the boundary conditions was made to accommodate finite depth single-layer walls investigated as part of an earlier investigation. This then allowed comparison with results obtained using the Runge-Kutta shooting method and served to verify further the working code.

6.8 Results for Stationary Modes.

6.8.1 General Results.

The rigid wall stability characteristics of the stationary Type 1 mode of disturbance have been shown in Figure 6.2 in the form of neutral curves but in considering the effects of wall compliance it is really what occurs between the bounds of neutral stability that is of primary interest. The most rapidly growing mode is the most dominant and likely to appear in experiments and how wall compliance affects the maximum growth rate in particular is considered. Changes in the form of neutral curves can be misleading if the growth rates in the unstable regions are not also analysed. Nevertheless neutral curves do allow a wide range of Reynolds numbers to be assessed and have been calculated for a compliant wall ($G_s = 1000\text{N/m}^2$) at rotational speeds of 20, 40 and 60 rad/s with the density of the wall material taken to be the same as that of the fluid. The resulting neutral curves are given in Figure 6.4 and compare the compliant wall results with the corresponding rigid wall curves. A striking feature is the enlarged region of instability at $\Omega = 20\text{rad/s}$ associated with the Type 2 mode although the growth rates within this region remain relatively small and it is shown that the critical Reynolds number for this mode is reduced from $R = 400$ to $R = 177$. However, the destabilising influence of wall compliance is not a consistent feature since the unstable Type 2 region is reduced to a small closed loop centred at $R = 300$ for $\Omega = 40\text{rad/s}$ and the mode becomes completely stable at $\Omega = 60\text{rad/s}$. Wall compliance is shown to have only a slight effect on the neutral boundaries for β and α_r with the lower branch neutral modes in terms of β extending beyond the rigid wall curve. The range of unstable wave angles, however, changes considerably at $\Omega = 20\text{rad/s}$ as a result of the extended Type 2 unstable region and then narrows significantly with the large angles associated with the Type 2 mode eliminated above $\Omega = 40\text{rad/s}$. In terms of the effect of wall compliance on the Type 1 instability these curves show that the critical Reynolds number can be increased slightly with increasing levels of wall compliance.

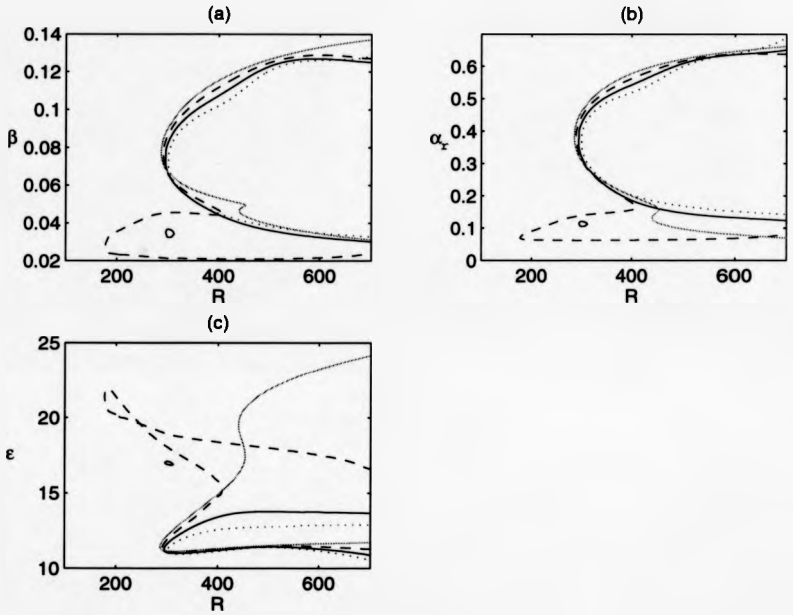

Figure 6.4: Neutral curves for stationary disturbances over rigid and compliant boundaries showing variation of R with (a) β, (b) α_r, (c) ε. Rigid wall : solid grey, $\Omega = 20$rad/s : - -, $\Omega = 40$rad/s : —, $\Omega = 60$rad/s : $\cdots$.

6.8.2 Stability Results for the Type 1 Instability

Stability results are then presented showing the degree of amplification which occurs at a number of different Reynolds numbers between $R = 300$ (just above the Type 1 critical value) and $R = 600$ for a rigid disc and the compliant wall ($G_s = 1000$ N/m^2) at rotational speeds of $\Omega = 20, 40$ and 60rad/s. Initial values of the Type 1 and 2 modes for the local iteration scheme were obtained by systematically decreasing the wall stiffness parameter and tracking the solutions from the rigid wall eigenvalues. Figures 6.5 and 6.6 show the local growth rates obtained for the Type 1 instability as a function of azimuthal wavenumber, β, and propagation angle, ε, respectively. It should be noted that direct comparisons between growth rates at fixed physical radial locations can be made between a specific compliant wall and the rigid wall if the Reynolds number is the same. (Rigid wall eigenvalues are unaffected by changes in rotation speed of the disc for fixed values of R.) However, comparisons between compliant walls at different rotation speeds but fixed Reynolds number will correspond to different physical locations.

Figure 6.5(a) shows the change in amplification rate at $R = 300$. Upper neutral points are shown to shift to lower values of β and the overall range of instability is reduced by increases in effective wall compliance with almost complete stabilisation occurring at $\Omega = 60$rad/s. Thus, for a high enough rotation speed (or sufficiently soft coating) the critical Reynolds number for the Type 1 branch will be substantially increased. At $R = 400$ and $\Omega = 20$rad/s it appears that a second range of unstable eigenvalues is produced outside the Type 1 unstable range at smaller values of β_r, but these growth rates are small compared to the Type 1 maximum value. This modified branch continues to be present at $\Omega = 40$rad/s but the sub-family of solutions then becomes stable. At $\Omega = 60$rad/s the character of the solution reverts back to being similar to that of the rigid wall shape with the disappearance of the sub-family of solutions. The additional branching at the two lower values of Ω is particularly evident in Figure 6.6(b) where larger propagation angles are produced with values more like those of the rigid wall Type 2 instability. Similar trends are seen in the plots for $R = 500$ and $R = 600$ where a substantial stabilising influence due to wall compliance is apparent. The maximum growth rate is shown to be successively reduced at each level of wall compliance and at all Reynolds numbers.

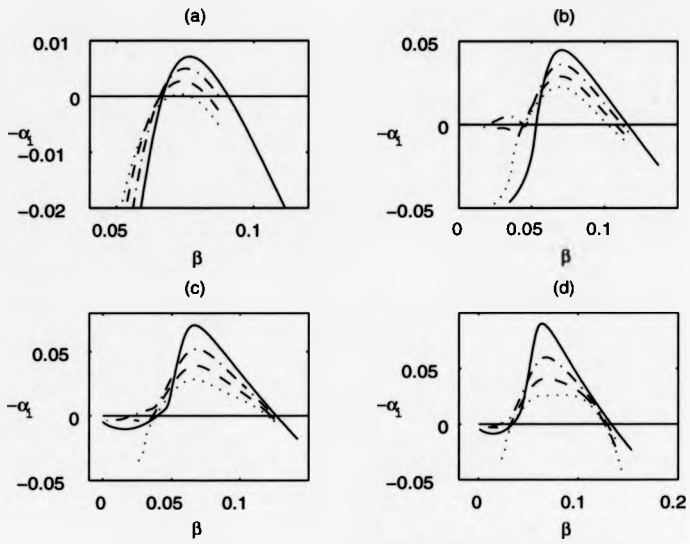

Figure 6.5: Amplification rates, $-\alpha_i$, for stationary Type 1 disturbances as a function of wavenumber, β. Rigid wall : —, $\Omega = 20$rad/s : $- \cdot -$, $\Omega = 40$rad/s : - -, $\Omega = 60$rad/s : $\cdots$. (a) $R = 300$, (b) $R = 400$, (c) $R = 500$, (d) $R = 600$.

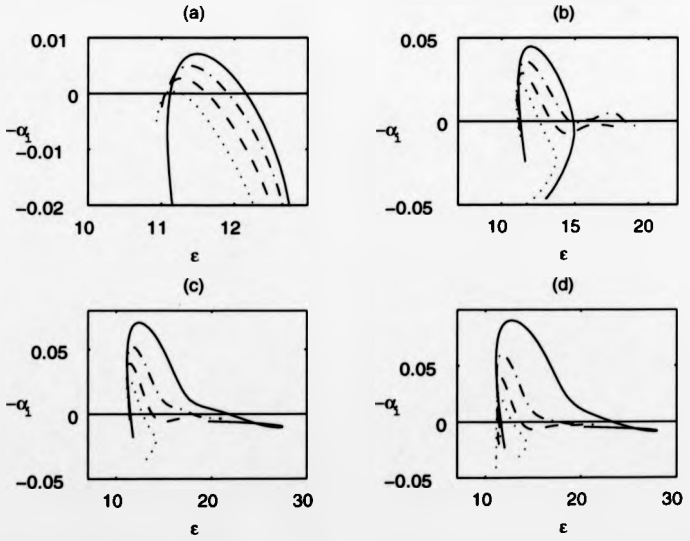

Figure 6.6: Amplification rate, $-\alpha_i$, as a function of wave angle, ε. Wall types as for above.

In terms of orientation of the spiral vortices associated with the Type 1 instability and the number of vortices connected with the most unstable mode the results are summarised in Table 6.1. This documentation shows that increasing levels of wall compliance tend to orientate the spirals associated with the most rapidly growing mode to slightly smaller angles. The corresponding azimuthal wavenumbers are also reduced and according to the formula of Malik *et al.* (1981), where the number of vortices is given by βR, this would imply a reduction in the number of vortices over the disc. However, the changes in β are only very slight so it is unlikely that any drastic changes would be observed in an experimental investigation. Apart from $R = 300$, where almost complete stabilisation occurs, it is shown that as wall compliance is increased there is a greater percentage reduction in maximum growth rate with increasing Reynolds number. Although the overall main unstable region is only slightly affected by this type of compliant boundary the results show that within these neutral bounds the effects on growth rate are significant.

Shown in Figure 6.7(a) and (b) is the variation of the radial component of the group velocity vector and the associated group velocity angle with Reynolds number respectively for the four types of boundary investigated. The magnitude of the group velocity generally lies in the range 0.05 - 0.1 with increases in Reynolds number reducing the value and greater degree of wall compliance increasing the magnitude. The same trend is seen in terms of the orientation of the outwardly directed group velocity vectors with angles ranging approximately $6° - 11°$.

Eigenfunctions giving the perturbation velocity component amplitudes at $R = 600$ for the rigid wall and compliant wall at $\Omega = 60$rad/s, where substantial stabilisation occurred, are shown in Figure 6.8. Owing to the form of the velocity conditions for zero frequency disturbances where

$$-i\omega\bar{\zeta}(0) = h(0),$$

the normal component, h, is still constrained to be zero at the interface. The other components are however free to take on non-zero values at the wall and, for the stationary case, are given by

$$\begin{aligned} f(0) &= -F'(0)\bar{\zeta}(0), \\ g(0) &= -G'(0)\bar{\zeta}(0). \end{aligned}$$

The eigenfunctions have been normalised such that the maximum perturbation amplitude is unity and this occurs in both boundary cases for the real part of the azimuthal velocity

component, g_r. The effect of the compliant boundary is seen to reduce the maximum amplitude of the normal velocity component whilst the imposition of the normalisation condition gives rise to notable values of f and g at the interface. The characteristic features of the two sets of eigenfunctions, however, remain essentially similar.

The wall displacements corresponding to this compliant case are shown in Figure 6.9(a) and (b). The displacement amplitudes have been normalised such that the normal displacement at the interface is unity (Figure 6.9(a)). The eigensolutions for the horizontal displacements have been combined to give the effective motion in the direction of propagation (Figure 6.9(b)). It can be seen that the wall is effective down to a dimensionless depth of approximately 20 which gives some indication of the finite depth a material wall of this kind would need to be in order to give comparable experimental results. From previous work (Chapter 4) where optimal wall properties were used the best results, as far as maximising growth rate reduction was concerned, were achieved when the boundary layer disturbances penetrated the full depth of the layer. Assuming this to be the case an estimate from the present results can be made for the dimensional depth this particular type of compliant wall would need to be. The wall length scale is the boundary layer displacement thickness, δ^*.

$$\delta^* = \left(\frac{\nu}{\Omega}\right)^{\frac{1}{2}}$$

Hence for $\Omega = 60$rad/s the value of δ^* is 0.129mm and therefore

$$\text{if} \quad \bar{z} \geq 20.0 \quad \text{then} \quad \frac{z}{\delta^*} \quad \Rightarrow \quad z \geq 2.58\text{mm}.$$

	Wall type	β	α_r	$-\alpha_i$	ε	% reduction
$R = 300$:	Rigid	0.076	0.37323	0.0071218	11.51	-
	$\Omega = 20$	0.075	0.37269	0.0049888	11.4	30.0
	$\Omega = 40$	0.074	0.37162	0.0027277	11.3	61.7
	$\Omega = 60$	0.073	0.37009	0.0003852	11.2	94.6
$R = 400$:	Rigid	0.071	0.33580	0.044751	11.94	-
	$\Omega = 20$	0.070	0.33894	0.036021	11.7	19.5
	$\Omega = 40$	0.070	0.34655	0.028846	11.4	35.5
	$\Omega = 60$	0.069	0.34642	0.022581	11.3	49.5
$R = 500$:	Rigid	0.0675	0.33107	0.070506	12.24	-
	$\Omega = 20$	0.068	0.32708	0.052037	11.7	26.2
	$\Omega = 40$	0.068	0.33566	0.039085	11.5	44.6
	$\Omega = 60$	0.066	0.33040	0.028479	11.3	59.6
$R = 600$:	Rigid	0.063	0.27626	0.090345	12.85	-
	$\Omega = 20$	0.067	0.32174	0.059938	11.8	33.7
	$\Omega = 40$	0.068	0.33551	0.040936	11.5	54.7
	$\Omega = 60$	0.087	0.43538	0.025934	11.3	71.3

Table 6.1: The effect of wall compliance on the most amplified mode of the Type 1 instability.

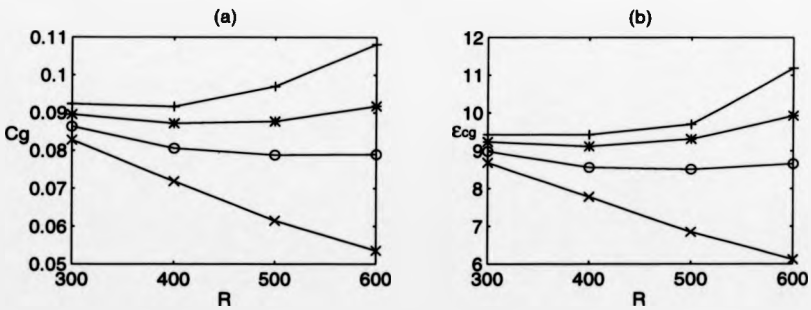

Figure 6.7: Variation of (a) group velocity magnitude and (b) angle at positions of maximum growth rate as a function of Reynolds number and wall type. (×) : Rigid wall, (o) : $\Omega = 20$rad/s, (∗) : $\Omega = 40$rad/s, (+) : $\Omega = 60$rad/s,

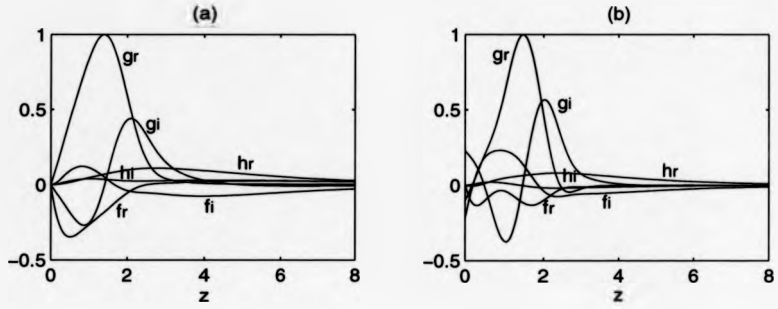

Figure 6.8: Eigenfunctions for Type 1 mode corresponding to position of maximum growth rate at R = 600. (a) Rigid wall, (b) Compliant wall at Ω = 60rad/s. Subscripts r and i refer to real and imaginary parts respectively.

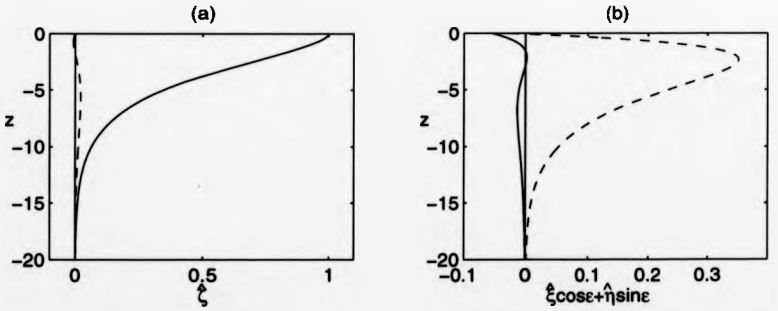

Figure 6.9: Wall displacement amplitudes at R = 600 and Ω = 60rad/s. (a) Vertical displacement, (b) Horizontal displacement in direction of propagation. Real part : —, Imaginary part : - -.

To gain a true sense of the effect of wall compliance amplitude ratios are perhaps a more realistic representation than local growth rates. In this case amplitude ratios are calculated by integrating $-\alpha_i$ from a fixed Reynolds number in an e^N-type of calculation. In conventional e^N calculations the lower integration parameter is taken to be the lower neutral point but in order to enable comparison with the results of Mack (1985) the integration is performed from a fixed Reynolds number of $R_o = 250$ such that

$$\ln\left(\frac{A_1}{A_o}\right) = \int_{R_o}^{R_1} (-\alpha_i) dR$$

where A_o is the initial disturbance amplitude and A_1 the corresponding amplitude at R_1.

The condition of constant βR is imposed throughout the integration, which as stated by Mack corresponds to the irrotationality condition of kinematic wave theory.

Although not a strict application of the e^N method similar deductions can be made from the results presented in Figure 6.10 which were obtained by numerical integration using the trapezium rule. The labels $R = 550, 600, 750$ and 850 in Figure 6.10(a)-(d) respectively refer to the Reynolds number for the last amplification curve. Previous e^N calculations for the rotating disc (Malik *et al.*, 1981) based on the transitional Reynolds number of $R = 520$ have indicated an N-factor of $N \approx 9$ for the predicted transition value. In the present calculations $R = 520$ gives an approximate value for N of 7 and this will be taken as an indication of the onset of transition. Wall compliance is thought to affect both the nonlinear and linear regimes and $N = 7$ is generally reckoned to correspond to the limit of linear theory. From Figure 6.10, where amplification curves are calculated in Reynolds number steps of 50, it can be seen that wall compliance raises considerably the value of R at which a value of $N = 7$ is attained. For the rigid wall a value of $R \approx 520$ gives a value of $N = 7$ which rises to $R \approx 550, 675$ and above 850 for the compliant wall at rotation speeds of 20, 40 and 60rad/s respectively. Indeed at the latter level of wall compliance the amplification curves begin to bunch up with each Reynolds number step so that the Reynolds number for which $N = 7$ increases sharply. The apparent discontinuity in the rigid wall amplification curves above $R = 500$ arises as a result in the change in nature of the lower branch of the instability. Wave angles at the point of maximum amplitude ratio for Reynolds numbers up to $R = 550$ are tabulated in Table 6.2 with rigid values agreeing well with those of Mack.

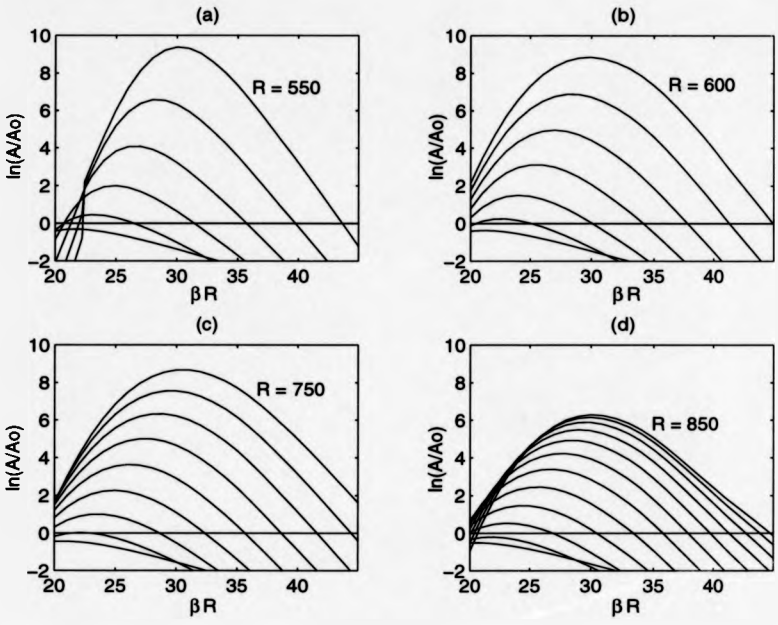

Figure 6.10: Amplitude ratios for the Type 1 stationary instability referenced to $R = 250$. (a) Rigid wall, (b) $\Omega = 20$rad/s, (c) $\Omega = 40$rad/s, (d) $\Omega = 60$rad/s.

Wall type	R	ε	βR	Wall Type	R	ε	βR
Rigid	350	12.4	23.0	Compliant	350	12.0	23.0
	400	13.1	25.0	$\Omega = 20$	400	12.5	24.0
	450	13.7	27.0		450	12.7	24.0
	500	14.8	28.0		500	13.0	27.0
	550	15.4	30.0		550	13.3	28.0
Compliant	350	11.8	22.0	Compliant			
$\Omega = 40$	400	12.0	24.0	$\Omega = 60$	400	11.8	23.0
	450	12.2	25.0		450	11.9	24.0
	500	12.4	26.0		500	11.9	29.0
	550	12.4	27.0		550	11.9	27.0

Table 6.2: Wave angle and value of βR at position of maximum amplitude ratio.

6.8.3 Stability Results for the Type 2 Instability.

Some interesting behaviour occurs for the Type 2 response to a compliant boundary. It appears that wall compliance of this kind can have both a stabilising and destabilising effect on this family of eigensolutions which has already been demonstrated by the neutral curve calculations and is shown further by the results in Figure 6.11. Results for $\Omega = 20$ and 40rad/s appear consistent with the usual response to wall compliance except at $R = 300$ where the mode becomes amplified but there is a definite change in character of the Type 2 solutions at $\Omega = 60$rad/s. As β is decreased the eigenmode undergoes considerable destabilisation and appears to reach some sort of plateau although the mode still remains damped for all β.

It thus appears that wall compliance lowers the critical Reynolds number for the Type 2 mode up to a certain degree of compliance after which the effect then becomes a stabilising one in terms of the onset Reynolds number.

Eigenfunctions at $R = 300$ for the Type 2 mode are given in Figure 6.12 at positions corresponding to the least stable eigenvalue. This shows the rigid wall eigensolution is altered quite significantly by the compliant boundary with large values of f and g at the wall/flow interface. This should be contrasted with the Type 1 results at $R = 600$ (Figure 6.8, p. 157) where only slight changes in the profiles occurred. This indicates that the compliant wall induces greater motion at the interface for this Type 2 mode which may be a reason for its adverse response to boundary compliance.

Wall eigenfunctions for the compliant case at $\Omega = 20$rad/s and $R = 300$ are given in Figure 6.13 which shows that boundary layer disturbances have some effect within the wall down to non-dimensional depths of greater than 50.0, a value over twice that in the example cited for the Type 1 instability. This is suggestive to some extent that this type of wall is not ideally suited to the Type 2 form of instability. Dimensional depths deduced from these results indicate values greater than 11.2mm which is considerably greater and physically quite large compared to previous examples. If wall compliance was to be used as a method of suppressing the Type 2 instability then the results so far appear to indicate that different wall structures may be required in order for wall compliance to have any beneficial effect on this form of instability.

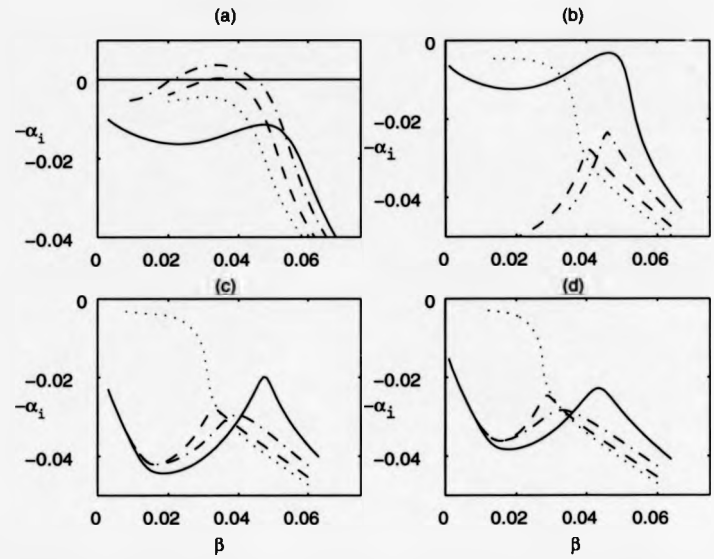

Figure 6.11: Amplification rates, $-\alpha_i$, for stationary Type 2 disturbances as a function of azimuthal wavenumber, β. Rigid wall : —, $\Omega = 20$rad/s : − · − , $\Omega = 40$rad/s : - - , $\Omega = 60$rad/s : · · ·. (a) $R = 300$, (b) $R = 400$, (c) $R = 500$, (d) $R = 600$.

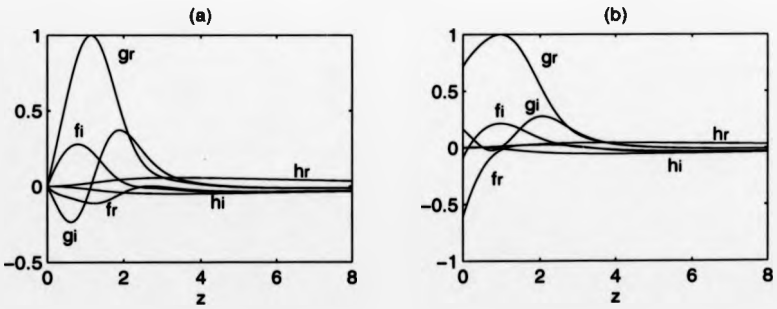

Figure 6.12: Eigenfunctions corresponding to least stable Type 2 mode at $R = 300$. (a) Rigid wall, (b) Compliant wall at $\Omega = 20$rad/s.

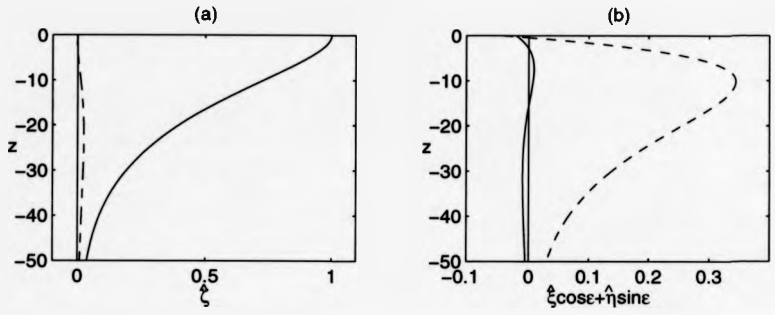

Figure 6.13: Wall displacement amplitudes for $R = 300$ and $\Omega = 20$rad/s. (a) Vertical displacement, (b) Horizontal displacement in direction of propagation. Real part : —, Imaginary part : - -.

6.9 Energy Equation.

An energy equation for three-dimensional disturbances in a three-dimensional boundary layer is derived in terms of cylindrical coordinates in an analogous manner to the two-dimensional cartesian version described in Chapter 4. The three-dimensionality of the problem as well as the use of the different coordinate system brings about additional terms compared to the energy description for the two-dimensional boundary stability problem. Initially the derivation will be in terms of a general three-dimensional mean flow field, $\boldsymbol{U} = [U, V, W]$, and a corresponding perturbation velocity and pressure field, $[\boldsymbol{u}, p] = [u, v, w, p]$, before introducing quantities specific to the rotating disc.

This energy equation will be used initially to assess the differing response to wall compliance of the two types of stationary instability.

The energy equation is defined in the usual way through the following combination of governing equations.

$$\text{Energy eqn.} = u(u\text{-mom. eqn.}) + v(v\text{-mom. eqn.}) + w(w\text{-mom-eqn.})$$

along with the imposition of the incompressibility condition $\nabla \cdot \boldsymbol{u} = 0$. The linearised momentum equations in terms of the generalised dimensional velocity and pressure fields

are as follows.

$$\begin{aligned}\frac{\partial u}{\partial t} &+ U\frac{\partial u}{\partial r} + u\frac{\partial U}{\partial r} + \frac{V}{r}\frac{\partial u}{\partial \theta} + W\frac{\partial u}{\partial z} + w\frac{\partial U}{\partial z} - 2\frac{Vv}{r} - 2\Omega v \\ &= -\frac{1}{\rho}\frac{\partial p}{\partial r} + \nu\left[\frac{\partial^2 u}{\partial r^2} + \frac{1}{r^2}\frac{\partial^2 u}{\partial \theta^2} + \frac{\partial^2 u}{\partial z^2} + \frac{1}{r}\frac{\partial u}{\partial r} - \frac{u}{r^2} - \frac{2}{r^2}\frac{\partial v}{\partial \theta}\right] \qquad (6.67)\end{aligned}$$

$$\begin{aligned}\frac{\partial v}{\partial t} &+ U\frac{\partial v}{\partial r} + u\frac{\partial V}{\partial r} + \frac{V}{r}\frac{\partial v}{\partial \theta} + W\frac{\partial v}{\partial z} + w\frac{\partial V}{\partial z} + \frac{Uv}{r} + \frac{uV}{r} + 2\Omega u \\ &= -\frac{1}{\rho r}\frac{\partial p}{\partial \theta} + \nu\left[\frac{\partial^2 v}{\partial r^2} + \frac{1}{r^2}\frac{\partial^2 v}{\partial \theta^2} + \frac{\partial^2 v}{\partial z^2} + \frac{1}{r}\frac{\partial v}{\partial r} - \frac{v}{r^2} + \frac{2}{r^2}\frac{\partial u}{\partial \theta}\right] \qquad (6.68)\end{aligned}$$

$$\begin{aligned}\frac{\partial w}{\partial t} &+ U\frac{\partial w}{\partial r} + u\frac{\partial W}{\partial r} + \frac{V}{r}\frac{\partial w}{\partial \theta} + W\frac{\partial w}{\partial z} + w\frac{\partial U}{\partial z} - 2\frac{Vv}{r} - 2\Omega v \\ &= -\frac{1}{\rho}\frac{\partial p}{\partial z} + \nu\left[\frac{\partial^2 w}{\partial r^2} + \frac{1}{r^2}\frac{\partial^2 w}{\partial \theta^2} + \frac{\partial^2 w}{\partial z^2} + \frac{1}{r}\frac{\partial w}{\partial r}\right] \qquad (6.69)\end{aligned}$$

Attention is drawn to the fact that when the energy equation is formed the terms $-2\Omega v$ and $2\Omega u$ cancel so that Coriolis effects do not play a part in the final energy balance.

Summation of the three combined equations gives rise to the following equation where $K = \frac{1}{2}(u^2 + v^2 + w^2)$ represents the kinetic energy of the perturbation.

$$\begin{aligned}\left\{\frac{\partial}{\partial t} + U\frac{\partial}{\partial r} + \frac{V}{r}\frac{\partial}{\partial \theta} + W\frac{\partial}{\partial z}\right\}K &= -uw\frac{\partial U}{\partial z} - vw\frac{\partial V}{\partial z} - w^2\frac{\partial W}{\partial z} \\ &\quad -u^2\frac{\partial U}{\partial r} - \frac{Uv^2}{r} - \frac{1}{\rho}\left[u\frac{\partial p}{\partial r} + \frac{v}{r}\frac{\partial p}{\partial \theta} + \frac{\partial p}{\partial z}\right] \\ &\quad +\nu\left[u\,\Delta\,u + v\,\Delta\,v + w\,\Delta\,w - \frac{u^2}{r^2} - \frac{2u}{r^2}\frac{\partial v}{\partial \theta} - \frac{v^2}{r^2} - \frac{2v}{r^2}\frac{\partial u}{\partial \theta}\right] \qquad (6.70)\end{aligned}$$

where $\Delta \equiv \frac{\partial^2}{\partial r^2} + \frac{1}{r^2}\frac{\partial^2}{\partial \theta^2} + \frac{\partial^2}{\partial z^2} + \frac{1}{r}\frac{\partial}{\partial r}$.

However, the pressure terms can be manipulated into a more convenient form as follows.

$$\begin{aligned}u\frac{\partial p}{\partial r} + \frac{v}{r}\frac{\partial p}{\partial \theta} + \frac{\partial p}{\partial z} = (\boldsymbol{u}\cdot\nabla)p &= \nabla\cdot(\boldsymbol{u}p) - p\nabla\cdot\boldsymbol{u} \\ &= \nabla\cdot(\boldsymbol{u}p) \text{ for incompressible fluids} \\ &= \left(\frac{\partial}{\partial r} + \frac{1}{r}\right)(up) + \frac{1}{r}\frac{\partial}{\partial \theta}(vp) + \frac{\partial}{\partial z}(wp)\end{aligned}$$

The viscous terms can also be rearranged and expressed in the form of a viscous dissipation contribution with correctional terms using the following identity.

$$\frac{\partial}{\partial x_i}(u_j\sigma_{ij}) - \sigma_{ij}\frac{\partial u_j}{\partial x_i} = u\,\Delta\,u + v\,\Delta\,v + w\,\Delta\,w - \left(u\frac{\partial}{\partial r} + \frac{v}{r}\frac{\partial}{\partial \theta} + w\frac{\partial}{\partial z}\right)\left(\frac{u}{r}\right)$$

Using these expressions then gives an energy equation of the form

$$\begin{aligned}\left\{\frac{\partial}{\partial t} \right. &+ \left. U\frac{\partial}{\partial r} + \frac{V}{r}\frac{\partial}{\partial \theta} + W\frac{\partial}{\partial z}\right\} K = -uw\frac{\partial U}{\partial z} - vw\frac{\partial V}{\partial z} - w^2\frac{\partial W}{\partial z} \\ &- u^2\frac{\partial U}{\partial r} - \frac{Uv^2}{r} - \frac{1}{\rho}\left[\frac{\partial}{\partial r}(up) + \frac{1}{r}\frac{\partial}{\partial \theta}(vp) + \frac{\partial}{\partial z}(wp) + \frac{up}{r}\right] \\ &+ \frac{1}{\rho}\left[\frac{\partial}{\partial x_i}(u_j\sigma_{ij}) - \sigma_{ij}\frac{\partial u_j}{\partial x_i}\right] + \nu\left[-\frac{u^2}{r} - \frac{2u}{r^2}\frac{\partial v}{\partial \theta} + \frac{2v}{r^2}\frac{\partial u}{\partial \theta} - \frac{v^2}{r^2}\right. \\ &+ \left.\frac{1}{r}\frac{\partial u}{\partial r} + \frac{1}{r}\frac{\partial v}{\partial r} + \frac{1}{r}\frac{\partial w}{\partial r} + \frac{1}{r}\left\{u\frac{\partial u}{\partial r} + \frac{v}{r}\frac{\partial u}{\partial \theta} + \frac{w}{r}\frac{\partial u}{\partial z}\right\}\right]. \end{aligned} \tag{6.71}$$

No non-dimensionalisation has yet taken place and all of the above quantities at this stage are dimensional. If the travelling wave disturbance form is assumed such that

$$\boldsymbol{u} = \hat{\boldsymbol{u}}e^{i(\alpha r + \beta r\theta - \omega t)} + \text{c.c.}$$

then the time derivative can be removed from Eq.(6.71) by time-averaging the perturbation terms and at the same time integration is performed across the boundary layer. Since the approximation $r = R$ will subsequently be applied (after non-dimensionalisation) and $O(\frac{1}{R^2})$ terms neglected the $O(\frac{1}{r})$ viscous terms are dropped at this stage to leave

$$\begin{aligned}\int_0^\infty \left\{U\frac{\partial}{\partial r} + \frac{V}{r}\frac{\partial}{\partial \theta} + W\frac{\partial}{\partial z}\right\}\overline{K}\,dz &= \int_0^\infty -\overline{uw}\frac{\partial U}{\partial z}dz + \int_0^\infty -\overline{vw}\frac{\partial V}{\partial z}dz \\ &+ \int_0^\infty -\overline{w^2}\frac{\partial W}{\partial z}dz - \int_0^\infty \overline{u^2}\frac{\partial U}{\partial r}dz - \int_0^\infty \frac{U\overline{v^2}}{r}dz - \frac{1}{\rho}\int_0^\infty \left[\frac{\partial}{\partial r}(\overline{up})\right. \\ &+ \left.\frac{1}{r}\frac{\partial}{\partial \theta}(\overline{vp}) + \frac{\partial}{\partial z}(\overline{wp}) + \frac{\overline{up}}{r}\right]dz + \frac{1}{\rho}\int_0^\infty \left[\frac{\partial}{\partial x_i}(\overline{u_j\sigma_{ij}}) - \overline{\sigma_{ij}\frac{\partial u_j}{\partial x_i}}\right]dz \end{aligned} \tag{6.72}$$

where an overbar indicates a time-averaged quantity.

The $\partial/\partial\theta$ terms subsequently vanish in the time average procedure since an axisymmetric distribution is assumed in the azimuthal direction (real β) and with some rearrangement the general dimensional form of the energy equation in cylindrical coordinates becomes

$$\int_0^\infty \underbrace{\left[U\frac{\partial \overline{K}}{\partial r}\right.}_{\text{a}} + \underbrace{\frac{1}{\rho}\frac{\partial}{\partial r}(\overline{up})}_{\text{b}} - \underbrace{\left.\frac{1}{\rho}\frac{\partial}{\partial r}\left\{\overline{u\sigma_{11}} + \overline{v\sigma_{12}} + \overline{w\sigma_{13}}\right\}\right]}_{\text{c}} dz =$$

$$\underbrace{\int_0^\infty \left[\left(-\overline{uw}\frac{\partial U}{\partial z}\right) + \left(-\overline{vw}\frac{\partial V}{\partial z}\right) + \left(-\overline{w^2}\frac{\partial W}{\partial z}\right)\right]dz}_{\text{I}} - \underbrace{\frac{1}{\rho}\int_0^\infty \left(\overline{\sigma_{ij}\frac{\partial u_j}{\partial x_i}}\right)dz}_{\text{II}}$$

$$\underbrace{-\frac{1}{\rho}\int_0^\infty \left(\frac{\overline{up}}{r}\right)dz + \frac{1}{\rho}(\overline{wp})_w}_{\text{III}} \underbrace{-\frac{1}{\rho}\left[\overline{u\sigma_{31}} + \overline{v\sigma_{32}} + \overline{w\sigma_{33}}\right]_w}_{\text{IV}} -$$

$$\underbrace{\int_0^\infty W\frac{\partial\overline{K}}{\partial z}dz - \int_0^\infty \overline{u^2}\frac{\partial U}{\partial r}dz - \int_0^\infty \frac{U\overline{v^2}}{r}dz}_{\text{V}}.$$

(6.73)

Terms easily identified from the two-dimensional cartesian version of this equation are the Reynolds stress production terms (I) and the viscous dissipation contribution (II). Term III contains pressure work terms where $(\overline{wp})_w$ represents the work done by the fluctuating pressure on the wall and an additional pressure term arises from the use of the cylindrical coordinate system. IV describes the work done on the wall by the viscous stresses. The element labelled V contains elements arising from streamline curvature effects and the three-dimensionality of the mean flow profile and have no corresponding two-dimensional cartesian counterparts. In the energy analysis of Faller (1991) similar contributions were described as being dependent upon the geometrical effects of the change of R with radius. (Rossby number terms). On the left hand side there is the average disturbance kinetic energy convected by the radial mean flow component (a) followed by the work done by the perturbation pressure (b) and viscous stresses across some internal boundary in the fluid (c).

The above energy equation is now non-dimensionalised and the velocity fields for the rotating disc taken as before (where r in this section refers to the dimensional radius) such that

$$\begin{aligned} \boldsymbol{U} &= [r\Omega F, r\Omega G, (\nu\Omega)^{\frac{1}{2}}H] \\ \boldsymbol{u} &= [r\Omega f, r\Omega g, r\Omega h]e^{i(\alpha r+\beta R\theta-\omega t)} + \text{c.c.} = r\Omega[\hat{f},\hat{g},\hat{h}] + \text{c.c.} \end{aligned}$$

Substitution of these forms and the use of the standard reference scales of the preceding analysis generates the non-dimensional energy equation specific to the rotating disc problem.

$$\frac{d}{dr}\int_0^\infty \left[F[\overline{\hat{K}}] + (\overline{\hat{f}\hat{p}}) - (\overline{\hat{f}\hat{\sigma}_{11}}) + \overline{\hat{g}\hat{\sigma}_{12}} + \overline{\hat{h}\hat{\sigma}_{13}})\right]dz =$$

$$\int_0^\infty \left[(-\overline{\hat{f}\hat{h}}F') + (-\overline{\hat{f}\hat{h}}G') + (-\overline{\hat{h}^2}\frac{H'}{R})\right]dz - \int_0^\infty \left(\overline{\hat{\sigma}_{ij}\frac{\partial\hat{u}_j}{\partial x_i}}\right)dz - \frac{1}{R}\int_0^\infty (\overline{\hat{f}\hat{p}})dz + (\overline{\hat{h}\hat{p}})_w$$

$$-(\overline{\hat{f}\hat{\sigma}_{31}} + \overline{\hat{g}\hat{\sigma}_{32}} + \overline{\hat{h}\hat{\sigma}_{33}})_w - \int_0^\infty \frac{H}{R}\frac{\partial\overline{\hat{K}}}{\partial z}dz - \int_0^\infty \frac{\overline{\hat{f}^2}F}{R}dz - \int_0^\infty \frac{\overline{\hat{g}^2}F}{R}dz \qquad (6.74)$$

The left hand side derivative generates a factor of $-2\alpha_i$ which can be taken outside of the integral and the right hand side integrals are then normalised by the value of the remaining integral so that the final energy equation takes the form :

$$-2\alpha_i = \text{normalised energy contributions.}$$

6.9.1 Energy results for stationary modes.

The energy calculation is carried out for the Type 1 instability at $R = 600$ and compares the statistics for the rigid wall with those of the compliant wall at $\Omega = 60$rad/s where a large reduction in the growth rate of the most unstable mode was achieved. For the Type 2 mode comparisons are made at $R = 300$ between the rigid wall and the $\Omega = 20$rad/s compliant case where the effect of wall compliance was destabilising. Since the disturbances are stationary the terms $(\overline{\hat{h}\hat{p}})_w$ and $(\overline{\hat{h}\hat{\sigma}_{33}})_w$ in the energy balance for the compliant case are exactly zero as a result of the constraint $h = 0$ at the wall. Some of the other terms in both the rigid and compliant examples turn out to be negligible and are omitted from the following figures.

In the numerical calculations both sides of the energy equation are found to agree to at least three significant figures.

Figure 6.14(a) compares the constituent terms in the energy equation for the selected modes at $R = 600$. The major influence of wall compliance on the Type 1 instability is seen to occur through reductions to the Reynolds stress production terms and through increased conventional viscous dissipation. The work done by the viscous stresses at the wall plays a minor role with other terms in the energy equation being negligible. G1 and G2 in the figure correspond to the so-called geometrical effects and represent the second and third terms labelled V in Eq.(6.73). Figure 6.14(b) presents the value of the Reynolds stress production term resolved in the direction of the group velocity vector and in the direction perpendicular to it followed by the viscous stress work terms in these directions. The relative Reynolds stress contributions for this mode are shown to increase with wall compliance which occurs largely as a result of the change in the angle of the group velocity vector (see Figure 6.7, p. 156), but the increased viscous dissipation term is sufficient enough to bring about the observed growth rate reduction. The lowering of growth rate therefore appears to be brought about solely by alteration to the mechanisms involved in the rigid wall case without contributions from any pressure work or any favourable contribution by viscous stress work terms at the wall. Figure 6.15(a) and (b) compare the Reynolds stress distributions across the boundary layer in the direction of energy transfer and perpendicular to the group velocity direction respectively. It can be seen that in the near wall region wall compliance brings about negative Reynolds stress compared the the totally positive rigid wall distribution although the net effect across the boundary layer is one of slight increase. In the normal direction no significant differences are observed.

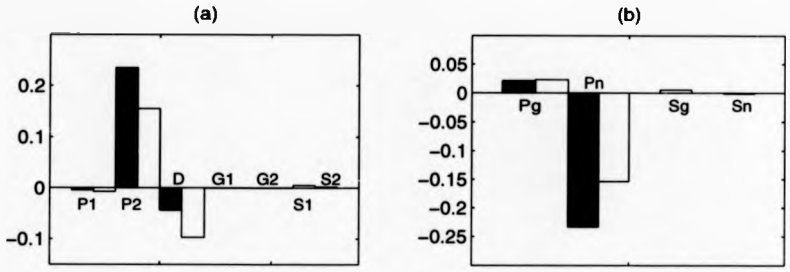

Figure 6.14: Comparison of numerical values between rigid and compliant contributions to terms in the energy balance equation at $R = 600$. Unshaded regions correspond to compliant wall at $\Omega = 60$rad/s. (a) P1 and P2 : Reynolds stress production terms in radial and azimuthal directions respectively, D : viscous dissipation, G1 and G2 : geometrical effects, S1 and S2 : work done by viscous stresses at the wall in radial and azimuthal directions respectively. (b) Pg and Pn : Reynolds stress production in group velocity and normal (n) directions, Sg and Sn : Work done by viscous stresses in ε_{cg} and n directions.

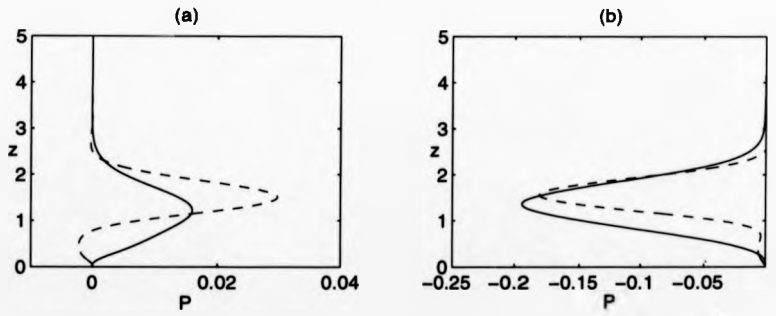

Figure 6.15: (a) Reynolds stress distributions in direction of group velocity, (b) Reynolds stress distributions normal to group velocity vector at $R = 600$. Rigid wall : —, Compliant wall : - -.

Characteristics of the Type 2 instability at $R = 300$ are shown in the same form in Figure 6.16(a) and (b). In this case the rigid wall values represent a stable mode and the viscous dissipation term is shown to dominate the rigid wall energy terms. Contributions to the energy balance from the so-called geometrical effects (G1 and G2) play a more significant role than in the Type 1 rigid case examined above and are shown to remove energy from the system. In the compliant wall example these terms remain essentially unchanged but the effect of compliance on the remaining terms is noticeably different to the results for the Type 1 instability. In this case the conventional viscous dissipation term is reduced in value and a large contribution to the energy production arises through the viscous stress term, $(\overline{f\sigma_{31}})_w$, (S1). When considering the contributions resolved in the group velocity and perpendicular directions it is evident that the work done by the viscous stresses at the wall is significant and suggests that it is these terms which are responsible for the destabilisation of the Type 2 mode in the presence of the compliant boundary. Reynolds stress distributions for these examples are shown in Figure 6.17(a) and (b) and the main differences from the Type 1 instability is the slight increase in production by the Reynolds stress in the group velocity direction at the wall but more significant is the noticeable reduction in peak value for the normal direction indicating an increase in positive Reynolds stress in this direction.

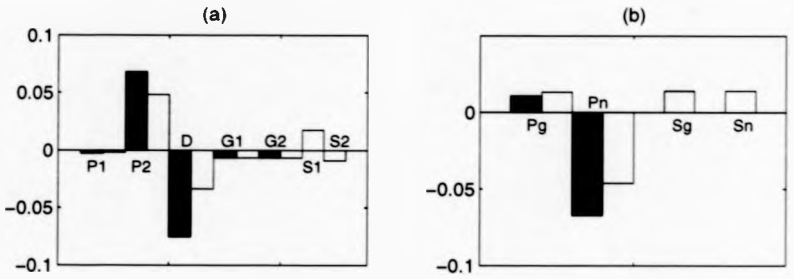

Figure 6.16: Comparison of numerical values between rigid and compliant contributions to terms in the energy balance equation at $R = 300$. Unshaded regions correspond to compliant wall at $\Omega = 20$rad/s. (a) P1 and P2 : Reynolds stress production terms in radial and azimuthal directions respectively. D : viscous dissipation. G1 and G2 : geometrical effects. S1 and S2 : work done by viscous stresses at the wall in radial and azimuthal directions respectively. (b) Pg and Pn : Reynolds stress production in group velocity and normal (n) directions. Sg and Sn : Work done by viscous stresses in ε_{cg} and n directions.

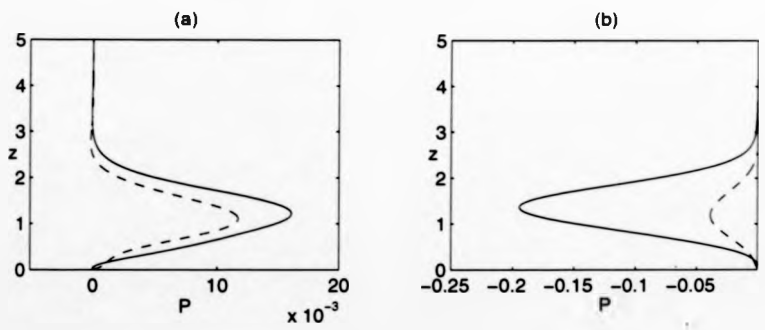

Figure 6.17: (a) Reynolds stress distributions in direction of group velocity. (b) Reynolds stress distributions normal to group velocity vector at $R = 300$. Rigid wall : —, Compliant wall : - -.

The difference in energy production in the normal direction for the two modes of instability also provides some possible mechanism for the occurrence of the Type 2 instability itself which is shown to arise theoretically only when Coriolis and streamline curvature effects are considered. No clear physical mechanism for the occurrence of this instability has been established in the existing literature on this subject. It is known for the Ekman layer, where a similar type of instability occurs, that flow in a direction outwards from the central rotation axis induces a motion (geostrophic flow) perpendicular to that outflow which is directed to oppose the rotation. In an analogous manner it is argued that this sort of Coriolis induced motion would also occur for radial flows (see Figure 6.18) with the effect of producing a greater Reynolds stress in that direction thereby providing encouragement for increased disturbance energy production and a route to instability. In the presence of a compliant boundary work done by viscous stresses is also likely to increase as a result of this motion thus enhancing, rather than controlling, the instability process by generating additional energy production contributions. In the results presented large viscous stress energy production terms are apparent compared to the negligible values in the Type 1 energy balance which gives support to this theory. At the Reynolds number previously considered for the Type 2 instability the rigid wall eigenvalue is stable but the Reynolds stress term normal to the group velocity vector is comparatively greater than for the Type 1 rigid wall instability indicating less energy dissipation due to negative Reynolds stress in this direction.

The Type 2 stationary mode first becomes unstable for a rigid boundary at $R = 440$ and energy budgets are presented in Figure 6.19 comparing Type 1 and 2 rigid wall instabilities for modes which have comparable growth rates at $R = 450$. From these results it can be seen that the viscous dissipation is greater for the Type 1 mode which balances the major Reynolds stress production term. In considering the Reynolds stress contributions resolved in the direction normal to the group velocity vector it is shown that the dissipation due to negative Reynolds stress in the Type 2 case is less than half that of the Type 1 mode whereas positive Reynolds stress is greater in the direction of group velocity for the Type 1 mode. It could therefore be argued that the Type 1 mode is prone to instability via positive energy production in the direction of group velocity whilst the Type 2 mode is susceptible to instability because less energy dissipation occurs normal to the direction of group velocity.

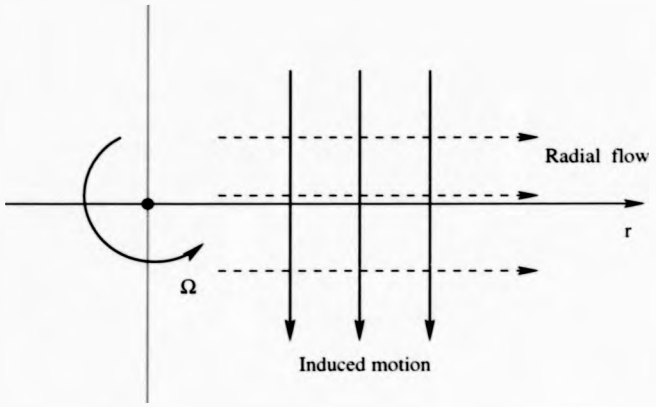

Figure 6.18: Representation of geostrophic flow.

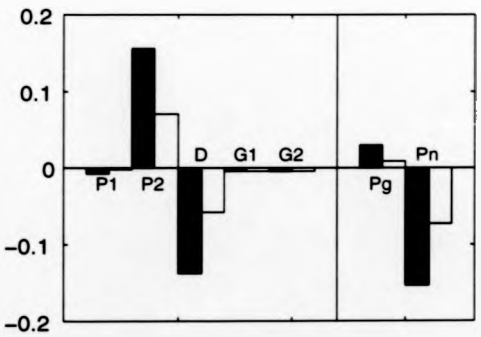

Figure 6.19: Energy budgets for stationary rigid wall Type 1 (shaded) and Type 2 instabilities at $R = 450$. Labels refer to terms defined in previous figures.

6.10 Stationary Vortex Structures.

Velocity vectors showing the form of the spiral vortices are calculated from the eigenfunctions and eigenvectors by plotting the vector

$$\left[\mathrm{Re}(\alpha F + \beta G) + a\mathrm{Re}([\alpha f + \beta g]E), \frac{H}{R} + a\mathrm{Re}(hE)\right]$$

where a is an amplitude and $E = \exp[i(\alpha r + \beta R\theta)]$.

Figure 6.20 shows the pattern formed by the Type 1 instability at $R = 600$ for the rigid wall and the compliant at $\Omega = 60$rad/s with $a = 0.1$. Since the basic character of the eigensolutions for this mode remains intact when the compliant boundary is used the patterns vary only in a subtle sense. The velocity vectors indicate the co-rotating vortices with centres located at $z \approx 1.25$ which remain largely unaffected by the presence of a compliant boundary so that wall compliance greatly affects the growth of these crossflow vortices but not the basic structure of the instability.

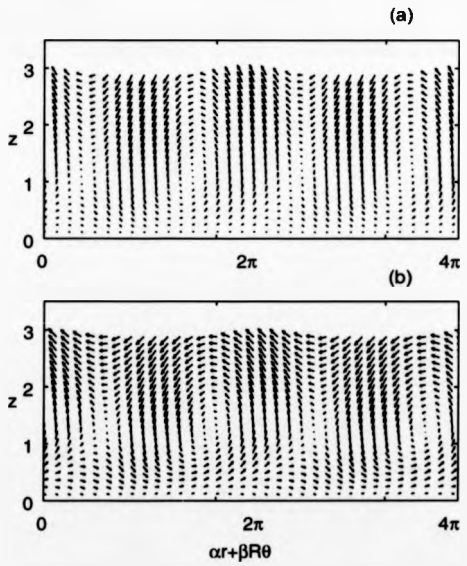

Figure 6.20: Vortex structure of Type 1 instability at $R = 600$. (a) Rigid wall, (b) Compliant wall at $\Omega = 60$rad/s.

6.11 Stability Results for Travelling-wave Modes.

In the study of travelling disturbances which become amplified in the rotating disc boundary layer the whole frequency range is scanned to produce a series of amplification curves as a function of azimuthal wavenumber at selected Reynolds numbers. The global scheme was used to locate the unstable reference rigid wall branches due to the Type 1 and 2 instabilities. For clarity only the point of maximum growth rate is extracted from each frequency curve since the most rapidly growing mode is the one of primary importance and likely to be detected in experiments. For the rigid wall maximum amplification rates are plotted against frequency in Figure 6.21(a) and (b) for $R = 300$ and 400 respectively. Negative values of frequency are taken to represent inwardly travelling disturbances given that the wavenumber vectors are restricted to point only outwards in the direction of increasing radius.

The Type 2 instability is shown to be dominant at $R = 300$ producing higher growth rates compared to those of the Type 1 mode of instability. The roles are reversed however when the Reynolds number is increased to $R = 400$. Growth rates for the Type 2 mode remain virtually unaltered in moving from $R = 300$ to $R = 400$ with the maximum value remaining near 0.022 whereas the Type 1 maximum value increases from 0.0089 at $R = 300$ to 0.052 at $R = 400$. Typical characteristics of this Type 2 mode are orientation at smaller, more negative wave angles with higher phase speeds than the Type 1 family of solutions. At the two Reynolds numbers used the Type 2 mode of disturbance becomes amplified only for positive frequencies and the unstable range extends to high frequencies and negative values of β.

Figure 6.22 shows results at $R = 300$ for the compliant boundary at rotation speeds of 20, 40 and 60rad/s referenced to the rigid wall maximum amplification envelope. The Type 1 instability is seen to be favourably affected by wall compliance with a reduction in maximum amplification rate across the whole frequency range but with greater effect on the inwardly travelling (negative frequency) waves resulting in a reduction in the unstable range of frequencies at this Reynolds number. The instability becomes almost completely stabilised at $\Omega = 60$rad/s with the frequency range of unstable modes reduced to primarily the stationary case. No marked differences arise in terms of the wavenumber, α_r, at each β value when wall compliance is introduced so that Figure 6.21(c) is generally still applicable in the compliant wall case. However, increasing the level of wall compliance shifts the overall maximum growth rate to frequencies of lower magnitude and consequently smaller values of β and wave angle. These observations are recorded in Table 6.3.

These calculations were repeated at the higher Reynolds number of $R = 400$ where for in-

wardly travelling disturbances the effects of wall compliance follow the same general pattern observed at $R = 300$. However, across a small band of positive frequencies ($0.0 < \omega < 0.02$) some anomalous results become evident as shown by the amplification curves across the entire unstable frequency range in Figure 6.23 where amplification rate is plotted against azimuthal wavenumber and each component curve corresponds to a different disturbance frequency. The compliant wall curves range from $\omega = -0.047$ (at the upper β range) moving to $\omega = 0.043$ as β is decreased. Also shown in this figure for reference are the maximum amplification envelopes for the rigid wall Type 1 and 2 branches. The greater concentration of curves indicates the position of the frequencies over which the irregular behaviour occurs. Within this sub-range amplification rates reach a peak following previous trends but after some subsequent reduction in growth rate the eigenmode appears to become more unstable again. This new growth becomes quite marked and rapid as frequencies increase within this range and produces high amplification rates above the rigid wall maximum. At the lower end of this frequency band the amplification rate is found to fall again producing a lower neutral point as indicated in Figure 6.23 where some curves protrude from the general envelope. At the upper end of this range where the large growth rates are produced the eigenmode becomes difficult to locate as β is decreased further owing to problems with numerical convergence.

The anomalous behaviour described above is found to occur across a range of β and ω at which the two rigid wall instabilities coexist (see Figure 6.21(b)) and is suggestive of some possible modal interaction between the two eigenmodes under the influence of wall compliance.

The response of the Type 2 mode differs considerably from that of the Type 1 instability. At both $R = 300$ and $R = 400$ amplification rates and wave angles are for the majority of unstable frequencies left virtually unaffected by the presence of a compliant boundary but at the lower end of the unstable frequency range the behaviour changes. At $R = 300$ the mode can become destabilised as demonstrated in the case of the stationary disturbances at $\Omega = 20$rad/s (§ 6.8.2). At $R = 400$, as the end of the unstable frequency band is approached, the eigenvalues begin to depart from their rigid wall counterparts to produce completely stable solution branches (rather like the change in character for the rigid wall stationary branches between $R = 400$ and $R = 500$ when the Type 2 branch becomes more stable). This occurs within the same frequency range as the unconventional Type 1 results further suggesting some interactive process between the two modes.

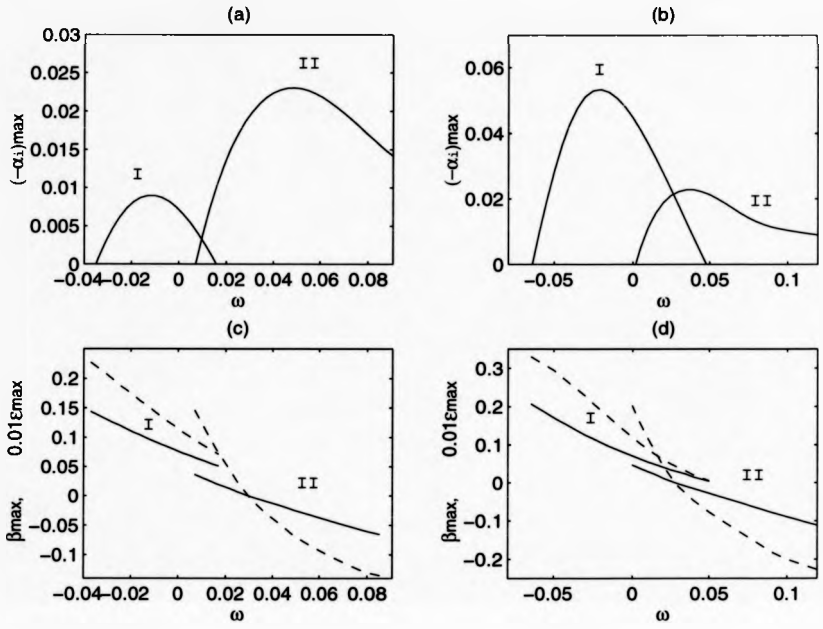

Figure 6.21: Most unstable travelling disturbances as a function of frequency, ω. Labels I and II refer to Type 1 and 2 modes of instability. (a) $R = 300$, (b) $R = 400$: Maximum growth rate against frequency. (c) $R = 300$, (d) $R = 400$: Variation of azimuthal wavenumber (—) and wave angle (- -) with frequency at position of maximum growth rate.

Wall type	$(-\alpha_i)_{max}$	ω_{max}	β_{max}	ε_{max}	ω-range
Rigid	0.0089395	-0.013	0.0980	15.37	$-0.035 - 0.015$
$\Omega = 20$	0.0056594	-0.008	0.0890	13.61	$-0.026 - 0.014$
$\Omega = 40$	0.0027896	-0.002	0.0765	11.85	$-0.015 - 0.012$
$\Omega = 60$	0.0003852	0.000	0.0730	11.16	0.0

Table 6.3: Parameters giving maximum growth rate of Type 1 instability for travelling disturbances at $R = 300$. Subscript max refers to the position of maximum growth rate across the whole frequency range.

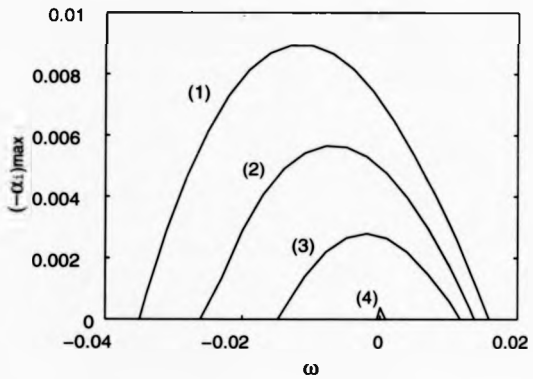

Figure 6.22: Effect of wall compliance on maximum growth rate across unstable frequency range at $R = 300$. (1) Rigid wall. Compliant wall at : (2) $\Omega = 20$rad/s, (3) $\Omega = 40$rad/s, (4) $\Omega = 60$rad/s.

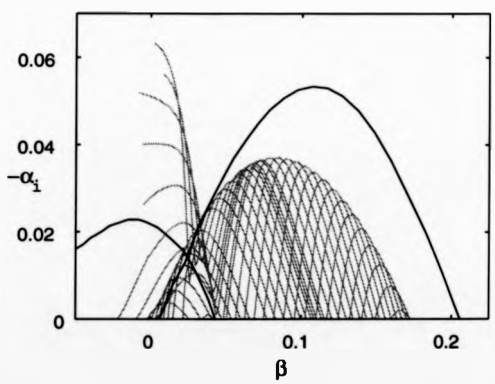

Figure 6.23: Amplification curves at $R = 400$. Grey lines indicate the amplification rate at a number of frequencies for the compliant wall at $\Omega = 20$rad/s. Black lines show the rigid wall maximum amplification envelopes.

It is known that the Type 2 instability is reliant on Coriolis and streamline curvature effects for its existence and theoretically these influences can be removed from the governing equations, thereby eliminating the mode from the stability analysis. If the influence of the Type 2 instability can be removed in this manner then it can be established whether the behaviour observed in the full problem does arise as a result of the presence of this second unstable mode. Removal of the Coriolis and streamline curvature effects decouples the sixth order system of stability equations (Eqs. 6.20 and 6.21) to leave the Orr-Sommerfeld equation.

6.11.1 Stability Results Using the Orr-Sommerfeld Equation.

The Orr-Sommerfeld equation for the rotating disc profile is as follows.

$$\left[i(D^2-\lambda^2)^2 + R(\alpha F + \beta G - \omega)(D^2-\lambda^2) - R(\alpha F'' + \beta G'')\right] h = 0 \qquad (6.75)$$

and appropriate rigid wall boundary conditions are

$$h(0) = h'(0) = 0.$$

$$h(\infty) = h'(\infty) = 0.$$

For the compliant problem the coupling conditions at the wall/flow interface are manipulated to give two boundary conditions for this fourth order problem from the three conditions required in the full sixth order problem. The following conditions were thus imposed where displacements horizontal to the surface and shear stresses are resolved in the direction of propagation to effectively reduce the stability problem to that of a two-dimensional case aligned in the direction of propagation. At the mean undisturbed wall position ($z = 0$) it is required that

$$\begin{aligned} \alpha\xi + \beta\eta &= \frac{i}{\omega}(\alpha f + \beta g) - \frac{i\zeta}{\omega}(\alpha F' + \beta G'), \\ \zeta &= \frac{i}{\omega}h. \end{aligned}$$

$$\begin{aligned} \alpha\bar{\tau}_{zr} + \beta\bar{\tau}_{z\theta} &= \frac{1}{R}\left[(\alpha F'' + \beta G'')\zeta + i(\alpha^2+\beta^2)h + (\alpha f' + \beta g')\right], \\ \bar{\tau}_{zz} &= -\pi + \frac{2h'}{R}. \end{aligned}$$

Results at $R = 300$ and $R = 400$ for this reduced problem are given in Figure 6.24. Similar results to the sixth order system are found at $R = 300$ but at $R = 400$ there is no evidence of any unusual behaviour and uniform growth rate reduction is calculated. This suggests that the Type 1 instability is affected favourably by wall compliance of this kind

but the presence of the Type 2 instability complicates the response of the Type 1 mode to wall compliance in some cases. As an aside attention is brought to the fact that the values obtained for the growth rates using the Orr-Sommerfeld equation are significantly higher than those calculated using the full system of equations and demonstrates the considerable stabilising influence of the Coriolis and streamline curvature effects.

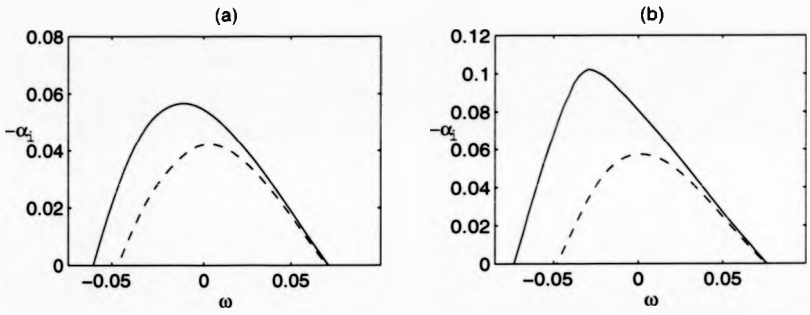

Figure 6.24: Effect of wall compliance on maximum amplification rates using the Orr-Sommerfeld equation. (a) $R = 300$, (b) $R = 400$, Rigid wall : —, Compliant wall ($\Omega = 40$rad/s) : - -.

6.11.2 Type 1/Type 2 Response to Wall Compliance.

From the results presented so far it is clear that the eigenmode structure of this compliant problem exhibits considerable complexity and in order to investigate the existing observations with some degree of clarity one particular frequency within the positive band of frequencies is selected for more detailed attention. In order to focus on a frequency of practical significance the behaviour of the modes with changes in Reynolds number is assessed and the lowest Reynolds number at which the apparent modal interaction first sets in is determined as a function of frequency at $\Omega = 20$rad/s. The results of this investigation are shown in Figure 6.25 for a number of selected frequencies. These results could also be interpreted as defining critical freestream speeds for the onset of this behaviour given the following relation.

$$U = r_e^* \Omega = R(\nu\Omega)^{\frac{1}{2}}$$

A minimum Reynolds number for the onset of this anomalous behaviour is found to be $R = 369$ which occurs for $\omega = 0.004$. Since this is the frequency at which the interaction is judged to first set in it is the one chosen for more rigorous analysis. A number of techniques will be used to establish whether the large values of $-\alpha_i$ found in the above calculations actually represent a physical instability and to speculate on the reasons for its occurrence.

The onset of this apparent interaction is seen by a change in the configuration of the family of eigensolutions. Below $R = 369$ the family of eigenmodes which correlate with the Type 2 rigid wall branch becomes increasingly unstable as β is decreased and can become significantly amplified. This branch and the branch associated with the Type 1 instability cross when both are damped near $\beta = 0.042$. At $R = 369$, however, both branches break near the cross over point of the lower Reynolds number cases and two new branches of eigensolutions are formed as demonstrated in Figure 6.26(a). As R is increased further the separation of the two curves is found to become more accentuated. The calculated group velocity at the separation point becomes extremely small (see Figure 6.26(b)) and based on the findings of Willis (1986) is suggestive of some form of modal coalescence leading to absolute instability. The investigations of Willis found that modal coalescence was signified by the existence of a zero group velocity at the point of coalescence between two modes (the T-S instability and TWF in this case) and a rapid increase in growth rate thereafter with a second damped branch of solutions also formed. Similar trends have been observed in this case except that the subsequent growth is not so acute.

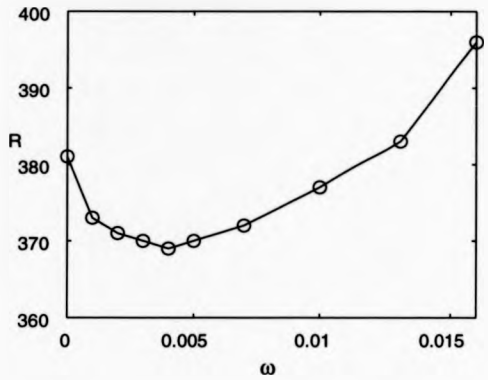

Figure 6.25: Minimum Reynolds numbers for onset of apparent interaction as a function of frequency for compliant wall at $\Omega = 20$rad/s.

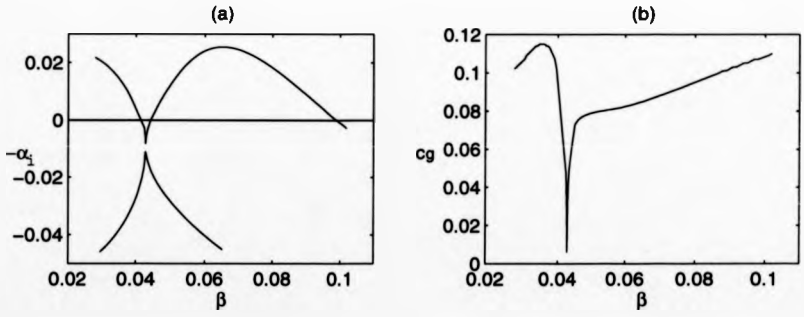

Figure 6.26: (a) Eigenmode structure and (b) group velocity of primary mode for compliant wall with $R = 369$, $\omega = 0.004$ and $\Omega = 20$rad/s.

The complete eigenvalue spectrum for $\omega = 0.004$ at $R = 400$ is plotted in the form $(-\alpha_i, \beta)$ in Figure 6.27. It can be seen that the sharp cusp points apparent at $R = 369$ have become smoothed out and that the two branches have moved further apart. The eigenvalues are also plotted in the form $(-\alpha_i, \varepsilon)$ and $(-\alpha_i, c)$ in Figure 6.28(a) and (b) respectively where c is the non-dimensional phase speed of the disturbance in the direction of propagation. It is also shown that the spectrum is further complicated by the presence of an apparent third set of eigenmodes which are characterised by fairly large values of $-\alpha_i$ and wave angles (see label 3 in Figure 6.28(a)). The group velocity vector associated with each set of solutions is found to be directed outwards in all cases. The third branch of eigensolutions appears to follow the lower portion of the rigid wall Type 2 branch but departs from this trend to produce eigenvalues which do not converge onto any rigid wall branch as wall compliance is decreased whereas the eigenvalues which constitute the other two branches are found to converge onto either a Type 1 or Type 2 rigid wall value. The movement of the labelled points in Figure 6.27 as $G_s \rightarrow \infty$ is as follows.

A,B,F $\rightarrow$ Type 1 rigid wall branch

C,D,E $\rightarrow$ Type 2 rigid wall branch

It is clearly evident that the eigenmode structure exhibits, not unexpectedly, a rich complexity. For the two-dimensional Blasius boundary layer over a compliant surface eigenmodes have been found to interact and even to coalesce (Carpenter and Garrad, 1985, Willis, 1986, Yeo, 1988.) and when eigenmodes coalesce a powerful absolute instability can result. Whilst the results presented here do not indicate definitely that modal *coalescence* has occurred the results in Figure 6.26 strongly suggest that it has. There is definite evidence of some form of modal interaction between the Type 1 and 2 instabilities. Figure 6.27 indicates that the Type 2 branch of solutions merges with the Type 1 branch to produce a modification to the Type 1 family of solutions with wall compliance promoting a new region of instability with potentially high amplification rates. At the same time two additional branches are formed; one consisting of damped modes formed from the two stable halves of the original Type 1 and 2 branches and a second which produces amplified modes but with growth rates less than those of the main branch.

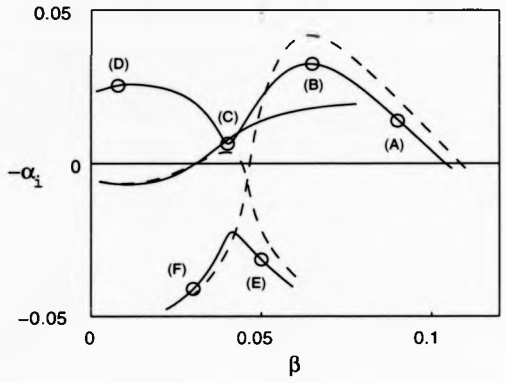

Figure 6.27: Eigenvalue spectrum at $R = 400, \omega = 0.004$ showing growth rate as a function of azimuthal wavenumber. Rigid wall branches : - -, Compliant wall ($\Omega = 20$rad/s) : —.

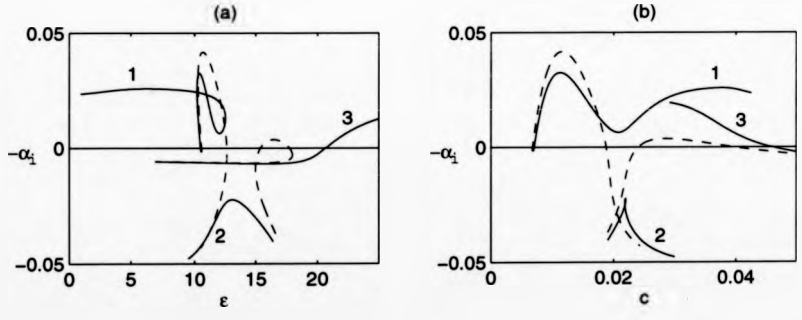

Figure 6.28: Eigenvalue spectrum at $R = 400, \omega = 0.004$ showing growth rate as a function of (a) wave angle, ε and (b) phase speed, c. Rigid wall branches : - -, Compliant wall ($\Omega = 20$rad/s) : —.

Flow eigenfunctions corresponding to points (B) and (D) in Figure 6.27 are presented in Figure 6.29 and clearly demonstrate the change in nature of the instability. It is interesting to note that the maximum perturbation velocity amplitude is with g_r in both cases but for the point (D) this occurs exactly at the wall/flow interface rather than some way into the boundary layer region which is usual for both modes of rigid wall eigenfunction. Such characteristics are often indicative of wall-based modes of instability where large amplitudes occur at the wall itself but there is nothing to suggest at this stage that this region of instability is of a hydroelastic nature.

The corresponding wall displacement amplitudes are shown in Figure 6.30 where similar observations to the stationary disturbance results are seen. The region of anomalous growth is found to produce a disturbance effect in the wall far in excess of that for the modified Type 1 instability.

So far only the case of $\Omega = 20$rad/s has been considered for this anomalous behaviour but it has already been demonstrated that wall compliance can have both a stabilising and destabilising influence on the modified stationary Type 2 mode. It is now investigated how the main unstable branch (branch 1) is affected by changes in rotation rate by considering $\Omega = 40$ and 60 rad/s. The resulting amplification rates are given in Figure 6.31 as a function of azimuthal wavenumber. It is seen that the portion of this unstable branch which corresponds to the modified Type 1 instability behaves as expected and is stabilised by increases in Ω (or effective wall compliance). However, the portion of the branch which appeared to be induced by the presence of a compliant boundary produces smaller growth rates as Ω is increased. It is also found that no behaviour of this kind occurs at $\omega = 0.004$ for rotation rates below $\Omega = 17$rad/s. Again this is evidence of a response to wall compliance which is adverse above a certain rotation rate but reverses to give a more positive response as the rotation rate is taken higher. The minimum point in the amplification curves is also seen to behave irrationally to the differing levels of wall compliance. From these results it is difficult to ascertain probable reasons for this kind of behaviour and the energy analysis of § 6.9 is more likely to reveal a more physical understanding.

Before considering the energy balance the effect of wall damping and Reynolds number on the main unstable branch is briefly considered. With the wall model used for the computations wall damping is incorporated through the use of a complex shear modulus as in Chapter 4.

$$G_s = G_s^R(1 - i\gamma_p)$$

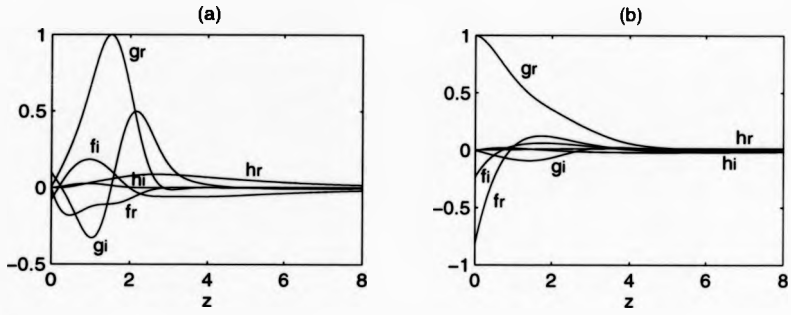

Figure 6.29: Flow eigenfunctions for compliant wall at $R = 400$, $\omega = 0.004$ and $\Omega = 20$rad/s for (a) Eigenmode (B) and (b) Eigenmode (D).

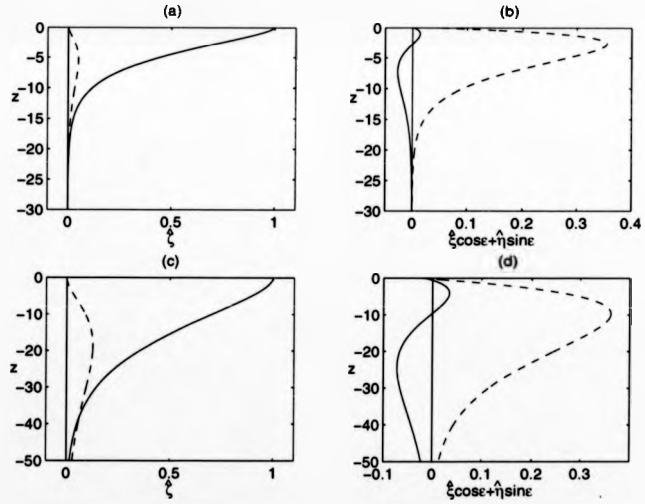

Figure 6.30: Wall eigenfunctions for compliant wall at $R = 400$, $\omega = 0.004$ and $\Omega = 20$rad/s. (a) Vertical displacement, (b) Horizontal displacement for eigenmode (B). (c) Vertical displacement, (d) Horizontal displacement for eigenmode (D). Real part : —, Imaginary part : - -.

Results for different damping coefficients are shown in Figure 6.32 where values of $\gamma_p = 0.0025$ and 0.005 are found to have a generally destabilising effect. The results are somewhat incomplete owing to the same convergence problems which plagued the undamped calculations in the lower β range. Increasingly small steps in the local iteration scheme were required to successfully locate the eigenvalues but after a certain point no further convergence was achieved. However, from the results shown it can be deduced that wall damping slightly destabilises the portion of the unstable region relating to the Type 1 mode and also enhances the modal interaction phenomenon with the growth rate at the point of interaction increasing with increased levels of wall damping. This would suggest that greater damping in the wall lowers the Reynolds number at which the onset of the interaction occurs and subsequently produces successively higher growth rates in the region of anomalous growth.

Raising the Reynolds number to $R = 500$ and 600 brings about reductions in the rigid wall unstable region but also produces the additional growth apparent at $R = 400$ as shown in Figure 6.33. It is observed, however, that the maximum growth rate of this additional region of instability remains unaffected by the changes in Reynolds number rather like the indifference of the rigid Type 2 mode to Reynolds number.

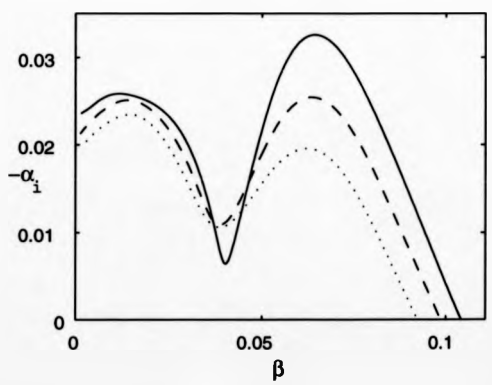

Figure 6.31: Effect of rotation rate on stability characteristics of the major unstable branch of eigensolutions at $R = 400$, $\omega = 0.004$. $\Omega = 20$rad/s : —, $\Omega = 40$rad/s : - -, $\Omega = 60$rad/s : ···.

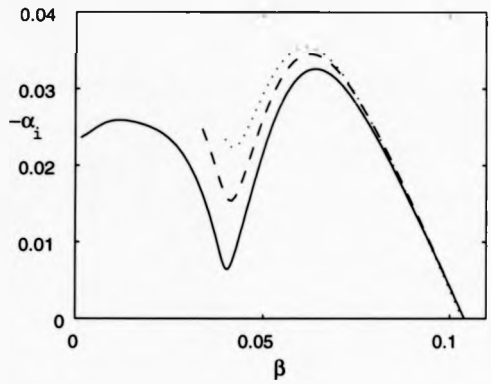

Figure 6.32: Effect of wall damping at $R = 400$, $\omega = 0.004$ and $\Omega = 20$rad/s. Undamped wall : —, $\gamma_p = 0.0025$: - -, $\gamma_p = 0.005$: · · ·.

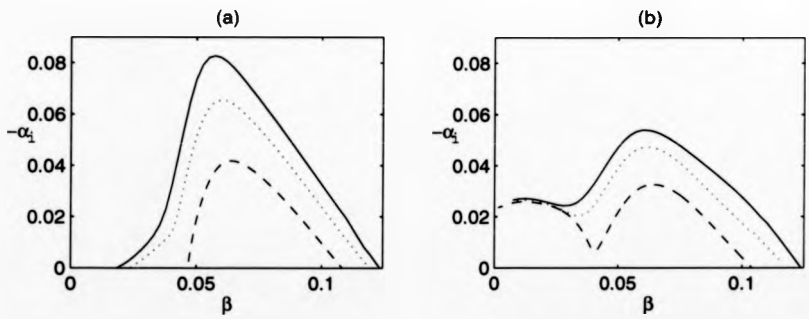

Figure 6.33: Effect of Reynolds number on main unstable branch at $\omega = 0.004$. (a) Rigid wall, (b) Compliant wall at $\Omega = 20$rad/s. $R = 600$: —, $R = 500$: · · ·, $R = 400$: - -.

6.11.3 Energy Results for Travelling-wave Mode.

Energy budgets are presented for eigenvalues along the main unstable branch at $R = 400$, $\omega = 0.004$ and $\Omega = 20$rad/s where the selected eigenvalues correspond to the points labelled A-D in Figure 6.27, p. 182. In moving from A to B the compliance modified Type 1 mode becomes amplified and reaches a maximum growth rate after which this decays to produce eigenvalue C with anomalous growth then occurring to produce another maximum value at D.

Results from the energy calculations are presented in two forms in Figure 6.34. Firstly the values obtained for the exact entries in the energy equation are given and then alongside are the Reynolds stress and viscous stress work terms resolved in directions parallel and perpendicular to the group velocity vector. In performing this latter manipulation of the results the dramatic variation of group velocity angle as β is decreased becomes apparent where sharp increases occur in the region of anomalous growth. For the larger values of β, in the region of the Type 1 instability, the group velocity angle, ε_{cg}, lies close to the angle of propagation, ε, but they diverge after the apparent modal interaction. Values of the angle for the selected points are given in Table 6.4.

For all the cases examined both the pressure work term, $(\overline{\tilde{h}\tilde{p}})_w$, and the work done by the normal viscous stress, $(\overline{\tilde{h}\tilde{\sigma}_{33}})_w$, were found to be insignificant.

Results for the eigenvalues A-D at $R = 400$ and for $\Omega = 20$rad/s are shown in Figure 6.34(a)-(d) with each graph drawn to the same scale to allow direct comparison. As the Type 1 eigenmode moves from A to B the main component of the energy equation responsible for the amplification is seen to be the viscous dissipation term which becomes reduced in magnitude indicating a reduction in energy dissipation via this route. The Reynolds stress production term is largely unaffected as are the geometrical contributions whilst the work done by the viscous stresses is seen to be negligible in both cases. At eigenvalue C reductions in the Reynolds stress term have occurred and viscous dissipation is further reduced despite the reduction in growth rate from B to C. For the first time the positive viscous stress work term, $(\overline{\tilde{f}\tilde{\sigma}_{31}})_w$ (S1) shows a slight contribution to the energy balance. Negative Reynolds stress in the direction normal to the group velocity is also shown to produce less dissipation compared to the previous two cases. This slight change in emphasis in the energy budgets indicates the start of the anomalous behaviour. In moving onto eigenvalue D where re-amplification has occurred the pattern of the energy budgets is quite different. Even though the growth rate is comparable to that of eigenvalue B the Reynolds stress production term, P2, has continued to decrease in value although P1, Pg and Pn all show a positive increase

with the size of ε_{cg} largely responsible for the latter two. A prominent feature in this case is the dramatically enhanced energy production contribution from the viscous stress term, S1, which is now comparable in numerical value to the Reynolds stress term P2 which was by far the dominant term in all of the previous cases. The contribution from $(\overline{\tilde{g}\sigma_{32}})_w$ (S2) is also increased. In viewing the energy budgets in terms of the group velocity and normal to it then Pg, Sg and Sn are all prominently positive and the negative Reynolds stress term, Pn, becomes further reduced in magnitude.

It is interesting to note that the geometrical terms, G1 and G2, are largely invariant across the range of eigenvalues considered and serve only to make up the energy balance.

It is shown that the anomalous growth observed at this frequency occurs through increased work done on the wall by the viscous stresses in all directions and it is again postulated that this is an effect of Coriolis forces in the system which induces motion perpendicular to the direction of propagation. This anomalous behaviour is, however, frequency dependent and competition must occur between the reductions gained in energy production by the Reynolds stress, which is the usual response to a compliant boundary, and the increase in energy production brought about by the additional viscous stress work terms, which are induced largely by the increased disturbance motion at the boundary (see Figure 6.29(b), p. 184).

The velocity distributions for eigenvalues B and D are already given in Figure 6.29 and bring about two observations on the distributions for h: firstly the values for both eigenvalue B and D at the wall are shown to be very small, which would explain the negligible contributions to the energy balance from the pressure and normal stress work terms, and secondly that the distribution range is an order of magnitude lower than that for the velocity components parallel to the disc surface. In this parallel direction the eigenfunction changes character at D to produce the largest magnitude at the wall rather than some way into the boundary layer as is the case for B where the values at the wall remain relatively small. When resolved in the direction of propagation and normal to it the velocity distributions show similar trends.

Profiles for the distributions of Reynolds stress and viscous dissipation are shown in Figure 6.35 for eigenvalues B-D where ε_{cg} has been used to resolve the components P1 and P2 into the directions associated with the group velocity (Pg and Pn). The distributions for C are generally reduced versions of the B profiles with peaks in Reynolds stress occurring at $z \approx 2$. However, for eigenvalue D the peak values moves in towards the wall and there is a large reduction in the negative distribution of Pn. For eigenvalues B and C the viscous

dissipation distributions also show a peak (or minimum value) near $z = 2$ but a change in the form of this distribution occurs with eigenvalue D where the greatest dissipation occurs in the near wall region although the integrated value is reduced in magnitude.

Figure 6.36 attempts to enlarge upon the reasons for stabilisation in both regions of instability as wall compliance is decreased as demonstrated in Figure 6.31. For eigenvalue B a conventional response to wall compliance occurs with systematic reductions in Reynolds stress production along with increased viscous dissipation in an analogous manner to rigid/compliant wall comparisons. For eigenmode D this remains the mechanism for the subsequent stabilisation with increases in Ω. The large viscous stress work terms, which are deemed to be responsible for the initial adverse response and the production of large growth rates, remain high but do not change greatly and the increased compliance continues to bring reductions in Reynolds stress and slightly increases viscous dissipation. These results suggest that if the wall could be made considerably more compliant then this anomalous growth could be controlled. However, the levels of wall compliance required to do this are likely to be so great as to induce other adverse effects such as hydroelastic modes of instability.

Eigenvalue	ε	ε_{cg}
A	10.266	11.5
B	10.379	8.80
C	12.095	7.04
D	6.216	36.2

Table 6.4: Angle of propagation, ε, and group velocity angle, ε_{cg}, for selected eigenvalues at $R = 400$, $\omega = 0.004$ and compliant wall at $\Omega = 20$rad/s.

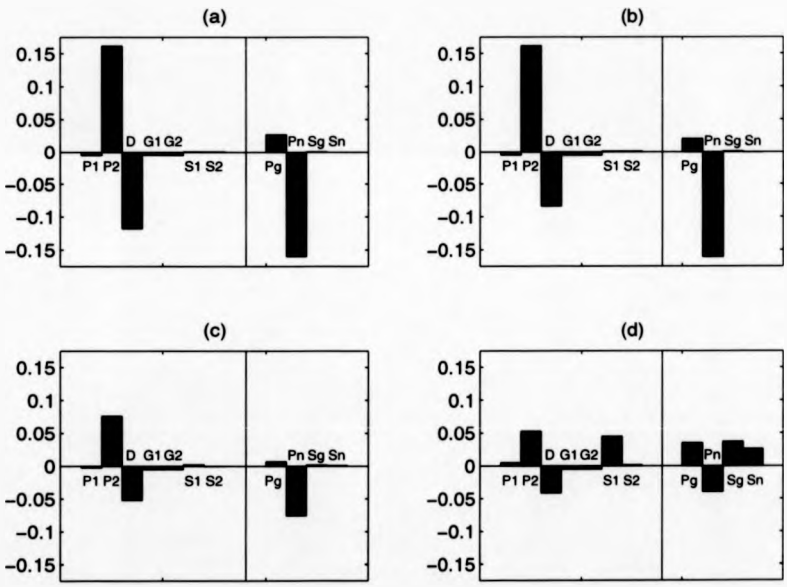

Figure 6.34: Energy budgets for compliant wall at $R = 400$, $\omega = 0.004$ and $\Omega = 20$rad/s. (a) Eigenvalue A, (b) Eigenvalue B, (c) Eigenvalue C, (d) Eigenvalue D. For labels refer to previous figures.

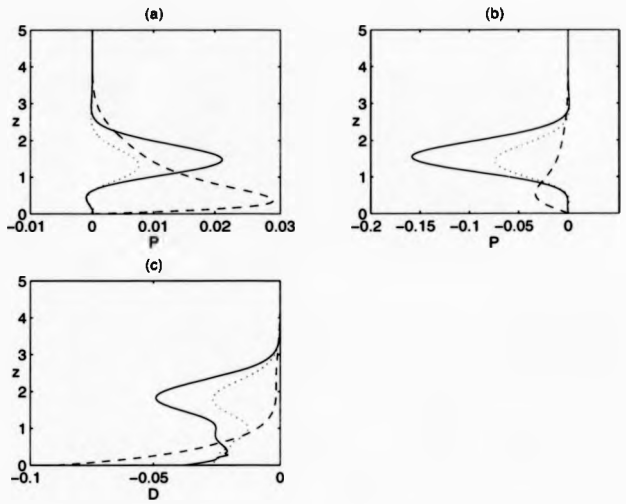

Figure 6.35: Reynolds stress and viscous dissipation distributions for compliant wall at $R = 400$, $\omega = 0.004$ and $\Omega = 20$rad/s. (a) Reynolds stress in group velocity direction, (b) Reynolds stress normal to group velocity, (c) Viscous dissipation. Eigenvalue B : —, Eigenvalue C : · · ·, Eigenvalue D : - -.

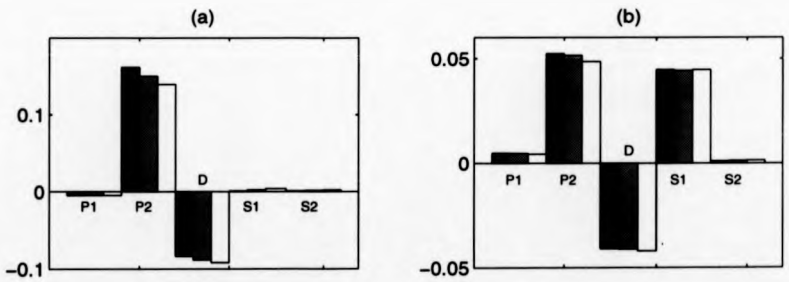

Figure 6.36: Effect of varying degrees of wall compliance on (a) Eigenvalue B and (b) Eigenvalue D at $R = 400, \omega = 0.004$. $\Omega = 20$rad/s : black, $\Omega = 40$rad/s : grey, $\Omega = 60$rad/s : white.

6.12 Wall-based Instability.

The presence of any wall-based instabilities in a compliant wall/flow problem will always limit the performance of the compliant boundary and the origins of such instabilities have already been discussed in terms of the free wave modes associated with the wall.

In previous two-dimensional investigations travelling-wave flutter has been identified as taking the form of waves propagating downstream with phase speeds close to the freestream value and is found to set in when the freestream speed exceeds a critical value, U_c. If the same such critical speed exists in the three-dimensional case and assuming the disc to be infinite in diameter then travelling-wave flutter should, theoretically, always exist at some location on the disc. This can be seen from the fact that the freestream speed associated with the rotating disc is defined in terms of the radius and rotation rate.

$$U_\infty = r_*^* \Omega$$

Therefore, either by increasing r_*^* (equally R) or Ω or both it will always be possible to find a value of U_∞ that exceeds U_c. In experimental investigations, however, where the disc is finite this obviously need not be so. What poses a problem in these investigations is the choice of parameter range in which to search for such solutions given that they must exist somewhere for some combination of R and Ω. Carpenter and Garrad (1986) assumed an inviscid approximation to obtain simple analytical expressions, using the plate-spring wall model, for critical onset speeds of hydroelastic modes, which then gives some indication of the parameter range across which instability of this type may occur. A key element in deriving these expressions is the existence of a minimum free wave speed for the wall. However, no such simple formulae are possible for the single layer viscoelastic wall where the minimum free wave speed corresponds to infinite wavenumber and with no form of global solver available wall-based instability modes are presently located by tracking eigenvalues from the no flow free wave solutions. This assumes that as the external flow speed is gradually increased some of the free wave modes may develop into instabilities once some threshold flow speed is exceeded.

It is expected that any hydroelastic form of instability is likely to set in where the freestream speed is at its maximum. Given that $U(z) = r_*^* \Omega (F \cos\varepsilon + G \sin\varepsilon)$ a maximum mean freestream speed occurs at $\varepsilon = \pm 90°$ and when $G(\infty) = -1$. Therefore the free wave modes were tracked within this wave angle range. The most unstable modes located using this method were found to correspond to an angle of $-90°$ and located in the negative β quadrants. Frequencies in this investigation were assumed to be positive throughout with

the signs of α and β then determining the inward or outward propagation of disturbances. In all cases the group velocity vector was found to be directed outwards so that eigenvalues with negative values of α_i are interpreted as physical instabilities. Results presented are not wide ranging, in so far as predicting exact onset conditions, but they do indicate the characteristics of the instability and its response to changes in the level of wall compliance, wall damping and Reynolds number.

Unstable modes were located at $R = 800$ and Figure 6.37(a) shows the maximum growth rate as a function of frequency at compliance levels set by $\Omega = 20$ and 40rad/s with increased wall compliance amplifying the instability . However, this also shows a maximum growth rate which appears to increase indefinitely with increasing frequency. This behaviour can probably be explained from the form of the free wave solutions where the minimum free wave speed occurs at infinite wavenumber with the physically unrealistic implication of maximum growth rate corresponding to infinite frequency. Accordingly frequency dependent damping was incorporated into the wall model such that the damping coefficient is proportional to frequency.

$$G_s = G_s^R(1 - i\omega\gamma_d)$$

For a given value of γ_d the effective damping then increases with frequency.

The inclusion of damping was found to have a significant stabilising effect on the instability as shown in Figure 6.37(b) but no overall maximum growth rate was found before the calculations were limited by numerical difficulties. For the level of wall damping set by $\gamma_d = 0.2$ the instability is shown to be only just unstable at $R = 400$ in the frequency range available. Phase speeds within the unstable frequency range presented were generally found to span 0.05 - 0.25 and so extend to considerably higher phase speeds than the Type 1 and 2 instabilities found in the rotating disc boundary layer.

The fact that the most rapidly growing modes at each frequency align themselves in the direction of maximum mean freestream velocity and the response to increased wall compliance and wall damping suggests that these modes can be identified as TWF.

Flow eigenfunctions for a selected frequency are shown in Figure 6.38. The distributions extend into only a fraction of the boundary layer and are confined to a much narrower region in comparison with the previous eigenfunctions of the flow-based instabilities and the normal component, h, now becomes a significant feature in the profiles. This is dominated by the radial and azimuthal components for the Type 1 and 2 instabilities and now has a maximum amplitude exactly at the wall/flow interface in common with the characteristics of TWF.

An energy balance calculation for this eigenvalue also shows dramatically different features to those found for the flow-based instabilities. The most striking features of Figure 6.39 are the large, negative contributions from the pressure work term, $(\overline{\hat{h}\hat{p}})_w$ (PW), which has been negligible in all previous cases and the stress work term, $(\overline{f\hat{\sigma}_{31}})_w$ (S1). These negative values indicate the transfer of disturbance energy from the fluid to the wall and are thus stabilising effects as far as the fluid is concerned but this transfer of energy to the wall feeds wall-based instabilities and is shown here to give rise to TWF.

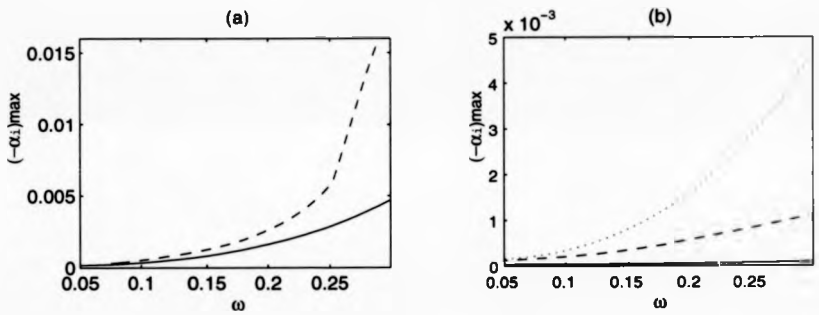

Figure 6.37: Maximum growth rate of TWF instability as a function of frequency. (a) $R = 800$ (undamped), $\Omega = 20$rad/s : —, $\Omega = 40$rad/s : - -, (b) $\Omega = 20$rad/s, $R = 800$ (undamped) : ···, $R = 800$, $\gamma_d = 0.2$: - -, $R = 400$, $\gamma_d = 0.2$: —.

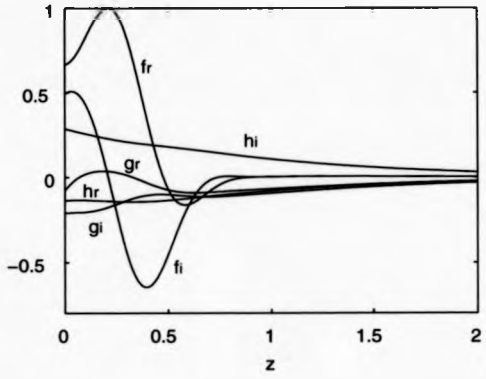

Figure 6.38: Eigenfunctions corresponding to most rapidly growing mode at $R = 800$, $\omega = 0.255$ and $\Omega = 20$rad/s (undamped).

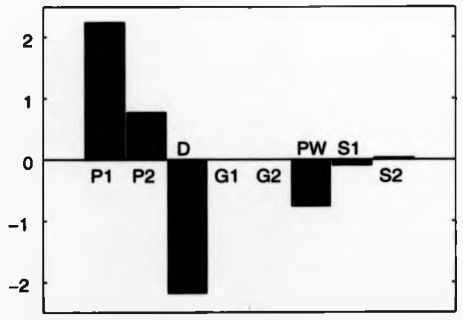

Figure 6.39: Energy balance for eigenvalue of previous figure. For labels refer to similar figures and text.

6.13 Summary.

The effect of an infinitely deep single layer viscoelastic compliant wall on instability in the rotating disc boundary layer has been investigated on both stationary and travelling-wave forms of the Type 1 and Type 2 instabilities.

The main initial interest centred around the Type 1 stationary instability which generates the spiral vortex pattern over a rigid disc and is generally considered to give rise to a common route to transition. Amplification rates at a number of Reynolds numbers were found to be significantly reduced by the presence of such a compliant boundary and the critical Reynolds number for the onset of this Type 1 instability was found to be delayed with increasing levels of wall compliance. Amplitude ratios were also calculated and assuming the rigid wall transitional Reynolds number to be $R \approx 520$ gave an N-factor near 7 in the present calculations. Introducing and raising the level of wall compliance was found to increase the value of R for which $N = 7$ up to $R = 850$ for a compliant wall of $G_s = 1000\text{N/m}^2$ rotating at $\Omega = 60\text{rad/s}$.

The effect of wall compliance on the Type 2 stationary mode was found to be sensitive to rotation rate (or degree of wall compliance) with the critical Reynolds number markedly reduced from $R = 400$ down to $R = 177$ at $\Omega = 20\text{rad/s}$. However, only a very small region of instability remained at $\Omega = 40\text{rad/s}$ with complete stabilisation occurring at $\Omega = 60\text{rad/s}$.

The disturbances associated with the Type 2 mode were found to penetrate the wall to depths over twice that due to the Type 1 mode. Flow eigenfunctions under the influence of wall compliance also varied considerably between the two modes. Only slight modification to the general rigid wall character was observed in the Type 1 case whereas large values of the velocity components parallel to the disc surface arose for the Type 2 case which was a significant departure from the profiles for the rigid wall.

An energy balance for the Type 1 instability revealed that the stabilising effect of the compliant boundary was seen to arise through reductions in the Reynolds stress production term and through increased viscous dissipation. For the Type 2 case, however, large contributions to energy production occurred through work done by viscous stresses at the wall and alongside this viscous dissipation was reduced leading to a destabilisation of this mode by wall compliance in some cases. Reynolds stress and viscous stress work components of the energy equation resolved in directions parallel and normal to the group velocity vector gave significant contributions to energy production compared to those of the Type 1 instability.

The energy balance observations leads to speculation on a possible physical mechanism for the occurrence of the Type 2 rigid wall instability which is known to be reliant on Coriolis

effects. It is suggested that the motion induced by Coriolis forces in the system, as a result of a radial outflow, would give rise to greater Reynolds stress in the direction normal to the radial motion thus promoting instability. Energy budgets do not in fact reveal positive Reynolds stress in this direction but reduced dissipation due to negative Reynolds stress is apparent in comparison with a Type 1 mode of comparable growth rate. The effect of the compliant boundary on the Type 2 instability would appear to substantiate this with the large viscous stress work terms arising as a result of the increased perturbation amplitudes at the wall which are no longer constrained to be zero in the presence of a non-rigid boundary.

The role of travelling-wave modes in transition over the rotating disc remains largely an unanswered question. However, purely on the basis of the global maximum amplification rate belonging to non-zero frequencies, their presence cannot be overlooked.

Eigenvalues were calculated across the complete unstable frequency range for both the Type 1 and 2 modes at $R = 300$ and 400. The presence of a compliant boundary at $R = 300$ was found to reduce both the maximum growth rate and unstable frequency range of the Type 1 instability, with almost complete stabilisation occurring at $\Omega = 60$rad/s. With successive increases in the degree of wall compliance the position of maximum growth rate was found to move towards the zero frequency mark and smaller values of β and wave angle.

At $R = 400$ the effect of the compliant boundary on the negative frequency (inwardly travelling) disturbances remained one of stabilisation but the results also show a band of positive frequencies which give rise to anomalous growth and high amplification rates. This phenomenon occurs for the frequency and β range over which the two rigid wall instabilities coexist. Through the use of the Orr-Sommerfeld equation, which eliminates Coriolis and streamline curvature effects, this behaviour was eradicated and growth rate reduction across the entire frequency range occurred which suggests that the presence of the Type 2 mode is responsible for the irregular behaviour in the full system.

The anomalous behaviour outlined above was found to be both frequency and Reynolds number dependent with a minimum Reynolds number for its occurrence determined to be at $R = 369$ for the frequency $\omega = 0.004$ when the disc is rotated at $\Omega = 20$rad/s. Further investigations with respect to this behaviour were carried out at $\omega = 0.004$ and $R = 400$. Eigenfunctions across the unstable β range were found to vary considerably with those in the region of anomalous growth producing large values of velocity components parallel to the disc surface at the wall and producing a disturbance effect far into the wall layer somewhat akin to the stationary Type 2 results.

An energy balance analysis revealed this anomalous growth to be associated with large viscous stress work terms at the wall and is considered to be a Coriolis effect.

Wall damping was found to have a slight destabilising effect across the spectrum at $\omega = 0.004$ but increasing the value of Ω resulted in reductions to growth rates not only in the region associated with the Type 1 instability but also in the region of new growth. Varying the Reynolds number at $\omega = 0.004$ and $\Omega = 20$rad/s reduced the Type 1 growth rates further but had little effect on the region of instability arising as a result of the compliant boundary. This insensitivity of growth rate to Reynolds number was also found for the Type 2 rigid wall instability. Across the bulk of the frequency range however the effect of wall compliance on the Type 2 instability was found to be negligible.

The results outlined above for travelling-wave modes indicate that the Type 1 instability alone is affected favourably by wall compliance of this type but the presence of the Type 2 mode of instability complicates the overall response. The compliant boundary appears to destabilise Type 2 modes with small disturbance frequency and when this coincides with the parameter range for Type 1 amplified modes a detrimental modal interaction is seen to occur. At the onset of this anomalous behaviour calculations reveal a very small value for the group velocity at the point of interaction strongly indicating that modal *coalescence* has occurred between the Type 1 and 2 instabilities. This suggests that wall compliance promotes modal coalescence leading to ***absolute*** instability.

Some unstable modes, identified as TWF, have been located and are found to be aligned with the direction of maximum freestream speed ($-90°$) so that they propagate in the negative azimuthal direction. Maximum growth rates, in both damped and undamped walls, are found to increase with increased frequency up to $\omega = 0.3$ beyond which calculations are curtailed by numerical difficulties. Growth rates calculated remain at least an order of magnitude lower than those associated with the Type 1 form of instability.

Wall damping was found to have a slight destabilising effect across the spectrum at $\omega = 0.004$ but increasing the value of Ω resulted in reductions to growth rates not only in the region associated with the Type 1 instability but also in the region of new growth. Varying the Reynolds number at $\omega = 0.004$ and $\Omega = 20$rad/s reduced the Type 1 growth rates further but had little effect on the region of instability arising as a result of the compliant boundary. This insensitivity of growth rate to Reynolds number was also found for the Type 2 rigid wall instability. Across the bulk of the frequency range however the effect of wall compliance on the Type 2 instability was found to be negligible.

The results outlined above for travelling-wave modes indicate that the Type 1 instability alone is affected favourably by wall compliance of this type but the presence of the Type 2 mode of instability complicates the overall response. The compliant boundary appears to destabilise Type 2 modes with small disturbance frequency and when this coincides with the parameter range for Type 1 amplified modes a detrimental modal interaction is seen to occur. At the onset of this anomalous behaviour calculations reveal a very small value for the group velocity at the point of interaction strongly indicating that modal *coalescence* has occurred between the Type 1 and 2 instabilities. This suggests that wall compliance promotes modal coalescence leading to ***absolute*** instability.

Some unstable modes, identified as TWF, have been located and are found to be aligned with the direction of maximum freestream speed ($-90°$) so that they propagate in the negative azimuthal direction. Maximum growth rates, in both damped and undamped walls, are found to increase with increased frequency up to $\omega = 0.3$ beyond which calculations are curtailed by numerical difficulties. Growth rates calculated remain at least an order of magnitude lower than those associated with the Type 1 form of instability.

CHAPTER 7

CONCLUSIONS.

The main findings in each of the chapters are now summarised together with the methods of solution. Possible areas of extension to the investigations are also proposed.

7.1 Stability Features of Rotating Channel Flow.

Rotating channel flow was used to study the influence of rotation on hydrodynamic stability through consideration of Coriolis effects which give rise to a strong instability mechanism thereby producing instability at much more modest Reynolds numbers and rotation rates compared to that associated with centrifugal instability.

A number of flows established within a plane channel subjected to constant rotation about a spanwise axis have been considered in both linear and weakly nonlinear analyses. The mean flow profiles were defined to interpolate between the well-studied plane Poiseuille flow and Couette flow so that the point of maximum velocity moved continuously from the centre to the wall of the channel.

Neutral curves have been calculated for a range of shear flows and rotation rates using a Chebyshev spectral collocation method which implements the two grid system of Khorrami (1991). This allows pressure points to be included in the calculations without having to specify any pressure boundary conditions. In conjunction with this numerical method a Newton algorithm was used in order to determine minimum critical points in the full three-dimensional (Ω, β, R) parameter space. The primary roll cell instability was found to first become unstable at the relatively low Reynolds number of $R = 66.45$ for plane Poiseuille flow decreasing to $R = 20.66$ for Couette flow with Ω increasing and β decreasing as the mean flow field moved towards Couette flow. The change in distribution of Coriolis force across the channel is proposed as a possible reason for the flow becoming less stable to rotation as Couette flow is approached. In all cases this form of instability occurs at Reynolds numbers much lower than that required for Tollmien-Schlichting (T-S) waves to become amplified so that the existence of the two instability forms for plane Poiseuille flow is unlikely since this would require unrealistically small rotation rates.

Generalisation can be made from the results on the existence of a three-dimensional neutral paraboloid surface for the whole family of shear flows with clearly defined minimum

points. Such neutral surfaces have not previously been studied in such detail.

The weakly nonlinear behaviour of the streamwise rolls has been studied using a Ginzburg-Landau formulation and accurate numerical values for the coefficients of this equation indicate supercritical bifurcation for all the mean flow states. However, the critical parameter, which is required to be positive for supercritical instability, decreases by an order of magnitude and approaches zero in moving from Poiseuille flow to Couette flow. This results in significantly larger roll cell amplitudes and suggests that Couette flow may behave differently in the fully nonlinear problem.

The Ginzburg-Landau formulation of the weakly nonlinear problem has advantages over the standard Stuart-Landau theory in that it can be used to study the stability of the roll cells to spanwise modulation which becomes important in systems of large aspect ratio when an Eckhaus-type instability can arise. A geometrical analysis approach to this has been done (Bridges and Cooper, 1995) to establish that the Eckhaus criterion is generally satisfied and demonstrates the existence of a band of stable wavenumbers within the linearly unstable region. However, no exact numerical results exist to corroborate this and therefore a direct numerical extension of the present work to consider the spanwise modulation of the rolls would be useful to relate to these analytical predictions. It may also be possible to exploit the analogy between the various channel flows considered and other more complex flow geometries, where the problem formulation may not be so straightforward, with an aim to understanding this side-band instability phenomenon.

One other feature of this work is the restriction to constant rotation rates whereas in real systems rotation rates are unlikely to remain rigidly fixed. Introducing a temporal variation in the rotation rate would surely disrupt the nature of the stationary rolls cells and could perhaps be considered using a direct numerical simulation approach.

7.2 Wall Compliance Effects on the Rayleigh Instability.

The effect of wall compliance on the inviscid Rayleigh instability has been considered for two-dimensional flows in the presence of an adverse pressure gradient. The majority of previous work in this field of flow stabilisation by external factors such as wall compliance has concentrated on zero pressure gradient flow where the instability arises through a viscous mechanism and gives rise to amplified T-S waves. However, in the presence of an adverse pressure gradient a point of inflexion is generated in two-dimensional velocity profiles which then gives rise to a much more powerful inviscid instability mechanism and produces growth rates typically an order of magnitude higher then those of the T-S instability.

Initial investigations neglected viscous effects on the disturbances and considered a polynomial approximation to the boundary layer profile. The use of a plate-spring model for the compliant wall allowed boundary conditions to be incorporated directly into the Rayleigh equation thus allowing a global spectral method to be used to calculate the complete eigenvalue spectrum. Optimal wall properties, rendering the compliant wall stable with respect to hydroelastic modes, were used to bring about reductions of up to 60% in maximum growth rate with parameters giving the greatest reduction clearly defined. Moving outside of this optimal parameter range, by decreasing the stiffness of the spring foundation, brought about the onset of the travelling-wave flutter (TWF) instability with growth rates comparable to those of the rigid wall Rayleigh instability produced under certain conditions. The inclusion of wall damping was found to have a marginally destabilising effect on the Rayleigh instability but was able to suppress the growth of the TWF instability. However, above a critical level of wall damping the Rayleigh and TWF modes were shown to undergo some form of coalescence.

The inclusion of viscous effects to model more realistically the wall/flow interaction followed, along with the use of the viscoelastic wall model, which resembles more closely those used in experimental work, and the more accurate flow representation of a Falkner-Skan velocity profile. Integration of the governing Orr-Sommerfeld equation was performed using a fixed step size fourth order Runge-Kutta shooting method in conjunction with Gram-Schmidt orthonormalisation to deal with the stiff nature of the Orr-Sommerfeld equation. This local iterative method was applied since the wall equations in this particular case generate boundary conditions which are transcendental in the eigenvalue, $\bar{\alpha}$, and no global scheme can be used. Again wall parameters were used which were calculated to generate walls marginally stable with respect to any hydroelastic instabilities, and results for a wide range of walls substantiate the findings of the inviscid analysis. In none of the cases are the results optimised to the particular boundary layer profile under investigation and in that sense are deemed to be conservative. An energy balance analysis revealed the stabilising effect to be borne out through reduced energy production by the Reynolds stress and increased energy dissipation through work done by the fluctuating pressure at the wall.

Although these results indicate that compliant walls can have a significant stabilising effect on the high growth rates of the inviscid Rayleigh instability they do not pertain to any possible transition delay partly because wall parameters have not been tailored specifically to the velocity profiles under consideration. The potential for such transition delaying

properties is shown to exist, but lengthy optimisation calculations would be required to substantiate this. Only one particular Falkner-Skan profile was considered here, corresponding to a moderately adverse pressure gradient, but characteristic wall properties could theoretically be determined across a range of adverse pressure gradients. The application of these flow configurations, however, is limited. This work focussed on a relatively simple flow configuration with the aim of establishing whether wall compliance could have any effect on such a powerful instability mechanism, but further attention would be better focussed on boundary layers related to systems of real significance. The question of instability in three-dimensional boundary layers, such as the rotating disc, then becomes more important.

7.3 Effect of Wall Compliance on Instability in Three-Dimensional Boundary Layers.

The effect of wall compliance on instability in three-dimensional boundary layers has been studied using the model problem of the boundary layer formed over a rotating disc. In this case two forms of instability can arise; an inviscid type (Type 1) generated by the presence of an inflexion point in the velocity profile which is of primary interest in application to practical systems and a second, viscous instability (Type 2) which is reliant on Coriolis and streamline curvature effects for its existence. This second mode is specific to the rotating disc (although a similar instability occurs in the Ekman layer) and as such cannot be generalised to all three-dimensional boundary layers. Nevertheless in real situations there will always be competition between different modes of instability, although those with inviscid mechanisms are likely to dominate, and the presence of all modes in the boundary layer must ideally be considered.

A single layer of viscoelastic material was taken as the compliant wall for a series of investigations. Previously attention has focussed, for the rigid disc, on the stationary Type 1 form of instability assuming this to lead to the onset of transition. Through a linear stability analysis, using a set of coupled equations which include Coriolis and streamline curvature effects, the response to the compliant boundary was assessed in comparison to rigid wall results. Boundary layer disturbances were assumed to grow spatially and the resulting eigenvalue problem solved via a Chebyshev-tau spectral technique with local iteration. Differing degrees of wall compliance were considered by fixing the shear modulus of the wall material and changing the rotation rate of the disc. Local amplification rates of the Type 1 disturbance were found to be reduced by the presence of the compliant boundary and an amplitude ratio calculation suggests that the transitional Reynolds number could be

raised to at least $R = 850$ for the type of wall investigated. The Type 2 instability, however, was found to behave anomalously to wall compliance with destabilisation and stabilisation occurring depending on the level of wall compliance considered. This is thought to be an influence of the Coriolis forces in the system which initially enhances the instability before the compliant wall effects can compensate to a greater degree.

A more general consideration of the instabilities in this boundary layer then followed by assessing the whole unstable frequency range where the Type 1 maximum growth rate occurs for a negative (or inwardly travelling) disturbance and is more amplified than the corresponding stationary mode. For all negative frequencies wall compliance systematically reduced maximum growth rates but across a small band of positive frequencies, where the Type 1 and 2 instabilities coexist, evidence is given for the occurrence of a modal interaction and coalescence resulting in a rapid increase in amplification rate. This detrimental response to wall compliance is shown to occur above a critical freestream speed and is likely to generate growth rates in excess of the original rigid wall values. Energy balances show the usual, positive, response to wall compliance to be associated with reduced energy production by the Reynolds stress and increased viscous dissipation. The undesirable growth resulting from the modal interaction, however, arises through large viscous stress work terms at the interface. The motion induced by the action of Coriolis forces contributes to these large work terms and it then appears that the Coriolis effects are able to outweigh the effects of the compliant wall as for the Type 2 stationary example. Conversely outside this overlap frequency band wall compliance effects dominate and the Type 2 instability remains largely unaffected by the compliant boundary. It has been demonstrated that the group velocity at the point of interaction between the two modes falls to an extremely small value which provides evidence to support the likelihood of modal coalescence and absolute instability.

In considering the Type 1 mode alone it has been demonstrated that a simple wall model can have significant effects on the growth of the instability with the implication that this form of instability in three-dimensional boundary layers could be controlled to a sufficient extent to give rise to some degree of transition delay. However, the present theoretical problem highlights the tentative nature of this statement if other modes of instability also exist. Here, Coriolis effects give rise to a second form of instability which is shown to interact with the dominant unstable mode and is likely to generate adverse effects. Of course such Coriolis effects will not be present in many real systems and this behaviour may not occur in practical examples.

A characteristic feature of both the destabilised Type 2 mode and the instability after

modal interaction is a significant disturbance effect penetrating the wall to large depths. It is conceivably possible that a wall could be designed to compensate for this behaviour thereby avoiding any modal interaction or coalescence. Therefore an extension to the present work may be to consider different wall constructions such as finite depth and/or multi-layer walls which in previous investigations have been shown to improve on the performance of the single layer wall. An overall response to a series of walls could then be characterised in order to determine some optimum form of wall construction.

Hydroelastic modes of instability prove difficult to locate using the present numerical method of solution owing partly to the local iterative scheme. Some preliminary results have been presented which appear to correspond to the TWF form of instability and the inclusion of frequency dependent wall damping was found to reduce growth rates across the frequency range considered but with restriction imposed by problems with numerical convergence no maximum amplification value was located.

To enlarge upon these results and to ensure that the most unstable modes have in fact been found a global eigenvalue search scheme would be of immense assistance. Alternative asymptotic methods such as those used by Carpenter and Gajjar (1990) which are computationally less demanding may also be of benefit in locating hydroelastic modes of instability which must occur somewhere if the disc is considered to be infinite. It has been clearly stated in the earlier text that the use of the viscoelastic wall model does not permit a global formulation of the eigenvalue problem. This is the case if the governing wall equations are solved exactly using analytic expressions. However, Yeo *et al.* (1995) have recently applied a global technique to this type of wall model in a two-dimensional temporal analysis involving the Blasius boundary layer. By solving the wall equations numerically in the same way as the governing fluid equations a generalised eigenvalue problem can be formed and it is proposed that a similar technique could be applied to the coupled fluid/compliant wall rotating disc system.

The semi-infinite wall domain can be mapped to the finite spectral domain through the use of an appropriate transformation and the three wall displacement amplitudes approximated by a finite Chebyshev series.

$$\xi(y) = \sum_{n=0}^{M} c_n T_n(y)$$

$$\eta(y) = \sum_{n=0}^{M} d_n T_n(y)$$

$$\zeta(y) = \sum_{n=0}^{M} e_n T_n(y)$$

with the fluid variables written as before.

$$h(y) = \sum_{n=0}^{N} a_n T_n(y)$$

$$\gamma(y) = \sum_{n=0}^{N} b_n T_n(y)$$

Discretising the fluid and wall equations then generates the following matrix polynomials.

$$\left.\begin{aligned}(\alpha^4 \boldsymbol{C}_4 + \alpha^3 \boldsymbol{C}_3 + \alpha^2 \boldsymbol{C}_2 + \alpha \boldsymbol{C}_1 + \boldsymbol{C}_0)\boldsymbol{a} + \boldsymbol{D}_0 \boldsymbol{b} = 0 \\ (\alpha^2 \boldsymbol{E}_2 + \alpha \boldsymbol{E}_1 + \boldsymbol{E}_0)\boldsymbol{b} + (\alpha \boldsymbol{F}_1 + \boldsymbol{F}_0)\boldsymbol{a} = 0\end{aligned}\right\} \text{Fluid}$$

$$\left.\begin{aligned}(\alpha^2 \boldsymbol{P}_2 + \boldsymbol{P}_0)\boldsymbol{c} + (\alpha \boldsymbol{Q}_1 + \boldsymbol{Q}_0)\boldsymbol{d} + \alpha \boldsymbol{R}_1 \boldsymbol{e} = 0 \\ \alpha \boldsymbol{S}_1 \boldsymbol{c} + (\alpha^2 \boldsymbol{T}_2 + \boldsymbol{T}_0)\boldsymbol{d} + \boldsymbol{U}_0 \boldsymbol{e} = 0 \\ \alpha \boldsymbol{X}_1 \boldsymbol{c} + \boldsymbol{Y}_0 \boldsymbol{d} + (\alpha^2 \boldsymbol{Z}_2 + \boldsymbol{Z}_0)\boldsymbol{e} = 0\end{aligned}\right\} \text{Wall}$$

where $\boldsymbol{a}$ and $\boldsymbol{b}$ are defined as previously, whilst $\boldsymbol{c} = [c_0, \ldots, c_M]^T$ and similarly for $\boldsymbol{d}$ and $\boldsymbol{e}$.

The problem becomes fully specified by the inclusion of the boundary conditions defining zero displacement at the base of the layer, fluid conditions at infinity and continuity of velocity and stress at the wall/flow interface. The first two stipulations do not involve α but the conditions at the interface generate polynomial expressions as follows.

Continuity of velocity conditions :

$$(\alpha^2 \boldsymbol{a}_2 + \alpha \boldsymbol{a}_1 + \boldsymbol{a}_0)\boldsymbol{c} + (\alpha^2 \boldsymbol{b}_2 + \alpha \boldsymbol{b}_1 + \boldsymbol{b}_0)\boldsymbol{e} + \alpha \boldsymbol{c}_1 \boldsymbol{a} + \boldsymbol{d}_0 \boldsymbol{b} = 0$$

$$(\alpha^2 \boldsymbol{e}_2 + \alpha \boldsymbol{e}_1 + \boldsymbol{e}_0)\boldsymbol{d} + (\alpha^2 \boldsymbol{f}_2 + \alpha \boldsymbol{f}_1 + \boldsymbol{f}_0)\boldsymbol{e} + \alpha \boldsymbol{g}_1 \boldsymbol{a} + (\alpha \boldsymbol{h}_1 + \boldsymbol{h}_0)\boldsymbol{b} = 0$$

$$\alpha \boldsymbol{k}_1 \boldsymbol{a} + \boldsymbol{l}_0 \boldsymbol{e} = 0$$

Continuity of stress conditions :

$$(\alpha^2 \boldsymbol{m}_2 + \alpha \boldsymbol{m}_1 + \boldsymbol{m}_0)\boldsymbol{c} + (\alpha^3 \boldsymbol{n}_3 + \alpha^2 \boldsymbol{n}_2 + \alpha \boldsymbol{n}_1 + \boldsymbol{n}_0)\boldsymbol{e} + (\alpha^3 \boldsymbol{p}_3 + \alpha^2 \boldsymbol{p}_2 + \alpha \boldsymbol{p}_1)\boldsymbol{a} + \boldsymbol{q}_0 \boldsymbol{b} = 0$$

$$(\alpha^2 \boldsymbol{r}_2 + \alpha \boldsymbol{r}_1 + \boldsymbol{r}_0)\boldsymbol{d} + (\alpha^3 \boldsymbol{s}_3 + \alpha^2 \boldsymbol{s}_2 + \alpha \boldsymbol{s}_1 + \boldsymbol{s}_0)\boldsymbol{e} + (\alpha^2 \boldsymbol{t}_2 + \alpha \boldsymbol{t}_1 + \boldsymbol{t}_0)\boldsymbol{a} + (\alpha \boldsymbol{u}_1 + \boldsymbol{u}_0)\boldsymbol{b} = 0$$

$$(\alpha^4 \boldsymbol{v}_4 + \alpha^3 \boldsymbol{v}_3 + \alpha^2 \boldsymbol{v}_2)\boldsymbol{c} + (\alpha^3 \boldsymbol{w}_3 + \alpha^2 \boldsymbol{w}_2 + \alpha \boldsymbol{w}_1)\boldsymbol{d} + (\alpha^3 \boldsymbol{x}_3 + \alpha^2 \boldsymbol{x}_2 + \alpha \boldsymbol{x}_1)\boldsymbol{e} + (\alpha^3 \boldsymbol{y}_3 +$$
$$\alpha^2 \boldsymbol{y}_2 + \alpha \boldsymbol{y}_1 + \boldsymbol{y}_0)\boldsymbol{a} + (\alpha^2 \boldsymbol{z}_2 + \alpha \boldsymbol{z}_1 + \boldsymbol{z}_0)\boldsymbol{b} = 0$$

where $\boldsymbol{a}_i, \ldots, \boldsymbol{z}_i$ are row vectors.

A generalised eigenvalue problem of the form $\boldsymbol{AV} = \alpha \boldsymbol{BV}$ can then be constructed where

$$\boldsymbol{V} = [\alpha^3 \boldsymbol{a}, \alpha^2 \boldsymbol{a}, \alpha \boldsymbol{a}, \boldsymbol{a}, \alpha \boldsymbol{b}, \boldsymbol{b}, \alpha^3 \boldsymbol{c}, \alpha^2 \boldsymbol{c}, \alpha \boldsymbol{c}, \boldsymbol{c}, \alpha^2 \boldsymbol{d}, \alpha \boldsymbol{d}, \boldsymbol{d}, \alpha^2 \boldsymbol{e}, \alpha \boldsymbol{e}, \boldsymbol{e}]^T .$$

In the work of Yeo *et al.* (1995) the wall terms were approximated by polynomials of the order M =15-20 and the fluid terms in the present investigation required N = 56. The above form of the generalised eigenvalue problem involves matrices of the order $6(N+1)+10(M+1)$ which using the above values for N and M corresponds to a matrix size of at least 512. If the problem is formulated in terms of the temporal eigenvalue then the size can be reduced to $2(N+1)+6(M+1)$ which is almost half the spatial formulation size. The QZ algorithm implemented to solve generalised eigenvalue problems of this kind has a solution time proportional to the cube of the matrix size so that the spatial problem will require about eight times that of the temporal global scheme. However, reasons of preference towards the spatial formulation have already been stated and a spatial global solver would be the only clear way of relating to the existing results. Thus although the global scheme is possible it would only be an efficient and worthwhile undertaking if sufficient computational power is available.

REFERENCES

Arnal, D., (1986), "Diagrammes de Stabilité des Profiles de Couche Limite Auto-Semables en Encoulement Bidimensional Incompressible, sans et avec Courant de Retour", Raport Technique OA No. 34/5018, Toulouse.

Alfredsson, P.A., and Persson, H., (1989), "Instabilities in Channel Flow with System Rotation", *J. Fluid Mech.*, **202**, pp. 543-557.

Balachandar, S., Street, C.L., and Malik, M.R., (1992), "Secondary Instability in Rotating-Disk Flow", *J. Fluid Mech.*, **242**, pp. 323.

Balakumar, P., and Malik, M.R., (1990), "Traveling Disturbances in Rotating-Disk Flow", *Theoretical and Computational Fluid Dynamics*, **2**, pp. 125-137.

Bassom, A.P., and Gajjar, J.S.B., (1988), "Non-stationary Cross-flow Vortices in Three-dimensional Boundary-layer Flows", *Proc. Roy. Soc. Lond. A* **417**, pp. 179-212.

Benjamin, T.B., (1959), "Shearing Flow Over a Wavy Boundary", *J. Fluid Mech.*, **6**, pp. 161-205.

Benjamin, T.B., (1960), "Effects of a Flexible Boundary on Hydrodynamic Stability", *J. Fluid Mech.*, **9**, pp. 513-532.

Benjamin, T.B., (1963), "The Three-fold Classification of Unstable Disturbances in Flexible Surfaces Bounding Inviscid Flows.", *J. Fluid Mech.*, **16**, pp. 436-450.

Benton, E.R., (1966), "On the Flow Due to a Rotating Disk", *J. Fluid Mech.*, **24**, pp. 781-800.

Benton, G.S., (1956), "The Effects of the Earth's Rotation on Laminar Flows in Pipes", *J.Appl. Mech.*, **23**, pp. 123-127.

Bridges, T.J., and Cooper, A.J., (1995), "Spanwise Modulation of Streamwise Rolls in Rotating Channel Flow", *Q. J. Mech. Appl. Math.*, **48**, pp. 257-284.

Bridges, T.J., and Morris, P.J., (1984), "Differential Eigenvalue Problems in which the Parameter Appears Nonlinearly", *Journal of Computational Physics*, **55**, No. 3, pp. 437-460.

Brown, W.B., (1959), "Numerical Calculation of the Stability of Cross Flow Profiles in Laminar Boundary Layers on the Rotating Disc and an Exact Calculation of the Stability of

the Blasius Velocity Profile", *Rep. No. NAI 59-5*, Northrop Aircraft Inc. Hawthorne, CA.

Brown, W.B., (1961) "A Stability Criterion for Three-dimensional Laminar Boundary Layers", In *Boundary Layer and Flow Control*, ed. Lachmann, G.V., **2**, Pergamon, New York, pp. 913-923.

Canuto, C., Hussaini, M.Y., Quarteroni, A., and Zang, T.A., (1988), *Spectral Methods in Fluid Dynamics*, Springer-Verlag.

Carpenter, P.W., (1990), "Status of Transition Delay Using Compliant Walls", *Viscous Drag Reduction in Boundary Layers*, ed. Bushnell, D M. and Hefner, J.N., **123**, *Progress in Astronautics and Aeronautics*, AIAA, Washington, DC, pp. 79-113.

Carpenter, P.W., (1993), "The Optimization of Multiple-Panel Compliant Walls for Delay of Laminar-Turbulent Transition", *AIAA J.*, **31**, pp. 1187-1188.

Carpenter, P.W., (1994) Private communication.

Carpenter, P.W., and Gajjar, J.S.B., (1990), "A General Theory for Two- and Three-Dimensional Wall-Mode Instabilities in Boundary Layers over Isotropic and Anisotropic Compliant Walls", *Theoretical and Computational Fluid Dynamics*, **1**, pp. 349-378.

Carpenter, P.W., and Garrad, A.D., (1985),"The Hydrodynamic Stability of Flows Over Kramer-type Compliant Walls. Pt 1. Tollmien-Schlichting Instabilities", *J. Fluid Mech.*, **155**, pp.465-510.

Carpenter, P.W., and Garrad, A.D., (1986), "The Hydrodynamic Stability of Flows Over Kramer-type Compliant Wall. Pt 2. Flow-induced Surface Instabilities", *J. Fluid Mech.* , **170**, pp. 199-232.

Carpenter, P.W., Joslin, R.D., and Morris, P.J., (1991), "A Note on the Occurrence of an Apparently Anomalous Spatially Growing Eigenmode for the Coupled Flow/Compliant-Wall", Internal Report, Department of Engineering, Univ. of Warwick.

Carpenter, P.W., and Morris, P.J., (1990), "The Effect of Anisotropic Wall Compliance on Boundary-Layer Stability and Transition", *J. Fluid Mech.*, **218**, pp. 171-223.

Cebeci, T., and Stewartson, K., (1980), "Stability and Transition in Three-Dimensional Flows", *AIAA J.*, **18**, pp. 398-405.

Chin, D., and Litt, M., (1972), "An Electrochemical Study of Flow Instability on a Rotating Disk", *J. Fluid Mech.*, **54**, pp. 613-625.

Chung, K.H., (1985), "Composite Compliant Coatings for Drag Reduction Utilising Low Modulus High Damping Silicone Rubber", Ph.D. Thesis, MIT.

Chung, K.H., and Merrill, E.W., (1984), "Drag Reduction by Compliant Surfaces Measured on Rotating Discs", Pres. at *Compliant Coating Drag Reduction Program Review*, Office of Naval Research, Washington, D.C.

Clarkson, M.H., Chin, S.C., and Shacter, P., (1980), "Flow Visualization in Boundary Layer Transition Regime on a Rotating Disk", *Acta Mechanica*, **35**, pp. 71-82.

Crouch, J.D., and Herbert, Th., (1993), "A Note on the Calculation of Landau Constants", *Phys. Fluids* **A5**, pp. 283-285.

Daniel, A.P., Gaster, M., and Willis, G.J.K., (1987), "Boundary Layer Stability on Compliant Surfaces", British Maritime Technology Ltd., UK, Report.

Davey, A., Hocking, L.M., and Stewartson, K., (1974), "On the Nonlinear Evolution of Three-Dimensional Disturbances in Plane Poiseuille Flow", *J. Fluid Mech.*, **63**, pp. 529-536.

Davies, C., and Carpenter, P.W., (1995), "Novel Velocity-vorticity Formulation of the Navier-Stokes Equations for Boundary-layer Disturbances", *Bull. Amer. Phys. Soc.*, **40**, No. 12, pp. 1956.

Denier, J.P., and Hall, P., (1991), "The Effect of Wall Compliance on the Görtler Vortex Instability", *Phys. Fluids* **A3**, pp. 2000-2002.

Dixon, A.E., Lucey, A.D., and Carpenter, P.W., (1994), "Optimization of Viscoelastic Compliant Walls for Transition Delay", *AIAA J.*, **32**, pp. 256-267.

Dominguez-Lerma, M.A., Cannell, D.S., and Ahler, G.,(1986), "Eckhaus Boundary and Wave-number Selection in Rotating Couette-Taylor Flow", *Phys. Rev.*, A **34**, pp. 4956-4970.

Drazin, P.G., and Reid, W.H., (1981), *Hydrodynamic Stability*, Camb. Univ. Press.

Duncan, J.H., (1988), "The Dynamics of Waves at the Interface Between a Two-Layer Viscoelastic Wall and a Fluid Flow", *J. Fluids and Structures*, **2**, pp. 35-51.

Eckhaus, W., (1965), *Studies in Nonlinear Stability Theory*, Springer.

Falkner, V.M., and Skan, S.W., (1930), "Some Approximate Solutions of the Boundary Layer Equations", *British Aero. Res. Council, Reports and Memoranda*, pp. 1314.

the Blasius Velocity Profile". *Rep. No. NAI 59-5*. Northrop Aircraft Inc. Hawthorne, CA.

Brown. W.B., (1961) "A Stability Criterion for Three-dimensional Laminar Boundary Layers". In *Boundary Layer and Flow Control*. ed. Lachmann. G.V., **2**. Pergamon. New York. pp. 913-923.

Canuto. C., Hussaini. M.Y., Quarteroni. A., and Zang. T.A., (1988). *Spectral Methods in Fluid Dynamics*. Springer-Verlag.

Carpenter. P.W., (1990). "Status of Transition Delay Using Compliant Walls". *Viscous Drag Reduction in Boundary Layers*. ed. Bushnell. D.M. and Hefner. J.N., **123**. *Progress in Astronautics and Aeronautics*. AIAA. Washington. DC. pp. 79-113.

Carpenter. P.W., (1993). "The Optimization of Multiple-Panel Compliant Walls for Delay of Laminar-Turbulent Transition". *AIAA J.*, **31**. pp. 1187-1188.

Carpenter. P.W., (1994) Private communication.

Carpenter. P.W., and Gajjar. J.S.B., (1990). "A General Theory for Two- and Three-Dimensional Wall-Mode Instabilities in Boundary Layers over Isotropic and Anisotropic Compliant Walls". *Theoretical and Computational Fluid Dynamics*. **1**. pp. 349-378.

Carpenter. P.W., and Garrad. A.D., (1985). "The Hydrodynamic Stability of Flows Over Kramer-type Compliant Walls. Pt 1. Tollmien-Schlichting Instabilities". *J. Fluid Mech.*, **155**. pp 465-510.

Carpenter. P.W., and Garrad. A.D., (1986). "The Hydrodynamic Stability of Flows Over Kramer-type Compliant Wall. Pt 2. Flow-induced Surface Instabilities". *J. Fluid Mech.*, **170**. pp. 199-232.

Carpenter. P.W., Joslin. R.D., and Morris. P.J., (1991). "A Note on the Occurrence of an Apparently Anomalous Spatially Growing Eigenmode for the Coupled Flow/Compliant-Wall". Internal Report. Department of Engineering. Univ. of Warwick.

Carpenter. P.W., and Morris. P.J., (1990). "The Effect of Anisotropic Wall Compliance on Boundary-Layer Stability and Transition". *J. Fluid Mech.*, **218**. pp. 171-223.

Cebeci. T., and Stewartson. K., (1980). "Stability and Transition in Three-Dimensional Flows". *AIAA J.*, **18**. pp. 398-405.

Chin. D., and Litt. M., (1972). "An Electrochemical Study of Flow Instability on a Rotating Disk". *J. Fluid Mech.*, **54**. pp. 613-625.

Chung. K.H.. (1985). "Composite Compliant Coatings for Drag Reduction Utilising Low Modulus High Damping Silicone Rubber". Ph.D. Thesis. MIT.

Chung. K.H.. and Merrill. E.W.. (1984). "Drag Reduction by Compliant Surfaces Measured on Rotating Discs". Pres. at *Compliant Coating Drag Reduction Program Review*. Office of Naval Research. Washington. D.C.

Clarkson. M.H.. Chin. S.C.. and Shacter. P.. (1980). "Flow Visualization in Boundary Layer Transition Regime on a Rotating Disk". *Acta Mechanica*. **35**. pp. 71-82.

Crouch. J.D.. and Herbert. Th.. (1993). "A Note on the Calculation of Landau Constants". *Phys. Fluids* **A5**. pp. 283-285.

Daniel. A.P.. Gaster. M.. and Willis. G.J.K.. (1987). "Boundary Layer Stability on Compliant Surfaces". British Maritime Technology Ltd.. UK. Report.

Davey. A.. Hocking. L.M.. and Stewartson. K.. (1974). "On the Nonlinear Evolution of Three-Dimensional Disturbances in Plane Poiseuille Flow". *J. Fluid Mech.*. **63**. pp. 529-536.

Davies. C.. and Carpenter. P.W.. (1995). "Novel Velocity-vorticity Formulation of the Navier-Stokes Equations for Boundary-layer Disturbances". *Bull. Amer. Phys. Soc.*. **40**. No. 12. pp. 1956.

Denier. J.P.. and Hall. P.. (1991). "The Effect of Wall Compliance on the Görtler Vortex Instability". *Phys. Fluids* **A3**. pp. 2000-2002.

Dixon. A.E.. Lucey. A.D.. and Carpenter. P.W.. (1994). "Optimization of Viscoelastic Compliant Walls for Transition Delay". *AIAA J.*. **32**. pp. 256-267.

Dominguez-Lerma. M.A.. Cannell. D.S.. and Ahler. G.(1986). "Eckhaus Boundary and Wave-number Selection in Rotating Couette-Taylor Flow". *Phys. Rev.* A **34**. pp. 4956-4970.

Drazin. P.G.. and Reid. W.H.. (1981). *Hydrodynamic Stability*. Camb. Univ. Press.

Duncan. J.H.. (1988). "The Dynamics of Waves at the Interface Between a Two-Layer Viscoelastic Wall and a Fluid Flow". *J. Fluids and Structures*. **2**. pp. 35-51.

Eckhaus. W.. (1965). *Studies in Nonlinear Stability Theory*. Springer.

Falkner. V.M.. and Skan. S.W.. (1930). "Some Approximate Solutions of the Boundary Layer Equations". *British Aero. Res. Council. Reports and Memoranda*. pp. 1314.

Faller, A.J., (1963), "An Experimental Study of the Instability of the Laminar Ekman Boundary Layer", *J. Fluid Mech.*, **15**, pp. 560-576.

Faller, A.J., (1991) "Instability and Transition of the Disturbed Flow Over a Rotating Disk", *J. Fluid Mech.*, **230**, pp. 245-269.

Faller, A.J., and Kaylor, R.E., (1966) "A Numerical Study of the Instability of the Ekman Boundary Layer", *J. Atmos. Sci.*, **23**, pp. 466-480.

Fedorov, B.I., Plavnik, G.Z., Prokhov, I.V., and Zhukhovitskii, L.G., (1976), "Transitional Flow Conditions on a Rotating Disk", *J. Eng. Phys.*, **31**, pp. 1448-1453.

Finlay, W.H., (1989),"Perturbation Expansion and Weakly Nonlinear Analysis for Two-Dimensional Vortices in Curved or Rotating Channels", *Phys. Fluids* A **1**, pp. 854-860.

Finlay, W.H., (1990),"Transition to Oscillatory Motion in Rotating Channel Flow", *J. Fluid Mech.*, **215**, pp. 209-227.

Finlay, W.H., Keller, J.B., and Ferziger, J.H., (1988), "Instability and Transition in Curved Channel Flow", *J. Fluid Mech.*, **194**, pp. 417-456.

Fox, L., and Parker, I.B., (1968), *Chebyshev Polynomials in Numerical Analysis*, Oxford Univ. Press, London.

Fraser, L.A., and Carpenter, P.W., (1985), "A Numerical Investigation of Hydroelastic and Hydrodynamic Instabilities in Laminar Flows over Compliant Surfaces Comprising One or Two Layers of Visco-elastic Material", In *Numerical Methods in Laminar and Turbulent Flow*, Pineridge, Swansea, Wales, UK, pp. 1171-1181.

Gad-el-Hak, M., (1986), "Boundary Layer Interactions with Compliant Coatings : An Overview", *Applied Mechanics Review*, **39**, No. 4, pp. 511-524.

Gaster, M., (1962), "A Note on the Relation Between Temporally Increasing and Spatially Increasing Disturbances in Hydrodynamic Stability", *J. Fluid Mech.*, **14**, pp. 222-224.

Gaster, M., (1987), "Is the Dolphin a Red Herring ?", *IUTAM Symposium on Turbulence Management and Relaminarisation, Bangalore, India*, ed. Liepmann, H.W., and Narasimha, R., Springer-Verlag, New York, pp. 285-304.

Godunov, S.K., (1961), "On the Numerical Solution of Boundary-Value Problems for Systems of Linear Ordinary Differential Equations", (In Russian), *Uspekhi Mat. Nauk*, **16**, pp. 171-174.

Gray, J., (1936), "Studies in Animal Locomotion. VI The Propulsive Powers of the Dolphin", *J. Experimental Biology*, **13**, pp. 192-199.

Gray, W.E., (1952), "The Effect of Wing Sweep on Laminar Flow", *RAE TM Aero 255*.

Greenspan, H.P., (1968), *The Theory of Rotating Fluids*, Camb. Univ. Press.

Gregory, N., Stuart, J.T., and Walker, W.S., (1955), "On the Stability of Three-Dimensional Boundary Layers with Application to the Flow Due to a Rotating Disk", *Philosophical Transactions of the Royal Society, London, Series A* **248**, pp. 155-199.

Guo, Y., and Finlay, W.H., (1991), "Splitting, Merging and Wavelength Selection of Vortices in Curved and/or Rotating Channel Flow due to Eckhaus Instability", *J. Fluid Mech.*, **228**, pp. 661-691.

Gyorgyfalvy, D., (1967), "Possibilities of Drag Reduction by the Use of Flexible Skin", *J. Aircraft*, **4**, pp. 186-192.

Hall, P., (1984), "Evolution Equations for Taylor Vortices in the Small-gap Limit", *Phys. Rev.* A **29**, pp. 2921-2923.

Hall, P., (1986), "An Asymptotic Investigation of the Stationary Modes of the Instability of the Boundary Layer on a Rotating Disc", *Proc. Roy. Soc. Lond. A* **406**, pp. 93-106.

Halleen, R.M., and Johnston, J.P., (1967), "The Influence of Rotation on Flow in a Long Rectangular Channel: an Experimental Study", *Department of Mechanical Engineering, Stanford University, Rep. MD-18*.

Hansen, R.J., and Hunston, D.L., (1974), "An Experimental Study of Turbulent Flows Over Compliant Surfaces", *J. Sound Vib.*, **34**, No. 3, pp. 297-308.

Hansen, R.J., and Hunston, D.L., (1983), "Fluid-Property Effects on Flow-Generated Waves on a Flexible Surface", *J. Fluid Mech.*, **133**, pp. 161-177.

Hart, J.E., (1972), "Instability and Secondary Motion in a Rotating Channel Flow", *J.Fluid Mech.*, **45**, pp. 341-351.

Jarre, S., Le Gal, P., and Chauve, M.P., (1991), "Experimental Analysis of the Instability of the Boundary Layer Over a Rotating Disk", *Europhys. Lett.*, **14** (7), pp. 649-654.

Johnston, J.P., Halleen, R.M., and Lezius, D.K., (1972), "Effects of Spanwise Rotation on the Structure of Two-Dimensional Fully Developed Turbulent Channel Flow", *J. Fluid Mech.*, **56**, pp. 533-577.

Jordinson, R., (1970), "The Flat Plate Boundary Layer. Part 1. Numerical Integration of the Orr-Sommerfeld Equation", *J. Fluid Mech.*, **43**, pp. 801-811.

Kármán, Th. von, (1921), "Über laminare und turbulente Reibung", *Zeitschrift für angewandte Mathematik und Mechanik*, **1**, pp. 233-252.

Khesghi, H.S., and Scriven, L.E., (1985), "Viscous Flow Through a Rotating Square Channel", *Phys. Fluids*, **28**, pp. 2968-2979.

Khorrami, M.R., (1991), "A Chebyshev Spectral Collocation Method Using a Staggered Grid for the Stability of Cylindrical Flows", *Int. J. Num. Meth. Fluids*, **12**, pp. 825-833.

Kitamura, O., (1973), "Experimental Investigation on Transition of the Boundary Layer Formed on a Rotating Disk", MS Thesis, Dept. Mech. Eng., Hokkaido Univ., Sapporo, Jpn.

Kobayashi, R., Kohama, Y., and Takamadate, Ch., (1980), "Spiral Vortices in Boundary Layer Transition Regime on a Rotating Disk", *Acta Mechanica*, **35**, pp. 71-82.

Kohama, Y., (1984), "Study on Boundary Layer Transition of a Rotating Disk", *Acta Mechanica*, **50**, pp. 193-199.

Kohama, Y., (1987), "Crossflow Instability in Rotating Disk Flow", *AIAA 87-1340*.

Kramer, L., and Zimmermann, W., (1985), "On the Eckhaus Instability for Spatially Periodic Patterns", *Physica D*, **16**, pp. 221-232.

Kramer, M.O., (1960), "Boundary-Layer Stabilization by Distributed Damping", *Journal of the American Society of Naval Engineers*, **72**, pp. 25-33; *Journal of the Aero/Space Sciences*, **27**, pp. 69.

Kramer, M.O., (1962),"Boundary-Layer Stabilization by Distributed Damping", *Journal of the American Society of Naval Engineers*, **74**, pp. 341-348.

Kristoffersen, R., and Andersson, H.I., (1993),"Direct Simulations of Low-Reynolds Number Turbulent Flow in a Rotating Channel", *J. Fluid Mech.*, **256**, pp. 163-167.

Landahl, M.T., (1962), "On the Stability of a Laminar Incompressible Boundary Layer Over a Flexible Surface", *J. Fluid Mech.*, **13**, pp. 609-632.

Lezius, D.K., and Johnston, J.P., (1976),"Roll-cell Instabilities in Rotating Laminar and Turbulent Channel Flows", *J. Fluid Mech.*, **77**, pp. 153-175.

Lilley, D.K., (1966), "On the Instability of Ekman Boundary Flow", *Journal of Atmospheric Sciences*, **23**, pp. 481-494.

Lin, C.C., (1945), "On the Stability of Two-Dimensional Parallel Flows", *Quarterly of Applied Mathematics*, **3**, pp. 117-142, 218-234, 277-301.

Lingwood, R.J., (1995), "Absolute Instability of the Boundary Layer on a Rotating Disk", *J. Fluid Mech.*, **299**, pp. 17-33.

Lucey, A.D., Carpenter, P.W., and Dixon, A.E., (1991), "The Role of Wall Instabilities in Boundary-Layer Transition over Compliant Walls", *Proceedings of Conference on Boundary Layer Transition and Control* (Cambridge, UK), Royal Aeronautical Society, London, England, pp. 35.1-35.10.

Mack, L.M., (1985), "The Wave Pattern Produced by Point Source on a Rotating Disk", *AIAA 85-0490*.

MacKerrell, S.O., (1987), "A Nonlinear, Asymptotic Investigation of the Stationary Modes of Instability of the Three-dimensional Boundary Layer on a Rotating Disc.", *Proc. Roy. Soc. Lond. A* **413**, pp. 497-513.

Magnus, J.R., and Neudecker, H., (1988), *Matrix Differential Calculus*, John Wiley and Sons, New York.

Malik, M.R., (1986a), "The Neutral Curve for Stationary Disturbances in Rotating Disk Flow", *J. Fluid Mech.*, **164**, pp. 275-287.

Malik, M.R., (1986b), "Numerical Simulation of Transition in a Three-dimensional Boundary Layer", *Proc. 10th Int. Conf. on Numerical Methods in Fluid Dynamics*, ed. Zhuang, F.G., and Zhu, Y.L., Springer Verlag, New York. (Lecture Notes in Physics series.)

Malik, M.R., Wilkinson, S.P., and Orszag, S.A., (1981), "Instability and Transition in Rotating Disk Flow", *AIAA J.*, **19**, pp. 1131-1138.

Marlatt, S.W., and Biringen, S., (1995), "Numerical Simulation of Spatially Evolving Ekman Layer Instability", *Phys. Fluids*, **7** (2), pp.449-451.

Marliani, G., Matzkeit, M., and Ram, V.I.V., (1994), "Longitudinal Vortices in the Channel Flow Caused by Coriolis Forces due to Rotation of the System", Pres. at *2nd European Fluid Mech. Conf.*, Warsaw, Poland.

Matsson, O.J., and Alfredsson, P.A.,(1990), "Curvature- and Rotation-induced Instabilities in Channel Flow", *J. Fluid Mech.*, **210**, pp. 537-563.

Morris, P.J., (1976), "The Spatial Viscous Instability of Axisymmetric Jets", *J. Fluid Mech.*, **77**, pp. 511-529.

Newell, A.C., and Whitehead, J.A., (1969), "Finite Bandwidth, Finite Amplitude Convection", *J. Fluid Mech.*, **38**, pp. 279-303.

Ng, L., Singer, B.A., Henningson, D.S., and Alfredsson, P.A., (1990), "Instabilities in Rotating Channel Flow", *Proc. Transition and Turbulence Workshop, NASA Langley Research Center*, Springer-Verlag.

Orszag, S.A., (1971), "Accurate Solution of the Orr-Sommerfeld Stability Equation", *J. Fluid Mech.*, **50**, pp. 689-703.

Owen, P.R., and Randall, D.J., (1952), "Boundary Layer Transition on the Swept Wing", RAE TM Aero 277.

Pohlhausen, K., (1921), "Zur näherungsweisen Integration der Differentailgleichung der laminaren Reibungsshicht", ZAMM **1**, pp. 252-268.

Rayleigh, Lord, (1880), "On the stability, or instability, of certain fluid motions", *Proc. London Math. Soc.*, **11**, pp. 57-70.

Riley, J.J., Gad-el-Hak, M., and Metcalfe, R.W., (1988),"Compliant Coatings", *Annual Review of Fluid Mechanics*, **20**, pp. 393-420.

Schlichting, H., (1968), *Boundary Layer Theory*, McGraw Hill, New York.

Scott, M.R., and Watts, H.R., (1977), "Computational Solutions of Linear Two-Point Boundary Value Problems via Orthonormalization", *SIAM J. Numer. Anal.*, **14**, pp. 40-70.

Sen, P.K., and Arora, D.S., (1988), "On the Stability of Laminar Boundary-Layer Flow Over a Flat Plate With a Compliant Wall", *J. Fluid Mech.*, **197**, pp. 201-240.

Singer, B.A., (1992), "A Weakly Nonlinear Theory Based Expansion for Wave Interactions in Rotating Channel Flow", *Phys. Fluids* **A1**, pp. 92-94.

Smirnov, E.M., and Yurkin, S.V., (1983), "Fluid flow in a Rotating Channel of Square Section", *Fluid Dyn.*, **18**, pp. 850-855.

Smith, N.H., (1946), "Exploratory Investigation of Laminar Boundary Layer Oscillations on a Rotating Disk", NACA Tech. Note No. 1227.

Speziale, C.G., (1982), "Numerical Study of Viscous Flow in Rotating Rectangular Ducts",

J. Fluid Mech., **122**, pp. 251-271.

Speziale, C.G., and Thangham, S., (1983), "Numerical Study of Secondary Flows and Roll-cell Instabilities in Rotating Channel Flow", *J. Fluid Mech.*, **130**, pp. 377-395.

Tatro, P.R., and Mollö-Christensen, E.L., (1967), "Experiments on Ekman Layer Instability", *J. Fluid Mech.*, **28**, pp. 531-543.

Tollmien, W., (1935), "Ein allgemeines Kriterium der Instabilität laminarer Geschwindigkeitsverteilungen", *Nachr. Wiss. Fachgruppe. Göttigen. Math.phys.Kl.*, **1**, pp. 79-114.

Tritton, D.J., and Davies, P.A., (1985), "Instabilities in Geophysical Fluid Dynamics" In *Hydrodynamic Instabilities and the Transition to Turbulence*, 2nd edn (ed. Swinney, H.L., and Gollub, J.P.), Topics in Applied Physics, Vol. 45, pp. 229-270, Springer.

Wilkinson, S.P., and Malik, M.R., (1983), "Stability Experiments in Rotating-Disk Flow", *AIAA 83-1760*.

Wilkinson, S.P., and Malik, M.R., (1985), "Stability Experiments in the Flow Over a Rotating Disk", *AIAA J.*, **21**, pp. 588-595.

Willis, G.J.K., (1986), "Hydrodynamic Stability of Boundary Layers over Compliant Surfaces", Ph.D. Thesis, University of Exeter, School of Engineering, England, UK.

Yamashita, I., and Takematsu, M., (1974), "A Numerical Study of the Instability of Three-Dimensional Boundary Layers", *Reps. of Res. Inst. for Applied Mech., Kyushu Univ., Japan.*

Yang, K., and Kim, J., (1991), "Numerical Investigations of Instability and Transition in Rotating Plane Poiseuille Flow", *Phys. Fluids* **A3**, pp. 633-641.

Yeo, K.S., (1988), "The Stability of Boundary Layer Flow over Single- and Multi-layer Viscoelastic Walls", *J. Fluid Mech.*, **196**, pp. 359-408.

Yeo, K.S., and Dowling, A.P., (1987), "The Stability of Inviscid Flows Over Passive Compliant Walls", *J. Fluid Mech.*, **183**, pp. 265.

Yeo, K.S., Khoo, B.C., and Zhao, H.Z., (1995), "The Absolute Instability of Boundary-layer Flow over Viscoelastic Walls", to appear in *Theoretical and Computational Fluid Dynamics.*

APPENDIX A

Functions Appearing in the Weakly Nonlinear Analysis of Chapter 2.

In the weakly nonlinear analysis of § 2.10 the following sequence of problems arises.

$$\boldsymbol{L}_c\boldsymbol{\Phi}_j = \boldsymbol{f}_j \qquad j = 1, 2, \ldots .$$

where

$$\boldsymbol{f}_1 = 0$$

$$\boldsymbol{f}_2 = \mathcal{J}\boldsymbol{f}_{212}Ae^{it} + \boldsymbol{f}_{22}A^2e^{2it} + \text{c.c.} + \boldsymbol{f}_{23}|A|^2$$

$$\boldsymbol{f}_3 = \mathcal{J}_1^2\boldsymbol{f}_{31} + R_2\boldsymbol{f}_{32} + |A|^2\boldsymbol{f}_{33}.$$

Terms which vanish in the solvability condition have been omitted. The vectors $\boldsymbol{f}_{jk}$ are expressed in terms of the first and second order solutions.

$$\boldsymbol{\Phi}_1 = [u_1, v_1, w_1, p_1]^T. \qquad \boldsymbol{\Phi}_{2j} = [u_{2j}, v_{2j}, w_{2j}, p_{2j}]^T, \quad j = 1, 2, 3.$$

$$\boldsymbol{f}_{212} = -\tfrac{2\mathcal{J}_c}{R_c}\begin{bmatrix} u_1 \\ v_1 \\ w_1 \\ 0 \end{bmatrix} - \begin{bmatrix} 0 \\ 0 \\ p_1 \\ w_1 \end{bmatrix}$$

$$\boldsymbol{f}_{22} = \begin{bmatrix} \mathcal{J}_c u_1 w_1 - u_1' v_1 \\ \mathcal{J}_c v_1 w_1 - v_1' v_1 \\ \mathcal{J}_c w_1^2 - w_1' v_1 \\ 0 \end{bmatrix}$$

$$\boldsymbol{f}_{23} = \begin{bmatrix} -2\mathcal{J}_c u_1 w_1 - 2u_1' v_1 \\ -2\mathcal{J}_c v_1 w_1 - 2v_1' v_1 \\ 0 \\ 0 \end{bmatrix}$$

$$\boldsymbol{f}_{31} = -\tfrac{2\mathcal{J}_c}{R_c}\begin{bmatrix} u_{21} \\ v_{21} \\ w_{21} \\ 0 \end{bmatrix} - \tfrac{1}{R_c}\begin{bmatrix} u_1 \\ v_1 \\ w_1 \\ 0 \end{bmatrix} - \begin{bmatrix} 0 \\ 0 \\ p_{21} \\ w_{21} \end{bmatrix}$$

$$\boldsymbol{f}_{32} = -\frac{1}{R_c^2}\begin{bmatrix} \hat{u}_1'' - \beta_c^2 \hat{u}_1 \\ \hat{v}_1'' - \beta_c^2 \hat{v}_1 \\ \hat{w}_1'' - \beta_c^2 \hat{w}_1 \\ 0 \end{bmatrix}$$

$$\boldsymbol{f}_{33} = \begin{bmatrix} -\hat{v}_1 u_{23}' - \hat{v}_1 u_{22}' - \hat{u}_1' v_{23} - \hat{u}_1' v_{22} - 2\beta_c \hat{w}_1 u_{22} - \beta_c \hat{u}_1 w_{22} + \beta_c \hat{u}_1 w_{23} \\ -\hat{v}_1 v_{23}' - \hat{v}_1 v_{22}' - \hat{v}_1' v_{23} - \hat{v}_1' v_{22} - 2\beta_c \hat{w}_1 v_{22} - \beta_c \hat{v}_1 w_{22} + \beta_c \hat{v}_1 w_{23} \\ -\hat{w}_1' v_{23} + \hat{w}_1' v_{22} - \hat{v}_1 w_{23}' - \hat{v}_1 w_{22}' - 2\beta_c \hat{w}_1 w_{22} + \beta_c \hat{w}_1 w_{22} + \beta_c \hat{w}_1 w_{23} \\ 0 \end{bmatrix}$$

APPENDIX B

Matrix Entries Defining Compliant Wall Boundary Conditions in Chapter 4.

The elements in the transformation matrices used to determine the compliant wall boundary conditions are as follows.

Matrix $\boldsymbol{Q}$ appearing of Eq.(4.64) :

$$\begin{bmatrix} -i\bar{\alpha}\sinh(\bar{\alpha}K_L l\bar{d}) & i\bar{\alpha}\cosh(\bar{\alpha}K_L l\bar{d}) & \bar{\alpha}K_T\cosh(\bar{\alpha}K_T l\bar{d}) & -\bar{\alpha}K_T\sinh(\bar{\alpha}K_T l\bar{d}) \\ \bar{\alpha}K_L\cosh(\bar{\alpha}K_L l\bar{d}) & -\bar{\alpha}\sinh(\bar{\alpha}K_L l\bar{d}) & i\bar{\alpha}\sinh(\bar{\alpha}K_T l\bar{d}) & -i\bar{\alpha}\cosh(\bar{\alpha}K_T l\bar{d}) \end{bmatrix}$$

where $l = L/\delta^*$.

Matrix $\boldsymbol{P}$ of Eq.(4.65) :

$$\begin{bmatrix} 0 & i\bar{\alpha} & \bar{\alpha}K_T & 0 \\ \bar{\alpha}K_L & 0 & 0 & -i\bar{\alpha} \\ \bar{\alpha}^3K_L P_1 & \bar{\alpha}^2(2\bar{G}_s K_L^2 + \bar{Y}_s(K_L^2-1)) & -2i\bar{\alpha}^2\bar{G}_s K_T & -i\bar{\alpha}^3 P_1 \\ 2i\bar{\alpha}^2\bar{G}_s K_L & i\bar{\alpha}^3 P_2 & \bar{\alpha}^3 K_T P_2 & \bar{\alpha}^2\bar{G}_s(K_T^2+1) \end{bmatrix}$$

where

$$P_1 = \left[-\frac{\bar{b}\bar{\omega}^2}{\bar{\alpha}}l + \bar{B}_p\bar{\alpha}^2 l^3\right], \quad P_2 = \left[-\frac{\bar{b}\bar{\omega}^2}{\bar{\alpha}^2}l + \bar{E}_p\bar{b}\,l\right] \quad \text{and} \quad \bar{Y}_s = \bar{K}_s + \frac{\bar{G}_s}{3}.$$

Matrix $\boldsymbol{D}$ of Eq.(4.67) :

$$\begin{bmatrix} -\frac{U'}{\bar{\omega}^2} & -\frac{1}{\bar{\alpha}\bar{\omega}} & 0 & 0 \\ \frac{i}{\bar{\omega}} & 0 & 0 & 0 \\ -\frac{iU'_w}{\bar{\alpha}} & \left(\frac{3}{R_{\delta^*}} - \frac{i\bar{\omega}}{\bar{\alpha}^2}\right) & 0 & -\frac{1}{\bar{\alpha}^2 R_{\delta^*}} \\ \frac{i\bar{\alpha}}{R_{\delta^*}} + \frac{iU''}{\bar{\omega}R_{\delta^*}} & 0 & \frac{1}{\bar{\alpha}R_{\delta^*}} & 0 \end{bmatrix}$$

APPENDIX C

Coefficients in Transformed form of Rotating Disc Stability Equations.

The coefficients in Eqs.(6.25) and (6.26) are as follows.

$$\tilde{A} = i\lambda^2\bar{\lambda}^2 - \bar{\lambda}^2 R(\alpha F + \beta G - \omega) - R(\alpha[mm'F' + m^2F''] + \beta[mm'G' + m^2G'']) + iH'\bar{\lambda}^2 m$$

$$\tilde{B} = i[4m^2m'm'' + m(m')^3] - i(\lambda^2 + \bar{\lambda}^2)mm' + R(\alpha F + \beta G - \omega)mm' - iH[m^2m'' + m(m')^2] + iH\bar{\lambda}^2 m - im^2m'H' - iFmm'$$

$$\tilde{C} = i[4m^3m'' + 7m^2(m')^2] - i(\lambda^2 + \bar{\lambda}^2)m^2 + R(\alpha F + \beta G - \omega)m^2 - 3iHm^2m'$$

$$\tilde{D} = 6im^3m' - iHm^3$$

$$\tilde{E} = im^4$$

$$\tilde{F} = 2G'm$$

$$\tilde{G} = 2(G+1)m$$

$$\tilde{V} = -iRm(\alpha G' - \beta F')$$

$$\tilde{W} = 2m(G+1)$$

$$\tilde{X} = -i\lambda^2 + R(\alpha F + \beta G - \omega) - iF$$

$$\tilde{Y} = imm' - iHm$$

$$\tilde{Z} = im^2$$